Cranfield University

Vasilios Zitounis

FATIGUE CRACK GROWTH RATES UNDER VARIABLE AMPLITUDE LOAD SPECTRA CONTAINING TENSILE UNDERLOADS

School of Industrial and Manufacturing Science

This thesis is submitted in partial fulfilment of the requirement for the Degree of Doctor of Philosophy

Cranfield University

School of Industrial and Manufacturing Science

Ph.D

2003-04

Vasilios Zitounis

Title: Fatigue Crack Growth Rates Under Variable Amplitude Load Spectra Containing Tensile Underloads

Supervisor: Prof. Phil E. Irving

28 October 2003

Abstract

An extensive research program was performed to investigate the load interaction effect of the combined action of small amplitude high R ratio cycles and large amplitude low R ratio underloads on the crack growth of large cracks. The study was driven by the needs of the damage tolerance approach in the helicopter structures, which requires robust knowledge on the crack growth behaviour of the advance high strength alloys under the characteristic helicopter spectra loading.

The study was conducted on three metallic alloys, Ti-10V-2Fe-3Al, Al8090 T852 and Al7010 T76351 using compact tension specimens (w=70mm, t=17mm). The potential drop technique was used for the measurements of the crack length. The crack opening loads were determined from the applied load versus crack opening mouth displacement curve using a curve fitting technique and crack opening displacement gauge.

The experimental results show that cracks can grow faster than the life predictions with no load interaction effects under spectra containing tensile underloads. The acceleration effects are different depending on the number of the small cycles, the K_{max}, the R ratio of the small cycles, the underload cycle and the material. Significant closure observations on the underloads and on the small cycles of variable amplitude loading spectra were made. Based on the test finding and on the studies of other researchers, it is suggested that the acceleration effects are mainly due to the reduction of crack opening point of the tensile underloads comparing with the Constant Amplitude Loading (CAL) data.

An extensive evaluation of the ability of FASTRAN model to predict the fatigue lives under the tested loading spectra was carried out. The evaluation focuses on the influence of the constraint factor a and the ΔK_{eff} curve inputs on the predictions. The model produces very good and consistent predictions for the three alloys, when the inputs represent adequately the actual fatigue mechanism. The model predicts the measured acceleration effects by reducing the closure level of the underloads.

ACKNOWLEDGEMENTS

These years have been for me a constant challenge, a difficult but pleasant journey towards personal knowledge and growth. The journey is near over and I feel the need to thank the people that stood by me all this time

I am immensely thankful to my supervisor Prof. Phil Irving for his invaluable support, advice and guidance throughout this year.

A 'thank you' goes to the project participants S. L. Jenkins, D. Matthews, B. Perrett, and J. W. Bristow. I would also like to acknowledge my present employers for their understanding and support.

My appreciation also goes to Tony Scott in the SIMS labs who gave me plenty of support on the test machines and equipment.

This thesis is dedicated to my family for their unconditional love and support and to all those people that believed in me and encouraged my efforts during these years.

Bristol 2003
Vasilios Zitounis

Ancient Greek *"είναι γάρ έν τό σοφόν, επίσταθαι γνώμην, οτέη εκυβέρνησε πάντα διά παντών"*

Modern Greek *"Η σοφία είναι ένα μόνο πράγμα: να γνωρίζεις ότι ο ορθός λόγος κυβερνά τα πάντα μέσα από τις εσωτερικές τους σχέσεις"*

English *"Wisdom is one thing: to understand with true judgment how all things are steered through all"*

Heraclitus

Table of Contents

Contents

Chapter 11

Table
Number Description Page

Chapter 10

Chapter 11

Frequently Used Symbols

a	**crack length**
a_f	**final crack length**
a_{in}	**initial crack length**
α	**acceleration factor associated with the crack growth rate**
	also: constraint factor
β	**acceleration factor associated with the number of cycles**
γ	**acceleration factor associated with the crack length increment**
C	**constant in Paris relation**
Δa	**crack length increment**
ΔN	**increment of number of cycles**
da/dN	**crack growth rate**
e	**measurement error**
E	**Young's modulus**
K	**stress intensity factor**
ΔK	**= K_{max}-K_{min}, stress intensity factor range**
K^*_{max}, $K_{max,T}$	**intrinsic threshold maximum intensity factor for crack growth**
ΔK^*_{th}, ΔK_T	**intrinsic threshold intensity factor range for crack growth**
K_0	**K at P_0**
K_{OL}	**overload stress intensity factor**
K_{IC}	**mode I critical value of K under plane strain, fracture toughness**
K_{max}	**maximum intensity factor**
K_{min}	**minimum intensity factor**
K_{PR}	**intensity factor at which fatigue crack starts to grow**
ΔK_{eff}	**effective stress intensity factor range**
ΔK_n	**small cycle stress intensity factor range (underloading spectrum)**
ΔK_u	**underload cycle stress intensity factor range (underloading spectrum)**
M	**exponent in the Paris relation**
N	**number of cycles**
n	**number of small amplitude cycles in an underloading spectrum**
P	**Load**
P_0	**crack opening load**
R	**load ratio**
R	**polar coordinate**
R_n	**small cycle load ratio (underloading spectrum)**
R_u, UR	**underload cycle load ratio (underloading spectrum)**
R_{tip}	**= K_w/K_{max}**
r_p	**plastic zone size**
r_c	**reverse plastic zone size**
t	**specimen thickness**
V	**voltage**
W	**specimen width**
Y	**geometry factor in the K relation**

ε	**strain**
θ	**polar coordinate**
σ	**material stress**
σ_0	**stress at crack opening load**
σ_{max}	**maximum stress**
σ_{min}	**minimum stress**
σ_{UTS}	**ultimate tensile strength**
σ_{YS}	**yield strength**

Acronyms

CAL	**Constant Amplitude Loading**
COD	**Crack Opening Displacement**
CT	**Compact Tension (sample)**
CVAL	**Complex Variable Amplitude Loading**
S-N Curve	**Stress-Life Endurance Cuve**
SVAL	**Simple Variable Amplitude Loading**

CHAPTER 1

INTRODUCTION

1.1 The Objective

Damage tolerance design philosophy, based on fatigue crack growth, is well established and applied in fixed wing aircraft. In contrast, helicopter components have been traditionally designed using safe life approaches. Damage tolerant design of helicopters requires data and understanding of how fatigue cracks develop in helicopter materials under helicopter load spectra.

The load spectra of many helicopter components consist of large numbers of load cycles at high R ratio (R>0.75). The rest of the spectrum consists of load cycles at R ratios between 0.4 and 0.7, with excursions to zero load. In cracked components, stress intensity ranges (ΔK) would be close to the threshold, ΔK_{th}. Prediction of fatigue crack growth rates requires an understanding of load interaction effects under these spectra.

The objective of this study is to investigate the effects between the low R ratio large amplitude cycles on the high R ratio small amplitude cycles, to estimate the fatigue crack growth mechanism under these conditions, establish the load interaction effects under typical helicopter spectra and improve the knowledge on their fatigue driving forces. The accurate establishment of the threshold intensity factor using different techniques and loading paths is necessary for the study because it sets the basis for the experimental procedure as it establishes the baseline where no crack growth is expected. Supporting tests, such that constant amplitude loading tests and metallography, are necessary to provide confirmation of the material properties and support the research with additional data. A linear summation model using CAL data was used to validate the test results. Some additional fatigue crack growth models were used to perform fatigue life prediction in order to validate their ability to predict the test results. The comparison between the test results and the life predictions was used as a tool to assess the model's fatigue mechanism against the experimental facts. The research uses three different metallic alloys. These are Ti1023, Al8090 and Al7010. The similarities or/and the differences of the fatigue crack growth behaviour on the alloys provide significant knowledge on the better understanding of crack propagation and the influencing parameters.

1.2 The Overview

This thesis has been constructed to give details on the facts, observations, arguments, and procedures in order to meet its objectives. Eleven chapters excluding the Introduction, were composed to present the series of logical thoughts.

Chapter 2 gives briefly the background of fatigue design of helicopter components. The design approaches adapted in the aerospace industry are defined and special attention is drawn on the issues of the successful application of the damage tolerance approach in helicopters.

Chapter 3 gives a detailed overview of the fundamental concepts of fracture mechanics, and its use in the characterization of the fatigue crack growth. These principles form the basis for the application of the damage tolerance approach in the fatigue design.

Chapter 4 presents the up to date research on the field of the fatigue driving mechanisms. The well-established concept of the reduced effectiveness of the applied cycle is examined and the various measurement techniques are reviewed.

The fatigue crack growth in the near threshold area and under the variable amplitude loading is examined in Chapter 5 under the light of the most recent research findings. Especially, the research of the load interaction effects of sequences containing underload cycles on crack propagation has been reviewed. The most representative fatigue prediction models are reviewed.

Chapter 6 describes the testing procedures followed in this research. The material properties of the three alloys used in this research, Ti1023, Al8090 and Al7010 are presented. The full details on the measurements of the crack growth are given. This includes the technique for the measurement of the crack length and the relative measurement errors, the developed software and measurement system. Also, details and justification reasons are given on the adopted method for the closure measurements and the relative measurement errors. The behaviour of the maximum crack growth is presented. The chapter also includes the full test

program on the threshold stress intensity factor range measurements, and the simple and complex variable amplitude loading tests.

Chapter 7 defines the parameters for the estimation and calculation of the load interaction effects during the fatigue loading. Also, the basic data input requirements and the adjusted parameters are determined in order to prepare the run of the different fatigue crack growth models used in this research

Chapter 8 shows the experimental results of the conducted test program. The test results include crack growth, crack growth rate and crack closure measurements. The experimental measurements were conducted under underloading sequences. The effects of the number of the high R ratio small cycles, the level of the maximum level of the stress intensity factor, the R ratio of the small and the underloads were measured on the three different material alloys. The effects of various versions of the helicopter spectrum were examined on the three alloys. The variable amplitude loading tests were supporting from constant amplitude loading data, fatigue threshold measurements and fractographic evidences.

An extensive discussion in the light of the objective of the study is presented in Chapter 9. The discussion aims to determine the experimental facts and correlate them with the current international research on the field of fatigue load interaction effects, fatigue crack growth mechanisms and life prediction models. Using a series of logical arguments based on the experimental findings, the fatigue analysis and the reported literature, the study leads to conclusions and suggestions about the fatigue crack growth mechanisms under the underloading and helicopter spectra and the examined fatigue life prediction models.

The correlation of the crack growth rates with the crack closure values are necessary to produce and assess the formation of the crack growth rate curve in terms of the effective part of the loading cycles. The procedure involves the determination of the crack growth rates of the underload cycles and their interpretation with the respective closure values. The crack growth rate calculations and the production of the ΔK_{eff} curve for each material alloy are given in Chapter 10.

Chapter 11 presents all the details of the fatigue crack growth live prediction on both underloading and complex helicopter spectra. The life predictions were carried out using FASTRAN model with three characteristic data inputs. The ability of the model to predict the effects of the different loading parameters on the crack growth is observed. Also, the study of different input reveals the effect of the model's constraint factor and the effective ΔK curve on the life predictions. The issues related with the life predictions are discussed at the end of the Chapter.

The conclusions of the present research are summarized and presented in Chapter 12. Suggestions about future work are put forward in this chapter.

CHAPTER 2

HELICOPTER DESIGN AGAINST FATIGUE

2.1 Introduction

Fatigue design of helicopter components has proven to be a difficult and challenging task. The aims of fatigue evaluation of a helicopter are to establish that within the working life, the expectation of catastrophic failure from fatigue origins is extremely remote and, additionally, the incidence of non-catastrophic cracking is maintained at a sufficiently low level to enable economic utilization of the aircraft structure to be maintained [1]. These aims have to be achieved within the framework of minimum weight and cost, and maximum performance.

In order to determine the fatigue life of helicopter components three basic factors must be known [2]. The first factor is the fatigue strength of the component. The information for this factor is usually obtained by Constant Amplitude Loading (CAL) tests of several specimens of the actual component in order to describe the stress amplitude versus cycles to failure (S-N). The second factor is the loads or stresses to be expected in service and the third factor is the frequency of occurrence of these loads or stress. It is impossible for the designer to know the exact flight load at the beginning. Previous loading information, which involves extensive flight load survey measured in many level flight at similar structures, is extremely important for the design

'Safe Life' approach and 'Damage Tolerance' analysis are the two possible ways of fatigue design. The fatigue design methods are described in FAA Advisor Circular (AC) 29.571 [3]. Safe life aims to ensure the initiation of crack will not occur in the structure during its service life. The approach implies that component's life can be predicted and therefore it will be repaired or replaced according to the manufacture's recommendations. The method uses S-N data or strain amplitude versus cycles (ε-N) data to predict structural component life. The Damage Tolerance approach assumes the existence of an initial flaw in the structure. With structural inspections, fatigue cracks growing from the flaws must be detected. Then, it must be ensured that the existence of these cracks does not reduce the strength of the structure below the design limit load. Otherwise, the structure must be repaired, replaced or withdrawn from service. Structural strength can be ensured if the dominant crack has not reached a critical dimension. The choice of the critical size for the fatigue crack may be based on the fracture toughness of the material, which express the critical load at which the crack initiates under

monotonic, quasi-static loading, the limit load for the particular structural part, the allowable strain or the permissible change in the compliance of the component (figure 2.1). Damage tolerance uses fracture mechanics for the prediction of slow flaw growth as defined in AC 29.571[4].

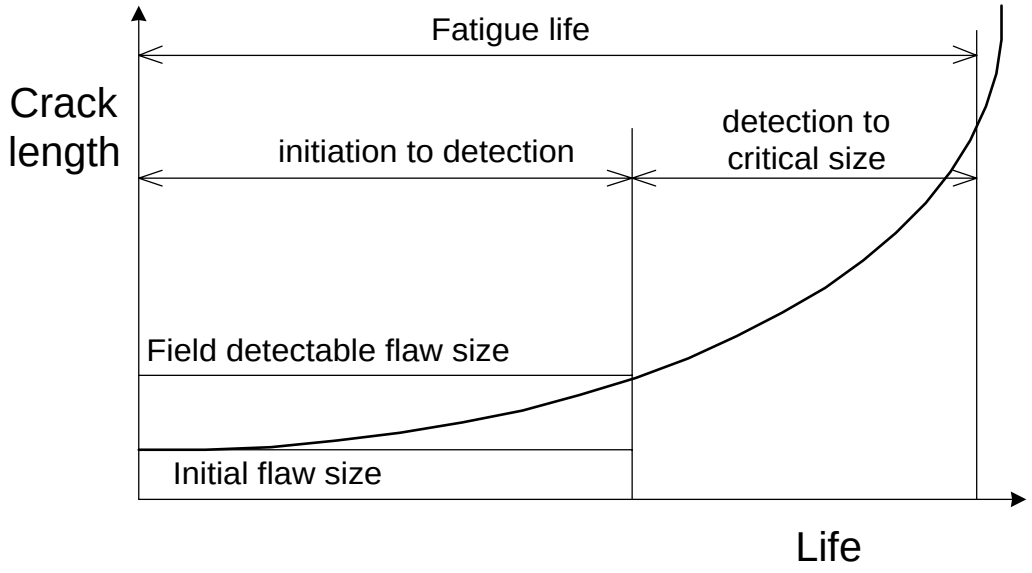

Figure 2.1_ Crack growth curve for a structural component

2.2 Issues Of Damage Tolerance Approach In Helicopters

Safe life methodology cannot guard against the unexpected and abnormal in the fatigue process and there have been occurrences of premature fatigue cracking originating from corrosion, accidental damage in service, damage in manufacture that had escape the inspection procedures, abnormal load situations and so on [5]. To guard against such incidents requires the introduction of damage tolerance analysis in design. Also, damage tolerance is considered to be superior to Safe Life because of some additional reasons. Safe Life uses S-N curves as the basic prediction tool. These curves have been derived by testing specimens under constant amplitude loading whereas the service loads are very complex [6]. The Miner ‘s rule is a simple criterion for predicting the extent of fatigue damage and uses the S-N curve to calculate the fatigue life of a component [7]. It does not into account load interaction effects of cycles, which play an important role in the total fatigue life.

The damage tolerance approach has been used in fixed wind aircraft for many years. This procedure is very desirable but is much more difficult to attain in helicopter dynamic components than in typical fixed wing structures [8]. One reason is because of the degree of freedom that enable helicopters to fly and the necessary interface between rotating and non-rotating parts [2]. Due to this reason, a highly variable loading is experienced by the structure. Another reason is the rapid accumulation of loading cycles and the consequent tie-in with the necessary inspection intervals and the procedures to enable the approach to work properly [2]. The high strength material used in the existing designs is another problem [9]. These materials usually have good performance under Safe Life design but might have undesirable fatigue crack growth properties.

Marquet and Struzik of Eurocopter [8] provide a good summary of the difficulties of application of Damage Tolerance design in helicopters. Two of these are a) the lack of understanding of fatigue crack growth in the near-threshold region and b) the lack of understanding of load interaction effects in helicopter load sequences and in particular the effect of the ground-air-ground cycle on crack growth.

There is a major design challenge to apply Damage Tolerance principles to all the vital parts of a helicopter structure. Efforts have been carried out by the manufacturs to successfully adapt this method to helicopters.

Messerschmitt-Bolkow-Blohm (MBB) Helicopters has already in operation many vital components designed with Damage Tolerance concepts such as the main rotor hub, the inner sleeve, the upper control assembly, the tail rotor control, the tail rotor shaft, and the engine mount system [10].

Bell Helicopter Textron has started to apply Damage Tolerance design approach to part of their structure [2]. One major helicopter component which some success has been recently achieved using this method is the main rotor metal blade. Another component, which holds even more promise, is the all-composite main rotor blade, which can exhibit very favurable damage tolerance characteristics. Such blades used on the Bell Model 214B have received FAA certifications. The manufacturer carried out an extensive test program including fatigue and static tests on coupons, structural elements and full-scale structure to develop the necessary information for the analysis.

CHAPTER 3

DAMAGE TOLERANCE APPROACH

3.1 Linear Elastic Crack-Tip Stress Field

The damage tolerance approach uses linear elastic fracture mechanics [11] to analyze crack or flaws. Irwin has presented solution for crack-tip stress distributions [12], using the analytical method of Westrgaard [13]. The solutions were associated with the three modes of fracture. Each mode involves different crack surface displacements (figure 3.1).

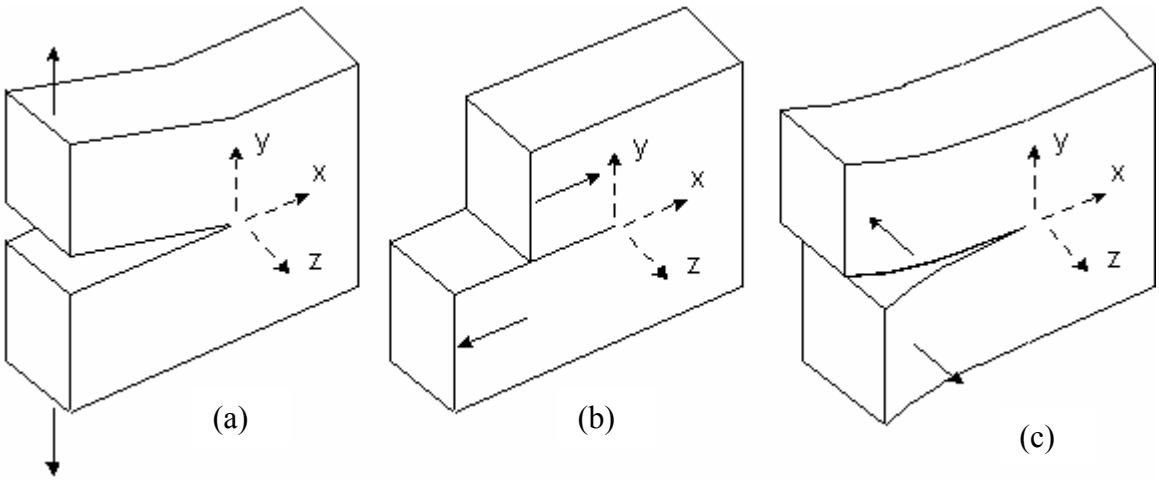

Figure 3.1_ The three basic mode of fracture. (a) Tensile opening (Mode I). (b) In-plane sliding (Mode II). (c) Anti-plane shear (Mode III)

Mode I is the tensile opening mode in which the crack faces separate in a direction normal to the plane of the crack.

Mode II is the in-plane sliding mode in which the crack faces are mutually sheared in a direction normal to the crack front.

Mode III is the tearing or the anti-plane shear mode in which the crack faces are sheared parallel to the crack front.

The present study is only concerned with Mode I fracture. Therefore, only Mode I stress crack-length relations will be presented. For the notation of figure 3.2, the crack tip stresses are found to be :

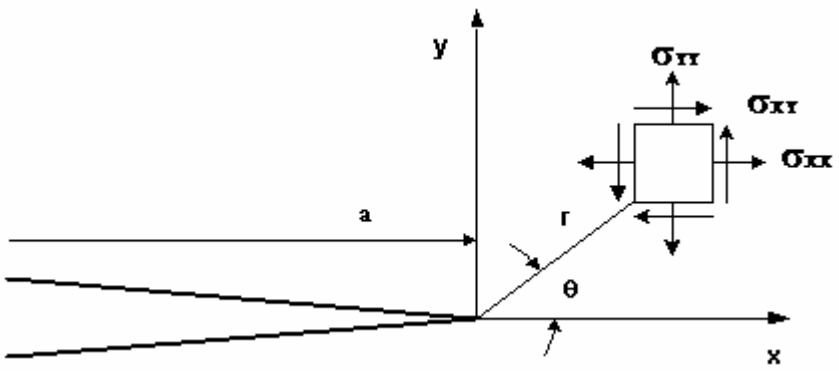

Figure 3.2_ Coordinate system and stresses at the near crack-tip region

$$\sigma_{YY} = \frac{K_I}{\sqrt{2\pi r}}\cos\frac{\theta}{2}\left(1+\sin\frac{\theta}{2}\sin\frac{3\theta}{2}\right)$$

$$\sigma_{XX} = \frac{K_I}{\sqrt{2\pi r}}\cos\frac{\theta}{2}\left(1-\sin\frac{\theta}{2}\sin\frac{3\theta}{2}\right) \qquad (3\text{-}1)$$

$$\sigma_{XY} = \frac{K_I}{\sqrt{2\pi r}}\left(\sin\frac{\theta}{2}\cos\frac{\theta}{2}\cos\frac{3\theta}{2}\right)$$

An important feature of Eq. 3-1 is the fact that stress field around the crack tip depends only on r and θ for a given value of K_I. The difference between structures with the same crack configurations lies in the magnitude of the stress field parameter K_I. K_I is defined as the stress intensity factor for Mode I and is expressed by the following equation:

$$K_I = Y\sigma_{yy}\sqrt{\pi\alpha} \qquad (3\text{-}2)$$

Where σ_{YY} is the applied stress, α is the crack length, and Y is a dimensionless factor that depends on crack length and component geometry. Stress intensity factors have been obtained for many crack geometries and several handbooks are available [14, 15].

The stress intensity factor is a measure of the intensity of the near-tip fields under linear elastic conditions. The factor provides a unique measure of the intensity of stress within an annular zone ahead of the crack tip. The outer zone is defined from the annular zone at which the eq. 3-2 deviates significantly from the full elastic solution [5]. The inner radius of the K-dominance region is dictated by the plastic zone, which is created from the yielding of the material when the near-

tip exceed the flow strength. In this area the linear elastic solution lose its validity because of the assumption of linear elastic behaviour.

The stress field around the crack tip expressed by Eq. 3-1, is proportional to $r^{-1/2}$. Theoretically, this means that at the crack tip the material is subjected to infinite stresses. This is not possible and what happens is that the material is plastically deformed near the crack tip. As a result stresses are lowered to a first approximation to the level of yield strength of the material (figure 3.3).

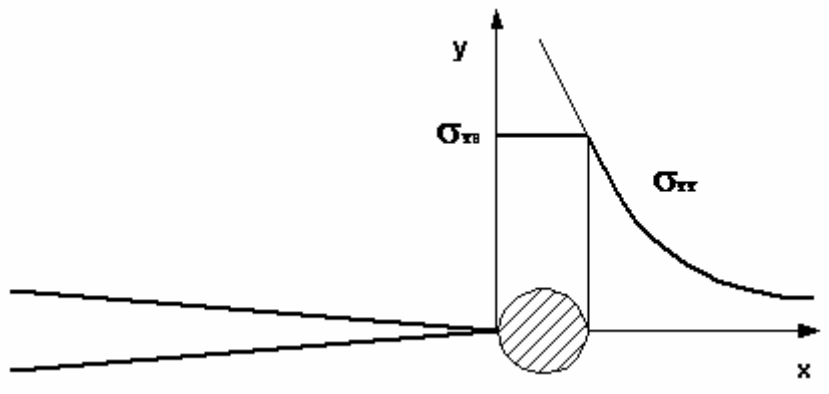

Figure 3.3_ Crack tip plastic zone under small-scale yielding condition

The stress intensity factor can characterised the crack propagation under the 'small-scale yielding' condition. This condition requires that the crack tip zone of the inelastic deformation be confined well inside the region of the K-dominance where the solution (Eq. 3-1), provided a reasonable approximation of the full solution.

3.2 Fracture Toughness

In linear fracture mechanics, fracture toughness of a material is called the limiting stress intensity factor that cause catastrophic fracture in all components made from the same material. Fracture toughness is a material property and a function of the mode of loading, the chemical environment, the material microstructure, the test temperature, the strain rate, and the state of stress (plane stress or plane strain) [16]. Since K relates load, crack length, and structural geometry, this factor allows one to relate fracture measurements of laboratory specimens with failure of a different structural component. The critical value of the

mode I stress intensity factor measured under plane strain conditions is commonly referred to as the fracture toughness K_{IC}.

3.2 Crack-Tip Plastic Zone Size

3.2.1. Monotonic Loading

3.2.1.1. The Irwin Approximation

A first estimation of the plastic zone size under monotonic loading can be derived if we consider the stress σ_{YY} at θ=0. The stress will be then expressed by the equation:

$$\sigma_{YY} = (K_I / \sqrt{2\pi r}) \quad (3\text{-}3)$$

Irwin [17] suggested that under small-scale yielding, the plastic zone will be a circular zone of radius r_p which can be derived for Eq. 3-3 when the stress σ_{YY} is equal to the yield stress of the material σ_{YS}.

$$r_p = (1/2\pi)(K_I / \sigma_{YS})^2 \quad (3\text{-}4)$$

This r_p underestimates the reality, because it ignores the re-distribution of stress field due to the plastic zone. Using the Von Mises yield criterion a better approximation of the plastic zone size can be derived. By this criterion, yielding occurs at a particular state of stress (σ_{XX}, σ_{YY}, σ_{ZZ}, σ_{XY}, σ_{YZ}, σ_{XZ}) when:

$$2\sigma_{YS}^2 = (\sigma_{XX} - \sigma_{YY})^2 + (\sigma_{XX} - \sigma_{ZZ})^2 + (\sigma_{YY} - \sigma_{ZZ})^2 + 6(\sigma_{XY}^2 + \sigma_{XZ}^2 + \sigma_{YZ}^2) \quad (3\text{-}5)$$

Combining the Eq. 3-1 and 3-5, the extent of the plastic zone ahead of the crack tip (θ=0) is given by the equations:

$$r_p = (1/\pi)(K_I / \sigma_{YS})^2, \quad \text{for plane stress}$$

$$r_p = (1/3\pi)(K_I / \sigma_{YS})^2, \quad \text{for plane strain} \quad (3\text{-}6)$$

In reality, the crack specimens have a certain thickness, which constrains the material in the interior, and hence creates near plane strain conditions. At and near the surfaces plane stress conditions will prevail since it is free of stresses (σ_{zz} =0). Based on the size of the plastic zone for each stress state condition, an estimation of the plastic zone shape though the thickness can be seen in figure 3.4. The plastic zone size is large at the free surface due to plane stress conditions and gradually decrease to a small size at the centre of the sheet where plane strain conditions prevail.

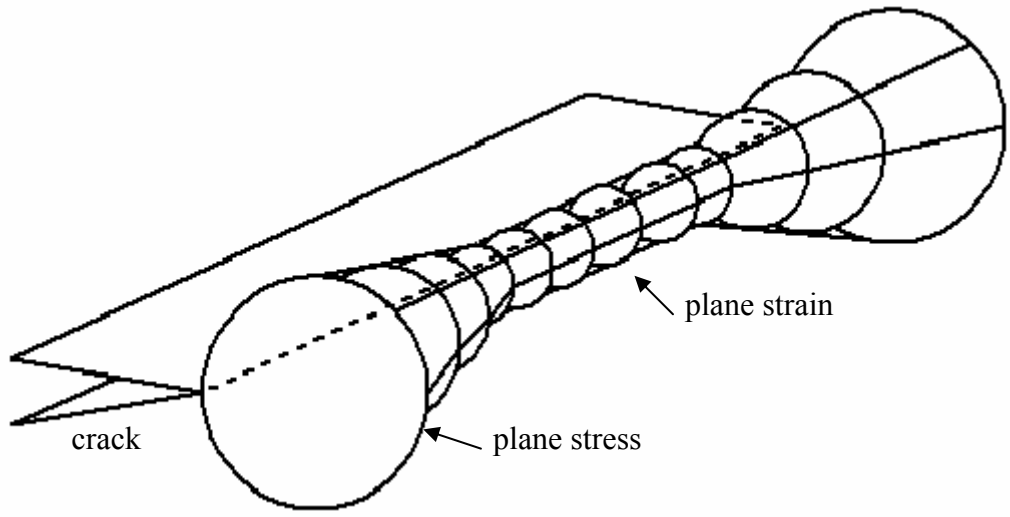

Figure 3.4_ Effect of thickness in the crack tip plastic zone size.

In figure 3.5, the plane stress and plane strain condition elements near the crack tip are shown. In the plane stress, when a load level is reached, a failure will occur on plane ±45°, due to the maximum shear stress on this plane. In the plane strain, because the σ_{xx}, σ_{yy} and σ_{zz} are active, a higher level of load must be reached for the failure to occur. Hence a smaller plastic zone is created and failure possibly occurs in the plane of the crack before a critical shear stress is achieved.

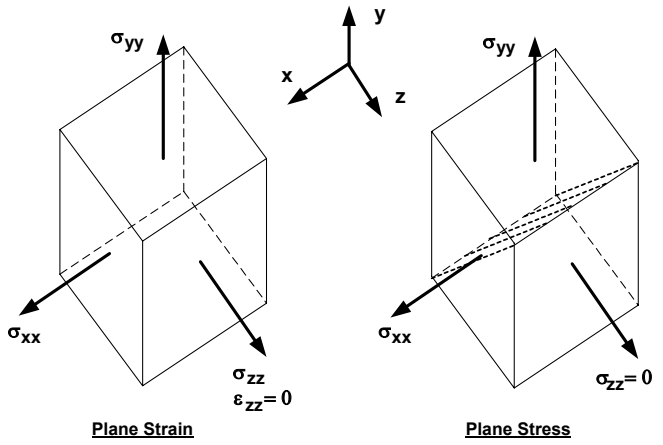

Figure 3.5_ Plane strain and plane stress elements near the crack tip.

3.2.1.2. The Dugdale Model

Another model for the crack tip plastic zone size has been proposed by Dugdale [18]. The plastic zone is considered as a narrow strip zone of r_p length ahead of the crack tip, which is loaded with σ_{YS} stress (figure 3.6). Dugdale suggested that the crack tip zone size is given by the equation:

$$r_p = (\pi/8)(K_I/\sigma_{YS})^2 \qquad (3\text{-}7)$$

The suggested estimation for r_P for plane stress compares well with the Irwin approximation, Eq. 3-4, although the different plastic zone shape.

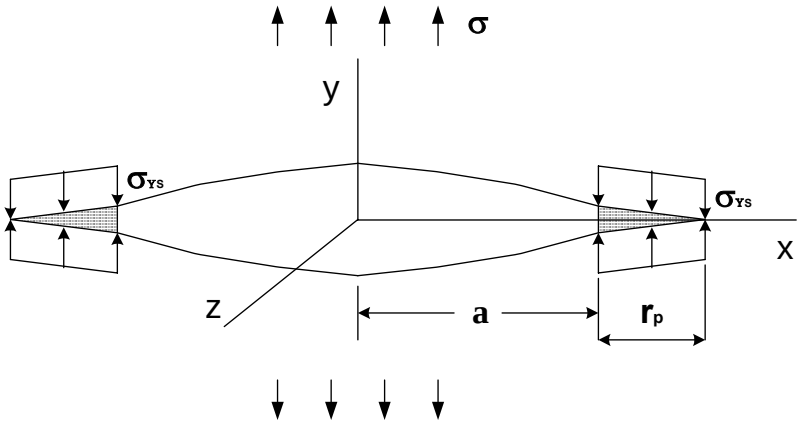

Figure 3.6_ Dugdale crack tip plastic zone strip model

3.3.2. Cyclic Loading

The application of stress σ on a cracked solid creates a stress field near the crack tip, which can be characterised by the stress intensity factor K_1 under small scale yielding conditions. Under this condition, the material yields ahead of the crack tip and develops a monotonic plastic zone of dimension given by the equation 3-7. When the direction of loading reverses, the local stress is reduced to a level corresponding to a stress intensity factor K_2. The re-distribution of the stresses in the near crack tip region because of the reduction form K_1 to K_2 will lead to reverse plastic flow and the formation of plastic zone in front of the crack tip [19] embedded within the monotonic plastic zone.

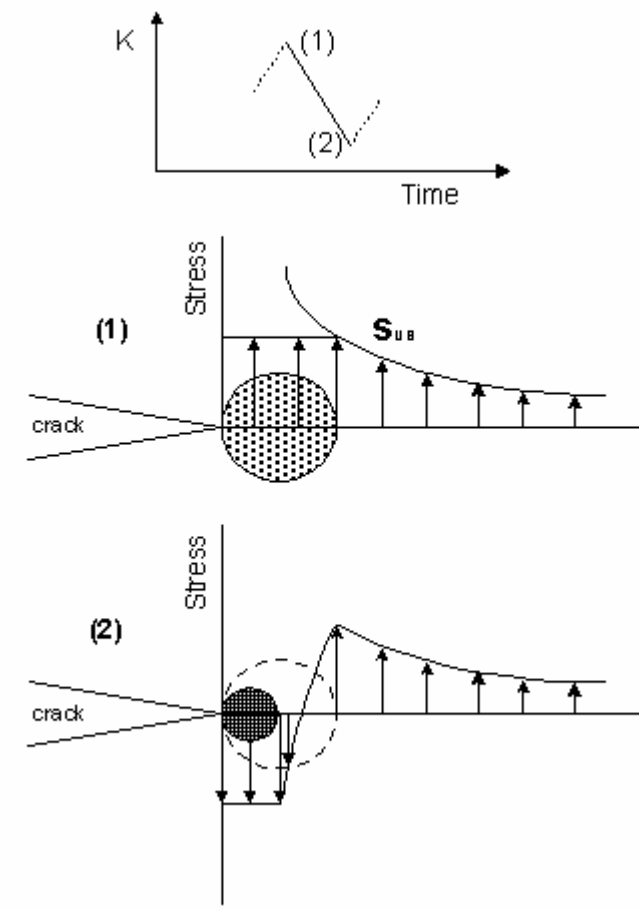

Figure 3.7_ Monotonic and reversed plastic zone development at the crack tip during cycling unloading

The stresses in the reversed plastic zone are equal to the yield stress σ_{YS} in compression. The size of this smaller plastic zone, which experience alternating tensile and compressive yielding, can be estimated by substituting $\Delta K=K_1-K_2$ and $2\sigma_{YS}$ for σ_{YS}, since the stresses move from tension to compression, in Eq. 3-7, for plane stress:

$$r_c = (1/\pi)(\Delta K / 2\sigma_{YS})^2 \qquad (3\text{-}8)$$

The size of the reverse plastic zone r_c and cyclic variations in the stress, strain and displacements depend only on ΔK and are independent of the maximum load K_1.

3.4 Characterization Of Fatigue Crack Growth

Damage Tolerance analysis assumes the preexistence of an initial flaw or defect in the component. The stress intensity factor K concept can be used to correlate the externally applied cyclic load to the component with the fatigue crack growth. For conditions of small-scale yielding, where the nonlinear zone at the crack tip is a mere perturbation in an otherwise elastic material, Paris, Gomez and Anderson [20] and Paris and Erdogan [21] postulated that the growth of a crack under cyclic loading could be governed by the law:

$$\frac{da}{dN} = C\Delta K^m \qquad (3\text{-}9)$$

where da/dN is the change in the crack length of the fatigue crack per load cycle (a is the crack length and N is the number of fatigue cycles) and ΔK is the is the stress intensity factor range defined as:

$$\Delta K = K_{max} - K_{min} \qquad (3\text{-}10)$$

K_{max} and K_{min} are the maximum and minimum stress intensity factors corresponding to the externally applied maximum σ_{max} and minimum σ_{min} load. Stress intensity factor correlates the externally applied loads with the near crack tip

stress conditions (Eq. 3-2) with the fatigue damage at the crack (Eq. 3-9). It become obvious that stress intensity range ΔK controls the fatigue crack growth rate. This fact enable the direct comparison of fatigue crack growth rates obtained from laboratory specimens with crack growth rates of structural components of the same material under the same stress intensity conditions.

The terms C and m in equation are empirical constants which are functions of the material properties and microstructure, fatigue loading sequence, mean stress or load ratio R ($R=K_{min}/K_{max}$), environment, loading mode stress state and test temperature [5].

The Paris power law relationship describes only a portion of the total crack growth of a material. Most materials show a sigmoidal variation of the crack growth rates with the ΔK as shown in figure 3.8. In this plot three distinct regime of crack growth can be identified: regime I which is the near threshold region, regime II governed by Paris law, and regime III in which high ΔK values cause very rapid crack growth rates leading to catastrophic failure.

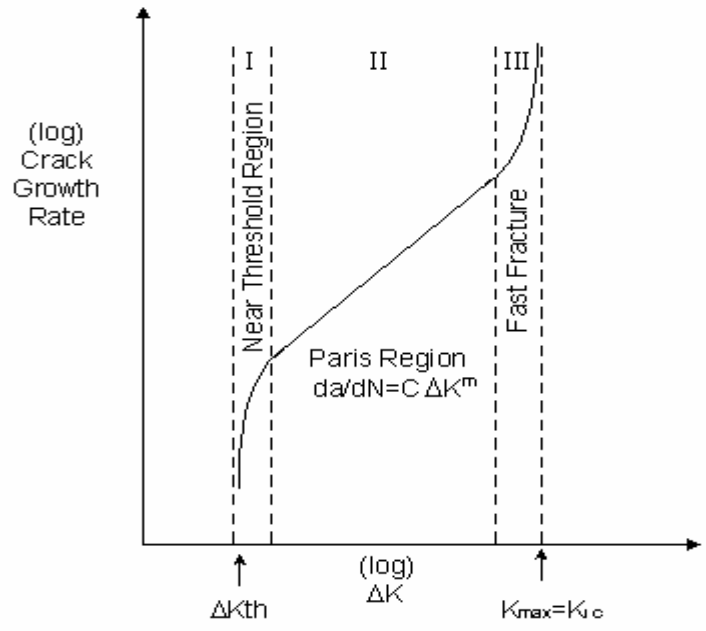

Figure 3.8_ Different regimes of fatigue crack propagation

The fatigue threshold ΔK_{th} is defined as the largest excursion of the stress intensity factor range which does not produce fatigue crack growth (or rates da/dN

≤ 10^{-10}m/cycle) under certain loading conditions [22]. The ΔK_{th} depends on loading parameters such that K_{max} and R ratio and the material. It has been suggested that the lower limit of ΔK_{th}, called ΔK_T, below which cracks do not propagate under any loading conditions, is a intrinsic property of the material [23]. At the other extreme is the very rapid increase in growth rates as K_{max} approaches the material's fracture toughness K_{IC}.

Threshold values have been found to depend on load ratio R, microstructure, environment, and crack tip constraints (such as constant R-ratio or constant K_{max} tests, etc.) and specimen geometry [16, 24].

Except for the threshold value of ΔK_{th} which is a lower bound condition for fatigue crack growth rate (the highest estimated value of ΔK), another two governing threshold conditions are reported: one relating to crack growth in single crystals, and one concerned with crack growth in polycrystalline materials [25].

Fatigue crack growth under cyclic loading occurs at stress intensity levels, $K_{max}=\Delta K/(1-R)$, that are well below the fracture toughness K_{IC}.

Because the empirical constants C and m are functions of test environment and loading conditions, changes in tests conditions can lead to changes to C and m and consequently to the crack growth rates. For fixed environment conditions, it is expected the fatigue crack rates to be strongly influenced not only by ΔK, but also by the load ratio, R. The fatigue crack growth is more accurately described by two parameters, stress intensity range, ΔK, and load ratio, R, or ΔK, and maximum stress intensity factor $K_{max}=\Delta K/(1-R)$. On that basis, Forman et al [26] have suggested the following expression to relate crack growth rates da/dN with ΔK and R.

$$da/dN = (C\Delta K^{m})/[(1-R)(K_{IC}-K_{max})] \qquad (3\text{-}11)$$

In general, many other model have used the following form:

$$da/dN = f(\Delta K, R) = f(\Delta K, K_{max}) \qquad (3\text{-}12)$$

It should be emphasised that the above crack growth models are empirical curve fits and they have no fundamental and analytical relevance. Models for fatigue crack growth are used for the original objective of damage tolerance approach, the prediction of fatigue life of a component.

CHAPTER 4

FATIGUE CRACK GROWTH MECHANISMS

4.1 Introduction

Various mechanisms have been proposed to explain fatigue crack growth under constant amplitude loading and complex fatigue loading histories. Examples of some of them are crack tip blunting and resharpening [27, 19], crack closure effects [28], cyclic hardening and residual stresses in the plastic zone [29, 30, 31]. Crack closure and residual stresses in the plastic zone have been considered the most important fatigue crack growth mechanisms and this can become clear by the amount of research on these topics. A more detailed presentation of these two mechanisms will be given in the next paragraphs.

It is often different mechanisms operate simultaneously at the overall crack growth. This fact makes difficult the identification of the individual contribution of each of these mechanisms to the overall crack growth rates. Therefore, this raises discussion and different opinions on the significance of each mechanism on the fatigue crack growth.

4.2 Effective ΔK and Crack Closure

When the material is stressed elastically under tension, the change of the applied stress from σ_o to σ_{max} will be a linear function of the displacement of the crack surface, called Crack Opening Displacement (COD). This behaviour is exhibited by the line II in the figure 4.1.

Elber first observed that fatigue cracks can close even during tension-tension far field loading [30]. He argued that a zone of residual tensile deformation is left in the wake of a fatigue crack tip. The deformed material causes contact between the fracture surface of the fatigue crack and results in a reduction of the applied amplitude ΔK, so that only a reduced part of it contributes to crack propagation. This mechanism is known as plasticity induced-closure. But, it has been found that there are some additional closure mechanisms like roughness induced-closure [16] and oxide induced-closure [5, 32], which can cause premature contact of the fatigue crack surfaces.

A typical variation of COD versus far field applied stress σ can be seen in figure 4.1. The recorded curve (curve I) can be separated in two parts. An upper linear part and a lower non-linear part. The two parts are distinguished at the opening stress σ_o. The linear part of the crack above this point expresses elastic behaviour. A saw cut instead of a fatigue crack will exhibit the fully linear behaviour of line II because of the non-existence of the plastic deformation on the wake of the crack. The similarity of the behaviour between the upper part of the curve describing a fatigue crack and the saw cut reveals that fatigue crack surfaces are not in contact at stress levels higher that σ_o. For lower values of stress than σ_o the curve I deviates from the linear behaviour. The slope of the curve becomes larger, the stiffness is higher and the specimen behaves as if the crack is shorter. This is the result of the crack being partially closed due to the contact of the fatigue crack surfaces. The contact of the crack surfaces starts at the crack tip and continues further away from the crack tip as the applied stress decreases (figure 4.2).

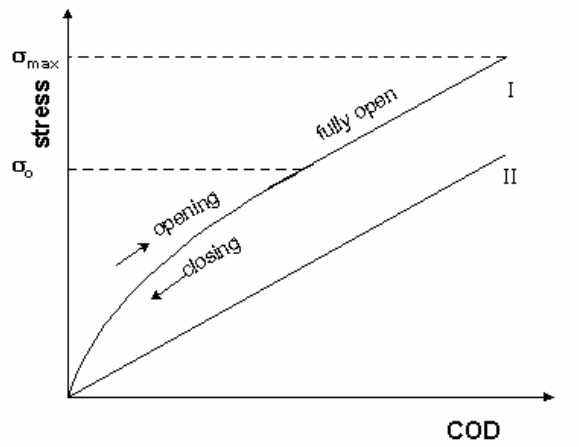

Figure 4.1_ Relationship between crack opening displacement (COD) and far field applied stress σ, (I) with the presents of crack closure and (II) without crack closure.

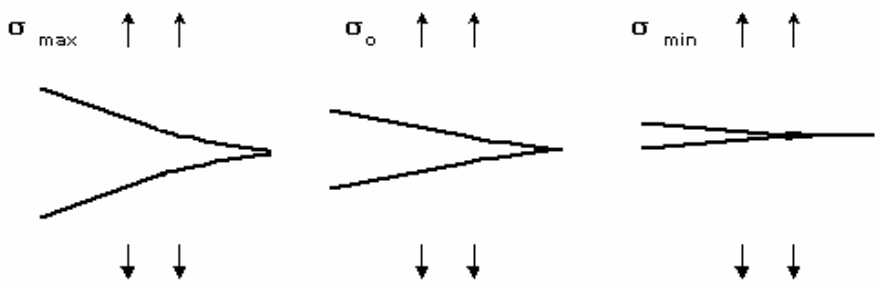

Figure 4.2_ Crack opening displacement at far field stress σ_{max}, σ_o, σ_{min}, in the presence of crack closure

Elber argued that the crack can propagate only during that fraction of the fatigue loading cycle in which the crack surfaces are separated (figure 4.3). The effective stress range $\Delta\sigma_{eff}$ and the effective stress intensity factor range ΔK_{eff}, which are responsible for crack growth are given by the equations:

$$\Delta\sigma_{eff} = \sigma_{max} - \sigma_{op} = U\Delta\sigma \tag{4-1}$$

$$\Delta K_{eff} = K_{max} - K_{op} = U\Delta K \tag{4-2}$$

where $\Delta\sigma=\sigma_{max}-\sigma_{min}$ and $\Delta K=K_{max}-K_{min}$ are the applied stress range and the stress intensity factor range. It is apparent that U is the quantity:

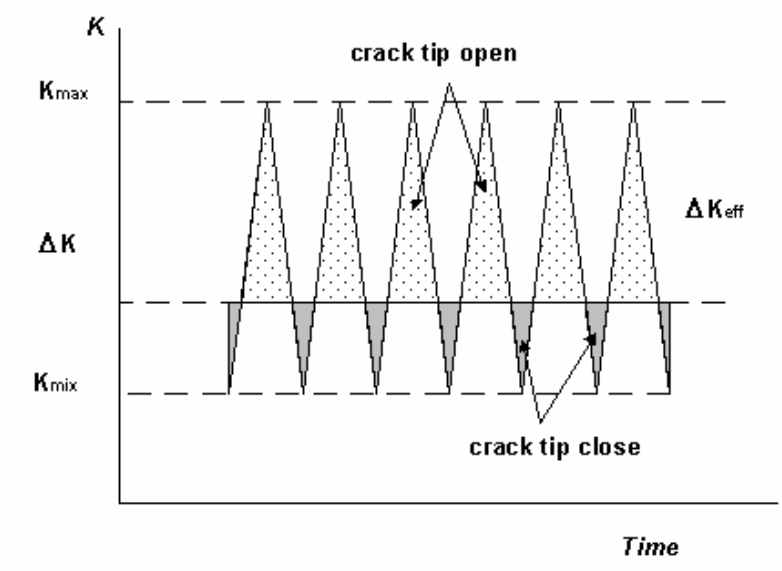

Figure 4.3_ Crack tip behaviour during the loading cycles at the presence of crack closure

$$U = \frac{\Delta\sigma_{eff}}{\Delta\sigma} = \frac{\Delta K_{eff}}{\Delta K} \tag{4-3}$$

The fatigue crack growth can be then characterised by a transformation of Paris equation:

$$da/dN = C(\Delta K_{eff})^m \tag{4-4}$$

Elber has proven that experimental data of da/dN versus ΔK which vary significantly with the load R ratio, collapse into the single and unique curve when they are reformed in terms of ΔK_{eff}. This means that Eq. 4-4 is a unique relationship between da/dN and ΔK_{eff} and that similar crack growth rates will occurs under the action of the same effective stress intensity range.

Hence, fatigue crack growth is influenced by conditions not only ahead of the crack tip but also behind of the crack tip and particularly the crack fracture surfaces. In the following paragraphs a detailed look will be given to plasticity and roughness induced-closure.

4.2.1. Plasticity Induced-Closure And ΔK_{eff}

During every cyclic loading, the stress field ahead of the crack tip causes the formation of a monotonic plastic zone and an embedded reverse plastic zone within the monotonic zone. During loading from minimum to maximum far field load, the crack advances through the residual tensile strains. As a result plastic deformation in the loading direction is left in the wake of the crack. This mean that the crack surface can contact while the specimen is still under a far field tensile stress. The phenomenon is known as plasticity induced-crack closure. Therefore, closure of the crack occurs as a result of plastic deformation of the material behind the crack. Elber was led to this fatigue mechanism based on measured crack opening displacement (COD) of the material near the crack edges as a function of the far field applied stress σ.

Although, there is a variety of experimental evidence [33, 34, 35, 36] supporting the role of plasticity induced closure in influencing crack growth, many observation on delay effects in a number of alloys are inconsistent with this mechanism [37, 38].

4.2.1.1 Plane Stress-Plane Strain

It has been shown in chapter 3 that the plastic zone size formed ahead of the crack tip varies with the thickness of the material. Hence, near the surface of the

material, plane stress prevails (σ_z=0) where as plane strain can describe better the conditions in the middle (e_z=0). The plastic zone size expected to be larger near the material surface due to plane stress conditions and smaller in the middle due to plane strain conditions.

Plastic zone size is directly associated with the plastic wake field of the fatigue crack and therefore with crack closure. Larger plastic zone size near the surface of the material should lead to the increase of the crack closure near the surface. It implies that fatigue cracks open first at the middle of the thickness and later at the material surface. As a result the ends of the crack near the surface will experience lower values of ΔK_{eff} and the crack edges will trail behind the part of the advancing crack front in the middle (figure 4.4).

Under plane stress conditions, the plastic wake field of the crack occurs by the material elongation in the loading direction. Negative plastic strain in the thickness direction (ε_z), which occurs at the surface of the material, is responsible for the extra material needed for the elongation in the loading direction. Budiansky and Hutchinson have analysed this type of fatigue crack closure [39]. Under plane strain conditions, negative plastic strain in the thickness direction is impossible because of ε_z=0. Pippan et al [35, 40, 41] have shown using dislocation mechanics as well as continuum mechanics that the elastically constrained plastic deformation during fatigue crack propagation gives rise to a rotation of the material in the wake, which in turn leads to the transport of the material in the crack growth direction and to crack surface contact near the crack tip. Because it is an elastic effect, no extra material layer remains on the crack surface. The elastic wedge formed is about the same size as the plastic zone. They have also shown that the shielding capacity of wedges is able to considerably shield a crack from the remote loading.

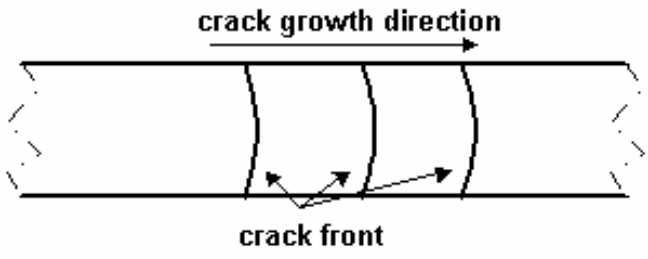

Figure 4.4_ Curved front of a growing crack

4.2.2 Roughness Induced-Crack Closure

Crack closure as discussed in the previous paragraph assumes a perfect fit between the crack fracture surfaces. In reality, the fracture surface contacts have a more complex nature. Therefore, mismatching of the two surfaces is highly likely. The resulted tortuous crack path provides the mechanism for the enhanced crack closure, which is called roughness induced crack closure.

Suresh provides a good summary of possible reason for the promotion of roughness induced crack closure [30]. Some of them are low stress intensity factor levels and ranges during a test, the occurrence of mixed mode sliding of crack surfaces, and the mismatch between the crack faces asperities. Roughness induced crack closure plays an important role in the crack growth of the near threshold regime. One can easily envisage the development of crack closure when crack tip opening displacements are comparable with the height of crack face roughness. Roughness induced crack closure is a mechanism by which some of the apparent microstructural effects on the fatigue crack growth can be rationalised.

Kim and Lee have studied the roughness induced crack closure using a single asperity model [42]. They found that crack closure behaviour during tests conducted at R ratios of –1, 0.0, 0.1, and 0.3 can be described effectively by their model. Jung and Antolovich [43] have developed a simple analytical model to predict variation of closure stress intensity factors as a function of crack length. From their analysis, the variation of closure stress intensity was shown to be directly correlated to the roughness dimension (or the asperity height) on crack surfaces. The resulted data appears to correlate very well with the analytical results. Parry et al. have studied roughness induced crack closure, modelling a deflecting crack with finite elements [44]. Among the others, they conclude that periodic crack deflections significantly increase crack closure levels in plane strain conditions, with the effect increasing as the deflection of the crack becomes more frequent.

4.3 Crack Tip Residual Stresses Effect

Residual stresses formed ahead of the crack tip due to the cyclic plastic deformation have an important role in fatigue crack propagation. A significant

number of researchers have suggested that residual stresses ahead of the fatigue crack tip are the dominant mechanism, which controls fatigue crack growth. Their research is reviewed in the following paragraphs.

Schijve observing the effects of load interaction [30] suggested that the retardation of a propagating crack by a single overload was due to residual compressive stresses around the crack front. The concept of residual stresses mechanism demands that tensile stresses ahead of the crack tip are a necessary condition for fatigue crack propagation. The study of the influence of residual stresses on fatigue crack growth rates is based on the determination of stress intensity factor K_{PR}. K_{PR} is defined as the stress intensity factor level of the loading cycle at which the fatigue crack experiences tensile stresses at the crack tip. Equivalently, K_{PR} is the stress intensity factor level at which the fatigue crack starts to propagate during the loading process. Lang has study the behaviour of K_{pr} intensity factor on various materials [31, 45, 46]. After extensive experimental work he suggested that the K_{pr} can be represented in general form as:

$$K_{PR} = f(R_{tip}) * K\max \tag{4-5}$$

Figure 4.5 shows a graphical representation of the above equation. For every unloading level UR after constant amplitude loading or an overload, K_{PR} can directly be obtained as a function of K_{max}. This is in contrast to the closure concept from Elber where K_{op} is a fixed value according to a fracture surface closure level, characteristic for crack growth at a specific R ratio value. Here, the respective curve is followed during the unloading cycle after each single tensile overload in a spectrum and each unloading cycle during a constant amplitude loading sequence.

Hence, the K_{PR} level of cycles with the same K_{max} depends on the value of Kmax and the subsequent unloading UR ratio (figure 4.6). In this case, when K_{max} and UR are the same, the same K_{PR} will be produced. This K_{PR} behaviour is described by the CAL and underloading master curve (figure 4.5). If we have a tensile overload in a load spectrum, only the $K_{max,OL}$ is needed and the subsequent unloading ratio (UR) to calculate K_{PR} (figure 4.7). When $K_{max,OL}$ and UR are the same, the same K_{PR} will be produced independently of the prior cycling history. This K_{PR} behaviour is described by the Single tensile overload master curve (figure 4.5).

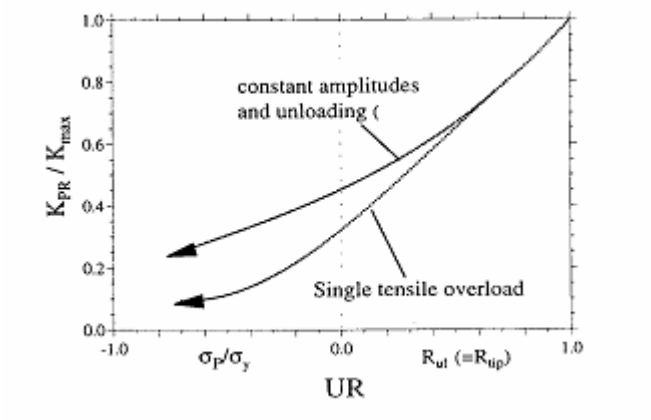

Figure 4.5_ K_{PR} for constant amplitude loading and a subsequent unloading cycle, and a single tensile overload [46, 47]

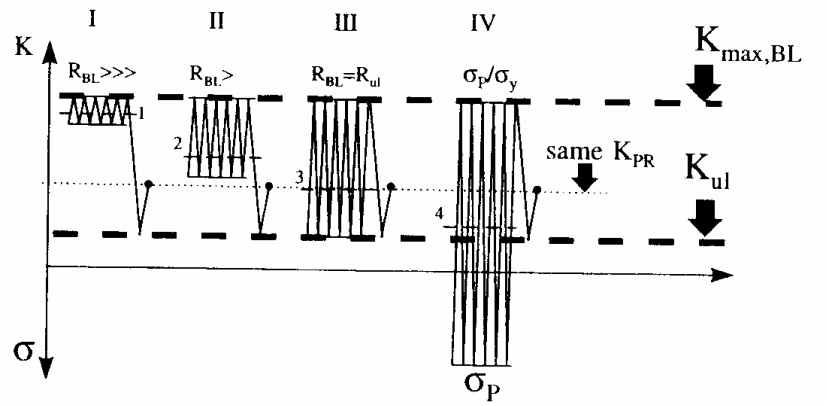

Figure 4.6_ Different sequences with the same K_{max} and the same unloading level K_{ul} yield the same K_{PR} value [46]

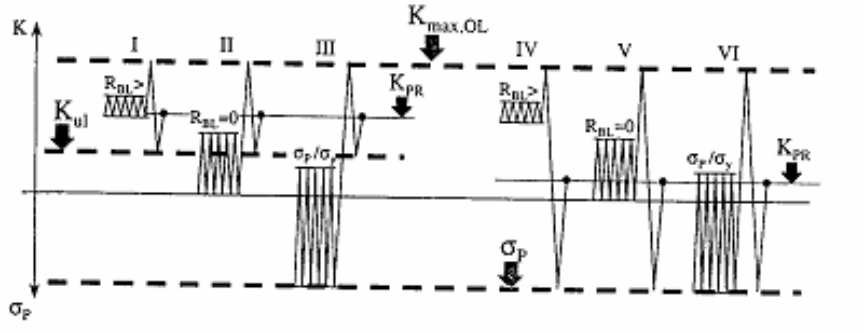

Figure 4.7_ Different sequences with the same tensile oveload level $K_{max,OL}$ and the same subsequent unloading ratio UR yield the same K_{PR} value [47]

Vasudeven, Sadananda et al. have reported very extensive work on the driving force of the fatigue crack behaviour of metals [38, 48, 49]. They support the idea that fatigue crack growth is governed by the applied loads and the various kinds of internal stresses ahead of the crack tip. They suggest that crack closure is very small or even non-existence and unable to rationalize fatigue crack growth behaviour [23, 50]. The basic points of the approach to fatigue are:

1. Fatigue is fundamentally a two-parametric problem because there are two driving forces required to obtain fatigue crack growth, K_{max} and ΔK.
2. Long crack growth represents the fundamental material behaviour, with two critical fatigue thresholds, $K^*_{max,th}$ and ΔK^*_{th} corresponding to two driving forces, that depend on the alloy microstructure, mode of slip and environment. The requirement of ΔK^*_{th} ensures a sufficient cyclic load amplitude to establish a characteristic cyclic damage, while the requirement in $K^*_{max,th}$ allows the peak load to break open the bonds in the cyclically damaged region. These two refer to the minimum conditions that are necessary for the crack to advance independent of crack closure and testing method.
3. Crack growth is driven by the total crack tip internal stresses i.e., the superimposition of the externally applied stress and the internal stresses that exist. All deviations from the steady state long crack growth behaviour can be accounted for by the presence of the internal stress gradients, like overload retardation, underload acceleration, ect.
4. Internal stresses exist due to defects, scratches, inclusions, welding or heat treatment, cold work, transformation induced stresses and plasticity.
5. The basic effect of the internal stress is to offset the total stress intensity at the crack tip relative to the externally applied stress, so that both K_{max} and K_{min} would generally be affected similarly. Consequently, the primary effect of the internal stress manifests through K_{max} and not the ΔK parameter.
6. Understanding and estimating the internal stresses is fundamental to the development of a reliable life model.

Also, they have shown that their approach to fatigue behaviour is consistent with the analysis of Lang and Marci [46] and Donald et al. [51]. Furthermore, Lang and Marci's work on K_{PR} elucidates the physical meaning of K_{max} threshold. K_{max} has to exceed K_{PR} to propagate and its existence is related to the residual stresses arising from the plasticity ahead of the crack tip and intrinsic material resistance to cracking under cycling loads. The idea of two critical parameters ($K^*_{max,th}$ and ΔK^*_{th})

have been supported by Wilkinson and Roberts [52]. They have been led to this conclusion using a dislocation model acting ahead of the crack tip. Liu has suggested crack tip dislocation emissions as the primary mechanism of fatigue crack growth rate [53].

The behaviour of both short and long cracks under constant amplitude loading conditions were investigated numerically and experimentally by Hammouda et al. [54]. They have used a crack tip deformation parameter based on numerical analysis to correlate fatigue crack growth rates.

Toyosada and Niwa recognise the significant role of the residual stresses ahead of the crack tip [55]. They have used the concept of K_{PR} stress intensity factor to explain their tests. The measurement of K_{PR} is subtracted from the compliance curve of the cracked body under cyclic loading, a technique that appears difficult to be applied because of the various signal amplifiers in their system. Recently, they have attempted to correlate K_{PR} with a characteristic crack tip plastic zone size in order to model the fatigue crack behaviour [56].

K_{PR} concept has been used by Tsukuda et al. [33] to correlate crack growth rate with ΔK_{eff}. The value of stress intensity factor at which compressive residual stresses turn to tensile ahead of the crack tip have been determined using a finite element model. Their analysis resulted a very good correlation for all R ratio CAL crack growth curves.

4.4 ΔK_{eff} Measurement Techniques

The determination of effective stress intensity range ΔK_{eff} experienced by the crack tip during fatigue loading is critical for the rationalisation of fatigue crack propagation. The effective stress intensity range ΔK_{eff} is given by the following function:

$$\Delta K_{eff} = K_{max} - K_o \qquad (4\text{-}6)$$

where K_{max} is the maximum stress intensity factor of a loading cycle, and K_o is the stress intensity level below which there is no fatigue damage to the crack tip. If crack growth is governed by crack closure $K_o=K_{op}$. According to the Lang approach to crack propagation $K_o=K_{pr}+\Delta K_T$ [31].

It becomes obvious that the explanation of fatigue crack growth with the crack closure mechanism must depend upon a valid and accurate measurement technique of crack closure. There is a big issue on how crack closure can be measured and which is the actual crack opening stress during a loading cycle. An accurate measurement of crack opening stress will lead to the actual calculation of ΔK_{eff} stress intensity range experienced during the loading cycle. The validity of crack closure measurement and consequently of ΔK_{eff} should be based on the correlation of crack growth rates of various test conditions. But it should be clear that crack closure values should be derived by the experimental data (from load-COD curve for example) based on mechanical and physical concepts and not upon the resulted correlation of fatigue crack growth rates. The correlation of fatigue crack growth rates must indicate whether crack closure is the dominant mechanism.

The most commonly used technique for crack closure measurement is the compliance technique. This technique uses the crack opening displacement (COD) response of the specimen to the variation of the far field applied load. A typical load versus COD curve can be seen in figure 4.8.

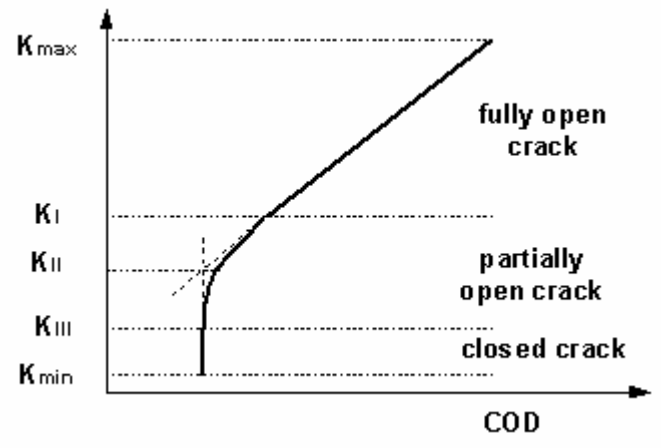

Figure 4.8_ Typical crack opening displacement response to far field load under the effect of crack closure

The linear relationship of load and COD represents a fully open crack. The crack is closed when no change of COD can be detected with load variation. A non-linear relationship of load and COD indicates a partially open crack. The non-linear compliance characteristics below the first point of crack wake contact (K_I) have been confirmed by studies of stress-strain distribution of the crack tip under the effect of crack closure [57].

Schijve [58] provided a very good survey of crack closure measurement techniques. He distinguishes the techniques of direct observations of crack closure like strereoimaging and testing transparent materials, compliance methods, and indirect observations based on fatigue crack growth, in which conclusions of crack closure are based on crack growth rates and striation observations.

Fleck [59] reported a complete review on crack closure measurement techniques. He recognised compliance method as one of the most important. He provides a full list of compliance techniques. In order to derive the COD curve in a thick specimen, they drilled two small holes at mid thickness, parallel to the loading direction, just behind the crack front. With a push-rod compliance gauge the COD can be measured through the holes at the mid thickness. It indicated a lower crack closure stress level than observed at the outside of the specimen surface, which is an indication of 3-D nature of crack closure. They have also concluded that crack closure is independent of crack length and that potential drop method often fails to characterise the closure behaviour due to failure of electrically closed cracks.

Yieshieng and Schijve [60] have study various methods for the determination of fatigue crack opening stress from the COD curve. Among them, it is a method called 'Tangent point method'. According to this method, the COD curve is divided to two parts (figure 4.9). The upper part of the curve is simulated by a linear function and the lower part by a second order polynomial. A necessary condition for the tangent point is that the coordinates and the slopes of the linear part and the second order part should be equal for both parts. Because the position of the tangent point is initially unknown, the position of point P is gradually changed. The errors of the regression are different for each position of the point. The point with the minimum error is selected as the tangent point looked for. The method has proven to be independent of the position of COD meter. The measured fatigue crack

opening stresses by this method were in good agreement with the observed effects on crack growth rates after an overload and after an overload and an underload.

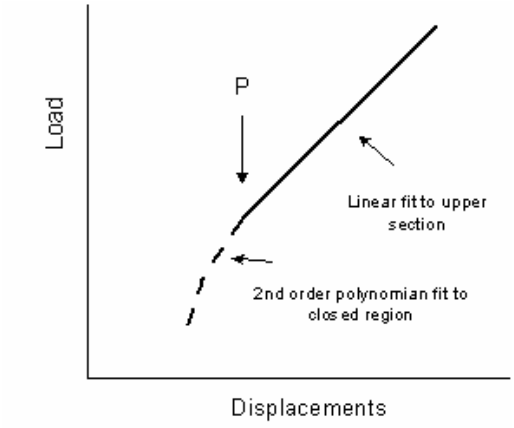

Figure 4.9_ Tangent point method

Tsukuda et al [33] have observed crack closure behaviour of CAL cycles in the Paris regime over a wide range of stress ratios, from 0 to 0.7 on a medium carbon structural steel. The measurements of crack closure were conducted using a surface strain gauge technique. Also, they have numerically studied closure behaviour under the same loading condition using finite element method (FEM). They have measured crack opening stresses up to R ratio of 0.5 although finite element methods show that crack closure exists even at R ratio of 0.7. Furthermore, the levels of σ_{op} obtained from the FEM analysis were not consisted with those from experimental measurements. The inconsistency of the crack closure measurements was attributed to the fact that the measurement method is not able to capture reliably the changes caused by the local crack closure very near the crack tip. It has been shown that even small plastic deformations very near the crack tip are able to considerably shield a crack from the remote loading [41]. A good correlation is observed between crack growth rates and ΔK_{eff} based on the σ_{op} value obtained from the FEM analysis over a wide range of R ratios.

The acoustic emission technique, COD method, back face strain gauge and surface strain gauge were used by Lee et. al [61] to measure crack closure during fatigue cycling of Al 8090. Fatigue crack growth rates versus ΔK_{eff} curves obtained by the acoustic emission technique gave the best fit for the high stress ratio (R=0.8) test, which implies that this technique is a reliable crack closure measurement method. COD method gave a very good correlation with the high R ratio test.

Different methods of closure measurements and issues related to the identification of closure points have been examined by Sinclair et. al [34]. Based on the compliance curves obtained from the crack mouth clip gauge and near tip strain gauge a systematic assessment of closure measurements has been made by a variety of non-subjective methods. For results obtained on a commercial Al alloy, it is shown that a curve fitting method based on a combination of linear and polynomial functions provides particularly sensitive and consistent crack closure measurements. The curve fitting method is very similar to the tangent point method used by Yieshieng and Schijve [60]. Further details and modifications of the curve fitting method will be given in the experimental procedures of the present study as this technique has been used to measure crack closure during our fatigue tests.

Brahma et. al [62] have used a COD gauge to measure the crack closure response of SENT aluminium specimens. The COD gauge accurately predicts crack opening stresses under various simple loading conditions. They emphasise the fact that the COD gauge indicates the crack opening stress at which the entire crack tip is open and it does not necessarily describes the actual crack tip opening stress. Their theoretical explanation of crack closure behaviour is based on the formation of a plastic wedge behind the crack tip.

Riemelmoser and Pippan [40] have studied roughness induced crack closure using a single and a multiple asperity model based on dislocation theory. They concluded that the compliance technique for measuring asperity-induced closure predicts too large a closure stress intensity factor. It is more likely that using the multiple asperity technique which is closer to reality, the compliance technique would measure the true closure crack tip stress intensity factor

Donald has introduced 'the adjusted compliance ratio' (ACR) method for the determination of ΔK_{eff} stress intensity range during a loading cycle [63]. He assessed that crack closure does not entirely isolate the crack tip from damaging strains due to cyclic loading and estimates ΔK_{eff} taking into account the additional cyclic crack tip strain below the opening load. The ARC method uses the COD measurements to determine the effective fraction of the loading cycle (figure 4.10):

$$ARC = \frac{C_s - C_i}{C_o - C_i} \tag{4-7}$$

$$\Delta K_{eff} = ARC \cdot \Delta K \tag{4-8}$$

where ARC is the adjusted compliance ratio, C_s is the inverse slope of secant drawn between minimum load-displacement and maximum load-displacement, C_o is the inverse slope of load-displacement above opening load and C_i is the inverse slope of load-displacement prior to the initiation of a crack. The advantages of the technique are that it does not require an estimation of the opening load and it is independent of the crack closure mechanism, specimen geometry and material. Estimation of ΔK_{eff} using various methods including ARC has been reported [64]. It was concluded that a good correlation of the crack growth rates in the near threshold regime was achieved using the ARC method.

Newman [65] has shown that crack tip damage for applied stresses less than the crack opening stress is negligible (less than 5% effect on crack growth rates) for the Paris crack growth regime. The analysis is based on the cyclic crack tip hysteresis energy and the plasticity induced crack closure model. Further details on this model will be given in the next chapters. Furthermore, he has reported that the effective stress intensity factor range calculated from the crack closure model for the ACR method produces crack growth rate trends opposite from the traditional crack closure method for cracks initiating from a sawcut or notch.

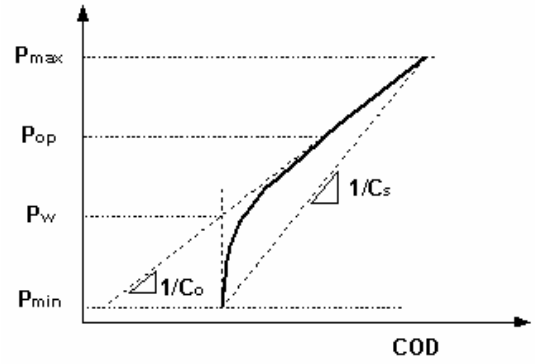

Figure 4.10_ Load-displacement curve showing the opening load and the adjusted compliance ratio technique

Lang [31] suggested that the idea of a ΔK_{eff} concept can be the result of two different potential processes that can lead to a reduced driving force (figure 4.11).

There is the closure concept which states that the loading cycle becomes less "effective" due to the contact of the fracture surface and also there are the residual compressive stresses in front of the crack tip, which are responsible for the reduction of ΔK to ΔK_{eff}.

It can be assumed that crack closure is the result of a wedge acting on the fracture surfaces. The action of the wedge force will transform the minimum load of the loading cycle from K_{min} to K_w. The amplitude experienced by the crack tip will be

$$\Delta K_{tip} = K_{max} - K_w \tag{4-9}$$

and the R ratio will be increased to the value :

$$R_{tip} = \frac{K_w}{K_{max}} \tag{4-10}$$

K_w corresponds to P_w load in figure 4.10 and is determined by the intersect point between the straight line which describes the load vs. displacement behaviour without the presence of closure and the vertical straight line which passes through the point of load vs. displacement curve where the minimum load is.

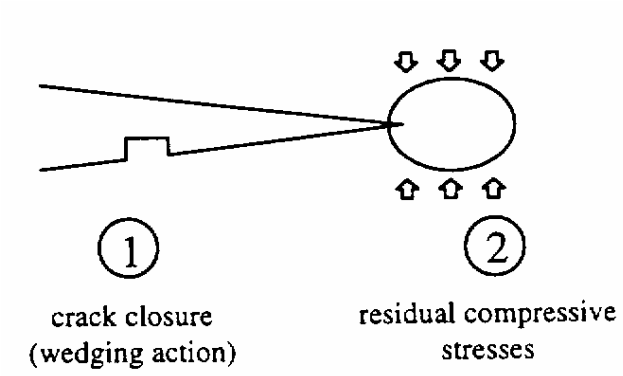

Figure 4.11_ Lang's proposed Model for fatigue crack propagation [31]

The effects of residual compressive stresses are taken into account by the introduction of the stress intensity factor K_{PR}. The most efficient and precise method from the Lang experiments is shown in Figure 4.12 and is denoted as CPLM

method, which stands for "crack propagation load measurement". Further details on the CPLM method will be given in the experimental procedures of this study. The effective part of the loading cycle, ΔK_{eff} , is then given by:

$$\Delta K_{eff} = K_{max} - K_{PR} - \Delta K_T \qquad (4\text{-}11)$$

ΔK_T is the threshold value of stress intensity factor at high R ratio (figure 4.13). The term ΔK_T is used because there is a loading range, which must be applied before the intrinsic threshold of the material, is overcome.

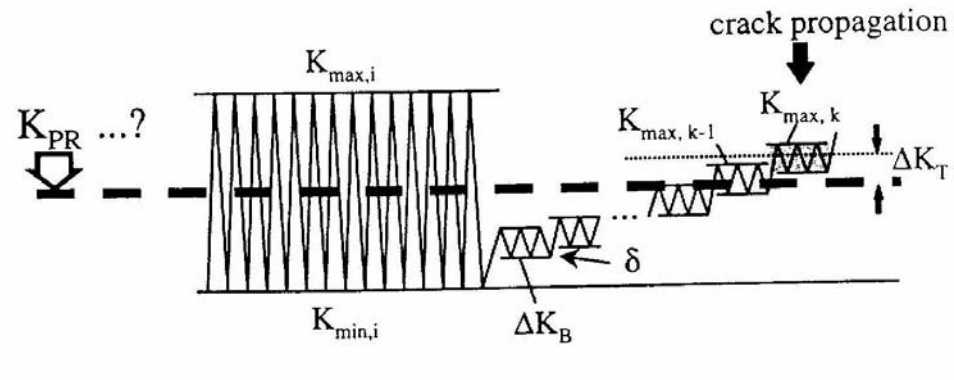

Figure 4.12_ Crack propagation load measurement (CPLM) method [31]

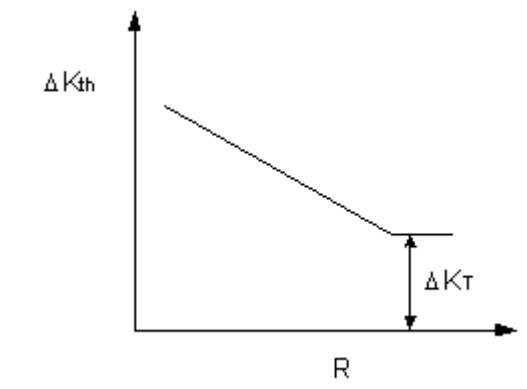

Figure 4.13_ Typical behaviour of threshold stress intensity factor at high R ratios

The method described above determines experimentally the lower limit of the effective stress intensity factor range ΔK_{eff} and it does not involve any measurement of crack opening displacement (COD). But it not yet clear if the measured ΔK_{eff} is a result of compressive residual stresses as Lang suggested [31] or crack closure. Zhang et al. [66] have used a very similar method to determine

ΔK_{eff} of various simple variable amplitude loading (SVAL) tests. They do not attribute the reduction of the effectiveness of the loading cycle to a specific mechanism such as crack closure or compressive residual stresses but they compare their results with model based solely on plasticity induced crack closure.

Wallhead and Edwards have measured crack tip shielding as a result of crack closure and determined ΔK_{eff} under various CAL and SVAL loading conditions using the non-destructive optical method of caustics [37]. Their crack closure results are not in agreement with other experimental evidence or theoretical models. They concluded that although transient changes like overloads produce dramatic change in crack growth rates, they do not change the crack tip stress field in the K-dominance zone. Therefore, the successful application of ΔK_{eff} as the fatigue driving force can only be justified on phenomenological rather than physical grounds.

CHAPTER 5

FATIGUE CRACK GROWTH – PREDICTION MODELS

5.1 Introduction

For a specimen subjected to constant amplitude loading of $\Delta\sigma_1$ at a specific stress R ratio, N_1 number of cycles is necessary to produce Δa_1 crack length increment (figure 5.1). The slope of the crack length curve at a given crack length represents the crack growth rate da/dN of the specific crack length and loading. Since ΔK stress intensity factor range includes both crack length and loading amplitude effects, crack growth rates can be related to ΔK.

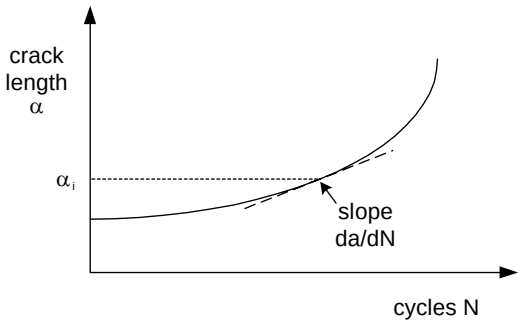

Figure 5.1_ Crack length increment under constant amplitude loading at a specific R ratio

Crack growth rates da/dN are function of ΔK, but this function depends on the stress ratio R. Constant amplitude loading at different R ratio will produce different crack growth rate response. ΔK_{eff} concepts, as defined by equation 3-6, have been extensively used to correlate fatigue crack propagation rate data under constant amplitude loading (figure 5.2). In principle, such results provide intrinsic material property data for component fatigue life prediction. This fact can lead to the use of ΔK_{eff} concept for the development of robust fatigue crack growth models and the prediction of fatigue behaviour of helicopter structures under various simple and complex loading conditions.

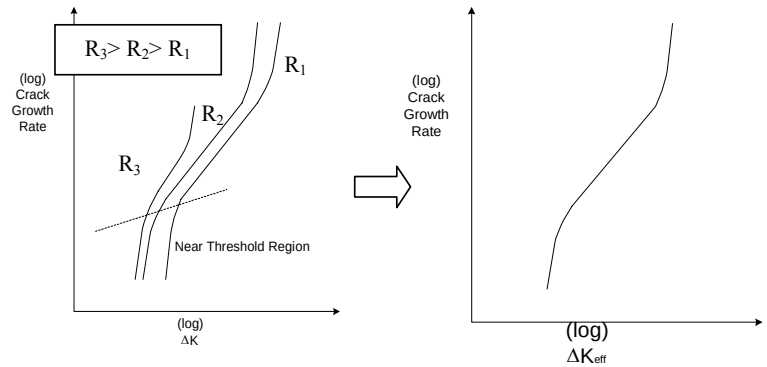

Figure 5.2 Crack growth rates for different R ratios and the formation of the unique ΔK_{eff} curve

5.2 Near Threshold Fatigue Crack Growth

The fatigue limit of the material is particularly important in engineering because almost every design faces the task of the determination of the fatigue crack growth threshold. Structural components are designed to operate under the fatigue threshold below which no fatigue damage is considered.

Fatigue crack growth threshold stress intensity range as well as fatigue of metals has been attributed to intrinsic and/or extrinsic mechanisms. Intrinsic mechanisms are caused by the inherent resistance of the material against fatigue crack growth. Residual stresses and plastic deformation in the front of the crack tip are considered intrinsic mechanisms. Extrinsic resistance to fatigue crack growth is caused by processed occurring behind the crack tip (plasticity and roughness induced crack closure). Further details on near-threshold fatigue can be found in an excellent review written by Larson, Chen, and Meshii [67]. The review deals with various aspects of near-threshold fatigue such as the effect of crack length, crack geometry, material strength, grain size, stress ratio R, crack closure and residual stresses.

Recommendations for ΔK_{th}-tests are given in the ASTM standards E647 [68]. The ASTM standards describe a loading procedure at which ΔK_{th} is determined for a fixed R ratio (figure 5.3b). Both K_{max} and K_{min} have to be reduced simultaneously with a fixed percentage to keep the R-value at a constant value until no crack propagation conditions are detected. The disadvantage of the method is that the measured values of ΔK_{th} can be affected by crack closure triggered during the loading shedding procedure. To measure the intrinsic fatigue threshold the K_{max} method is proposed. In this method, the imposed K_{max} is held fixed and ΔK is progressively reduced by raising the R ratio. The argument here is that when the maximum stress intensity factor of the fatigue cycle is held fixed, the size of the maximum plastic zone at the crack tip remains unchanged. Therefore, load reductions would not be expected to cause retardation effects typical of variable amplitude fatigue. Furthermore, closure of the crack faces is virtually eliminated for the high load ratio levels at which ΔK_{th} is measured.

It is well documented that microstructure influences fatigue crack growth and its effect is most significant in near-threshold growth rates when the crack tip

plastic zone approaches that of the local microstructure [69, 70]. Pippan et al. compared coarse and fine microstructures of TiAl sheets and they have found that finer microstructures exhibit lower threshold stress intensity factor ranges [71]. Kardomateas and Carlson showed that the required stress intensity factor range for crack growth decreases with increasing positive load ratio R values. The load ratio effects on the fatigue crack growth and on fatigue threshold stress intensity range can be predicted through a micro-mechanical analysis based on the plastic crushing of a single asperity. Crack closure has been suggested as the possible mechanism for the threshold stress intensity range by many other researchers [72].

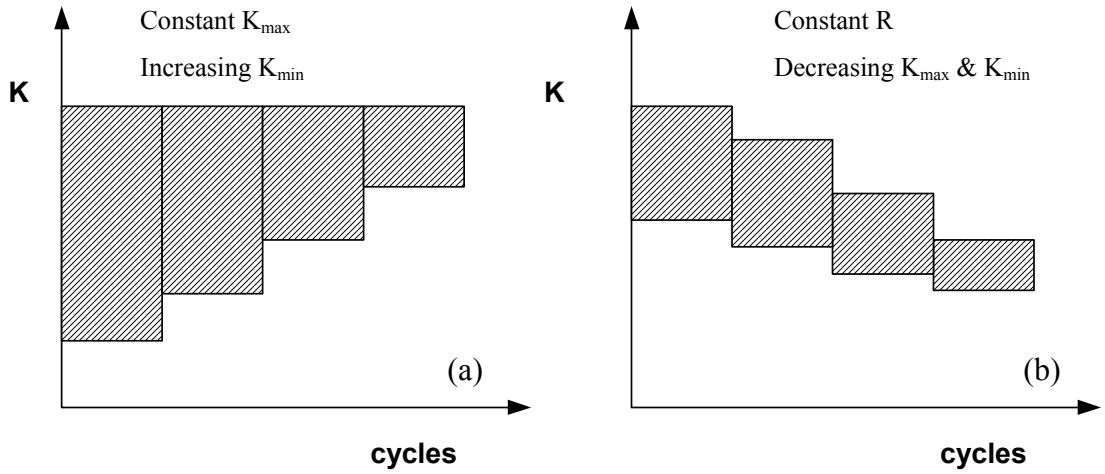

Figure 5.3_ Fatigue threshold determination techniques, a) constant K_{max} method, b) constant R ratio method

It has been found that near-threshold growth rates and threshold values depends on K_{max} stress intensity level [73]. The effect of K_{max} on thresholds and crack growth rates depends on the nature of the material.

Although, the concept of crack closure is not generally accepted as the mechanism responsible for the threshold stress intensity range of the materials. Various models have been developed that predict the ΔK_{th} at different load ratios without invoking crack closure. A microstructural model which uses simple, conventional mechanical and cyclic fatigue properties has been proposed by Li and Edwards [74]. Recently, Riemelmoser et al. present a model which explains the existence of a threshold and the near threshold regime [36]. The model is based on the discretization of the plastic strains around of the crack tip in terms of geometrically necessary dislocations. Hence, extrinsic resistance to fatigue crack

growth (crack closure) is neglected. Dislocation models have been used by many researchers to model threshold fatigue behaviour without the involvement of crack closure [75]. Lenets and Nicholas measured different threshold stress intensity values ΔK_{th} for Ti alloy IMI 834 using two different load patterns [76]. The discrepancy was attributed to the crack tip shielding associated with residual stresses in the front of the crack rather than with fracture surface contact behind the crack tip. M. Lang and C. Marci proposed that ΔK_{th} is material property [29]. Their concept based on the idea that ΔK_{th} characterises the maximum stress intensity range in which only reversible dislocation movement can occur at the crack tip. In other words ΔK_{th} cause only elastic deformation at the crack tip and therefore no fatigue damage is possible.

Vasudevan et al. proposed that for a fatigue crack to advance, two threshold stress intensity criteria are to be met simultaneously instead of a single one (ΔK_{th}), which is normally assumed. These are: (a) a critical cyclic stress intensity ΔK (ΔK^*_{th}) and (b) a critical maximum stress intensity ($K^*_{max,th}$). Several fatigue phenomena, i.e. the effect of microstructure, environment, and load ratio can be rationalised in terms of these two parameters without invoking crack closure. Extensive research by the researchers on wide range of materials that supports the above rationale has been reported [77-80].

Vasudevan et al. have plotted the threshold stress intensity factor versus K_{max} for a variety of available experimental data on fatigue thresholds. These plots show how fatigue cracks begin to advance when intrinsic values of both ΔK_{th} and $K_{max,th}$ are exceeded for a given constant amplitude loading conditions. Vasudevan et al. thus demonstrate for a wide range of alloys that the threshold for fatigue crack growth is governed by critical values of both ΔK and K_{max}.

Boyce and Ritchie support the concept of the existence of two fatigue thresholds ΔK^*_{th}, and $K^*_{max,th}$ [81]. They show that $K^*_{max,th}$ threshold is independent of R ratio and ΔK^*_{th} decreases with increasing R ratio below a critical $R_c \sim 0.5$. This effect was attribute to crack closure. For R ratio values larger than 0.5, where no crack closure exists, ΔK^*_{th} has a different dependance on the load R ratio and is approximately linear with the increase of K_{max}. This behaviour has been observed by various others researchers [82] based on descrete dislocation analysis. The observations are consistent with the Vasudevan et al approach to the fatigue threshold behaviour.

5.3 Variable Amplitude Loading

Most structural components experience variable amplitude loading. These kinds of loading can range from simple overloads and/or underloads during constant amplitude loading to complex variable loading. In order to predict fatigue life, it is necessary to study the effect of load spectrum on crack growth rates and to understand the mechanism driving the crack propagation under these conditions. It is well established that the effects of load interactions under load spectrum are nonlinear. The behaviour of fatigue cracks under variable amplitude spectra has been studied intensively over the past 20 years [83, 84]. For many load sequences, delay effects are found, compared with the growth rates predicted by a linear summation. On the other hand, non-conservative fatigue life predictions have been reported for spectra containing underload excursions [85]. Additionally, accelerated crack growth rates have been observed under typical helicopter spectra [84, 86].

5.3.1 Simple Variable Amplitude Loading

Many variable amplitude loading (VA) tests have been carried out with simple load spectra in order to see how fatigue crack growth rates change by the load amplitude. Although the simple VA tests are different from the service load histories, the experiments have a significant contribution to the understanding of the interaction effects during the fatigue crack growth. The understanding is essential for developing crack growth prediction models for complex VA loading.

5.3.1.1 Tensile Overload Effects

During fatigue crack growth under constant amplitude loading, load excursions to higher stresses named as overloads can in result retardation of crack growth or even complete crack arrest. Typical crack growth behaviour following a single tensile overload can be seen in figure 5.4.

Under the effect of constant amplitude loading at a stress intensity range $\Delta K=K_{max}-K_{min}$, crack propagates at constant crack growth rate da/dN. The application of the overload at K_{OL} will cause an initial acceleration to the crack growth rates. The re-application of the baseline stress intensity range ΔK will have

as a result an extended period of retarded crack growth rates. The minimum retardation of crack growth rates will be observed at a short crack length increment after the application of the overload. After that point, crack growth rates begin to increase and eventually catch up with the pre-overload value.

Although fatigue crack growth responses due to single overloads in a variety of materials and conditions have been studied over the past years [68, 84, 85, 89], there is still a big discussion about the underlying physical mechanism. Fatigue crack closure and residual stress ahead of the crack tip are the two most popular mechanisms for the rationalisation of crack growth delay after an overload.

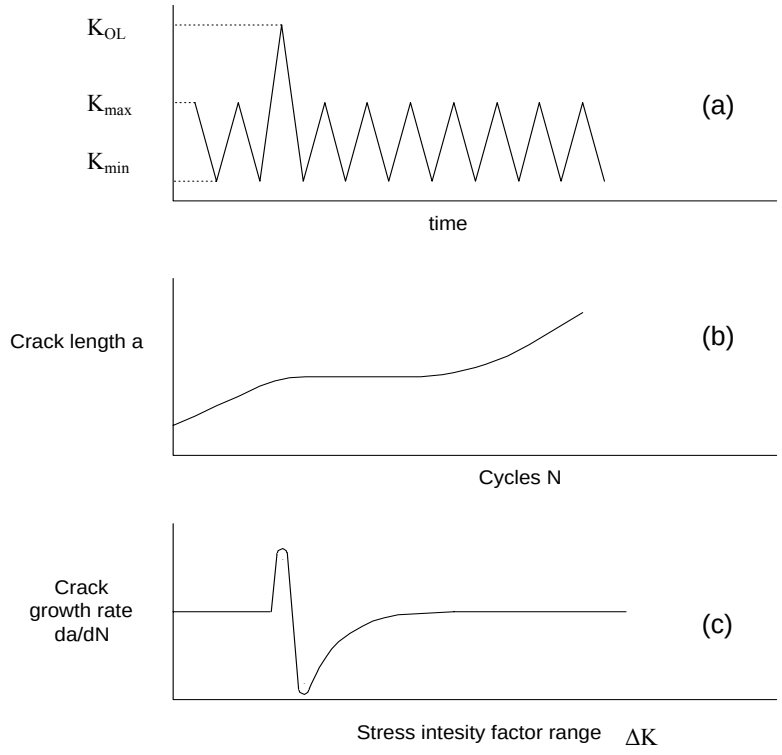

Figure 5.4_ Typical response to tensile overload (a) during constant amplitude loading. (b) Crack growth affected by the application of overload, (c) and crack growth rate response showing delayed retardation

Crack closure is a consequence of plastically elongated material left in the wake of the crack by previously created plastic zones. A load excursion causes a larger plastic zone than the baseline load and thus leaves more plastic deformation in the wake of the crack later on. Thus, crack opening load is increased and the effective stress intensity factor range is reduced. This explains the crack growth

retardation after the overload. Crack closure mechanism has been used intensively for the explanation of overload effects [87, 88].

The role of residual stresses in the crack tip plastic zone has been examined in terms of the crack growth delay following an overload [39, 43, 90, 91]. A single tensile overload causes a large residual tensile deformation ahead of the crack tip and corresponding large compressive residual stresses at the end of the overload cycle. Consequently the K_{PR} stress intensity factor increases and the effective stress intensity factor range decreases. This implies that retardation in the crack growth rate occurs under the baseline loading. The behaviour of K_{PR} has been examined both numerically [92], and experimentally [39] in various alloys and loading condition. However, their ability to take into account the observed effects is questionable [93].

5.3.1.2 Underload Effects

Usually, it is common to ignore the contribution to crack growth from compressive loading [94]. A review of papers on compressive loading and compressive load excursion by Carlson and Kardomateas [95] found that several recent investigations have concluded that it is incorrect to ignore compressive load excursions (by setting them to zero) as compressive load cycles do contribute to crack growth. It is obvious that periodic underloads during constant amplitude loading effects on crack growth rate have to be examined and explained in order to improve design. Very little progress has been made in the research of underload effects in fatigue life. It is observed that underloads followed by constant amplitude loading reduce the fatigue life [96] and cause acceleration in crack growth rate [85] compared with their linear summation damage.

Topper et al. have studied the behaviour of crack opening stresses under spectra consisting of tension-compression underloads followed by the baseline constant amplitude small cycles [97, 98]. The R ratio of the baseline small cycles was –1, 0, 0.5 and 0.8. They found that the crack opening stress level dropped immediately after the application of the underload and then gradually increased with subsequent constant amplitude cycling. It reached a steady state level after a large number of cycles. The observed crack opening stress behaviour had an obvious acceleration effect on the crack growth rates of the baseline when its R

ratio was low. At high R ratios (0.8), changes in crack opening stress had no effect on the crack growth rates because their level was always lower than the minimum stress of the loading cycles.

It has been found that crack growth acceleration effects are influenced by the number and the R ratio of the small baseline cycles between the underload [85, 99]. Accelerated crack growth rates exhibit a maximum at a specific number of small cycles. This effect is greatly influenced by the loading conditions and the material.

Fatigue crack closure [92, 99, 101], strain hardening ahead of the crack tip due to the underloads and the influence of the mean stress [85] have been suggested as the underlying mechanisms responsible for the accelerated crack growth behaviour. Topper and Yu [100] suggested that the compressive underloads caused the squeezed crack tip to have decreased crack closure stress and thus increased stress intensity factor range of the baseline constant amplitude cycles at low R ratio. Accelerated crack growth rates have been attribute to the decreased crack opening stress of the large underloads [92, 99].

Russ and Johnson [101] have conducted a finite element analysis to investigate the crack tip deformation response under the combined application of the baseline and the underload cycles. Baseline constant amplitude cycles were at R ratio of 0.7 and underloads at R ratio 0.1. They observed an increased displacement in the vicinity of the crack tip resulting from the application of the underload. Because baseline cycles are free of closure, they suggested that the changes in the conditions ahead of the crack tip because of the application of the underload must cause an increase in the effectiveness of the baseline cycles. Lang et al. [29, 40] have measured the effectiveness of baseline loading and underloads in terms of residual stress distribution ahead of the crack tip and they have reported that there is no significant difference in the crack growth response between these two different loading conditions. The author believes that a possible increase in the effectiveness of the high R ratio cycles is not able to explain crack growth accelerated affects. In contrast, the crack tip deformation is very likely to change the point that crack surfaces come into contact and therefore to reduce the crack opening stress and increase the effectiveness of the underload cycle. The fraction of the crack closure decrease must depend on the number of the small cycles between

the underloads, the maximum stress intensity factor K_{max}, the R ratio of the baseline and underload cycles and the material.

Because crack growth acceleration effects depend on the loading conditions and the material, it is possible that sequences containing underload cycles will not cause accelerated crack growth rates. Hawkyard et al. [102, 103] and Yang [104] have studied underload sequences in different titanium alloys and both have concluded that the linear summation damage of the cycles according to their constant amplitude response can predict the fatigue behaviour during the tests.

5.3.2 Complex Variable Amplitude Loading

Aircraft components experience various types of load spectrum depending on the position in the structure and on the flight conditions. Because of the great importance of the complex varying loads in design, many researchers study the effects of various loading spectra on fatigue life of various aeronautical alloys [103, 105-108]. A characteristic helicopter load spectrum can be seen in figure 5.5 [84]. The figure shows part of Rotorix 16 spectrum. Rotorix 16 spectrum, which is a typical load spectrum developed for a location on the titanium rotorhead of a transport helicopter, consists of a large number of vibratory load cycles at high R ratio (R>0.75) and mean stress. The rest of the spectrum consists of load cycles at R ratios between 0.4 and 0.7, with excursions to zero load. Cycle range of the high R ratio small cycles is 16% of the peak load in the sequence. In cracked components, stress intensity ranges (ΔK) of these cycles would be close to the threshold, ΔK_{th}. More details about the creation of Rotorix spectra can be found in reference 84.

The high R ratio vibratory cycles typically make up 90% of the fatigue loads in a helicopter loading spectrum. Therefore the knowledge of the behaviour and the effects of these cycles are essential in the prediction of the fatigue crack growth life and in the design of helicopter components against fatigue. Buller has studied the effect of progressively omitting small range cycles from the original helicopter spectrum [84, 109]. He found that the omission of small cycles caused an increase of the number of flights to failure for the specimen. The tests were conducted in Ti 1023 and Al 7010. The increased fatigue life due to the omission of small cycles was greater in Ti 1023. Al 7010 was less sensitive to vibratory load cycles. The

accelerated crack growth rates comparing with the constant amplitude crack growth behaviour of the sequences containing small high R ratio cycles was attributed to the accelerated crack growth rates of the small cycles due to the presence of the low R ratio underload cycles. The significance of the effect of the small range cycles in the crack growth rates of transport wing aircraft spectra has also been pointed out by Abelkis [102, 105]. Under the same kind of spectrum, Ranganathan's tests on Al 8090 have shown a decreased fatigue life of 2.1 times the predicted life using linear summation calculations based on constant amplitude loading data [110].

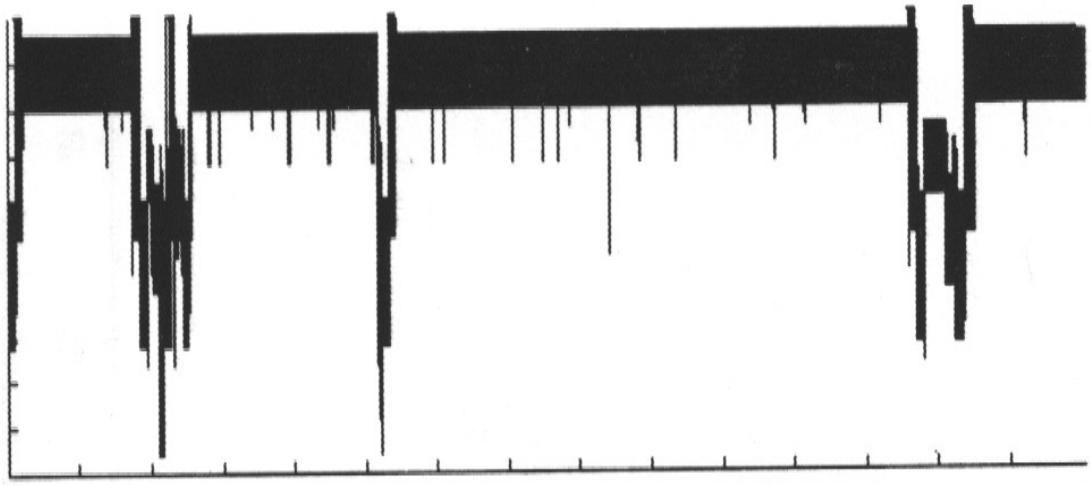

Figure 5.5_ Typical load spectrum of helicopter rotorhead component [84]

A review of crack growth processes and the prediction methodologies under variable amplitude loading is given by Wanhill and Schijve [111]. They reported an important observation from crack growth rate tests conducted under flight simulation loading. Flight simulation tests conducted on thin specimens of ductile alloys showed an initial decrease in crack growth rate per flight with increasing fatigue crack length whereas thicker specimens shown an immediate rise in crack growth rates [112]. Their results were attribute to the conditions behind the crack tip which affect the level of crack closure. In thinner specimens, where plane stress conditions prevail, the crack tip plastic zones due to the peak loads are large and so the crack closure load levels are enhanced which cause crack growth retardation. In thicker specimens, where plane strain conditions prevail, the effect of retardation is reduced and cracks grow faster.

Fatigue crack closure has been used to explain the crack propagation process under complex loading spectra. Because of the 3D nature of crack closure and the

great variation of the crack tip plastic zones during the complex loading, which have a very significant influence on the crack closure levels, modeling fatigue crack propagation has been proven a difficult task. However, crack closure measurements and estimations have been used to calculate the ΔK_{eff} for crack growth predictions.

Kim and Song [113] have measured crack closure in random loading sequences and found that crack closure level fluctuate only slightly during a random loading block. Crack closure levels were found to be dependent on the largest load cycle in the sequence [114]. Newman has investigated crack closure behaviour under spectrum loading using a strip-yield model [115]. The calculated crack opening stresses follow a very irregular pattern while the cyclic loads are applied. He noted the they tend to oscillate about a mean value and he used an equivalent crack opening stress concept to describe crack closure behaviour which would greatly reduce the computer time required to complete a simulated test.

Nevertheless, the underlying mechanisms responsible for the accelerated crack growth rates under helicopter sequences not yet clear. Further study of interaction effects between the high R ratio small cycles and the low R ratio large cycles must be conducted in order to understand the cause of the reduced fatigue lives of the components. Accurate crack closure measurements must be taken to assess the role of fatigue crack closure in the acceleration of crack growth rates in various alloys.

5.3.3 Prediction Models

The most significant aim of fatigue research is the development of models for prediction of fatigue life of structural components. Many efforts have been carried out in this direction. Many models have been presented providing accurate results under specified load conditions. Unfortunately, no model has yet succeeded in predicting accurate results of fatigue life under any loading condition. Most of the prediction models work on the cycle-by-cycle basis. The final crack length and fatigue life prediction occurs as a sum of each individual crack length increment produced by each cycle.

Fatigue life prediction models can be distinguished in non-interaction and interaction models. Non-interaction models are also known as fatigue crack growth

linear summations. In non-interaction models, load interaction effects are not considered. A linear summation of crack growth is that obtained by summing the crack growth increments Δa=da/dN as obtained in constant amplitude loading, assuming no interactions between succeeding load cycles. Hence, the comparison between the test results and the linear summations can lead to the determination of the interaction effect occurring under the studied spectrum. Linear summation techniques predicted lives longer than the fatigue test results, revealing accelerated crack growth rates. Retardation effects are associated with the opposite observations. The fatigue crack growth life prediction program AFGROW [116] has proven a very effective tool for life predictions without load interaction effects. Three other models are available in AFGROW. These are the Willenborg model, the Closure model and the Wheeler model. In order to specify material properties, tabulated data are provided to AFGROW. Then, AFGROW produces a fitted crack growth curve that is used for the linear summation predictions.

Three categories of interaction prediction models can be classified (table 5.1): the yield zone models, such as the Willenbong [117] model, the crack closure models such as [118] and strip yield models such as the Newman's model [115, 119]. Lazzeri has reviewed fatigue crack growth prediction models for aeronautical structures [120] and concluded that strip yield models are the most reliable crack growth prediction method in comparison with various complex variable amplitude loading models [121].

Table 5.1_ Three categories of crack growth prediction models

Type of model	Crack Closure Used	Crack Closure relation
yield zone models	No	-
crack closure models	Yes	empirical
strip yield models	Yes	calculated

Yield zone model are based on the assumptions that the retardation in crack growth is due to the increased levels of residual compressive stress ahead of a fatigue crack induced by overloads. These residual stresses cause a reduction in crack tip stress intensity factor by an amount K_{red}. Many researchers have proposed advanced models on the above assumption for the predictions crack growth retardation, acceleration and load effects [88, 122-125].

Recently, Lang has used K_{PR} concept to model crack growth behaviour [29]. Since K_{PR} represents the load level at which the stresses ahead of the crack tip switch from compressive to tensile, he argued that the residual compressive mechanism is the responsible for the crack growth propagation. Complex loading histories can be divided into 3 categories, I, II, and III. Figure 5.6 shows the three different types of loading cycles. Type I is the cycle at which K_{PR} level is between the levels K_{PR} after constant amplitude conditions and 1 overload. For cycles type II, K_{PR} is lower than the maximum stress intensity factor of the cycles but higher that the constant amplitude level, and for type III, K_{PR} lies higher than K_{max} of the loading cycle.

The model defines the driving force for fatigue crack growth as

$$\Delta K_{eff} = K_{max} - K_{PR} - \Delta K_T \qquad (5\text{-}1)$$

where ΔK_T is the intrinsic threshold value of the material which has to be determined experimentally. Additionally, experimental determination of the two master curves $K_{PR}=f(UR)K_{max}$ for constant amplitude and 1 overload (figure 5.7), the transition function of K_{PR} between the two master curves and the decline function describing the K_{PR} behaviour after 1 overload is necessary. The calculation of the fatigue crack growth rates is based on a function $da/dN=f(\Delta K_{eff})$. A computer code for this model is not yet unavailable.

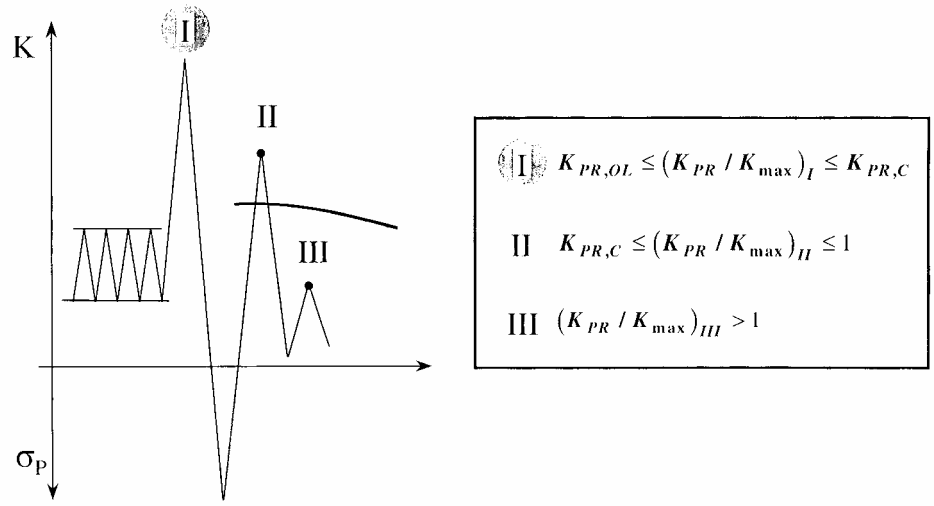

Figure 5.6_ The definition of the three different types of cycles according to the K_{PR} model.

On the other hand, crack closure models, based on the assumption proposed by Elber [26], that not all the load excursion is active for propagation, but only a part of it. The crack is assumed fully or partial closed. This implies that crack propagation occurs over part of the nominal stress intensity factor $\Delta K_{eff}=K_{max}-K_{op}$, where K_{op} is the stress intensity factor in which crack start to open. The calculation of the fatigue crack growth rates is based on a function $da/dN=f(\Delta K_{eff})$. K_{op} is not constant but depends on the load history. Crack opening stress is determined experimentally using various types of measurements such as direct measurements of crack closure and crack opening displacement under various simple variable loading conditions. The simplest crack closure model was proposed by Schijive [126]. Other models based on the same concept proposed by various researchers [127-130].

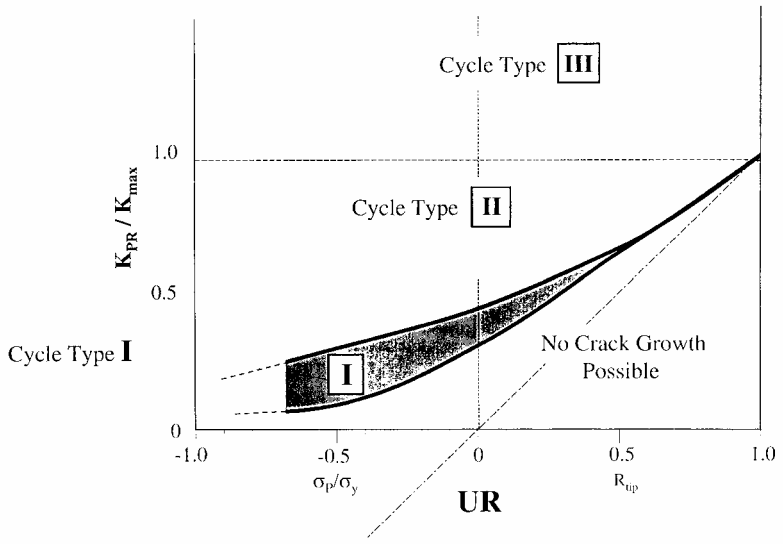

Figure 5.7_ The corresponding area of each type of loading cycle in the K_{PR}/K_{max} versus the unloading UR ratio [31].

Finite element studies have proven the creation of plastically deformed material in the wake of the crack under cyclic loading and [131, 132] confirmed the occurrence of crack closure and interaction effects. Because such calculations can not be made for many cycle, a simple approximation of the elastic-plastic stress and displacement solution must be used. Such an approximation can be provided by Dugdale model [15]. Strip yield models are based on Dugdale model, but modified to leave plastically deformed material in the wake of the crack. Many researchers have suggested models based on these principles [133, 134].

Newman has developed a very powerful analytical crack closure model [115, 119]. The model is called FASTRAN. Figure 5.8 shows a schematic of the model at maximum and minimum applied stress. The model is composed of three regions: (1) a linear-elastic region containing a circular hole with a fictitious crack of half-length c`+ρ, (2) a plastic region of length ρ, and (3) a residual plastic deformation region along the crack surface. The physical crack is of length c`- r, where r is the radius of the hole. The length of the compressive plastic zone is ω. The flow stress σ_0 is the average between the yield stress and the ultimate strength of the material. Region 2 and 3 are composed of rigid-perfect plastic bar elements. The elements ahead of the crack tip are plastically deformed under fatigue loading. The elements behind the crack tip are broken and they can carry only compressive loads when they are in contact. Hence, when the crack propagates, plastically deformed material is left in the wake of the crack. This deformation is represented by the broken elements behind the crack tip which simulate plasticity induced crack closure. Plane stress/plane strain transitions are included by changing the plastic constraint factor α and so the stress level of σ_0 used in the Dugdale model. The value for α varies form 1 plane stress to 3 for plane strain conditions. Further details on the determination of factor α will be given in the experimental section of this study.

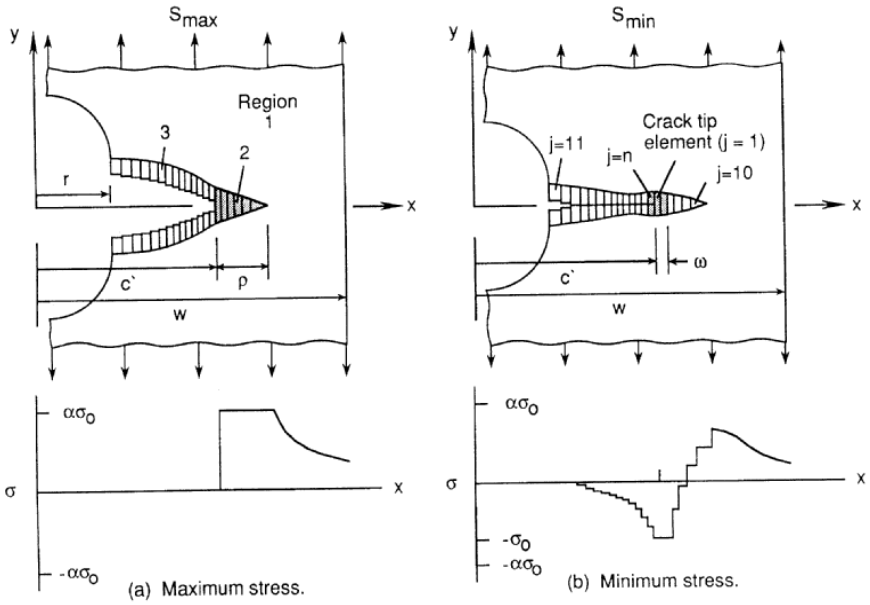

Figure 5.8_ Schematic of Newman's analytical crack closure model under cyclic loading [115, 119].

The function, which relates the crack growth rates and the effective stress intensity factor ΔK_{eff} is given by the equation:

$$dc/dN = C_1 \Delta K_{eff}^{C2} \frac{1-(\Delta K_0 / \Delta K_{eff})^2}{1-(K_{max}/C_5)^2} \quad (5\text{-}2)$$

where:

$$\Delta K_0 = C_3 (1 - C_4 \frac{S_0}{S_{max}}) \quad (5\text{-}3)$$

$$K_{max} = S_{max} \sqrt{\pi c} F \quad (5\text{-}4)$$

$$\Delta K_{eff} = (S_{max} - S_0 \sqrt{\pi c} F) \quad (5\text{-}5)$$

The crack opening stresses S_0 are calculated from the analytical closure model [119, 135]. The constants C_1 to C_5 are determined to best fit the experimental data under constant amplitude loading.

CHAPTER 6

EXPERIMENTAL PROCEDURES

6.1 Introduction

Constant and Variable Amplitude Loading fatigue crack growth tests were conducted on three different metallic alloys, using compact tension (CT) specimens, on an Instron 8500 digitally controlled fatigue test machine. The capacity of the machine is 50 kN. Loading was performed under load control and laboratory environmental conditions (temperature 18-23 ^{o}C and humidity ~15%). The sample materials were titanium alloy Ti-10V-2Fe-3Al (Ti 1023), and aluminium alloys Al 8090 T852 (Al8090) and Al 7010 T73651 (Al7010).

6.2 Materials

6.2.1 Titanium Alloy Ti-10V-2Fe-3Al

6.2.1.1 Mechanical and Fatigue Crack Growth Properties

Ti-1023 belongs to the near beta (β) or solute-lean beta alloy class where the body centred cubic (bcc) β phase is predominant [154]. The chemical composition of the alloy is given in table 6.1.

Table 6.1 _ Chemical composition of titanium alloy Ti-1023

Element	Al	C	Fe	H	N	O	V	Y	Balance
Comp. %wt	2.6-3.4	0.05	1.6-2.2	0.015	0.05	0.13	9-11	0.005	Ti

The mechanical properties were determined by GKN WHL, for the Ti1023 same material plate from which the coupons were manufactured. A full description is given in ref. [86]. and can be found in the table 6.2. The alloy has a high ultimate strength (σ_{uts}) of 1146 MPa and 0.2% proof stress (σ_{YS}) of 1048 MPa. Its plane strain fracture toughness is 63.9 MPa $m^{1/2}$.

Samples were machined so that the crack plane was perpendicular to the L-direction with the crack growing in the transverse direction. Fatigue crack growth

rates of Ti 1023 under constant amplitude loading at R load ratios of 0.1, 0.4, 0.7 and 0.9 obtained from ref. [86] can been seen in figure 6.1.

Table 6.2_ Mechanical properties of Ti-1023

Parameter	Description	Ti-1023
σ_{UTS}	Ultimate Tensile Strength	1146 MPa
σ_{YS}	Yield Strength	1048 MPa
	Elongation	8.4 %
K_{IC}	Fracture Toughness	63.9 MPa $m^{1/2}$
E	Youngs Modulus	114 GPa

6.2.1.2 Metallography

In order to examine the Ti1023 microstructure, short sections of the material were prepared through all directions, L-T, L-S and T-S. Metallographic sections were prepared using conventional methods. The sections were mounted in polymer, polished and etched using Kroll's reagent in order to examine the microstructure. To get pictures of the material in the three directions (figure 6.3), polarized light was used with the optical microscope. The pictures show the characteristically large β grains of the alloy. β gains were more elongated in the longitudinal direction than in the transverse direction. α phase is evenly dispersed within the large β grains. The grain directions in relation with the crack and the crack growth can be seen in figure 6.2. The grain direction designation has applicability to all three materials.

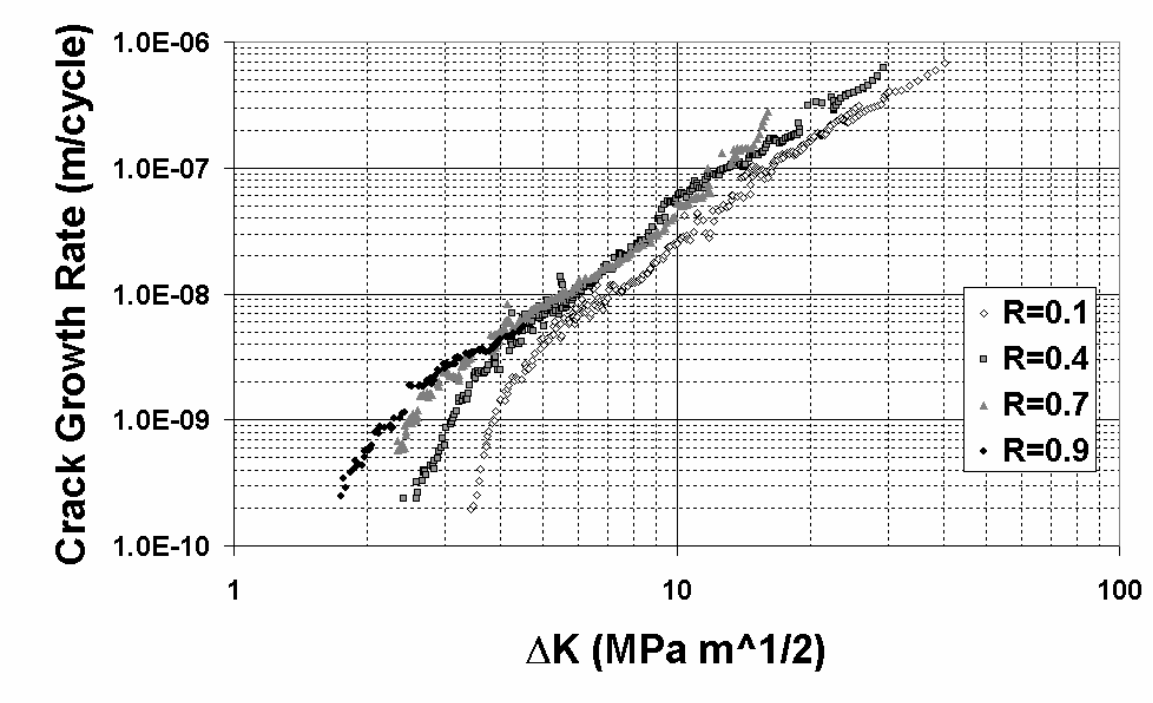

Figure 6.1_ Constant Amplitude Loading fatigue crack growth rates for four different R ratios for Ti1023 [86]

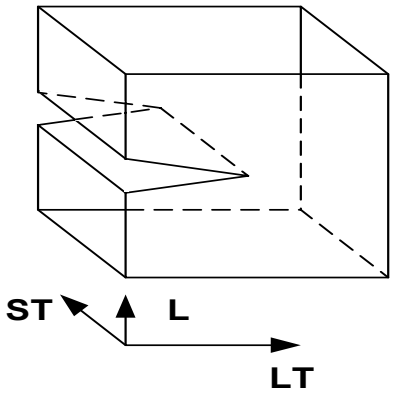

Figure 6.2_ L, LT, and ST grain direction in relation with the crack for the three alloys.

MAG
x500
(L-LT)

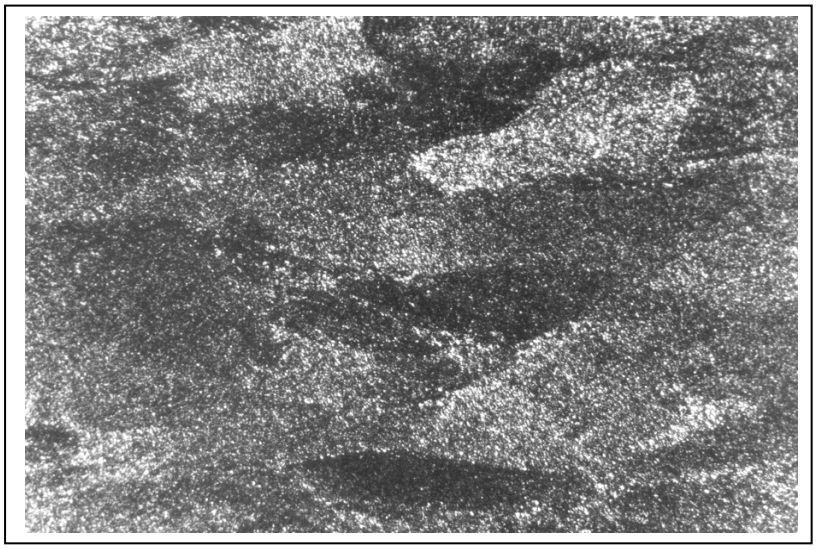

MAG
x500
(LT-ST)

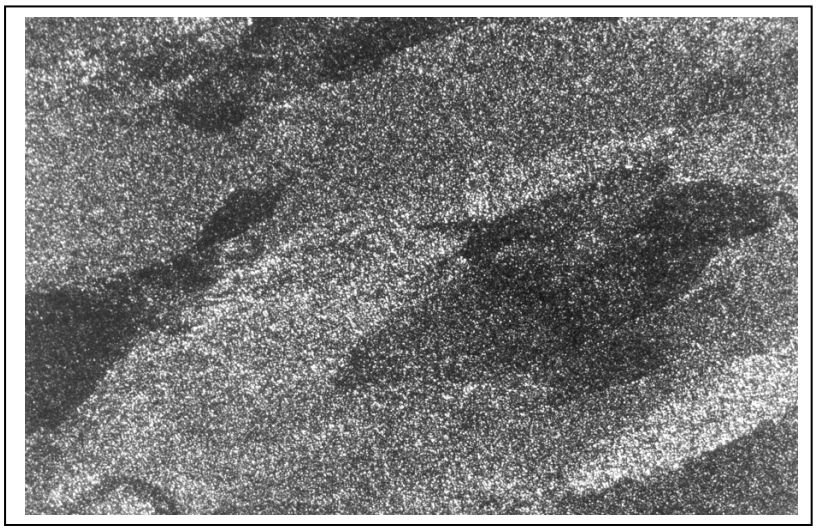

MAG
x500
(L-ST)

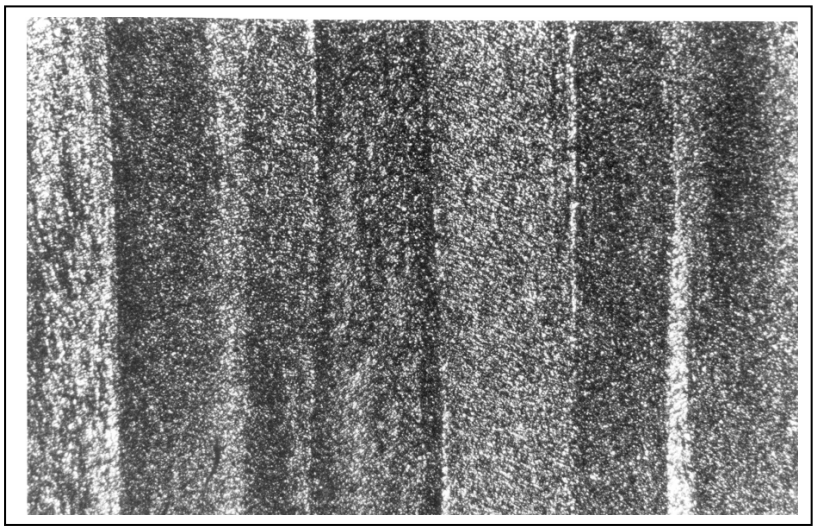

Figure 6.3_ Microstructure of Ti1023. The pictures provided by optical microscope with polarized light.

6.2.2 Aluminium Alloy Al 8090 T852

6.2.2.1 Mechanical and Fatigue Crack Growth Properties

Al 8090 is a low density aluminium-lithium alloy alternative to conventional aluminium alloys used in the aerospace industry. The benefits of this alloy are a 8-10% density reduction and 8-10% increase in elastic modulus comparing with the Al 7010-T7451 properties [146]. The specified chemical composition of the alloy is given in table 6.3.

Table 6.3 _ Specified chemical composition of titanium alloy Al 8090

Element	Si	Fe	Cu	Mn	Mg	Cr	Zn	Ti	Zr	Li	Balance
Comp. %wt	0.04	0.05	1.2	<0.01	0.8	<0.01	0.05	0.03	0.11	2.4	Al

The mechanical properties were determined by GKN WHL, for the material plate from which the coupons were manufactured. Full description is given in ref. [146]. The properties of Al 8090 can be seen in the table 6.4. The alloy has an ultimate strength (σ_{uts}) of 490 MPa and 0.2% proof stress (σ_{YS}) of 410 MPa. Its plane strain fracture toughness is 24 MPa $m^{1/2}$.

Table 6.4 _ Mechanical properties of Al 8090

Parameter	Description	Al 8090 T852
σ_{UTS}	Ultimate Tensile Strength	487 MPa
σ_{YS}	Yield Strength (2%)	380 MPa
	Elongation	7.5%
K_{IC}	Fracture Toughness	24 MPa $m^{1/2}$
E	Youngs Modulus	80 GPa

Fatigue crack growth rates of Al 8090 under constant amplitude loading (CAL) at R load ratios of 0.1, 0.4, 0.7 and 0.9 [146] can been seen in figure 6.4. Fatigue crack growth rates at each R ratio do not form a smooth sigmodial curve. It can be identified that the higher the R ratio the lower the value of ΔK_{th}. Also, there is an increase in the amount of scatter of the data at low R ratios. This behaviour has been attributed to the strong anisotropic microstructure resulting in distinct fracture types and consequently very different fracture surfaces [146].

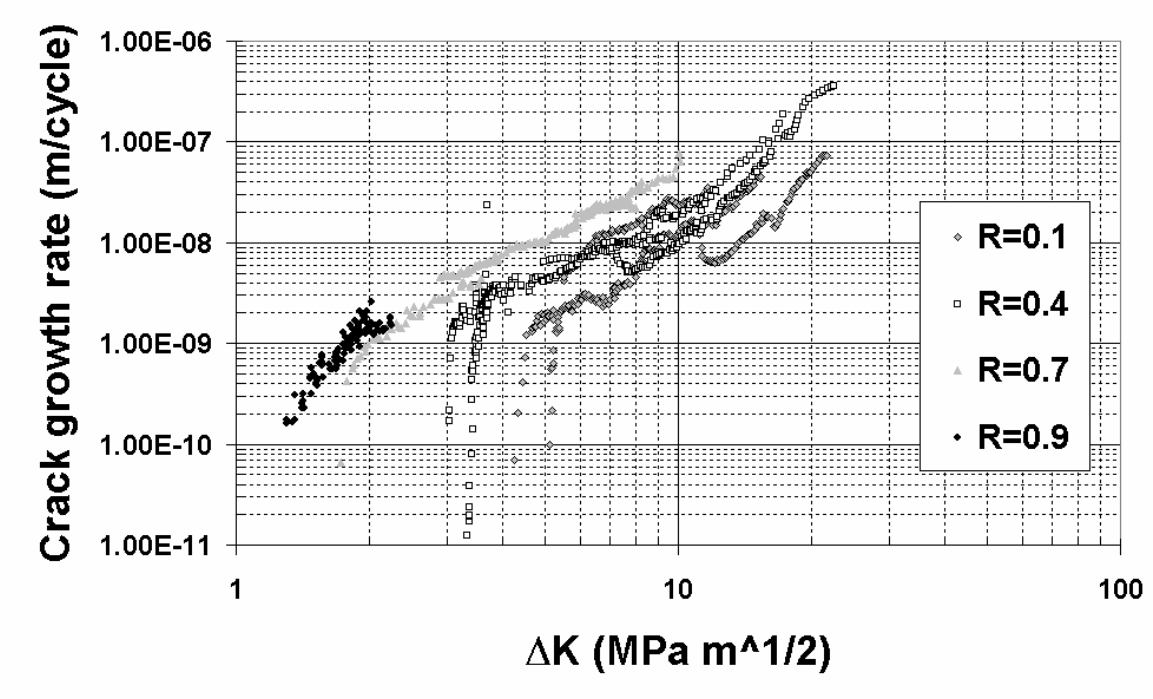

Figure 6.4_ Constant Amplitude Loading fatigue crack growth rates for four different R ratios for Al8090 [146]

6.2.2.2 Metallography

In order to examine the Al8090 microstructure, short sections of the material were prepared through all directions, L-T, L-S and T-S. Metallographic sections were prepared using conventional methods. The sections were mounted in polymer, polished and etched using molybdic acid, saturated solution, and hydrofluoric acid 5% as reagent. The pictures reveal very large and elongated grains in the L-S direction, very thin and elongated in the L-T direction (figure 6.5). More rounded grains were observed in the S-T direction. The above observations are consistent with the observations in ref. [146]. A grain size was measured around 0.5 mm in line with L, 50 μm in line with S and 20 μm in line with T. Also, it has been emphasized that there are distinctly different crack propagation mechanisms produced by low ΔK (near threshold region) and higher ΔK test conditions due to alloy's characteristic structure [146].

MAG
x200
(L-ST)

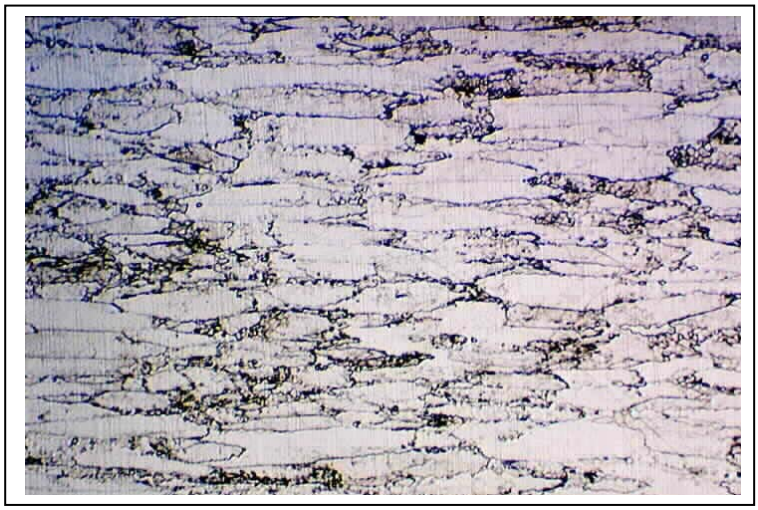

MAG
x200
(L-LT)

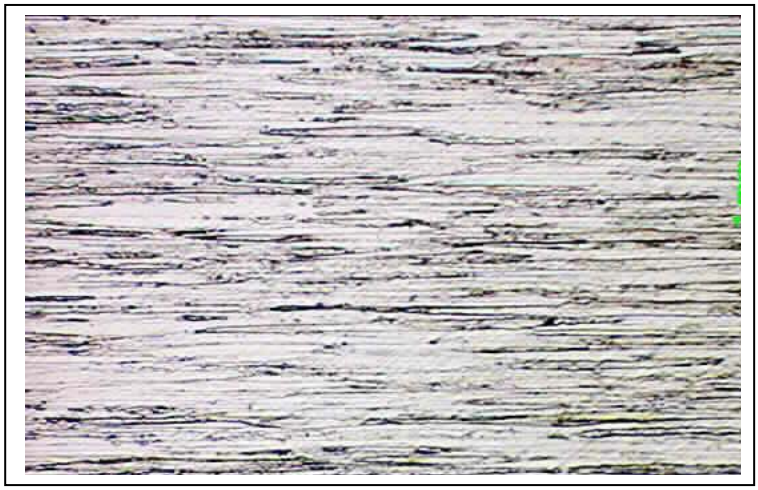

MAG
x200
(ST-LT)

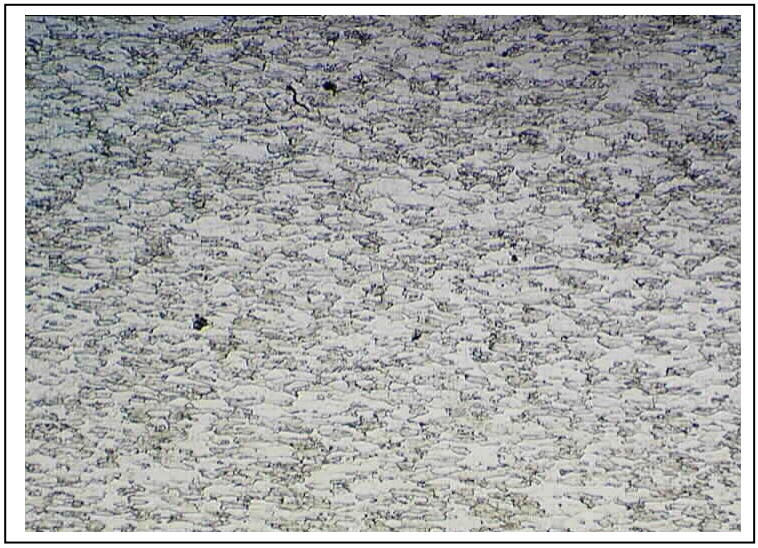

Figure 6.5. Al 8090 pictures provided by optical microscope

6.2.3 Aluminium Alloy Al 7010 T T76351

6.2.3.1 Mechanical and Fatigue Crack Growth Properties

The aluminium alloy 7010 was developed to have higher static strength, and fracture toughness properties in comparison with the widely used 7075 aluminium alloy. Al7010 has good corrosion properties which are a result of reduced quench sensitivity in thick section because of added zirconium [155]. Table 6.5 shows the chemical composition of AL 7010 T73651.

Table 6.5_ Specified composition of 7010 aluminium alloy

Element	Si	Fe	Cu	Mn	Mg	Cr	Zn	Zr	Al
Wt%	0.05	0.07	1.6	0.01	2.3	0.01	5.9	0.11	Balance

Mechanical properties of Al7010 can be seen in the table 6.6. The properties were determined for the material plate from which the coupons were manufactured [147]. The alloy has ultimate strength (σ_{uts}) of 518 MPa and 0.2% proof stress (σ_{YS}) of 456 MPa. Its plaine strain fracture toughness is 33.5 MPa $m^{1/2}$.

Table 6.6_ Selected mechanical properties of 7010 T73651

Parameter	Description	Al 7010 T73651
σ_{UTS}	Ultimate Tensile Strength	518 MPa
σ_{YS}	Yield Strength (2%)	456 MPa
	Elongation	14.7%
K_{IC}	Fracture Toughness	33.5 MPa $m^{1/2}$
E	Youngs Modulus	70 GPa

Fatigue crack growth rates of Al7010 under constant amplitude loading (CAL) at R load ratios of 0.1, 0.4, 0.7 and 0.9 [147] were determined experimentally and can been seen in figure 6.6. Fatigue crack growth rates of each R ratio form distinctive curves of each R ratio. It can be identified that the higher the R ratio the lower the value of ΔK_{th}.

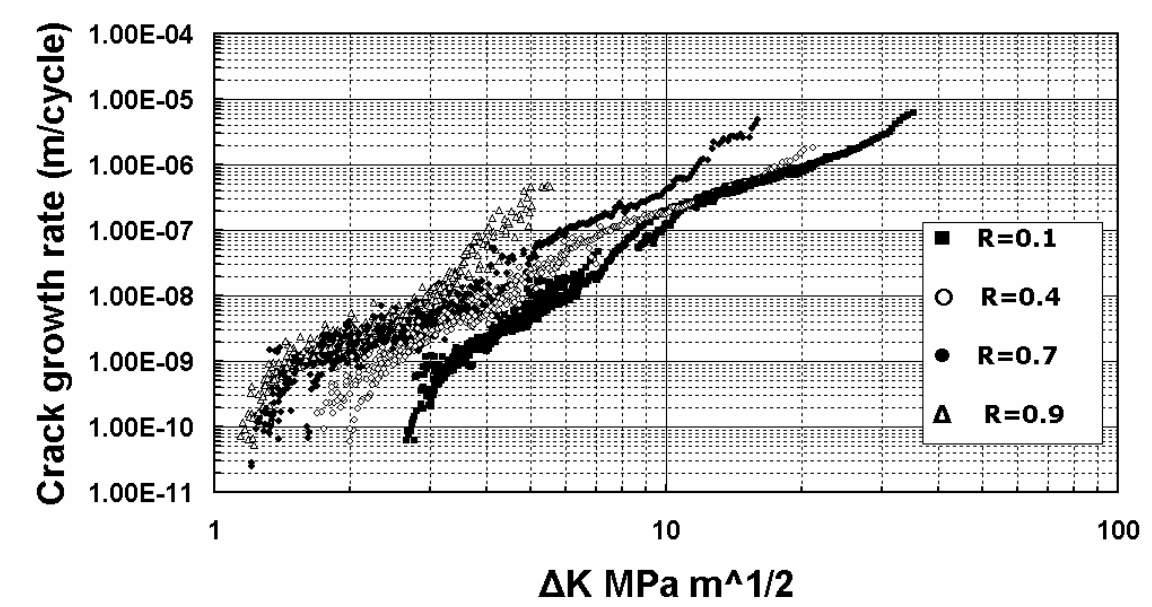

Figure 6.6_ Constant Amplitude Loading fatigue crack growth rates for four different R ratios for Al7010 [147]

6.2.3.2 Metallography

The microstructure of Al7010 plate from which the coupons were manufactured was examined and reported in ref [84]. The alloy has normal elongation of the grain structure with respect to the rolling direction. The grain boundaries are clearly visible and the inclusions are evenly distributed.

(L-LT)

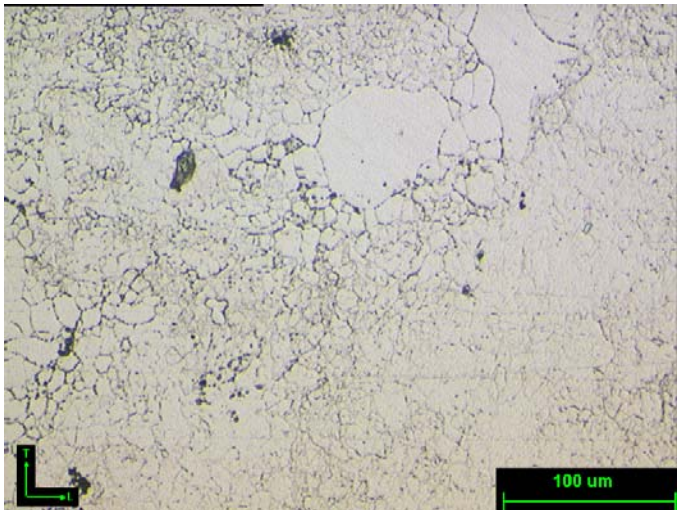

(L-ST)

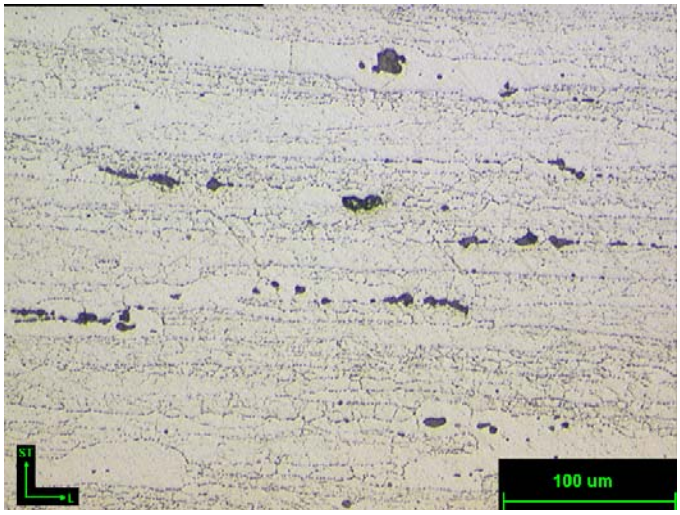

(ST-LT)

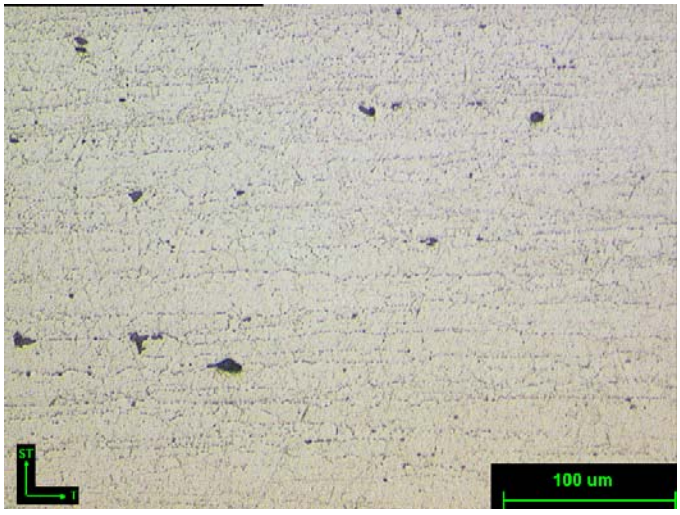

Figure 6.7_ Al7010 pictures provided by optical microscope

6.3 Specimen Design

All tests were performed on Compact Tension (CT) samples with a thickness of 17.5 mm and a W dimension of 70 mm. The specimens were manufactured from a plate. The sample manufacturing was performed by Cranfield University and GKN WHL according with ASTM E 647-93 [67]. The specimens were machined so that the crack could propagate in the L-LT orientation from a chevron type notch of length a=14mm. A full drawing of the sample is shown in figure 6.8. The assembly of CT specimen grips used for the tests is shown, in Appendix A.

In the case of the aluminium alloy plate, the compact tension samples were machined from the plate with the loading direction parallel to the rolling (L) direction in the plate, with crack growing in the transversee (LT) direction, and the thickness of the CT sample in the ST direction (figure 6.2). The surface of each sample was 2 mm from the top and bottom surface of the plate.

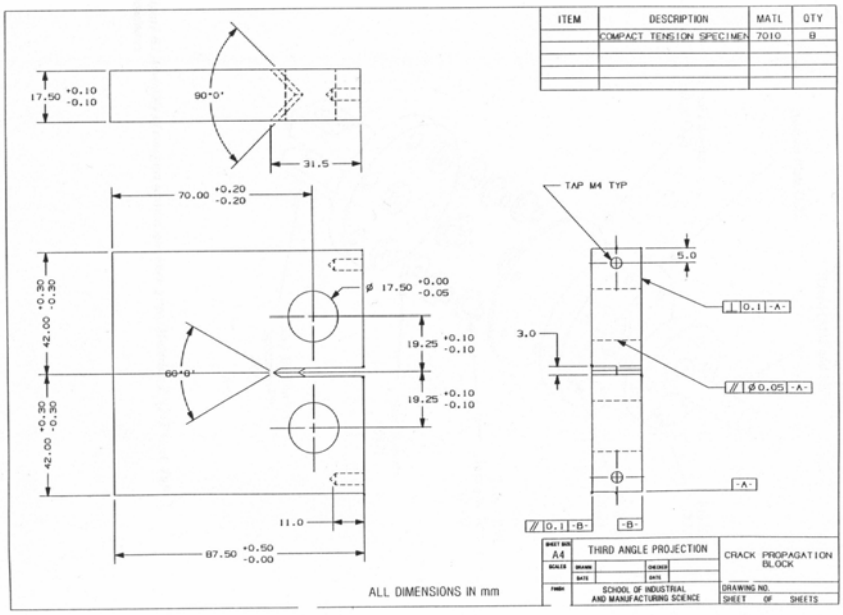

Figure 6.8_ Dimensions of compact tension samples

The stress intensity factor K for CT specimens in term of applied load is given by [156]:

$$K = \frac{P}{tW^{1/2}} f(a/W) \qquad (6\text{-}1)$$

where

$$f(a/W) = \frac{(2+a/W)(0.886+4.64a/W-13.32(a/W)^2+14.72(a/W)^3-5.6(a/W)^4)}{(1-a/W)^{3/2}} \qquad (6\text{-}2)$$

where: a = crack length
W = specimen width = 70mm
t = specimen thickness = 17.5mm
P = applied load

Equations (6-1) and (6-2) are valid for 0.24<a/W<0.7

6.4 Measurement of Fatigue Crack Growth

6.4.1 DCPD and Crack Length Calibration for CT Specimens

Crack length data can be derived from potential drop measurements using a relationship between crack length and potential for the particular specimen geometry. The method is called Direct Current Potential Drop (DCPD) technique. The technique is based on the fact that the changes in the crack length cause the change in the material area that the current flows through the specimen. Therefore, for a fixed value of current, the changes in the crack length alter the resistances and hence the potential changes. An assessment of D-C potential techniques for monitoring fatigue crack growth has been presented by Wei and Brazil [157].

When determining specimen crack lengths from potential measurements, it is desirable to eliminate problems associated with measuring voltage changes in a fatigue crack growth metallic specimen [84]. One problem is the drift in the measurements of potential caused from the changes in the resistivity of material specimen, measurement device and current source due to the changes of temperature. Normalizing the voltages (V_x/V_y) measured at each probe pair

mounted on the specimen, the problems are eliminated. V_x is the changing voltage measured across the crack mouth and V_y is the reference voltage on a dummy specimen. The resulting ratio is independent of temperature changes. To eliminate problems of electrical shorting because of crack closure the current is pulsed so that the voltage measurement is taken at maximum tensile load when the fracture faces should be fully separated. A further normalization of test voltage potential ratio $(V_x/V_y)/ (V_x/V_y)_0$ helps to reduce errors associated with the difference in positioning of the probes between specimens. The ratio $(V_x/V_y)_0$ is the voltage ratio of the V_x and V_y probes at the start of the test when the crack length is at 14mm. Finally, to eliminate the problem of thermoelectric forces generated in the circuit, voltage measurements are taken with the current off, and subtracting it from the voltage measured with the current on ($V_i = V_{oni} - V_{offi}$).

The application of the above techniques enhances the ability of the DCPD system to measure small increments of crack growth.

To use the DCPD for measuring crack lengths, the relationship between specimen crack length and potential for the particular specimen must be established. In this manner, crack length data can be derived from potential drop measurements. A third order polynomial relationship between potential drop ratio $(V_x/V_y)/ (V_x/V_y)_0$ and normalized crack length a/W of the specimen was produced by Buller [84] for the supplied CT specimen (W=70mm, t=17.5mm, initial crack=14mm):

$$a/W = A_0 + A_1((V_x/V_y)/(V_x/V_y)_0) + A_2((V_x/V_y)/(V_x/V_y)_0)^2 + A_3((V_x/V_y)/(V_x/V_y)_0)^3 \quad (6\text{-}3)$$

where a/W is the normalized crack length and the coefficients are:

A_0=0.0357
A_1=-0.4020
A_2=0.77384
A_3=-0.2037
R^2=0.9995

To determine the calibration curve, a test was run under CAL conditions. A travelling microscope of 10μm resolution was used to make the crack length

measurements. Then, the crack length measurements were correlated with the corresponding measurements of the voltage ratio from the DCPD system.

The ratio $(V_x/V_y)_0$ is the voltage ratio of the V_x and V_y measured at each pair of probes at the start of the test. (V_x/V_y) is the voltage ratio measured periodically throughout the test. Figure 6.9 shows a plot of the calibration curve produced by equation (6-3) and the data points used for the calibration.

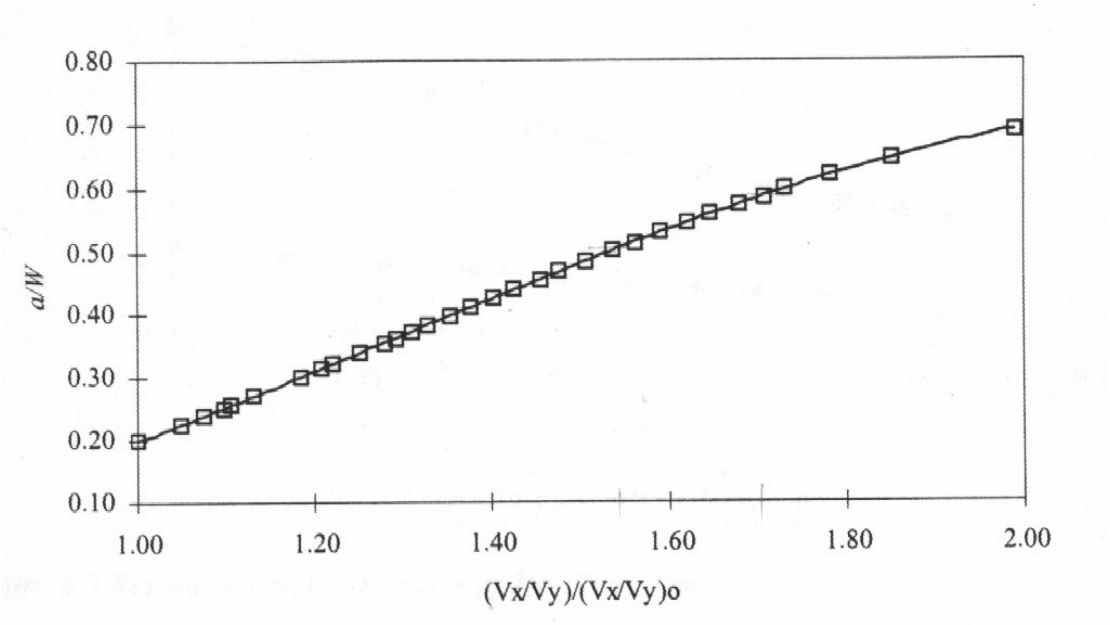

Figure 6.9_ DCPD calibration measurements and calibration curve for the compact tension specimen [84]

6.4.2 Software Development

The necessary software was developed using LabView 5.1 package, in order to be able to control the process of a variety of tests and collect the crack growth data. The fatigue tests that can be conducted by the new electrical potential system include K-decreasing tests under constant-R or constant-K_{max} [67] for the determination of threshold, tests of constant amplitude loading followed by certain number of underloads or overloads. The software is also responsible for the transformation of potential data to crack length and for the redefinition of applied load on the specimen if it is necessary in the test. Flowcharts of the four basic softwares developed for this research can be found in appendix B, flowcharts 1 - 3.

During the tests it is not possible for the crack increment between each measurement to be very large (>10^{-5}m/cycle). Loose probes will cause non-consistent potential measurements and hence non-consistent large crack increments per measurement step. A subroutine was designed to attack this problem. If the recorded crack length is unacceptably large (more than 8% of the previous measurement) the program sets the crack length equal to the previous value. 5 equal values of the crack length will cause the termination of the program. The cause of this problem will be a loose connection in the potential drop circuit, most possibly at the probes.

6.4.3 DCPD System

A new electrical potential system for the long crack length measurements under various loading conditions was constructed. Figure 6.11 shows a diagram of the system. It is able to carry out constant amplitude (CAL) and K-decreasing tests for the determination of threshold values of ΔK.

The system consists of an Instron 8500 test machine, a digital microvoltmeter (DVM), current source and two computers. The system uses the direct current potential drop (DCPD) technique [157] to measure crack length.

The fatigue tests were carried out in load control on an Instron 8500 digitally controlled servo-hydraulic fatigue test machine. The machine was equipped with a 50kN load cell.

The main computer (PC1), using the developed software, controls everything in the system (figure 6.10). In this manner, all the required test parameters can be continuously adjusted by the computer, and all the necessary crack length and crack growth data can be acquired. The modification of the system with the introduction of PC2 was necessary because the main computer was unable to command and gather test data at the same time. This kind of handling was used for CVAL tests where the system had to command the load sequence continuously due to its complexity, and require potential reading at frequent times. Therefore, the introduction of a second computer was necessary to solve the handling conflict. Hence, the second computer has the application control of the loading spectrum, whilst the first computer has the control of the DCPD measurement system.

A GPIB (General Purpose Interface Board) is responsible for the control of Instron test machine, DVM and current source. A 32-bit data acquisition card was placed into the computer in order to collect data from the DVM and the Instron test machine.

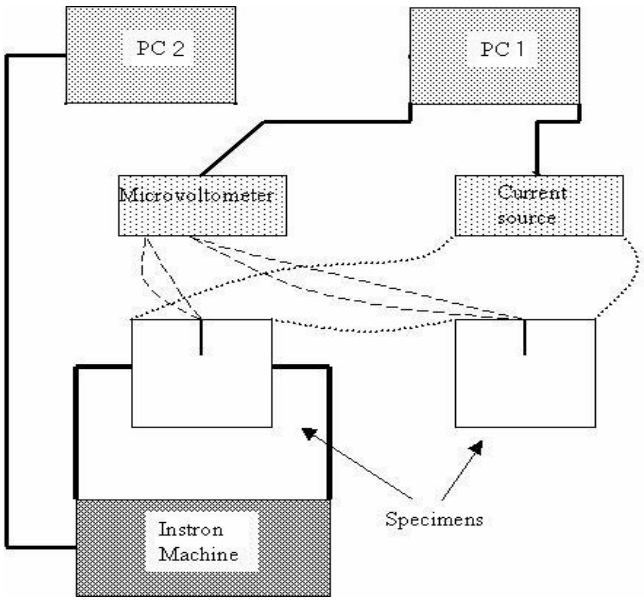

Figure 6.10 _ Schematic diagram of the electrical potential system

6.4.4 Resolution of the DCPD System

The resolution of the measurement system is defined as the smallest measurable change in crack length per 100nV (resolution of DVM) voltage increment. The resolution of the system depends on the DVM, the value of the fixed current supplied to the system's circuit, the geometry of the specimen, the location of the voltage measurement probes on the specimen and the electrical resistivity of the specimen material.

The resolution of the measurement system for each alloy can be seen in table 6.7. Also, the resolution is better as the material's resistivity becomes higher. This is because of the higher voltage values for a fixed current. It is obvious that higher power supply current values will improve the resolution. Buller has shown that for a similar measurement system, the resolution improves as the crack length increases [84].

Table 6.7_ Resolution of the DCPD Measurement System at a/W=0.20

	Material		
	Ti 1023	Al 8090	Al 7010
Resolution (μm)	3	~11	10.5

6.4.5 Accuracy of the DCPD System

In order to determine the characteristics of the system noise, a static test was set up with a dummy test sample and a reference specimen with a pre-existing crack for each alloy. The system was left to take potential measurements every minute throughout a period longer than 18 hours. Then, the potential measurements were translated to crack length with calibration curve. The mean value and the standard deviation of the set of the crack length values were calculated. The accuracy of the system for a single measurement was defined as the first standard deviation of the data. The results for Ti 1023, Al 8090 and Al 7010 are shown in Table 6.8.

Table 6.8_ Statistics of the crack length measurements of the DCPD system for each material

Material	Period (hours)	No of Measurements	Min (mm)	Max (mm)	Mean (mm)	Standard Deviation (mm)
Ti 1023	15.06	1084	22.46	22.52	22.48	0.014
Al 8090	25.05	1503	14.38	15.06	14.80	0.094
Al 7010	17.3	1038	14.25	14.61	14.45	0.084

Table 6.9 shows the accuracy of a single crack length measurements. During fatigue crack growth test program, each recorded value of the crack length by the computer was the average of 15 DCPD measurement.

The signal average technique states that there is a factor of $\sqrt{M}$ in the accuracy of the measurement, when the averaging of M measurements is performed [158]. The improvement factor on the accuracy is 3.873 for the averaging of 15 measurements.

Hence the theoretical accuracy of the system for Ti 1023 is ± 3.6 μm. Long term drift limits are ± 27.5 μm. The accuracy of the system for Al 8090 is ± 24.3 μm

and long-term drift limits are ± 342 μm. The accuracy and long-term drift for Al 7010 is ± 21.7 μm and are ± 182 μm, respectively.

The system has better accuracy when the samples have higher resistivity values. Hence, the system is more accurate for Ti 1023 samples when it is compared with the aluminium alloys.

Table 6.9_ Accuracy of the DCPD measurement system for each material

Material	Accuracy for 1 measurement (mm)	Accuracy for 15 measurements (mm)
Ti 1023	0.014	3.6
Al 8090	0.094	24.3
Al 7010	0.084	21.7

6.4.6 Estimation of Measurements Errors in Crack Length and Crack Growth Rate

The crack length measurements are used for the determination of the crack growth rates (da/dN) and hence the measurement error will propagate to the crack growth rate values.

The crack growth rates are calculated for small increments of the crack length Δa. The increments are between 0.0001 and 0.001 m.

So, $$da/dN = \frac{\Delta a}{\Delta N} \pm e(\frac{\Delta a}{\Delta N}) \quad (6\text{-}4)$$

Because there is no error in the cycle counting

$$e(\frac{\Delta a}{\Delta N}) = \frac{e(\Delta a)}{\Delta N} \quad (6\text{-}5)$$

But, $$e(\Delta a) = e(a_2 - a_1) = e(a_2) + e(a_1) = 2e(a) \quad (6\text{-}6)$$

So, $$da/dN = \frac{\Delta a}{\Delta N} \pm \frac{2e(a)}{\Delta N} \quad (6\text{-}7)$$

It can be seen from the above equation that the crack growth rate error depends on the number of cycles during the crack increment Δa. The variation of the error as a function of ΔN for each material can be seen in figure 6.11. The da/dN errors are described by the functions:

$e(da/dN) = 7.23 \cdot 10^{-6} / \Delta N$ for Ti1023

$e(da/dN) = 4.86 \cdot 10^{-5} / \Delta N$ for Al8090

$e(da/dN) = 4.34 \cdot 10^{-5} / \Delta N$ for Al7010

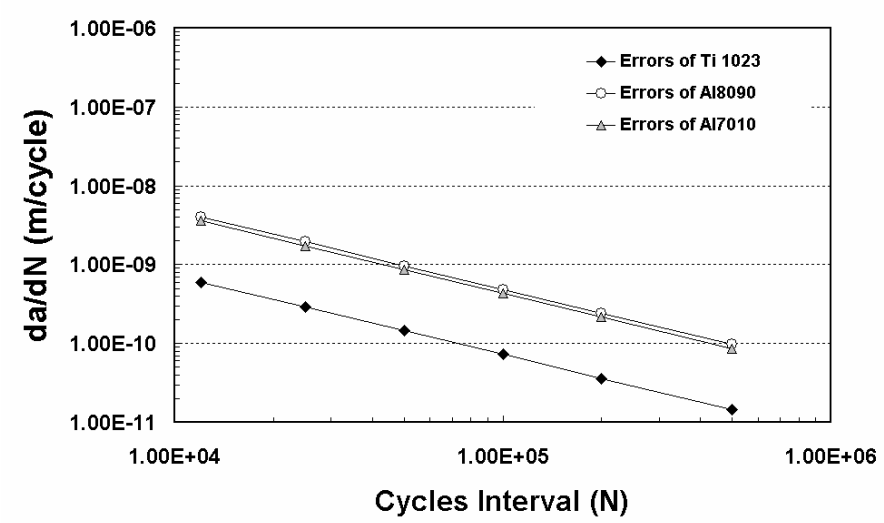

Figure 6.11_ Error values of fatigue crack growth rates for Ti1023, Al8090, and Al7010 in relation with the number of cycles interval that the measurement was conducted.

6.5 Fatigue Testing

The fatigue testing program was developed and performed in the context of this research includes threshold stress intensity range measurements, various SVAL and CVAL tests. In the following paragraphs, details will be given on the every test parameter such as cycles loading cycles sequences, values of stress intensity factors, loading R ratios, initial crack lengths, testing frequency, and specimen identification information.

6.5.1 Threshold Measurements

Two different techniques were used for the determination of threshold values of stress intensity factor ΔK_{th}. These are the constant R ratio and constant K_{max} techniques.

In constant R ratio technique tests, electrical potential data was converted into crack length during the test and used as input data to the software controlling the test machine load so as to maintain constant load R ratio as the crack grow, but with ΔK decreasing by reducing K_{max} and K_{min} , to approach a threshold ΔK_{th}. Similarly, in the constant K_{max} technique, the test machine controlled the load so as K_{max} were maintained constant, and threshold ΔK_{th} was approached by raising only K_{min}. Figure 6.12 shows the distinctive load path of the two techniques for the approach of threshold $\Delta K_{th.}$

The rate of approach to the threshold was consistent with the maximum rates of stress intensity reduction suggested in ASTM E647. The decrease of ΔK in every step was 3.5% of the previous value for tests at constant R, and 3.0% for tests with K_{max} constant. The decrease of ΔK was done every 0.1mm of crack increment. The samples were first precracked at constant amplitude of ΔK and K_{max} lower than the initial values of the test to avoid possible interaction effects with previous tests. The loading was then modified to fix the desired R ratio or K_{max} value, and then the crack was grown, maintaining the R ratio or K_{max} value at that level, reducing the ΔK until a maximum growth rate of 10^{-10} m/cycle was achieved. Each data point in the da/dN-ΔK plots was calculated by dividing 0.1mm of growth increments by the number of cycles it took to grow the increments. The test frequency was 20 Hz.

Threshold measurements were conducted on Ti 1023, Al 8090, and Al 7010. Tables 10, 11, and 12 give the details of the initial loading conditions, the initial crack length and the applied technique for each test. Each test is individually designated.

Table 6.10_ Details of threshold tests carried out on Ti10123.

Material	Test notation	Test Technique	Initial Conditions				Specimen ID
			K_{max} (MPa $m^{1/2}$)	ΔK (MPa $m^{1/2}$)	R	Crack length (m)	
Ti 1023	1Ti07th1	R Constant	22.66	6.8	0.7	0.0301	2ccT40
	1Ti07th2		22.66	6.8	0.7	0.026	2ccT40
	1Ti07th3		26.00	7.8	0.7	0.020	2ccT40
	1Ti07th4		26.66	8	0.7	0.014	2ccT40
	1Ti09th1		40	4	0.9	0.0201	2ccT33
	1Ti09th2		41	4.1	0.9	0.0200	2ccT17
	1Ti09th3		31	3.1	0.9	0.0212	2ccT19
	1Ti09th4		41	4.1	0.9	00204	2ccT28
	1Ti8th	K_{max} Constant	10	9	0.1	0.0142	2ccT27
	1Ti9th		15	10.5	0.3	0.0207	2ccT27
	1Ti10th		20	12.5	0.4	0.028	2ccT27
	1Ti15th		25	12.5	0.5	0.0145	2ccT23
	1Ti20th		9	9	0	0.0327	2ccT32
	1Ti25th		8	8	0	0.0215	2ccT23

Table 6.11_ Details of threshold tests carried out on Al8090 and Al7010.

Material	Test notation	Test Technique	Initial Conditions				Specimen ID
			K_{max} (MPa $m^{1/2}$)	ΔK (MPa $m^{1/2}$)	R	Crack length (m)	
Al 8090	1A807th1	R Constant	18.33	5.5	0.7	0.0147	CCT12
	1A807th2		18.33	5.5	0.7	0.0197	CCT12
	1A809th1		21.5	2.15	0.9	0.020	CCT1
	1A809th2		21.5	2.15	0.9	0.0275	CCT1
	1A801th1		11.1	10	0.1	0.0156	CCT10
	1A801th2		11.1	10	0.1	0.0235	CCT10
	1A803th1		12.86	9	0.3	0.015	CCT9
	1A803th2		12.86	9	0.3	0.0227	CCT9
	1A87th	K_{max} Constant	7	7	0	0.027	CCT12
	1A810th		10	8	0.2	0.031	CCT1
	1A820th		15	10.5	0.3	0.0145	CCT7
	1A825th		20	12	0.4	0.023	CCT7
Al 7010	1A712th	K_{max} Constant	12	9.6	0.2	0.145	CCT3
	1A718th		18	9	0.5	0.0155	CCT8
	1A724th		24	8.4	0.65	0.022	CCT3
	1A730th		30	6.5	0.8	0.0225	CCT8

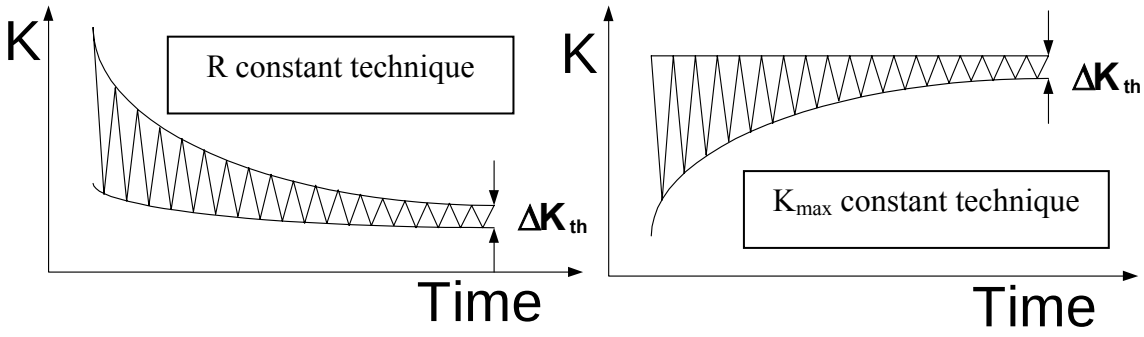

Figure 6.12._ The R and K_{max} constant techniques for the determination of the threshold ΔK and near threshold crack growth rates.

6.5.2 SVAL Testing

Various types of SVAL sequence were tested in order to understand the interaction effect between underloads and small amplitude cycles at high R ratio.

6.5.2.1 Underload Cycles after Threshold

For the set of R constant threshold tests on Ti 1023, after the establishment of ΔK_{th} a certain number **n** underloads to zero load was applied. The application of underloads was followed by 10^6 CAL cycles at ΔK_{th} and R ratio, which were previously established, in order to record the effects of the underloads cycles on the subsequent crack growth. The numbers of underloads and the other test parameters can be found in table 6.12. Underload cycles applied at a frequency of 1 Hz and threshold range cycles at a frequency of 20 Hz.

Table 6.12_ Number of underloads following the establishment of threshold on Ti1023

	Ti 1023							
Test	*1Ti07th1*	*1Ti07th2*	*1Ti07th3*	*1Ti07th4*	*1Ti09th1*	*1Ti09th2*	*1Ti09th3*	*1Ti09th4*
Number of underloads	50	20	5	1	50	20	5	1

6.5.2.2 Sequences containing small cycles and one Underload Cycle

SVAL fatigue testing was conducted in order to study the interaction effects between the baseline small cycles and tension-tension load excursions to small load

values. A large number of the fatigue tests were based on the loading cycle sequence of figure 6.13. One pass of this sequence consists of small and large amplitude cycles. K_{max}, ΔK_n and R_n ratio are the load characteristics of the small amplitude cycles. Stress intensity range ΔK_n is equal to the threshold stress intensity range of the material at the R_n. Large amplitude cycles have the same maximum stress intensity factor K_{max}. Stress intensity range is ΔK_u. The large cycle load ratio R_u is always lower than the R_n ratio of the small cycles. Maximum stress intensity factor of small and large cycles was kept at the same value because any difference in K_{max} level would act as overloading and consequently would have created retardation effects. These effects would greatly complicate the results analysis, and the effort to understand the fatigue crack growth mechanism of the underloads.

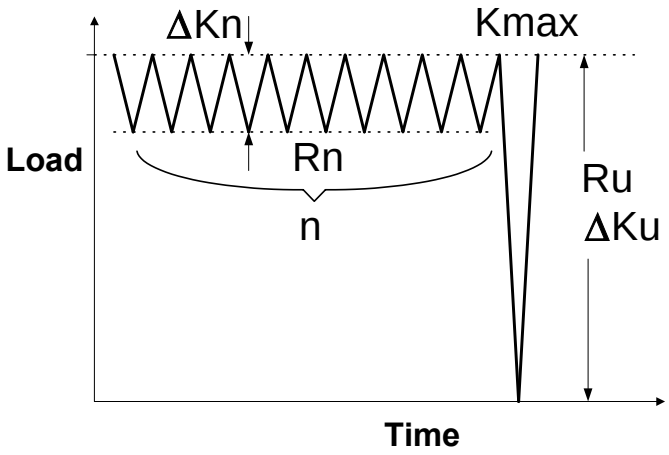

Figure 6.13._ One pass of the SVAL sequence that contains a simple combination of small and underload loading cycles

The effects of the underloading sequences on crack growth rates is a function of K_{max}, ΔK_n, ΔK_u, R_n, R_u, and the number of the small cycles n. Also, it is expected that the action of these sequences on different materials will be governed by different mechanisms. The aim of the developed test program was to cover the effects of all the above variables on the crack growth mechanism. Ti 1023, Al 8090, and Al 7010 were the materials used for this set of tests. Test frequency was between 5 and 12 Hz.

Tables A1-A3 shows the values of each parameter for every underloading SVAL test that was conducted. During each test, a certain number of sequence passes were applied. The target was either a specific number of total cycles to be

completed successfully or a specific crack growth increment to be achieved. The total number of cycles (small and underloads) applied during each test can be found on tables A1-A3. The number of applied cycles was set before the beginning of the test, in order to achieve a crack growth increment larger than 0.6 mm. Such a crack growth increment was considered necessary to fully eliminate any possible load interaction effect caused from fatigue history of the crack.

In addition, before each test, the crack was grown constant ΔK. The values of ΔK and K_{max} were lower than those of the test values for an increment of around 1 mm. This procedure is called precracking. The precracking was conducted to eliminate load interaction effects from the fatigue history of the crack. In some selected precracking procedures, fatigue data have been collected and used to determine crack closure loads and the ΔK_{eff} curve. The exact values of the precracking procedures can be seen in tables A4-A6 for Ti 1023, Al8090 and Al7010, respectively.

Crack closure measurements were conducted in a large number of the fatigue tests. Closure data was acquired during the large underload cycles and during the baseline cycles if it was necessary and possible. Tests where crack closure measurements were conducted are noted on the tables A1-A6.

Additionally, a few CAL tests were conducted on each of the three materials. The crack was left to grow under constant amplitude load for a defined crack increment or a number of cycles. These tests were conducted in order to establish the fatigue crack growth rates and crack closure levels at various constant amplitude loading levels. CAL tests were carried out at different crack lengths and material specimens on Ti1023, Al 8090 and Al7010 alloys. The loading condition and crack lengths of each test and materials are shown in tables A4-A6 together with the precracking procedures.

Crack growth rates were measured throughout each test. Crack closure data were recorded for a specific number of tests (tables A1-A6). Fatigue crack growth rates occurring at around 1 mm of crack growth increment were used in the results analysis, in order to avoid possible load interaction effects on the recorded data due to the changes in load conditions between tests. The same approach was followed for the crack closure measurements wherever it was necessary.

The tests were conducted under load control. The stress intensity factors referred on the tables A1-A6 are the values at the beginning of the tests. The values raised as the crack propagated. The increase of the stress intensity factors values is not very significant since most of the tests had a crack growth increment of around 2 mm, and therefore an increase of less than 10% in the stress intensity range. Consequently, it can be considered that the K_{max} remains at the same level.

6.2.2.3 Block Loading

Two SVAL tests were conducted in order to investigate the interaction effects between small amplitude cycles at R = 0.9 and large amplitude cycles at R = 0. These SVAL tests consist of a sequence of CAL cycles and / or SVAL cycles. In the following paragraphs, details will be given on the loading conditions and the starting crack length for each test. The two alloys used for these tests were Ti 1023 and Al 8090.

During the test designated as **R11T**, transient effects between the CAL at R=0 and ΔK=15.7 MPa $m^{1/2}$ and SVAL test with cycle sequence 1 underload after 10 small threshold cycles and K_{max}=15.7 MPa $m^{1/2}$ have been recorded on Ti1023. The test was divided in 3 parts. Firstly, CAL crack growth rates are established. After a load sequence of 10 small cycles at R_n=0.9 followed by 1 underload to zero was applied for 1mm. At the end, CAL cycles with the initial loading condition are reapplied for 1.3 mm. Table 6.13 provides details on loading conditions and crack lengths. Figure 6.14 shows the load pattern of this test.

Table 6.13_ SVAL test R11T conducted on CT specimens on Ti1023

Material	Sequence (underload/ Small cycles)	K_{max} (MPa $m^{1/2}$)	R_n	R_U	a_{start}(m)	Crack length increment (m)	Specimen Identity
Ti 1023	CAL	15.7	0	-	0.0273	0.0014	C222 15
	1/10	15.7	0.9	0	0.0287	0.001	C222 15
	CAL	15.7	0	-	0.0297	0.0013	C222 15

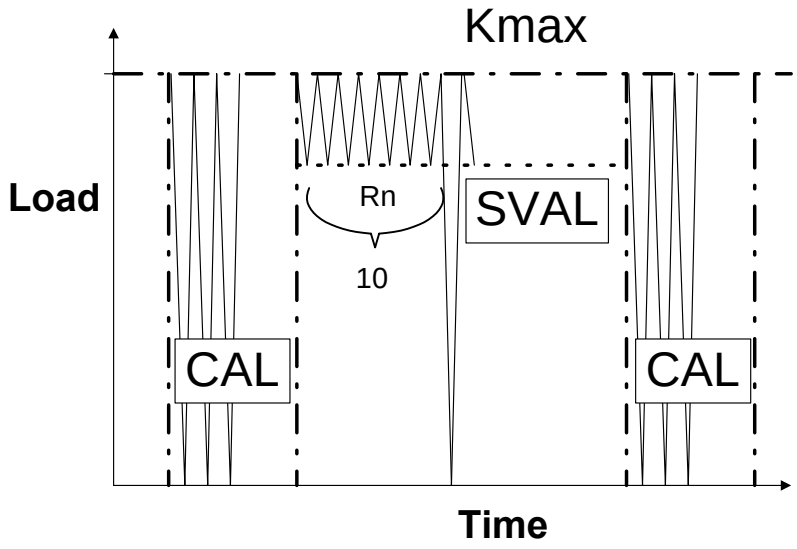

Figure 6.14_ The load sequence during the test R11T.

The transient effects between the CAL at R=0 and ΔK=14.1 MPa $m^{1/2}$ and SVAL test with cycle sequence 1/10 and K_{max}=14.1 MPa $m^{1/2}$ on Al 8090 were observed during tests **R11A8** on Al8090. The test was divided in 3 parts. Firstly, a load sequence of 10 small cycles at Rn=0.9 followed by 1 underload to zero were applied for 55000 cycles. After, CAL cycles are applied for 1 mm and at the end the same SVAL sequence is reapplied for 66000 cycles. Table 6.14 provides details on loading conditions and crack lengths. Figure 6.15 shows the load pattern of the test.

Table 6.14_ Details of the test R11A8 conducting on CT specimens on Al8090

Material	Sequence (underload/ Small cycles)	K_{max} (MPa $m^{1/2}$)	R_n	R_U	a_{start}(m)	Crack length increment (m)	Specimen Identity
Al 8090	1/10	14.1	0.9	0	0.0165	0.00104	CCT 15
	CAL	14.1	0	-	0.0176	0.00092	CCT 15
	1/10	14.1	0.9	0	0.0185	0.000304	CCT 15

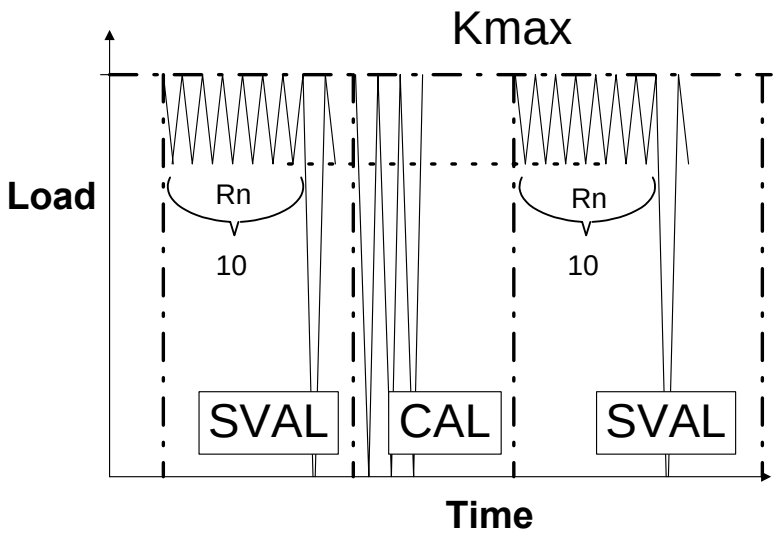

Figure 6.15_ The load sequence of the test R11A8

6.5.3 Complex Variable Amplitude Loading

In CVAL tests, the loading parameters were held constant and the crack allowed to grow, the stress intensity values produced by the loads increasing with increasing crack length. In these tests, pairs of values of cycles and potential were recorded by a PC based system, and converted into pairs of values of crack length and cycles and then into stress intensity and crack growth rates da/dN.

The loading spectrum used for the testing was ROTARIX [84]. Four different variants of the Rotarix spectrum were used. Rotarix is a spectrum derived from strain measurements on the Westland Lynx rotorhead using the same sequence of manoeuvres as was used in the generation of the HELIX and FELIX (12) helicopter spectra. HELIX and FELIX were derived from strain measurements made on helicopter blades for hinged blades and fixed blades respectively. Identical procedures were used to derive the Rotarix spectrum, but substituting strain measurements made on the rotorhead, for the measurements made on the blades, in each of the manoeuvres in the sequence.

A schematic of a section of ROT 16 is shown in figure 6.16. ROT 16 represents a fixed sequence of 140 sorties or 190.5 hours of flight. Turning points in the sequence are represented by levels, the levels being numbered from zero to 100 in

intervals of 4. The levels or load units can be considered as a multiplication factor to a load. The outcome gives the applied load. The maximum applied load respects to the maximum load unit, which is 100.

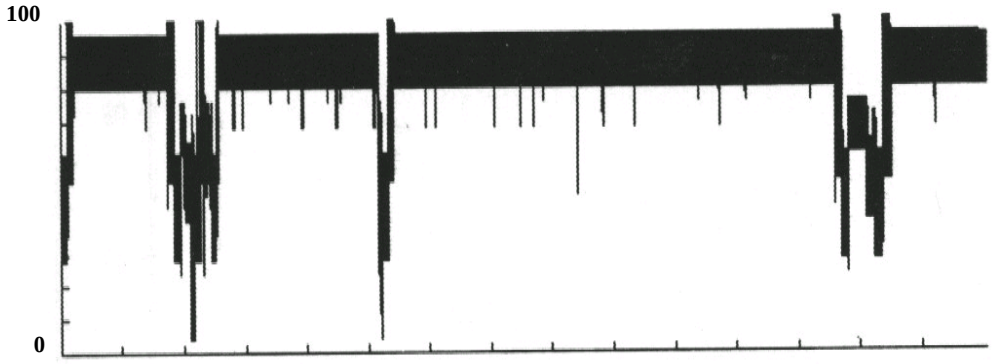

Figure 6.16_ Load sequence from a short section of ROTARIX 16 load history. Load range is from 0 to 100 load units.

The load range and R ratio of the Rotarix-16, 20, 24 and 32 spectra were examined. The analysis produced the load range and R ratio distributions, which are shown in Figure 6.17. The outline provides data about the load amplitude and the R ratio of the cycles in the Rotorix series.

In its full form (ROTORIX 16) the sequence consists of 1.98 X 10^6 cycles. 90% of these cycles are of load range unit 16 or below, which originate in the rotor motion. There are 3 other variants of the spectrum in which cycles of progressively larger range have been removed. These are:-

ROT 20, containing cycles of Range 20 and above, 1.13 X10^5 cycles
ROT 24, containing cycles of Range 24 and above, 1.11 X 10^5 cycles
ROT 32, containing cycles of Range 32 and above. 5.14 X10^4 cycles

It will be seen that the majority of the cycles in Rotorix-16, are composed of cycles with R ratio greater than 0.81, and are of amplitude between 10 and 20 load units. In Rotorix-20 these are largely removed, the remaining cycles are at R ratios dominated by cycles with R between 0.5 and 0.75, and with larger cycle ranges of 25-35 load units. These trends towards progressively larger cycle ranges and reduced R continue in Rotorix-24 and 32, as the threshold for cycle removal is raised.

Consequently, the large numbers of small cycles in ROT 16 have R values of 0.7-0.9. These are interspersed with load excursions to lower loads caused by Ground-Air-Ground (GAG) cycles and other manoeuvre loads. Thus ROT 16 is dominated by large numbers of high R cycles with underloads, whereas ROT 32 will be a spectrum consisting of larger lower R ratio cycles without underloads.

To begin the variable amplitude tests, CT samples were precracked under constant amplitude loading, at R ratio of 0.1 and at peak loads which would give the desired K_{max} value for the variable amplitude tests at the starting crack length. This K_{max} value was 10 MPa $m^{1/2}$ for the 7010 and 8090 aluminium alloys, and Ti 1023 titanium. The K_{max} values were chosen so that the level 16 cycles in ROTARIX would be at or just over the threshold level for the material in question. Table 6.15 gives the loading conditions and crack length for each CVAL test.

Table 6.15_Crack lengths and loading data for CVAL tests

		Ti 1023	Al 8090	Al 7010				
Spectrum		Rot16	Rot16	Rot16	Rot16	Rot20	Rot24	Rot32
Initial Crack Length	Mm	29.2	33.0	30.0	15.9	16.3	16.3	15.7
Final Crack Length	Mm	29.7	37.1	32.1	Failure	failure	failure	failure
K_{max}	MPa $m^{1/2}$	10	10	10	10	10	10	10

6.5.4. Fractography

A selection of Ti1023, Al8090 and Al7010 specimens from the tests were broken open after the test to reveal the fracture surface under optical. Observations of the fracture pictures were made in relation to the fracture roughness. The correlation of the fracture surface features with observation occurring from the crack growth measurements was examined. The crack growth direction is indicated in the individual pictures.

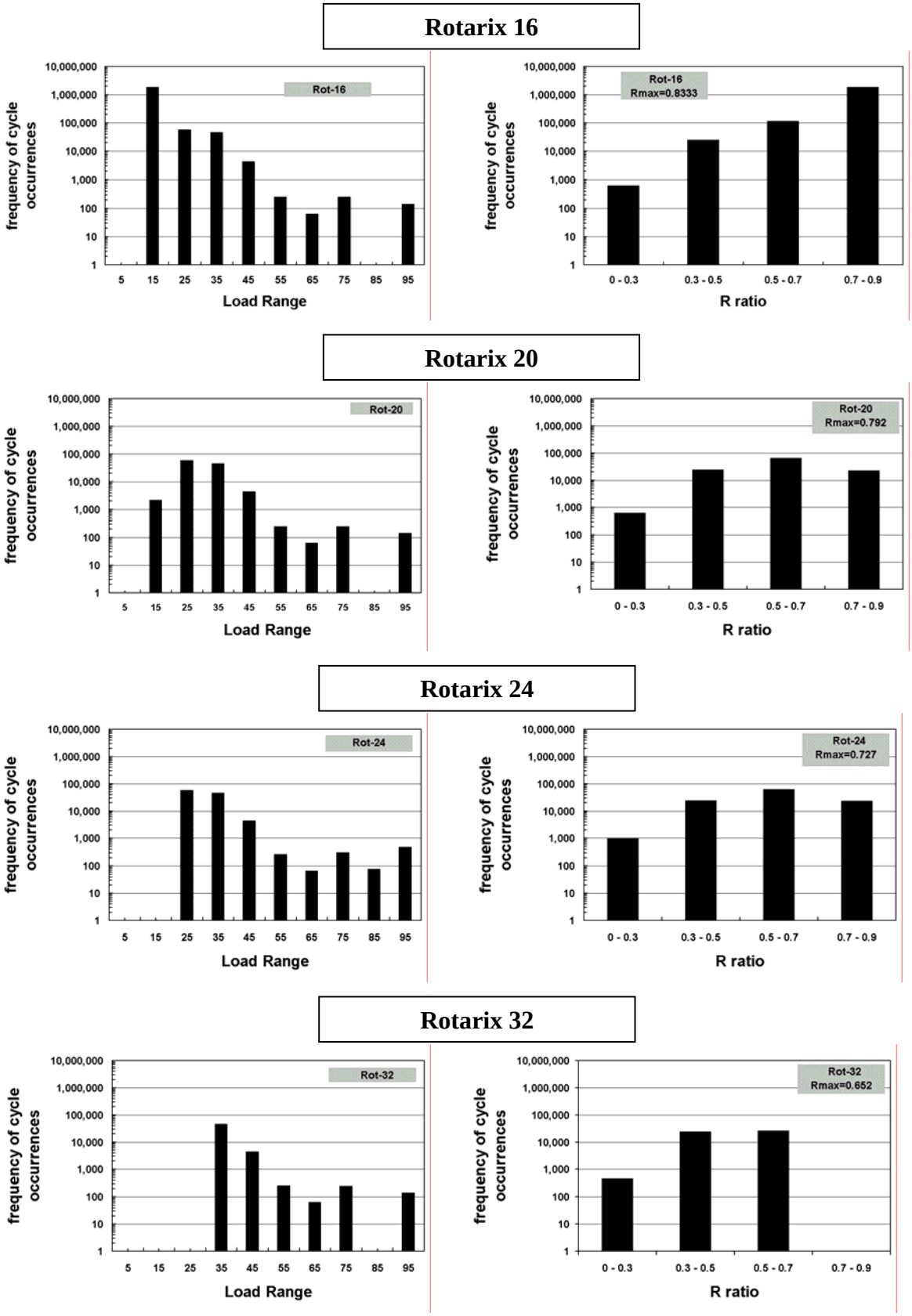

Figure 6.17_ Load range and R ratio levels for the loading cycles of the four Rotarix omission levels (Rot16, Rot20, Rot24, Rot32)

6.6 Fatigue Crack Closure Measurements

Crack closure information during CAL and SVAL were obtained using the compliance technique. This technique uses the crack opening displacement (COD) response of the specimen to the variation of the far field applied load. A crack opening displacement gauge (CODG) was used to obtain displacement data. The far field load data was obtained via the Instron control tower.

The compliance technique has been recognized as one of the most important crack measurement techniques [55, 59]. The use of CODG provides the global COD of the specimen. Hence, it is expected that the crack closure level will be directly related to response of crack surfaces through the entire specimen thickness.

6.6.1 The Crack Opening Measurement System

A CODG was used to gather compliance information. According to the manufacturer, the strain accuracy is +/- 0.005% of the transducer capacity or +/- 0.25% of the reading, whichever is greater, and the resolution is 1 part of 60,000 of +/- 100% of the range in use (16 bit).

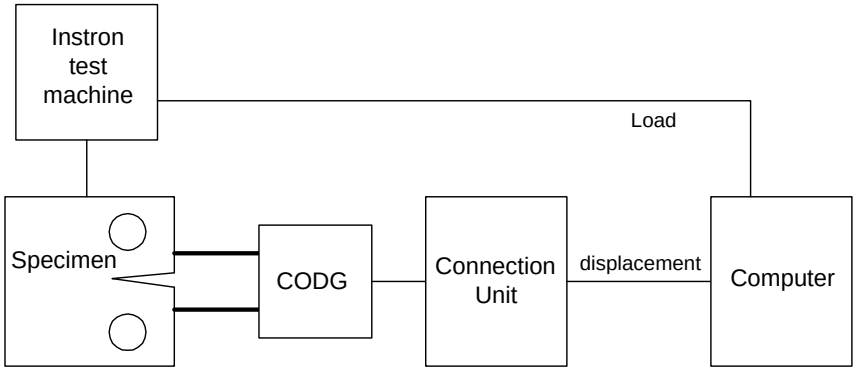

Figure 6.18_ Crack closure measurement system.

The set up of the devices used for recording of the compliance curves can be seen in figure 6.18. The applied load was acquired directly from the Instron test machine. The data acquisition card was the interface between the computer and the Instron test machine. The COD response of the CT specimen was measured by the CODG. One thousand points per cycle were collected at each measurement. The frequency of the test remained unchanged because of the ability of the card to

acquire data very fast. The readings were transferred to the data acquisition card and finally to the computer hard disk through digital connection unit. The calibration for the CODG was defined as voltage change of 0.25V per 1mm of CODG displacement. The calibration function of the applied load P (KN) with respect to the electrical signal V (Volts) of the machine control tower was 5kN per 1V with an 0.1% error.

6.6.2 Load and Crack Mouth Displacement Signals

Figure 6.19 shows a typical example of the input load and crack mouth displacement signal measured on Ti1023. The applied load has been recorded with great accuracy. The displacement waveform presents a degree of scatter. It was estimated at 5μm (figure 6.19). The performance of the connection unit had a direct impact on the noise level of the measured displacement signal.

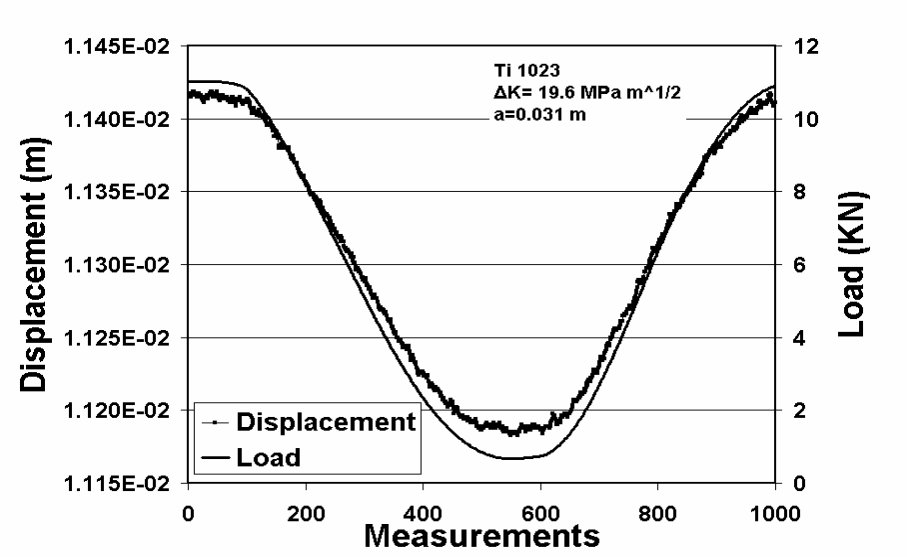

Figure 6.19_ Original load and displacement measurement of a loading cycle on Ti1023 using the crack closure measurement system.

In order to reduce the noise of the signal and proceed to the creation of the compliance curve where the closure point could be determined, the input displacement was filtered by a cascade form of the IIR filter. The digital filter was set to eliminate the high frequencies on the signal (lowpass), since the original signal has a low frequency comparing with the noise. The filter is a software

developed by National Instruments Corporation. Load data obtained via the Instron control tower was not filtered.

Figure 6.20 shows the crack mouth displacement measurements before and after the application of the filter. The displacement waveform is much smoother after the filtering. The resulted compliance curve after the application of the filtering is shown in figure 6.21. The curve has the shape of a typical compliance curve and was used for the determination of the crack opening load.

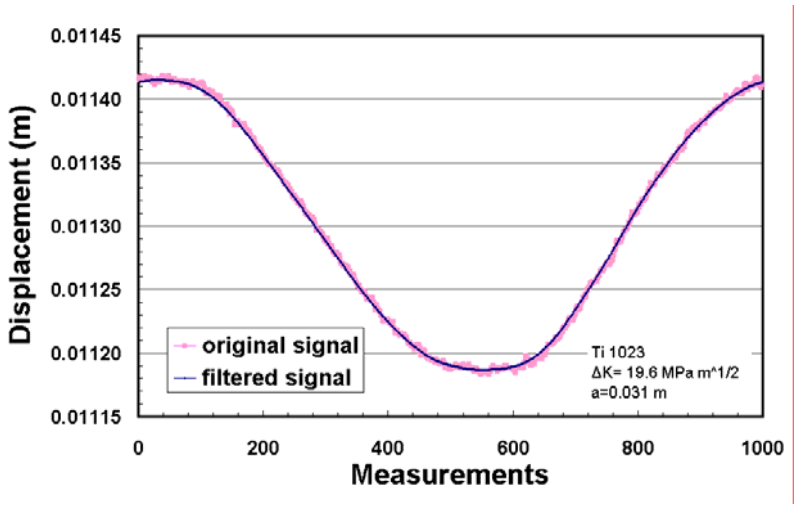

Figure 6.20_ Comparison of the original and the produced filtered displacement signal.

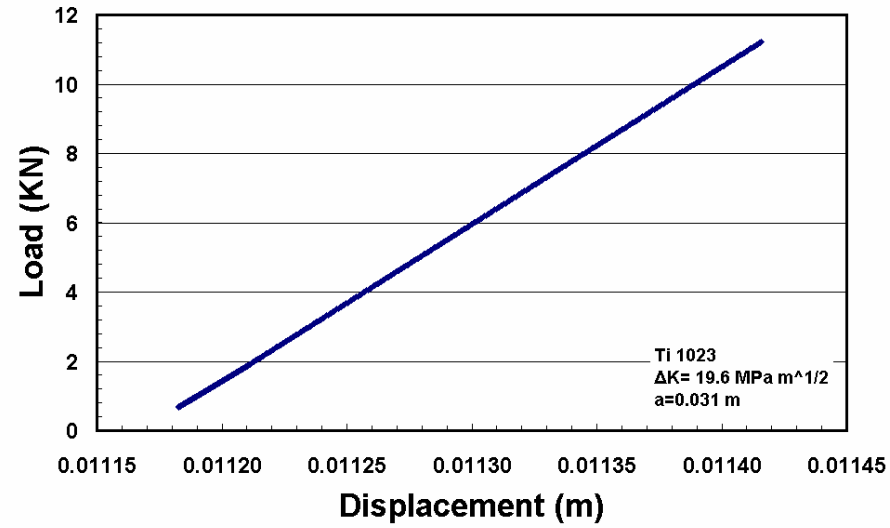

Figure 6.21_ A typical load-displacement curve using the filtered displacement signal.

6.6.3 The Crack Opening Determination Technique

A typical Al8090 load-displacement curve is presented in figure 6.23 and is compared with a straight line in order to justify if there is a deviation from the linearity. A deviation from the linearity occurs at some point of the loading cycle.

The basic approach used to detect the closure point from load vs. displacement curves is a curve fitting analysis, which is called the mean value method. According to this method, the curve is divided into two parts about the assumed closure point along the curve (figure 6.22a). In the upper part, a straight line is fitted. A second order polynomial curve is fitted in the lower part. Then, the absolute difference in co-ordinates between the beginning of the straight line and the end of the second order polynomial section is obtained. Because the crack closure point is initially unknown, the position of point P, which divides the curve, gradually changed. The distribution of the absolute difference in co-ordinates was produced (figure 6.22). For the compliance curve of figure 6.23, the distribution of these residual errors is shown in figure 6.24. It is possible that the minimum value of the distribution could well be offset the lowest peak of the distribution curve and not accurate representation of the closure point (figure 6.22). Thus, only the 10% of minimum values of the differences are selected because it is only in this small range that the closure point is likely to be. The mean value and the standard deviation of the selected values are calculated (figure 6.24). At the point where the mean value occurs, the closure load is considered and the standard deviation is an indication of the error in the calculated value.

Based on the above approach, the closure point occurs at the load P_o = 7.7 kN or 0.66 K_o/K_{max} and the errors is estimated as 0.3 kN or 0.03 K_o/K_{max} or 5% of P_o (figure 6.24). The crack opening load error of 5% to 10% of the test measurement is considered as the typical measurement error for this study.

The method for the crack opening determination described above is a small variation of the method suggested by Yieshieng and Schijve [59] and by Sinclair et. al [59]. Sinclair et. al consider as closure point the point at which the absolute difference in co-ordinates between the straight line and the second order polynomial section reaches a minimum. Yieshieng and Schijve determined the closure point as the point at which both the difference in co-ordinates and slope of the linear part and the second order part have a minimum regression error. Figure

6.24 shows a typical distribution of the absolute difference in co-ordinates calculated during the mean value method used in this study. It becomes obvious that the selection of the minimum value of the distribution is not able to determine the crack closure point successfully and consistently.

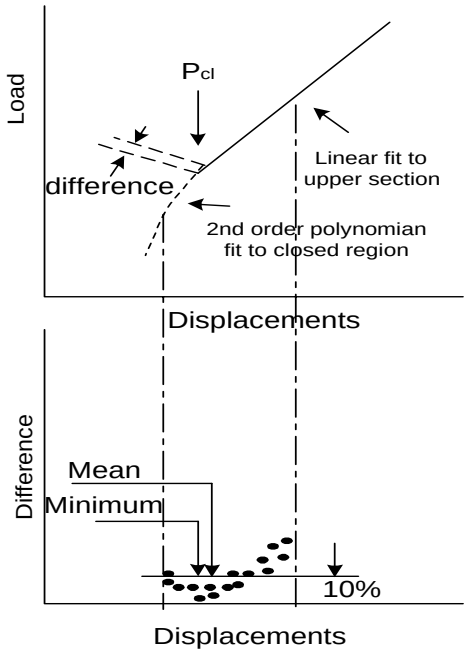

Figure 6.22_ Graphical description of the curve fitting technique used for the determination of the crack opening load.

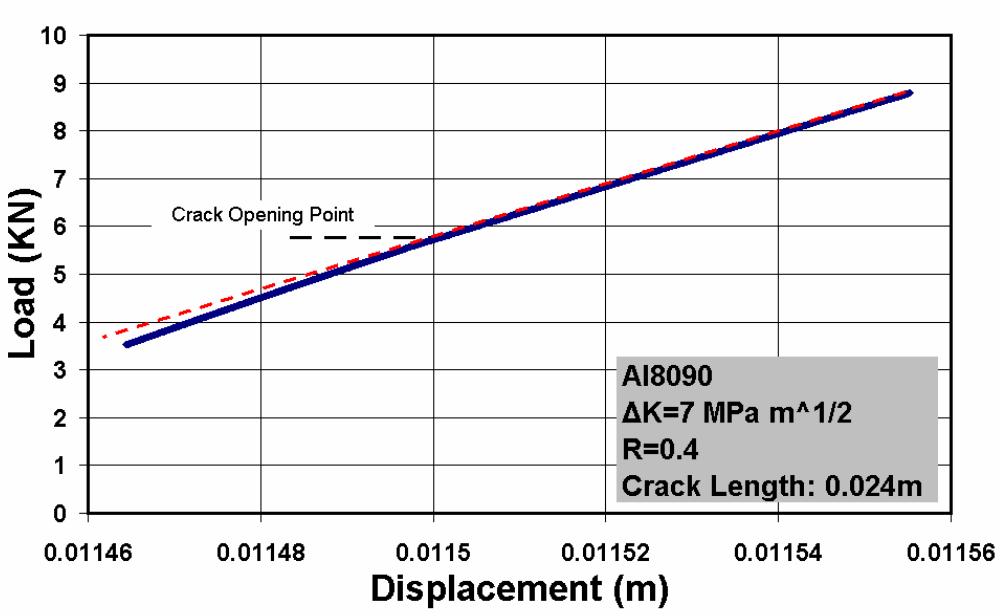

Figure 6.23_ A typical Al8090 load-displacement curve is compared with a straight line.

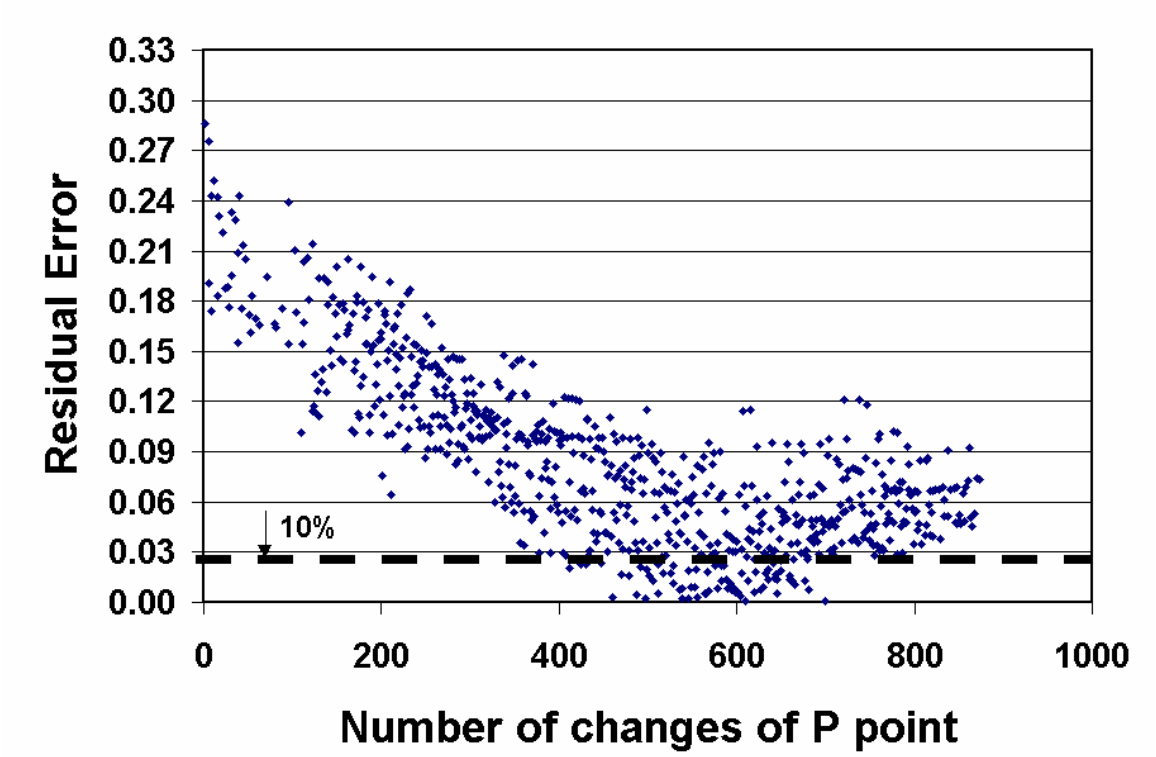

Figure 6.24_ A typical distribution of the absolute difference in co-ordinates of the upper and the lower fitted curves calculated from the technique for the determination of the crack opening load.

6.7 Behaviour and Normalization of the Maximum Crack Mouth Displacement

The values of the maximum displacement, d^{i}_{max}, occurring at each cycle of the recorded loading sequence were abstracted from the filtered signal (figure 6.25). Because the experimental scatter is high, the mean values of the maximum displacement, d_m, for each individual cycle in the sequence during the test were calculated. Hence, a mean value of the maximum displacement of the first, second, etc. cycle of the sequence in the test is derived. Figure 6.26 shows the procedure that was followed. The mean values, d_m, are expected to reduce the experimental scatter and reveal the trend of changes of maximum displacement within a sequence.

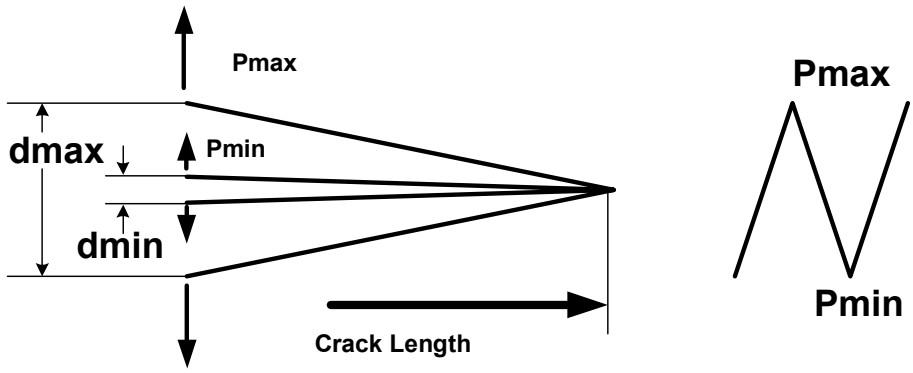

Figure 6.25_ Location of the maximum and minimum displacement of the crack during a cycle.

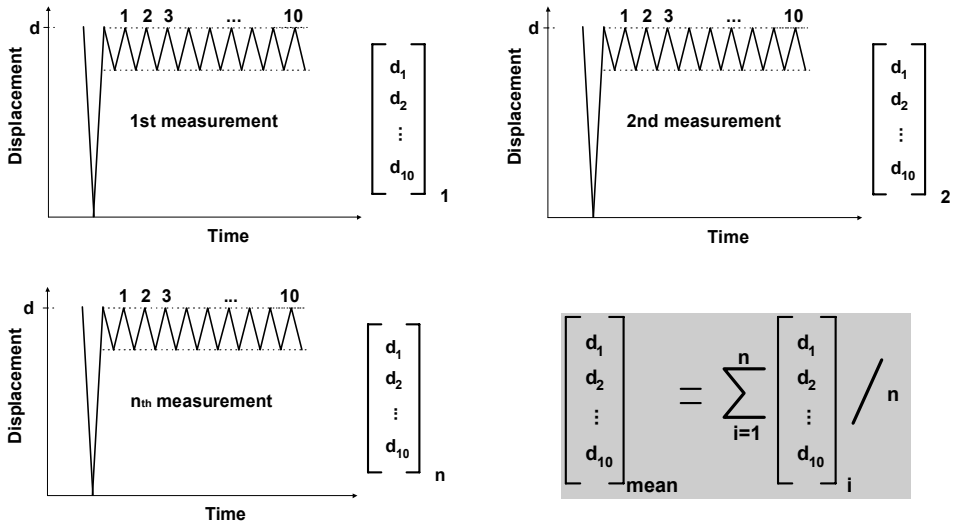

Figure 6.26_ The procedure followed for deriving the mean value of the maximum displacement of the first, second, etc. cycle of the sequence in the test.

When the material is stressed elastically the d_{max} will be the same for similar loading conditions. Thus, it is expected that ΔK_{th} cycles, which cause no crack growth, will have the same d_m at the same crack length. Changes in the plastic deformation of the plastic zone around the crack tip will alter the d_m from the elastic behaviour (figure 6.27).

The maximum displacement d_{max} of the crack mouth is a function of the applied load, the crack length and the material properties [156]. Direct comparison of the d_m from the different SVAL tests will not lead to a valid conclusion, since the d_m is referred to different load and crack lengths each time.

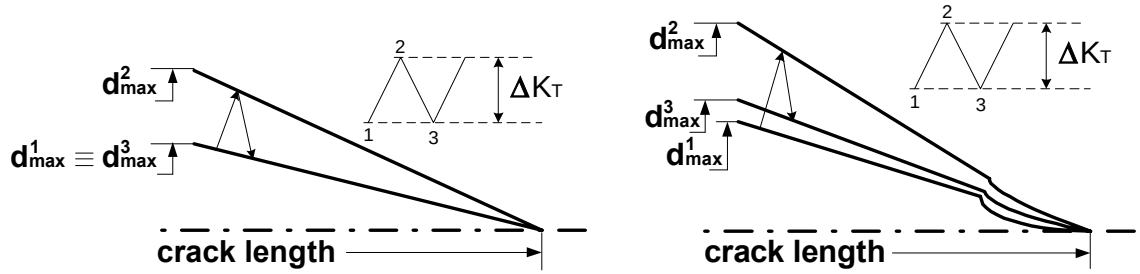

Figure 6.27_ Changes in the plastic deformation of the plastic zone around the crack tip will alter the d_m from the elastic behavior.

δ_0 is the displacement of the crack mouth in the CT specimen and is expressed as [156]:

$$\delta_0 = \frac{P \cdot V(a)}{E \cdot t} \quad \text{or} \quad \frac{\delta_0}{P \cdot V(a)} = \frac{1}{E \cdot t} \tag{6-8}$$

where, P the applied load, E the Young Modulus, t the specimen thickness and V(a) a function of the crack length.

The quantity $\frac{\delta_0}{P \cdot V(a)}$ is expressed in m/N and is independent of the applied load and the crack length. It is a function of the material and the specimen thickness. Therefore, the factor $1/(PV(a))$ can be used to normalize the d_m measurements, so that measurements at different crack lengths and load values can be directly compared.

The normalization of the d_m and d_m increment, Δd_{mn}, which is the difference between the normalized $d_m^{(i)}$ at i small cycle and the normalized $d_m^{(1)}$ at 1st small cycle, offers the advantage of the direct comparison between the d_m behaviour from different SVAL tests.

CHAPTER 7

ANALYSIS TOOLS

7.1 Introduction

It is necessary to assess the performed fatigue tests in terms of their damage and the measured fatigue crack growth rates. Therefore, the use of theoretical analysis tools, which will enable the comparison of the test results with the theoretical predictions, has been introduced. The tools used in this research were the linear summation calculation based on CAL data and performed by AFGROW software, and the FASTRAN model. In the following paragraphs details are given on the above analysis tools, the material inputs for each case and various raised issues.

7.2 Linear Summation Calculations

To justify whether the fatigue load interaction affects exist in the fatigue tests, a comparison has to be made between the measured fatigue life in the tests and the theoretical damage caused by the crack growth of CAL cycles at the same loading characteristics. The theoretical damage calculation will allow the determination of the fatigue life caused by the spectrum without taking into account the load interaction effects between the loading cycles. The calculation of the theoretical damage based only on CAL crack growth rates will be referred as linear summation calculation in the rest of the document. The comparison between the linear summation calculation of a SVAL spectrum and the actual fatigue life and crack growth observations will reveal whether the crack propagates faster than it is expected.

The kind of the effect that the loading cycles have on the crack propagation is assessed by the introduction of three acceleration factors. The acceleration factors are noted as α, β and γ and they defined as:

$$\alpha = \frac{\text{Crack growth rate measured in test } (da/dN)_t \text{ at a specific } \Delta K}{\text{Crack growth rate calculated by linear summation of the constant amplitude crack growth responce } (da/dN)_f \text{ at the same } \Delta K}$$

$$\beta = \frac{\text{Total number of cycles for the crack to grow equal to the measured length calculated by linear summation of the constant amplitude crack growth responce } (\Delta N_f)}{\text{Total number of cycles of the test } (\Delta N_t)}$$

$$\gamma = \frac{\text{final crack length increment measured in test } (\Delta a_t)}{\text{final crack length increment calculated by linear summation of the constant amplitude crack growth responce } (\Delta a_f)}$$

It becomes obvious by the definitions that acceleration factor α shows how much faster (or slower) the crack propagates compared with the spectrum's linear summation. The acceleration factor α is referred to the comparison of crack growth rates of the same stress intensity range (figure 7.1a). Useful conclusions can not be derived by the comparison of crack growth rates at different ΔK levels. The acceleration factors α calculated in the present study are referred to the crack growth rates after around 1 mm of crack propagation. This means that the comparisons were made at a ΔK level of around 10% higher than the initial ΔK value. The reason is that at the beginning of the test a small influence from the crack loading history still exists and therefore has a small effect on the crack growth rates.

Acceleration factors β shows how many times larger is the theoretical prediction of the total number of cycles it took to growth a crack to the final test crack length than the recorded number of loading cycles during the experiment. The acceleration factor β is valid only when the number of cycles of the test and the prediction are referred to the same crack increment (figure 7.1b). Acceleration factors β calculated in the present study are referred to the final crack length of the test.

Acceleration factors γ shows how many times larger is the fatigue damage caused by the action of the loading cycles during the test than the linear summation calculation of the crack growth. The acceleration factor γ is valid only when the measured and predicted crack growths are referred to the same number of total loading cycles (figure 7.1c). Acceleration factors β calculated in the present study are referred to the total number of loading cycles at the end of the test.

From the definition of the acceleration factors occurs that if there are no significant load interaction effects in the test and the fatigue life can be predicted by the linear summation calculation, the accelertion factors α, β and γ will be equal to unity. A factor lower than the unity means that the linear summation calculates a smaller fatigue life than the test measurements and hence retardation effects are predominant within the loading sequence.

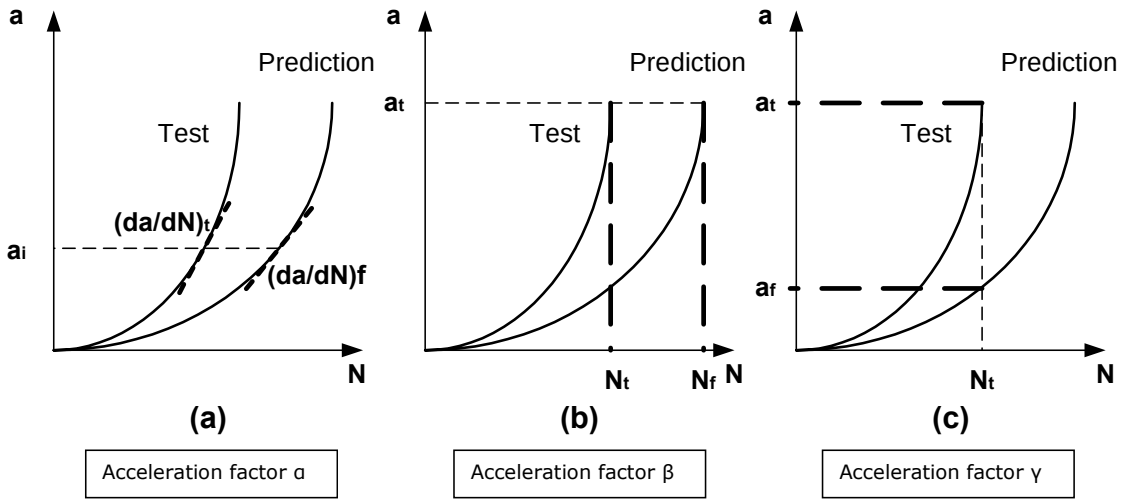

Figure 7.1_ Graphical representation of the acceleration factors α, β and γ.

7.2.1 Estimation of Measurements Errors (factors a, β, γ)

Acceleration factor α is defined as the ratio of the measured crack growth rate over the predicted crack growth rate based on the CAL at a certain ΔK value. Since measured crack growth rates are used for the calculation of factor α, the corresponding error will propagate to the final factor result. It is assumed that $(da/dN)_{CAL}$ is free of errors because it is a predicted value.

So, $$\alpha = \frac{da/dN}{(da/dN)_{CAL}} \pm e\left(\frac{da/dN}{(da/dN)_{CAL}}\right) \qquad (7\text{-}1)$$

Where

$$e\left(\frac{da/dN}{(da/dN)_{CAL}}\right) = \frac{e(da/dN)}{(da/dN)_{CAL}} = \frac{2e(a)}{\Delta N (da/dN)_{CAL}} \qquad (7\text{-}2)$$

From the above equation, the error in the factor α is inversely proportional to the number of cycles that the measured crack growth rate da/dN is based on and the predicted $(da/dN)_{CAL}$ value. Hence, faster crack growth rates tend to reduce the error on factor α. Considering ΔN=10,000 cycles as an typical value, the e(α) is given by the figure 7.2 for each material.

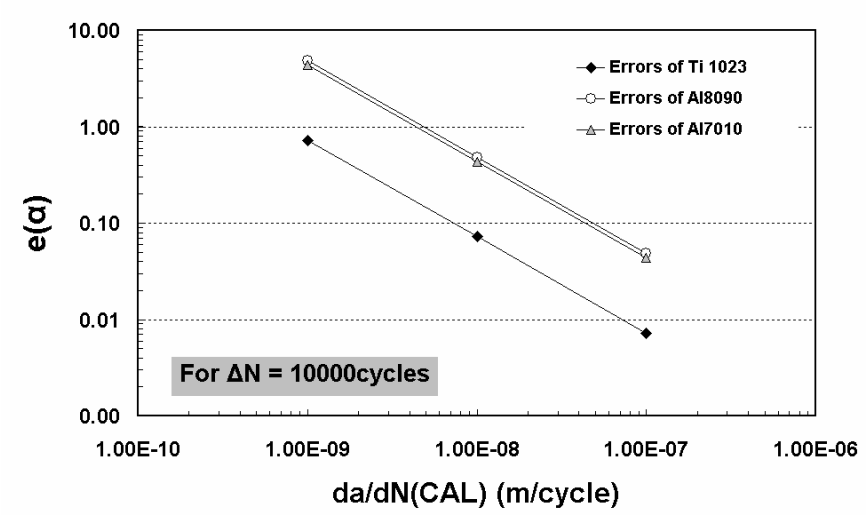

Figure 7.2_ Error values of the acceleration factor α for Ti1023, Al8090, and Al7010 in relation with the crack growth rate for a given cycle interval, which the growth rate calculation was conducted .

Larger number of cycles ΔN produces slow crack growth rates since the crack growth rate were measured for a fixed crack length increment. But, slow crack growth rate increase the error e(α). Therefore, the effect of $(da/dN)_{CAL}$ is inverely proportional to the effect of ΔN.

Similarly, the acceleration factors β and γ can be expressed as

$$\beta = \frac{N_t}{N_{CAL}} \pm e\left(\frac{N_t}{N_{CAL}}\right) \tag{7-3}$$

$$\gamma = \frac{a_t}{a_{CAL}} \pm e\left(\frac{a_t}{a_{CAL}}\right) \tag{7-4}$$

Following the same procedure as in the case of factor α, the estimated error for factor γ is:

$$e(\gamma) = e(\frac{a_t}{a_{CAL}}) = \frac{e(a)}{a_{CAL}} \tag{7-5}$$

The error band in the calculations of the factor β is given by the distance (in cycles) AC in figure 7.3. Because the AO=OB=e(α) is small, it can be assumed that the points A, B, O have the same crack growth rate. Hence, the $e(N_t)$ can be calculated by the relationship:

$$e(N_t) = \frac{e(a)}{da/dN} \tag{7-6}$$

Consequently, the error in the factor β is :

$$e(\beta) = e(\frac{N_t}{N_{CAL}}) = \frac{e(N_t)}{N_{CAL}} = \frac{e(a)}{N_{CAL} \cdot da/dN} \tag{7-7}$$

The error in the calculation of factor β is reversed proportional to the crack growth rate that the calculation is taking place. Hence, faster crack growth rates reduce the error on factor β.

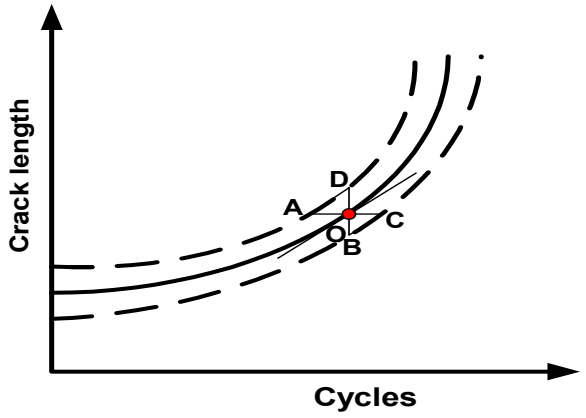

Figure 7.3_ The error band in the calculations of the factor β.

7.3 AFGROW Software and Models

AFGROW is a computer software package, which performs fatigue life predictions. It has been developed by James A. Harter and Analytical Services and Materials at the US Air Force Research Laboratory, Wright-Patterson AFB, OH. [116]

There are four models available within the package. These are the linear summation calculation function, the Willenborg model, the Closure model and the Wheeler model. The simplest one is the linear summation calculation function. This function uses only the material's CAL data without involving any manipulation caused by the sequence of the loading cycles in the spectrum. The Willenborg, the Closure and the Wheeler models have not been used in this study. Their ability to predict the fatigue life under CVAL spectra has been shown to be limited [159].

Linear summation calculation of the SVAL spectra tested in this research has been carried out using the linear summation function of AFGROW. The basic concept behind the linear summation function of AFGROW is depicted in figure 7.4. The software calculates the stress intensity range and R ratio of the i cycle based on the values of the maximum load, turning points i1 and i2, and the material geometry. Then, using the calculated fitted curve for the specific R ratio, it allocates the crack growth rate da/dN for the specific ΔK. Providing that one cycle is involved, the crack increment is derived. This increment is then added to the previously calculated crack length a_{i-1} and the current crack length a_i is derived.

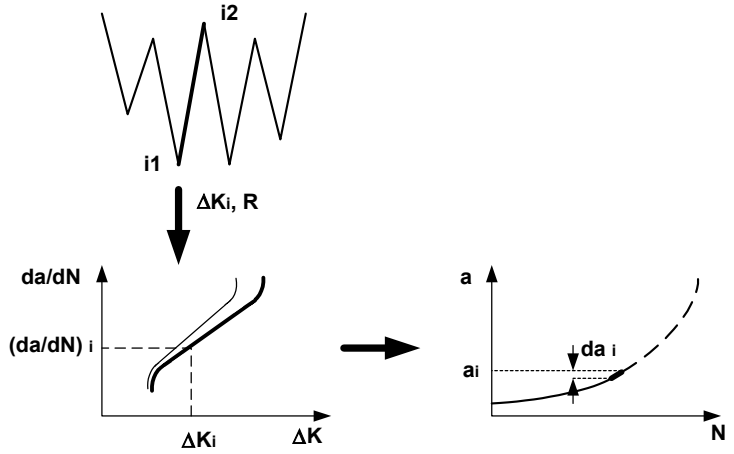

Figure 7.4_ Graphical representation of the procedure followed by the AFGROW model to calculate the crack increments.

Crack growth increments produced by individual load cycles are calculated from a plot of da/dN Vs ΔK. Hence the function da/dN=$f(\Delta K)$ must be provided. The input material CAL data was provided in tabular format. AFGROW software performs a fitting procedure to the input curves and uses the results as the basic relationship between the stress intensity factors and the crack growth rates. It is obvious that the result of the curve fitting of the raw CAL data on the life prediction is very critical. A good curve fitting will produce a good representation of the fatigue life without load interaction effects.

In addition to the requirements for constant amplitude crack growth data, the material properties, the specimen geometry and the loading characteristics must be provided to the model to carry out a fatigue life prediction. The material properties for Ti1023, Al8090 and Al7010 can be seen in tables 6.2, 6.4 and 6.6 in the Experimental section. The Compact Tension specimen geometry was used. The dimension can be seen in figure 6.8. The initial crack length was different for each fatigue life prediction depending on the initial crack length of the respective test. Loading spectrum is provided in terms of a series of turning points and the maximum applied load.

Figure 7.5 shows the fitted curves that AFGROW created and used in the linear summation calculation and the CAL fatigue crack growth rates for Ti1023 alloy. Agreement between the original experimental data (points) and the resulted fitted curves used in the analysis (lines) is remarkably good. The same conclusion can be drawn if one observes the fitting results on Al8090 and Al7010 in figure 7.6 and 7.7, respectively. The curve fitting at the low R ratio crack growth data of Al8090 can be considered as the best estimation of the material behaviour as the experimental CAL data exhibits a high degree of scatter.

The selection of AFGROW was based on the fact that the software calculates the fatigue life without applying any kind of manipulation between the fitted curves and the calculation of the crack growth rates and consequently the fatigue life. The life prediction is solely depends on the successful representation of the raw CAL crack growth data, which indeed was successfully achieved.

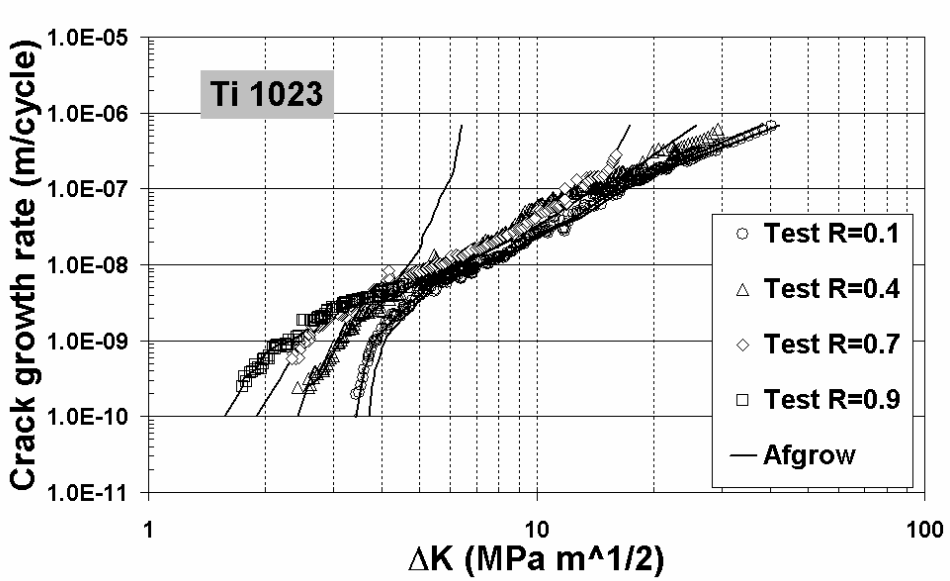

Figure 7.5_ The fitted curves that AFGROW created and used in the linear summation calculation and the CAL fatigue crack growth rates for Ti1023 alloy.

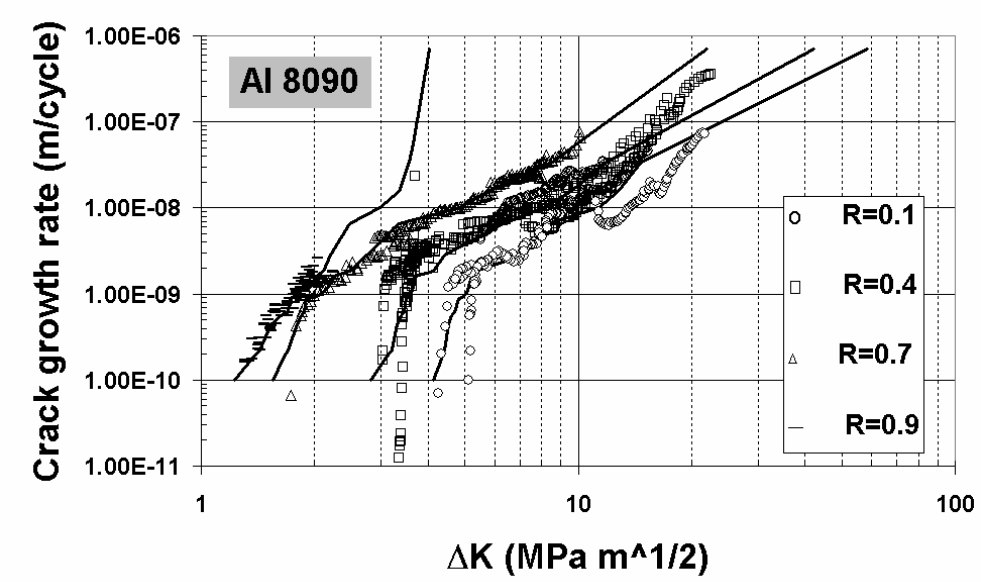

Figure 7.6_ The fitted curves that AFGROW created and used in the linear summation calculation and the CAL fatigue crack growth rates for Al8090 alloy.

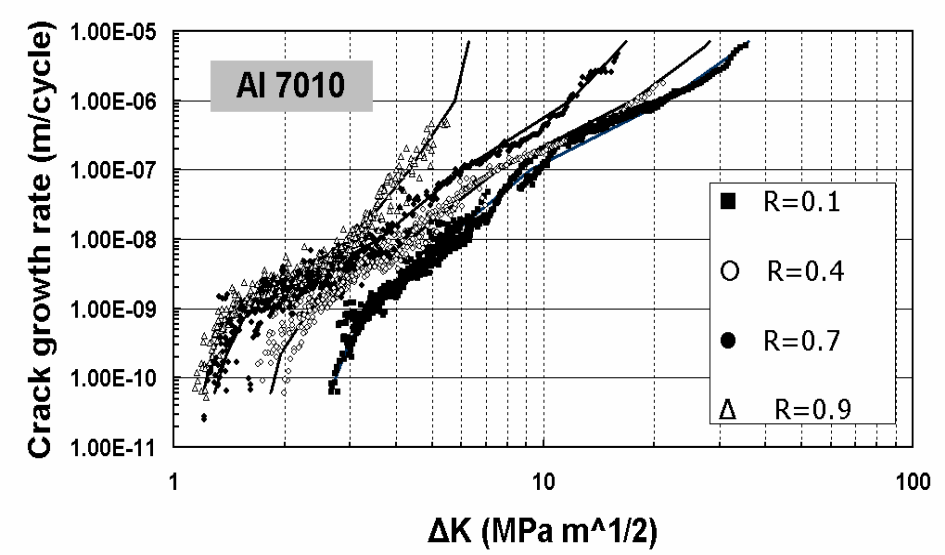

Figure 7.7_ The fitted curves that AFGROW created and used in the linear summation calculation and the CAL fatigue crack growth rates for Al7010 alloy.

7.4 FASTRAN Model and Software

The FASTRAN program is written and maintained by Newman at NASA/Langley Research Center, VA. FASTRAN is a life prediction code based on the crack closure concept. The program calculates crack length against cycles from a user specified initial crack size to failure for many common crack configurations found in structural components. Newman developed the closure model used in FASTRAN. This model is inextricably linked with FASTRAN and is the only crack growth model that can be used in the program.

The life prediction method used in FASTRAN is built around an analytical crack closure model. This model is based on plasticity-induced fatigue crack closure and is used to calculate the stress level at which the crack tip becomes fully open during cycling loading. The applied cycle loads may be constant amplitude, variable amplitude, or spectrum loading. Crack closure is caused by residual plastic deformation remaining in the wake of an advancing crack. The program uses the crack closure concept to account for load interaction effects (acceleration and retardation). The crack opening stresses, as a function of load history and crack length are calculated from the model.

A computer program DKEFF was also developed to analyze laboratory specimen data to obtain the effective stress intensity factor against crack growth rate relations used by FASTRAN.

This model assumes that crack growth rate data for all stress ratios may be reduced to a single curve using constraint parameters (alpha values). The single curve is based on the concept of an effective change in the stress intensity factor for a given load cycle (ΔK_{eff}). Newman uses a number of alpha values (for various crack growth rates and stress states) to collapse the crack growth data to a single curve. The effective stress intensity factor range is the difference between the maximum stress intensity for a given load cycle and the minimum stress intensity factor required to open the crack tip. This assumes that the crack tip is fully closed when unloaded and a certain amount of tensile load must be applied to open the crack and overcome the effect of a plastic wake behind the crack tip. Then, from the established unique relationship between ΔK_{eff} and crack growth rates and using the crack closure concept for taking into account the load interaction effects, crack growth increments can be calculated for every loading cycle. Figure 7.8 shows a diagram of the procedure that FASTRAN follow to carry out a fatigue life prediction.

At the maximum applied stress and when the crack is fully open, the effects of state of stress on plastic zone size and displacements are approximately accounted for by using a constraint factor, a. The constraint factor is used to elevate the tensile flow stress for the intact elements, which the code uses to model the plastic zone. The effective flow stress $\alpha\sigma_0$ under simulated plane stress conditions is σ_0 (usual Dugdale model) and under simulated plane strain conditions is $3\sigma_0$.

To make life predictions, the ΔK_{eff} as a function of the crack growth rate must be obtained for the material of interest. Fatigue crack growth rate data should be obtained over the widest range in rates possible (from threshold to fracture), especially if spectrum load prediction are required. The user determines the effective stress intensity factor range against crack growth rate relation using the computer program DKEFF.

In order to obtain accurate results using the FASTRAN model one must always attempt to find the most correct constraint factor for a given material and specimen

geometry. To do this, constant-amplitude crack growth data was provided to the computer code DKEFF and then used to calculate the effective stress-intensity factor versus rate for a given constraint value.

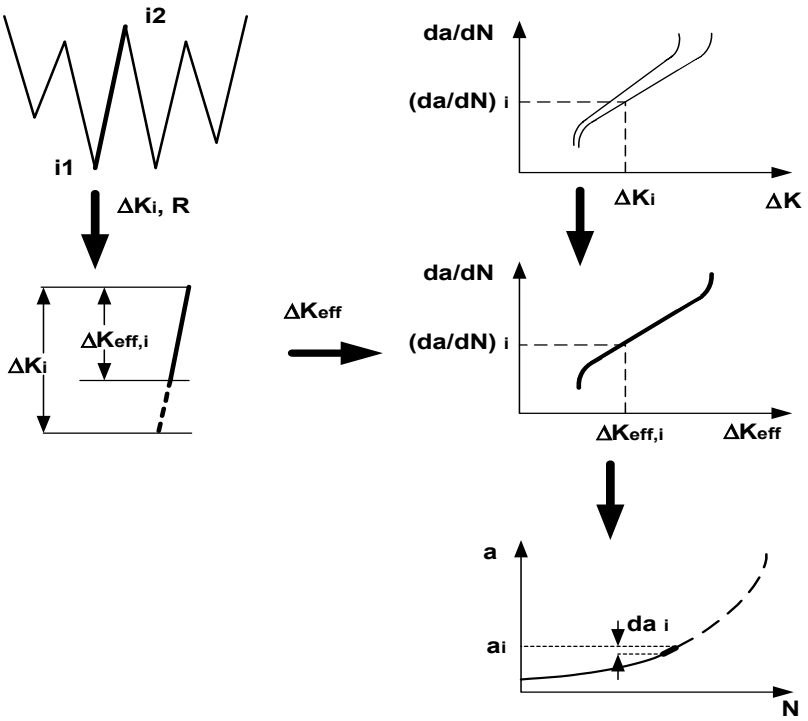

Figure 7.8_ Graphical representation of the procedure followed by the FASTRAN model to calculate the crack increments.

Under constant amplitude loading, the only unknown in the equations is the constraint factor α. The constraint factor is determined by finding a value of α that will correlate the constant amplitude fatigue crack growth rate data over a wide range in stress ratios. The correlation should produce a unique relation between ΔK_{eff} and crack growth rate. In the large crack threshold regime for some materials, the plasticity induced closure model may not be able to collapse the threshold data onto a unique ΔK_{eff} rate relation because of other forms of closure such as roughness and oxide induced closure. It is suggested that the high stress ratio (R>0.6) data be used to establish the ΔK_{eff} relationship because is closure free.

In order to find the most appropriate alpha value for the fatigue life prediction, different constraint factors (ranging from 1 to 3) have to be provided into the DKEFF program each time until a single value was found which compressed the data points into the tightest band on the ΔK_{eff}-rate curve. By comparing the various plots, one is able to select a value for the constraint factor. This value is

then entered into the FASTRAN model. Once the correct constraint is determined and the ΔK_{eff}-rate plot is compressed, one is able to select a more accurate threshold, fracture toughness, and stress-intensity factor versus rate (da/dN) values to be input into FASTRAN. These are usually selected on the high side of the plot, as it was suggested previously, acting as a built in safety factor, as predictions tend toward faster crack growth and shorter material life.

In addition to the requirements for constant amplitude crack growth data, the material properties, the specimen geometry and the loading characteristics must be provided to the model to carry out a fatigue life prediction. The initial crack length was different for each fatigue life prediction depending on the initial crack length of the respective test. Loading spectrum is provided in terms of a set of parameters such that maximum and minimum applied load and number of cycles.

The value of constraint factor, a, was determined for Ti1023, Al8090, and Al7010 following the procedure described previously. Different values of alpha were initially provided into the DKEFF program. These values were ranged from 1, to 3. Hence, different correlation of the constant amplitude loading data in terms of the effective stress intensity factor ranges were calculated for each alloy. Then, based on which alpha value compressed the data points into the tightest band on the ΔK_{eff}-rate curve, the selections of the constraint factor were made. The selected values of the constraint factor, a, for each material can be seen in table 7.1. Figures 7.9-11 show the ΔK_{eff} -curves for the alpha values that was considered, for Ti1023, Al8090, Al7010.

It has to be noted that the constraint factor α is 1 for plane stress and 3 for plane strain. The constraint factor for Ti1023, Al8090 and Al7010 was chosen as 1 since this value collapsed the crack growth data best. The specimen used was with 17.5mm thickness definitely a plaine strain case. A calculation with high constraint factor value (like 2.5) did not collapse the constant R ratio crack growth data da/dN to one tight curve. A FASTRAN crack growth calculation with the pertaining plane strain factor would thus lead to longer lives.

In this study, FASTRAN life predictions were conducted for selected single and complex amplitude loading spectra, using the corresponding constraint factor for each material. Considering measured crack closure levels and experimentally determine ΔK_{eff}-curves with FASTRAN life predictions, useful conclusion can be

drawn about the predominant mechanism governing the fatigue crack propagation under the tested sequences.

Table 7.1_ Constraint factor, alpha values for four metallic alloys

	Ti1023	Al8090	Al7010
Constraint Factor, alpha	1	1	1

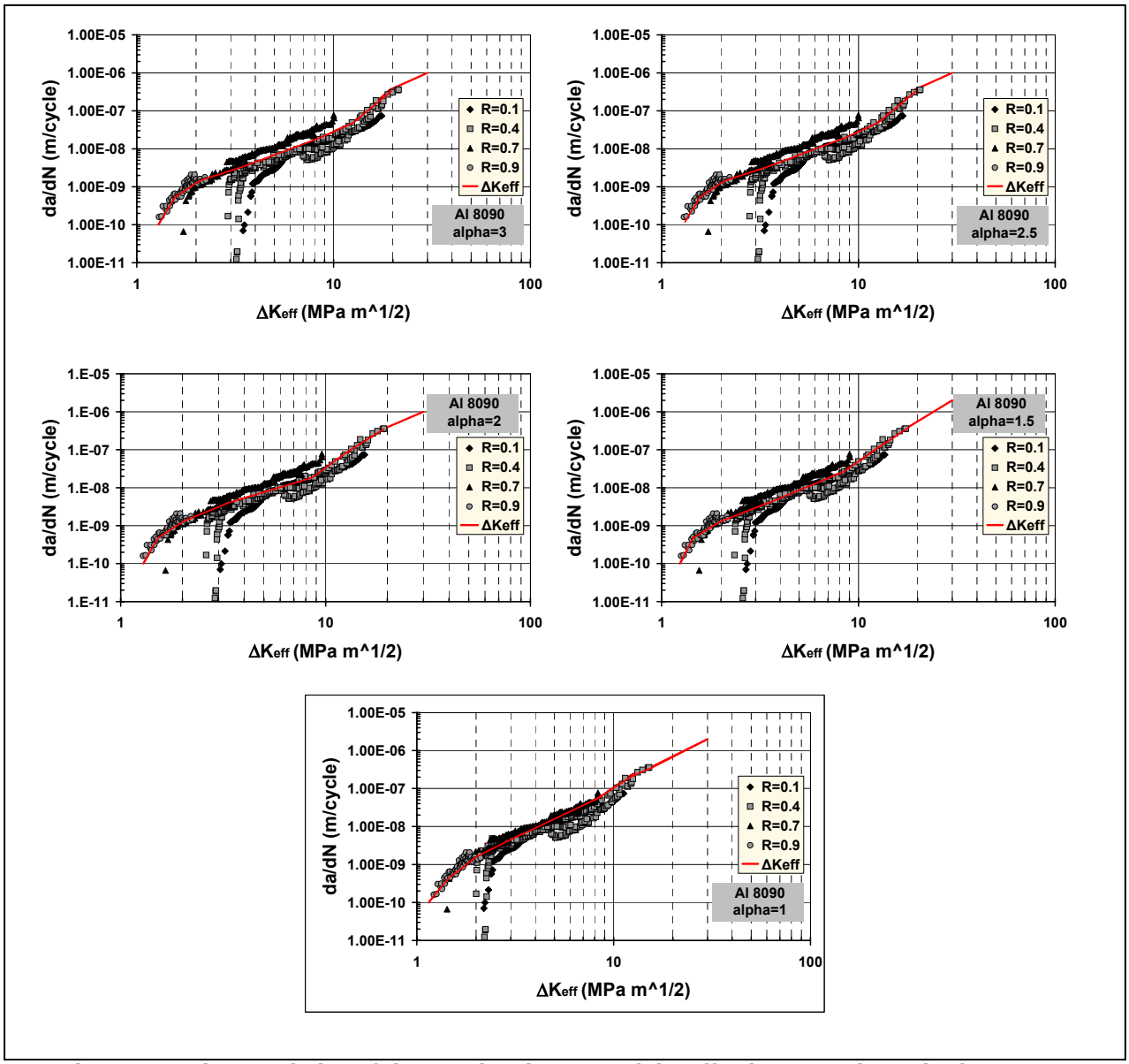

Figure 7.9_ The correlation of the CAL data in terms of the effective stress intensity factor ranges for Al8090. The selection is highlighted.

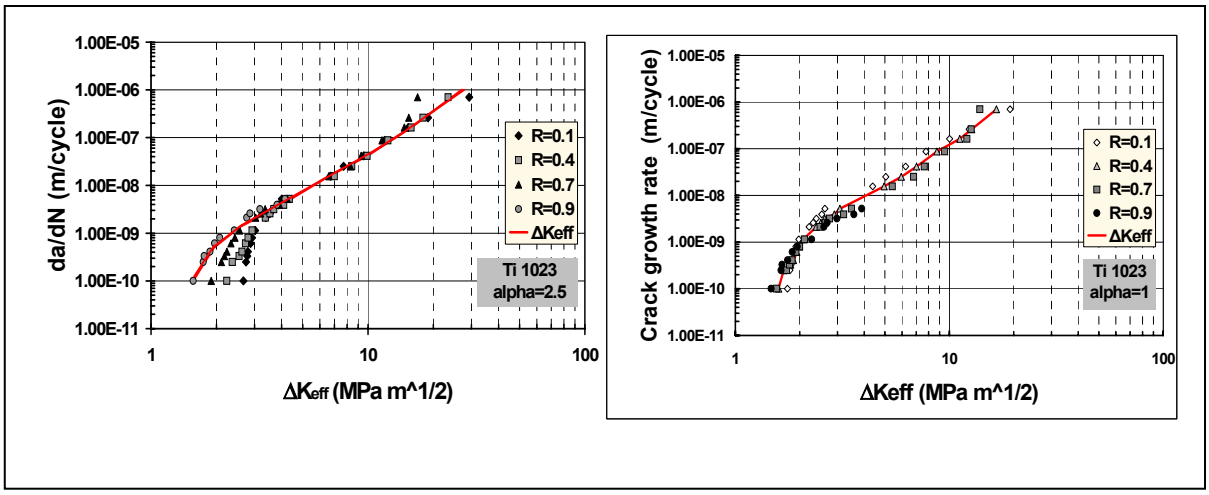

Figure 7.10_ The correlation of the CAL data in terms of the effective stress intensity factor ranges for Ti1023. The selection is highlighted.

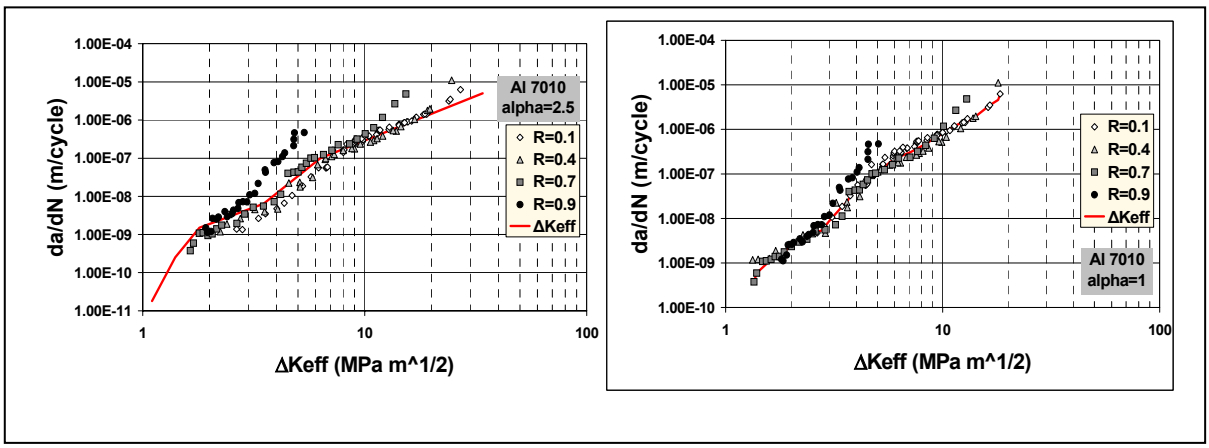

Figure 7.11_ The correlation of the CAL data in terms of the effective stress intensity factor ranges for Al7010. The selection is highlighted.

CHAPTER 8

EXPERIMENTAL RESULTS

8.1 Introduction

The results of the test program on the three different alloys are presented in this section. Initially, the chapter gives the experimental measurements and observation on tests carried out under Constant Amplitude Loading and near threshold fatigue crack growth behaviour. Simple Variable Loading tests with focus on the underload effects and the related load interaction effects follow. Information on crack growth under Complex spectra is given at the end of the chapter. The measurements of the crack growth rates, acceleration factors crack opening load and variations in the crack mouth maximum displacement are the quantities reported in this chapter.

8.2 CAL Tests

Crack growth rates and crack closure measurements of the CAL cycles and the precracking procedures were used in order to generate CAL crack closure data, which will allow the direct comparison of SVAL with CAL crack opening levels and to support the ΔK_{eff} curve with more points. The CAL and the precracking procedure were carried out at various loading conditions and crack lengths. The outline of the tests in terms of crack growth rates and crack closure levels is summarised in table A10, A11 and A12 for Ti 1023, Al8090 and Al7010, respectively.

Figures 8.1, 8.2, and 8.3 show the fatigue crack growth rates for Ti 1023, Al8090 and Al7010, respectively, measured in the tests. The constant R ratio crack growth rates for R = 0.1 are also plotted together with the test results.

The measured crack growth data for R = 0.1 do not fall into the CAL baseline curve very well. The observation applies for all three materials. The reason is that often cracks grow at different rates due to the load transient effects. The scatter is also affected by the nature of the material. Hence, Al8090 exhibits bigger scatter in the measured CAL crack growth rates compared with Al7010 and Ti 1023.

The measured crack closure loads during the each CAL and precracking test are given in table A10-A12. At R = 0, crack closure loads are 0.42 K_{max} for Ti1023, 0.6-0.7 K_{max} for Al8090 and around 0.55 K_{max} for Al7010 (table 8.1).

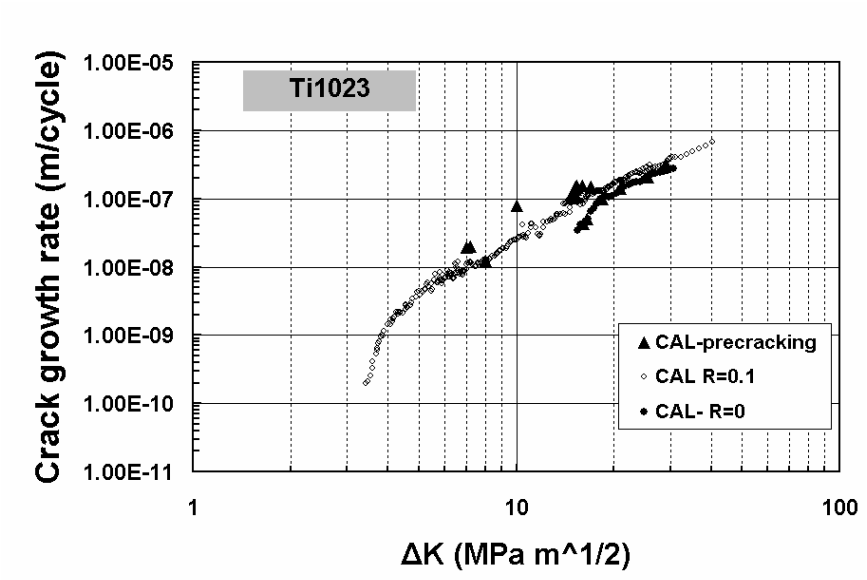

Figure 8.1_ CAL crack growth rates measurements and respective CAL baseline curve [86] for Ti1023.

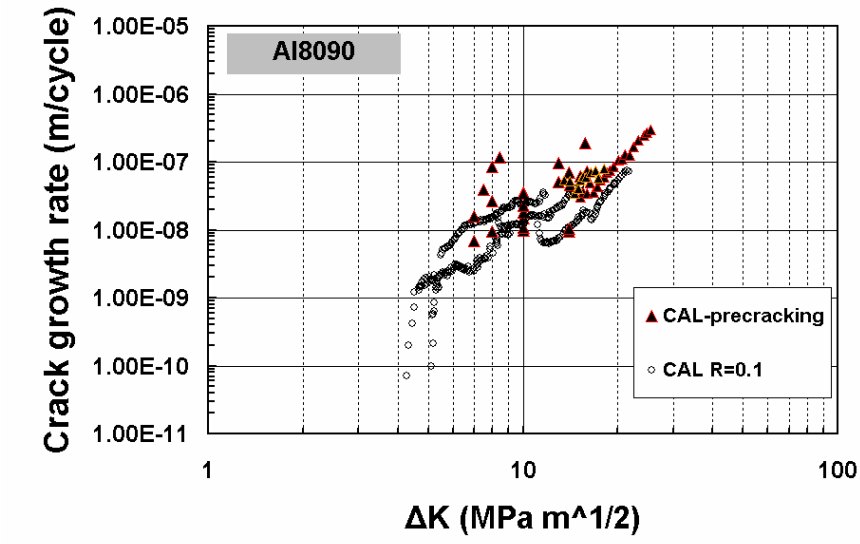

Figure 8.2_ CAL crack growth rates measurements and respective CAL baseline curve [146] for Al8090.

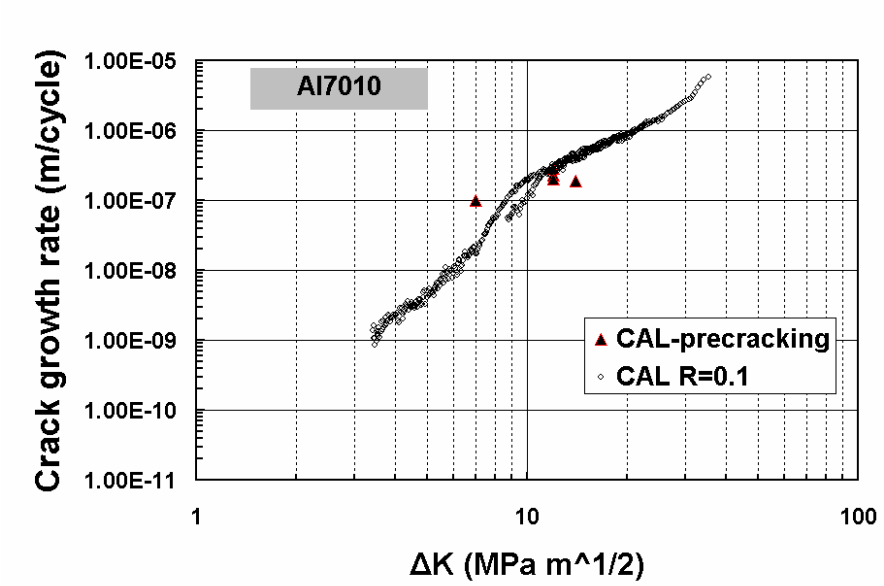

Figure 8.3_ CAL crack growth rates measurements and respective CAL baseline curve [147] for Al7010.

Table 8.1_ CAL crack closure measurements for the three materials.

	Ti1023	Al8090	Al7010
CAL Closure Load (K_0/K_{max})	0.40-0.44	0.6-0.8	0.54-0.56

8.3 Threshold Measurements

The results of threshold stress intensity factor range ΔK_{th} measurements for Ti1023, Al8090, and Al7010 are presented in the following paragraphs. The tables 8.2-4 summarise the results for each threshold test.

A typical crack length, a, versus the applied loading cycles, N, curves is shown in figure 8.4. The figure shows the crack propagation during an R ratio constant test at R = 0.9. Both techniques worked adequately resulting in a continuous and smooth decrease in the crack growth rates until practically the final stop of the crack propagation at a certain level of loading.

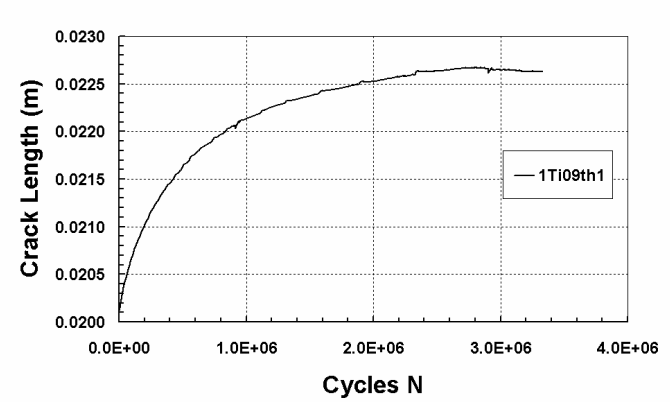

Figure 8.4_ Typical crack growth propagation during an R constant K-decrease test on Ti1023. (Tests 1Ti09th1)

8.3.1 Ti1023 Threshold Measurements

Table 8.2 shows the ΔK_{th} values determined during the threshold tests on Ti1023. The average value of ΔK_{th} is 1.9 and 1.57 MPa $m^{1/2}$ at R ratio of 0.7 and 0.9, respectively. Starting and finishing K_{max} values can also be found in this table. There is a noticeable effect of R ratio in these data.

The range of ΔK_{th} values is between 1.78 MPa $m^{1/2}$ at K_{max} = 8 MPa $m^{1/2}$ and 1.53 MPa $m^{1/2}$ at K_{max} = 25 MPa $m^{1/2}$. Starting R ratios were as low as 0, finishing R ratios at threshold were 0.8-0.95. The behaviour of the crack growth rates appears to change between the K_{max} values of 10, 15 and 25 MPa $m^{1/2}$. The intrinsic value, ΔK_T obtained in these tests, 1.57 MPa $m^{1/2}$, was identical to that found in the constant R testing for R ratio of 0.88 and above.

8.3.1.1 Fractogrphy

Figure 8.5 are low magnification photos of the crack fracture surface created by the precracking and the 1Ti15th K-decreasing tests. The beginning and the end of the precracking are designated on the pictures with the horizontal arrows. The near-threshold area is the upper part of the picture. The vertical arrow indicates the direction of the crack growth.

The test appears to form a very similar fracture surface. The main characteristic is that the surface deformation is high at the beginning of the test where R ratio is low and ΔK is high, and gradually transformed to a smooth surface at the near threshold area where R ratio is high and ΔK is low. Hence, slower crack growth rates, da/dN, seem to form smoother fracture surfaces.

Table 8.2_ Threshold test results for Ti1023 using the two techniques.

Material	**Test notation**	**Test Technique**	**Initial Crack length** (m)	**Final Conditions**			
				$K_{max,th}$ *(MPa $m^{1/2}$)*	ΔK_{th} *(MPa $m^{1/2}$)*	*R*	*Crack length (m)*
Ti1023	1Ti07th1	R Constant	0.0301	6.3	1.89	0.7	0.0352
	1Ti07th2		0.026	6.7	2.01	0.7	0.0297
	1Ti07th3		0.020	6.2	1.86	0.7	0.0243
	1Ti07th4		0.014	6.17	1.85	0.7	0.01885
	Average			6.33	**1.9**	**0.7**	
	1Ti09th1		0.0201	16.33	1.63	0.9	0.0227
	1Ti09th2		0.0200	15.8	1.58	0.9	0.02275
	1Ti09th3		0.0212	15.6	1.56	0.9	0.0231
	1Ti09th4		00204	15.2	1.52	0.9	0.0231
	Average			15.7	**1.57**	**0.9**	
	1Ti10th	K_{max} Constant	0.0142	10	1.74	0.83	0.0197
	1Ti15th		0.0207	15	1.54	0.9	0.027
	1Ti20th		0.028	20	1.46	0.93	0.0348
	1Ti25th		0.0145	25	1.53	0.94	0.0214
	1Ti9th		0.0327	9	1.64	0.82	0.03835
	1Ti8th		0.0215	8	1.78	0.78	0.0264

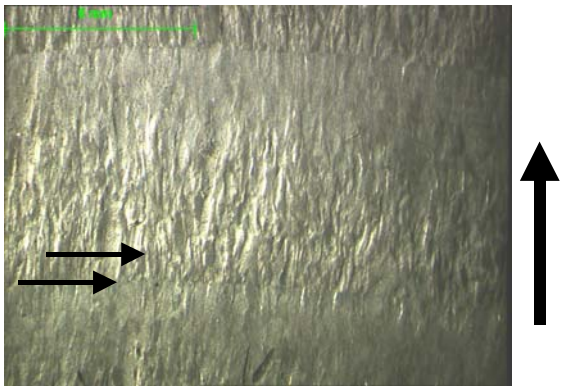

Figure 8.5_ Ti1023 fracture surface produced from a precracking procedure ΔK=10 MPa $m^{1/2}$ R=0.1 (between the horizontal arrows) and from Test 1Ti15th (threshold test at K_{max}=15 MPa $m^{1/2}$). Growth direction is indicated by the vertical arrow.

8.3.2 Al8090 Threshold Measurements

Table 8.3 shows the ΔK_{th} values determined during for constant R ratio tests for R values of 0.1 to 0.9. The average value of ΔK_{th} is 4.11, 3.25, 1.65 and 1.41 MPa $m^{1/2}$ at R ratio of 0.1, 0.3, 0.7 and 0.9, respectively. Starting and finishing K_{max} values can also be found in this table. There is a noticeable effect of R ratio in these data.

Table 8.3 also gives the ΔK_{th} values determined during for K_{max} constant tests. The range of ΔK_{th} values is between 1.68 MPa $m^{1/2}$ at K_{max} = 7 MPa $m^{1/2}$ and 1.44 MPa $m^{1/2}$ at K_{max} = 20 MPa $m^{1/2}$. Starting R ratios were as low as 0, finishing R ratios at threshold were 0.75-0.95. There is a noticeable absence of any effect of R ratio in the data at K_{max} > 10 MPa $m^{1/2}$. The intrinsic value, ΔK_T obtained in these tests, 1.41 MPa $m^{1/2}$, was identical to that found in the constant R testing for R ratio of 0.83 and above.

Table 8.3_ Threshold test results for Al8090 using the two techniques.

Material	Test notation	Test Technique	Initial Crack Length (m)	Final Conditions			
				$K_{max,th}$ (MPa $m^{1/2}$)	ΔK_{th} (MPa $m^{1/2}$)	R	Crack length (m)
Al8090	1A807th1	R Constant	0.0147	5.41	1.62	0.7	0.0186
	1A807th2		0.0197	5.58	1.68	0.7	0.0236
	Average			5.58	**1.65**	**0.7**	
	1A809th1		0.020	13.63	1.36	0.9	0.0224
	1A809th2		0.0275	14.6	1.46	0.9	0.0305
	Average			14.13	**1.413**	**0.9**	
	1A801th1		0.0156	4.4	4.0	0.1	0.0216
	1A801th2		0.0235	4.7	4.22	0.1	0.029
	Average			4.55	**4.11**	**0.1**	
	1A803th1		0.015	4.6	3.25	0.3	0.0213
	1A803th2		0.0226	4.6	3.24	0.3	0.0287
	Average			4.6	**3.25**	**0.3**	
	1A87th	K_{max} Constant	0.027	7	1.68	0.76	0.0316
	1A810th		0.031	10	1.28	0.87	0.0368
	1A820th		0.0145	15	1.44	0.9	0.0208
	1A825th		0.023	20	1.15	0.94	0.0298

8.3.2.1 Fractogrphy

Figure 8.6 is low magnification photo of the crack fracture surface created 1A801th1 K-decreasing tests and a precracking procedure. The end of the test is the white line on the right hand site of the pictures. The near-threshold area is also indicated between the lines.

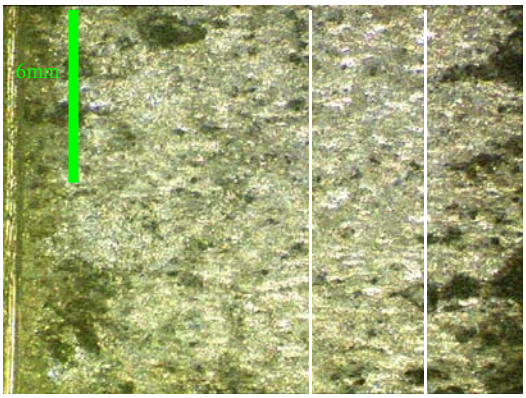

Figure 8.6_ Al8090 fracture surface produced from a precracking procedure ΔK=8 MPa $m^{1/2}$ R=0.1 (on right part of the picture) and from Test 1A801th1 (threshold test at R=0.1, $\Delta K_{initial}$=10 MPa $m^{1/2}$). The middle part shows the near threshold region. Growth direction is from the left to the right. Specimen CCT10

The test 1A807th1 appears to form a similar fracture surface, where the main characteristic is that the surface deformation is high at the beginning of the test where R ratio is low and ΔK is high, and gradually transformed to a smoother surface at the near threshold area where R ratio is high and ΔK is low. The reduction of the number of the black marks on figure 8.6 indicates that the surface becomes smoother comparing with the starting period of the test. Hence, on Al8090, slower crack growth rates, da/dN, seem to form smoother fracture surfaces. Although the near-threshold area is significantly rougher than those in the Ti1023 test.

8.3.3 Al7010 Threshold Measurements

ΔK_{th} values of Al7010 determined using K_{max} constant techniques are shown in table 8.4. The range of ΔK_{th} values is between 1.25 MPa $m^{1/2}$ at K_{max} = 12 MPa $m^{1/2}$ and 1.37 MPa $m^{1/2}$ at K_{max} = 30 MPa $m^{1/2}$. Starting R ratios were as low as 0.17,

finishing R ratios at threshold were 0.9-0.95. There is a notable absence of any effect of R ratio in these data. Practically, all four test have resulted similar crack growth rates, especially in the near threshold area. The tests end up at around the same value of ΔK. Hence, the intrinsic value of 1.32 MPa $m^{1/2}$, ΔK_T obtained in these tests, was similar to that found in the constant R testing for R ratio of 0.9 and above.

Table 8.4_ Threshold test results for Al7010 using the K_{max} techniques.

Material	Test notation	Test Technique	Initial Crack Length (m)	Final Conditions			
				$K_{max,th}$ (MPa $m^{1/2}$)	ΔK_{th} (MPa $m^{1/2}$)	R	Crack length (m)
Al 7010	1A712th	K_{max} Constant	0.145	12	1.25	0.9	0.0202
	1A718th		0.0155	18	1.35	0.93	0.0209
	1A724th		0.022	24	1.33	0.95	0.0278
	1A730th		0.0225	30	1.37	0.95	0.0281

8.4 SVAL Testing

8.4.1 Effects of Underloads on the Threshold Stress Intensity Factor

In order to investigate the effects of the underload cycles on the ΔK_{th} values, a certain number of underloads at R = 0 were applied after the establishment of the threshold. After the underload cycles, fatigue cycling was applied for 10^6 cycles at the previously established ΔK_{th} level and the crack growth rates were measured. Table 8.5 contains the crack growth rates measured after the application of the underload cycles and the related test details.

Increasing the number of underload cycles appears to have a insignificant effect on the threshold value of ΔK when this was established at a high R ratio, in the present case 0.7 and 0.9. The effects of up to 50 underload cycles are not significant, considering the range of the recorded threshold values of ΔK and the crack growth rates at the establishment of threshold.

Table 5. Crack growth rates of the R=0.9 cycles after the application of a number of underloads on Ti1023.

Ti1023								
Test	*1Ti07th1*	*1Ti07th2*	*1Ti07th3*	*1Ti07th4*	*1Ti09th1*	*1Ti09th2*	*1Ti09th3*	*1Ti09th4*
R_{th}	0.7				0.9			
Number of underloads	50	20	5	1	50	20	5	1
Crack growth rate after the underloads (m/cycle)	$2\ 10^{-10}$	$1.9\ 10^{-10}$	$< 10^{-10}$	$< 10^{-10}$	$< 10^{-10}$	$< 10^{-10}$	$< 10^{-10}$	$< 10^{-10}$

8.4.2 Underload Testing

8.4.2.1 Ti1023 – Sequences containing an underload

8.4.2.1.1 Small Cycles at R_n=0.7

The effects of the sequences containing small cycles at the 1.9 MPa $m^{1/2}$ ($\Delta K_{th}^{0.7}$) and ratio R_n=0.7 and underloads at R_u=0, on the fatigue crack growth rates of Ti 1023 were studied. The number of small and underload cycles was varied from 1 to 1000 and 1 to 50, respectively and the K_{max} was 6.86 MPa $m^{1/2}$.

The test results can be found in table A7. The majority of the crack growth rates are below the 10^{-10} m/cycle, which is considered as the limit growth rate for the threshold. Hence, the underload cycles in the spectrum have no detectable effect on the crack growth rates. Test 71 showed crack growth rates higher than 10^{-10} m/cycle. In relation to the CAL linear summation, no significant load interaction effects were observed in the tests.

8.4.2.1.2 Effect of the number of small cycles (R_n = 0.9)

In this set of tests, the maximum applied load P_{max} remains the same for the entire loading spectrum. Hence, the maximum stress intensity factor K_{max} of the small and underload cycles was the same. The starting value of K_{max} was 15.7 MPa $m^{1/2}$. The R_u ratio of the underloads is zero, which makes ΔK_u = 15.7 MPa $m^{1/2}$.

Starting ΔK_n was 1.57 MPa $m^{1/2}$ and R_n ratio was 0.9. The number of n small cycles was varied from 1 to 1000.

A loading sequence is defined as a specific number of cycles, which are repeatedly applied until the end of the test. Figure 8.7 gives an example of the crack growth increment response versus the number of applied cycles for few fatigue tests. Also, the fatigue damages based on the linear summation calculation of the CAL data of the material for each case were plotted. For the exhibited cases, the linear summation calculation is under-predicting the fatigue damage. Load interaction effects exist between the small and the underload cycles, which lead to accelerate behaviour of the crack propagation. The degree of the acceleration effects varies depending on the type of the sequence, in the present case on the number of the small cycles.

The fatigue crack growth rates $(da/dN)_{sequ}$ measured during each test performed in this series can be seen in figure 8.8. These crack growth rates are referred to the overall crack propagation under the applied spectrum and do not correspond to the damage caused by individual loading cycles. The crack propagates at a rate of 7 10^{-8} m/cycle for sequences of 1underload/1small cycles to the near threshold crack growth rate of 2 10^{-10} m/cycle for sequences of 1u/1000s. Similar sequences cause similar crack growth rates, as it was expected.

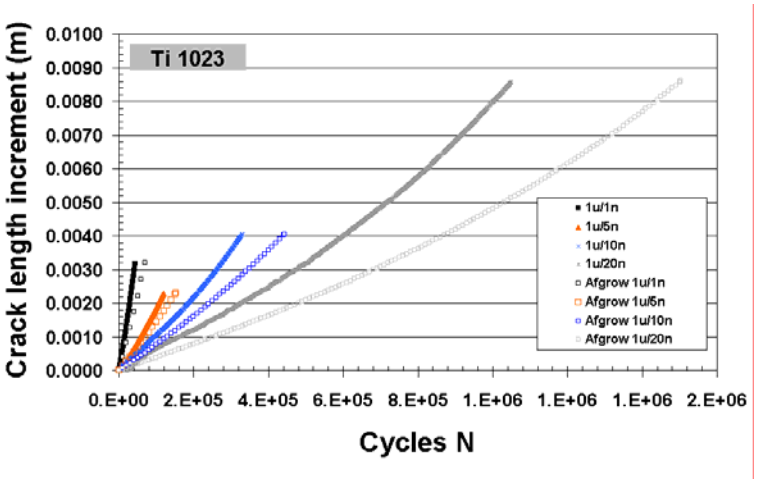

Figures 8.7_ Typical crack growth curves and the corresponding AFGROW linear sum for underloading sequences

The characteristic values of $(da/dN)_{sequ}$ were selected from each test to be used in the further analysis. These $(da/dN)_s$ values correspond to the crack growth

increment of around 1.5 mm. The values are presented in the table A7 and they are plotted together with linear summation prediction in terms of the number of the small cycles n in the figure 8.11. The $(da/dN)_s$ reduces as the number of the small cycles increases and the underloads become more rare.

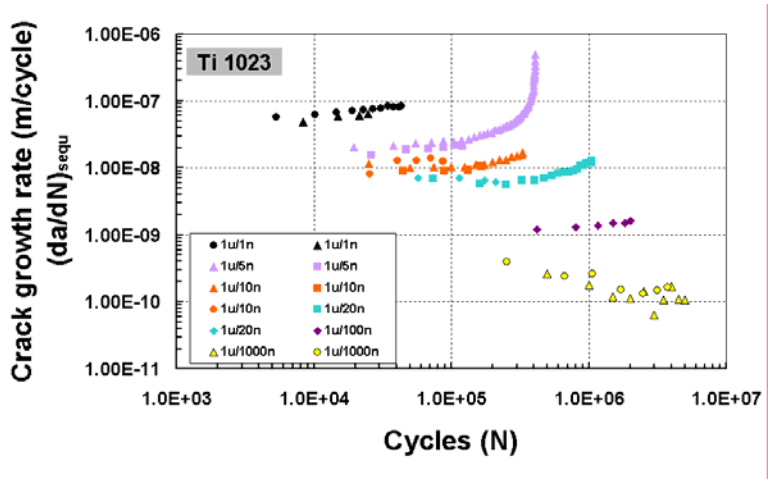

Figures 8.8_ The crack growth rates of the underload SVAL sequences on Ti1023.

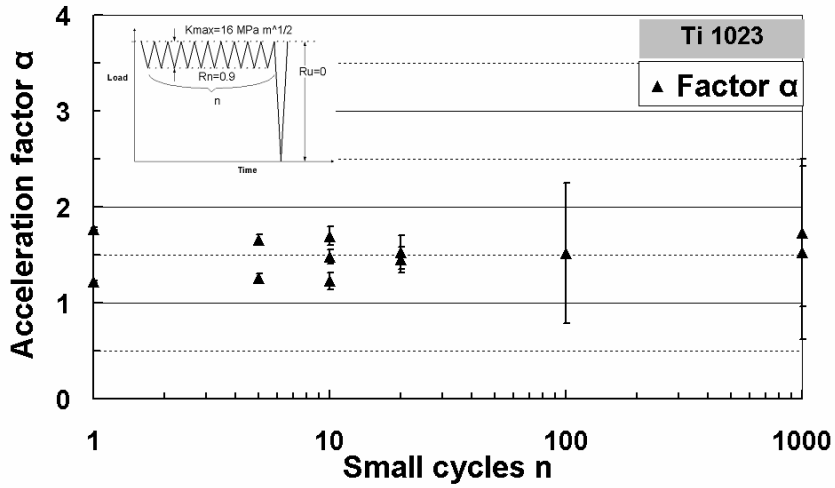

Figures 8.9_ The variation of the acceleration factor α in terms of the n small cycles in the sequence on Ti1023. Error bands are indicated.

Figure 8.9 gives the variation of the acceleration factors α as the number of the small cycles in a sequence changes from 1 to 1000. The values are listed in table A7. The factor α has a constant value between 1 and 2 throughout the range 1 to 1000. The degree of scatter varies between ±0.1 and ±0.9. Figure 8.10 gives the variation of the acceleration factors β and γ as the number of the small cycles

in a sequence changes from 1 to 1000. Factors β and γ and their trends are very similar to factor α. Scatter bands can be observed on the plots 8.9.

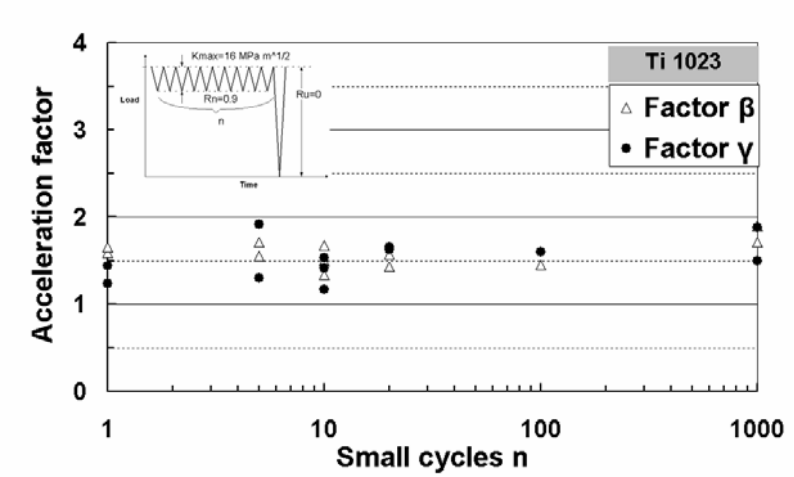

Figures 8.10_ The variation of the acceleration factor β and γ in terms of the n small cycles in the sequence on Ti1023.

Figure 8.12 gives the measured crack opening level as the crack grows under 1u/10s sequence. The mean value of the crack opening load was derived. The mean values of the crack opening point in the loading cycle can be found in table A7 in MPa $m^{1/2}$ and in fractions of the maximum load. The crack opening loads remain at the same level throughout the crack growth of 1mm. The mean value of opening stress intensity factor K_o is $0.29K_{max}$. The scatter in the closure measurements is determined at $0.05\ K_o/K_{max}$.

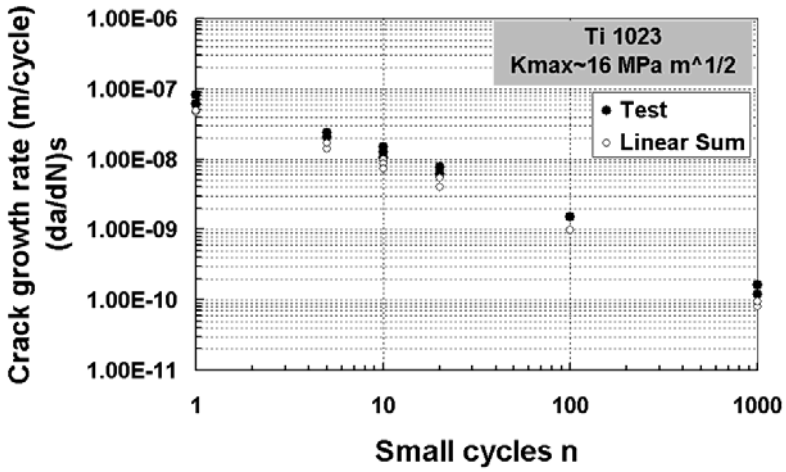

Figure 8.11_ The $(da/dN)_s$ values and the linear summation prediction in terms of the number of the small cycles n on Ti1023.

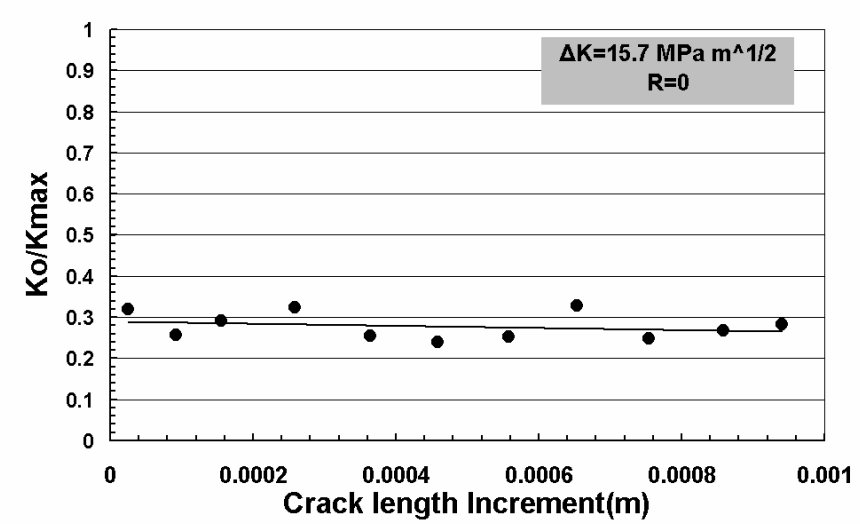

Figure 8.12_ The measured crack opening level as the crack grows in test 2Ti1u10s3 (1u/10n).

In addition, the values of the maximum displacement occurring at each cycle d^{i}_{max} of the recorded loading sequence were obtained from the input displacement signal. The values of the normalized d_m increment, Δd_{mn}, during the test were calculated and are plotted for each small cycle in the figure 8.13. The Δd_{mn} increases as the small cycles are applied. The normalized d_m at the 10^{th} cycle is 1.5 10^{-7} m/N larger than at the first cycle.

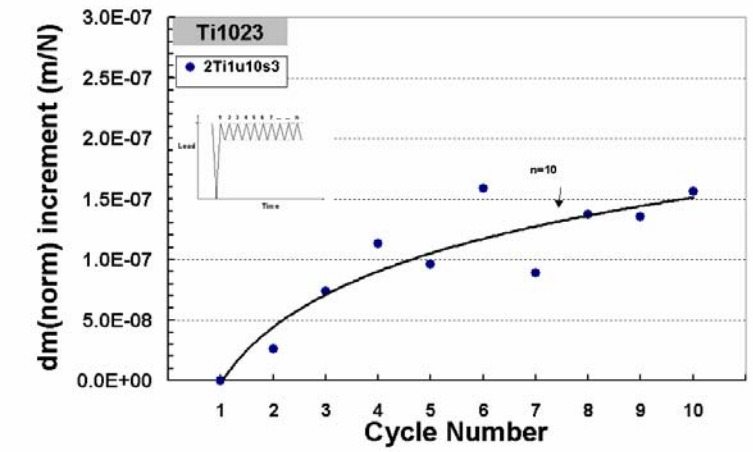

Figure 8.13_ The variation of the normalized dm as the small cycles at R_n=0.9 are applied.

8.4.2.1.3 Effect of the K_{max}

Three additional SVAL tests were conducted in order to investigate the effect of K_{max} on the acceleration factor α. 10 small cycles following by 1 underload was the selected cycle sequence. K_{max} was 7.85, 19.63, and 26.17 MPa $m^{1/2}$ for these three tests. Stress intensity range of small cycles was kept at the threshold of 1.57 MPa $m^{1/2}$. The loading conditions and the crack length can be found in table A7.

The characteristic values of $(da/dN)_{sequ}$ were selected from each test to be used in the further analysis. The values are presented in the table A7 and they are plotted in terms of K_{max} in the figure 8.14. The $(da/dN)_s$ reduces as the level of K_{max} becomes lower. The fatigue crack growth rate $(da/dN)_s$ values, which correspond to the same crack growth increment were also calculated for the CAL linear sum fatigue damage. The values based on the CAL data are lower than the experimental measurements.

The values of the factors α were calculated and presented in table A7. Figure 8.15 gives the variation of the acceleration factors α as a function of K_{max}. The acceleration factors α, which represent the effects in terms of the crack growth rates, are between 1 and 2 with a trend to increase as the K_{max} increases. At low values of K_{max}, acceleration is very close to 1, which means that prediction based on CAL crack growth rates are close to the measured SVAL crack growth rates.

The acceleration factors β and γ were also calculated and presented in table A7. Figure 8.16 gives the variation of the acceleration factors β and γ as a function of the K_{max}. The β values are around 1.5 for K_{max} larger than 15 MPa $m^{1/2}$. The factor γ values are almost identical.

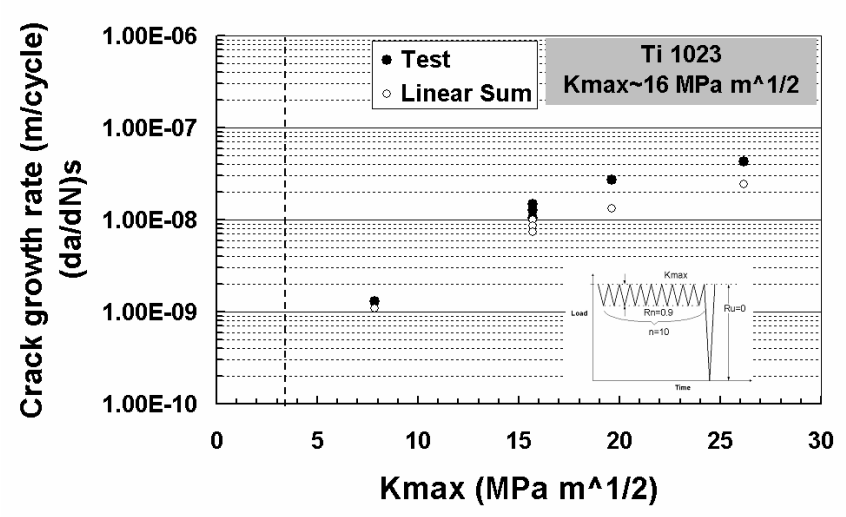

Figure 8.14_ The $(da/dN)_s$ values and the linear summation prediction in terms of the number of the K_{max} on Ti1023 for sequence 1u/10n.

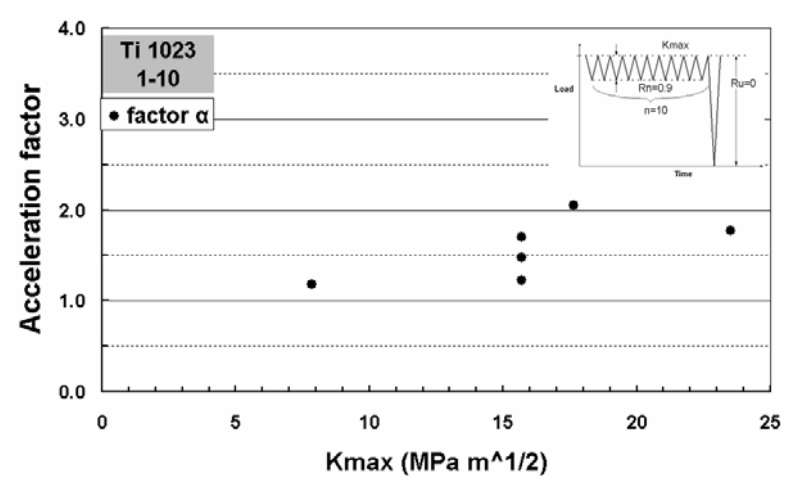

Figure 8.15_ The variation of the acceleration factor α in terms of the K_{max} on Ti1023.

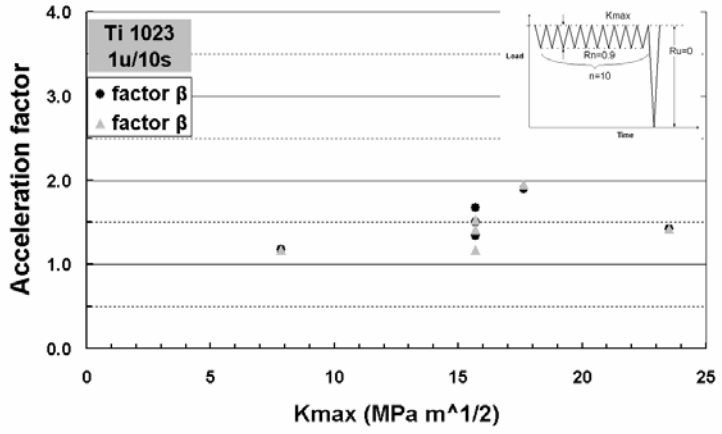

Figure 8.16_ The variation of the acceleration factor β and γ in terms of the K_{max} on Ti1023.

The mean values of the crack opening load of the underload cycles for each test in MPa $m^{1/2}$ and in fraction of the maximum load in the loading cycle can be found in table A7. Figure 8.17 gives the measured crack opening level in terms of K_{max}. The crack opening levels of the underload cycles in the SVAL sequence is between 0.2 and 0.3 K_{max}. A small trend is observed on the opening loads to decrease as K_{max} increases.

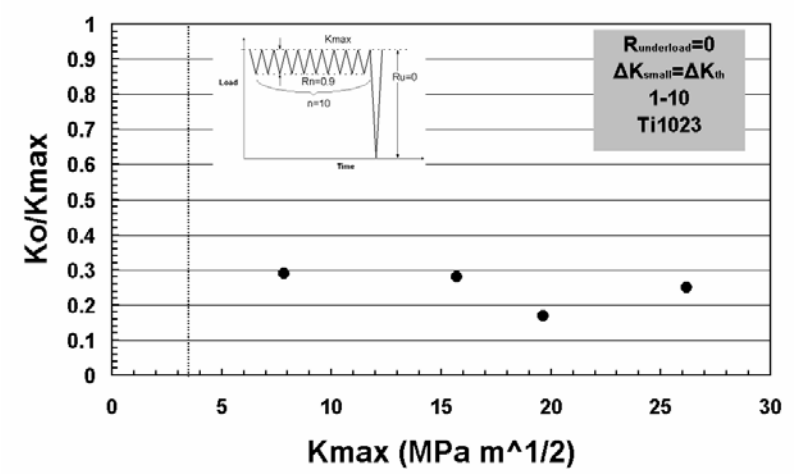

Figure 8.17_ The variation of the crack opening level in terms of K_{max} on Ti1023.

The values of Δd_{mn}, during the tests are plotted for each small cycle in the figure 8.18. The fitted curves on the experimental data reveal that when the applied K_{max} is high enough, in the present case larger than 15 MPa $m^{1/2}$, the Δd_{mn} increases for a given cycle number. The same does not apply when the K_{max} is low. The same K_{max} limit seems to distinguish accelerated and non-accelerated crack growth behaviour.

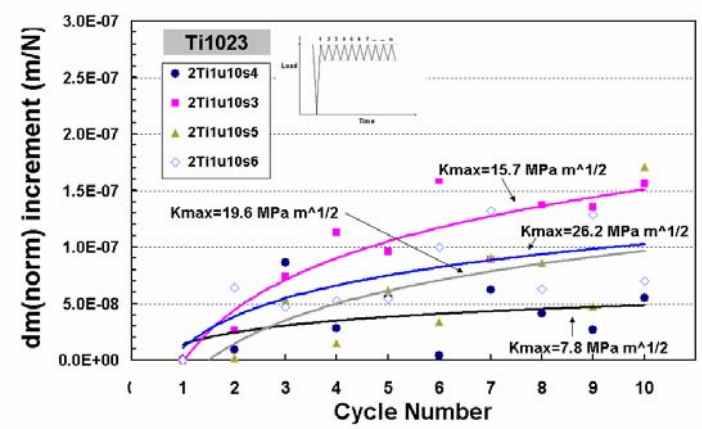

Figure 8.18_ The variation of the normalized dm with the small cycles (R_n=0.9) and the K_{max} level.

8.4.2.1.4 Effect of the R_u ratio of the Underload Cycles

Two additional SVAL tests were conducted to investigate the effect of the R ratio of the underload cycles on the crack growth rates. The underload ratios R_u were 0.3 and 0.5. Tests sequence was 10 small cycles followed by 1 underload. K_{max} was at the value of 15.7 MPa $m^{1/2}$. Loading test conditions and crack lengths can be seen in table A7.

The fatigue crack growth rates were measured during each test and the $(da/dN)_s$ were determined (figure 8.19). Sequences containing cycles at R_u = 0.3 have similar crack growth rates with sequences with underload at R_u = 0, despite the difference in R ratio of the underloads. The fatigue crack growth rate $(da/dN)_s$ values for the CAL linear sum fatigue damage were also calculated at the same crack length. Again, the linear predicted values are lower than the measurements.

The values of the factors α was calculated and presented in table A7. Figure 8.20 gives the variation of the acceleration factors α as a function of R_u. Acceleration factor α trends are the same as factors β and γ. Factor α is around 1.5 for the sequences containing underload cycles at the R_u ratio of 0 and close to 1 when underloads have R_u ratio of 0.5. Sequences containing underload cycles at R_u ratio of 0.3 exhibit a factor α of 2.5.

The acceleration factors β and γ were also calculated and presented in table A7. Figure 8.21 gives the variation of the acceleration factors β and γ as a function of the R_u. The factors α, β and γ values exhibit similar behaviour in terms of R_u.

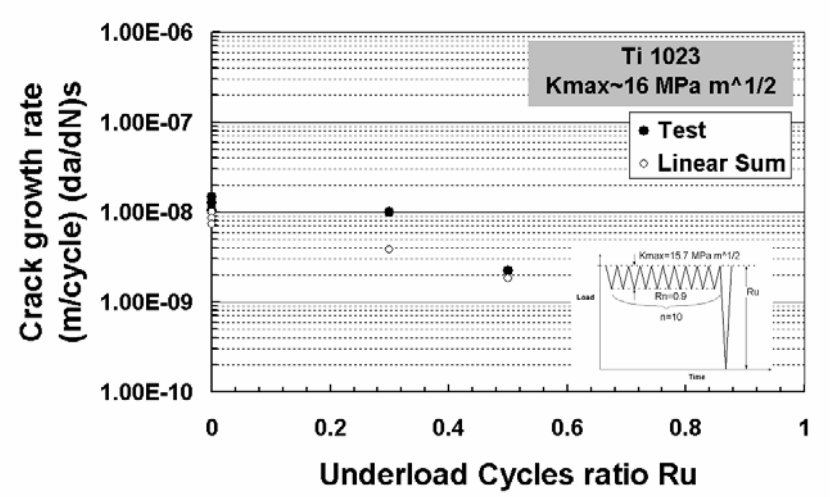

Fatigue 8.19_ The $(da/dN)_s$ values and the linear summation prediction in terms of the number of the R_u on Ti1023.

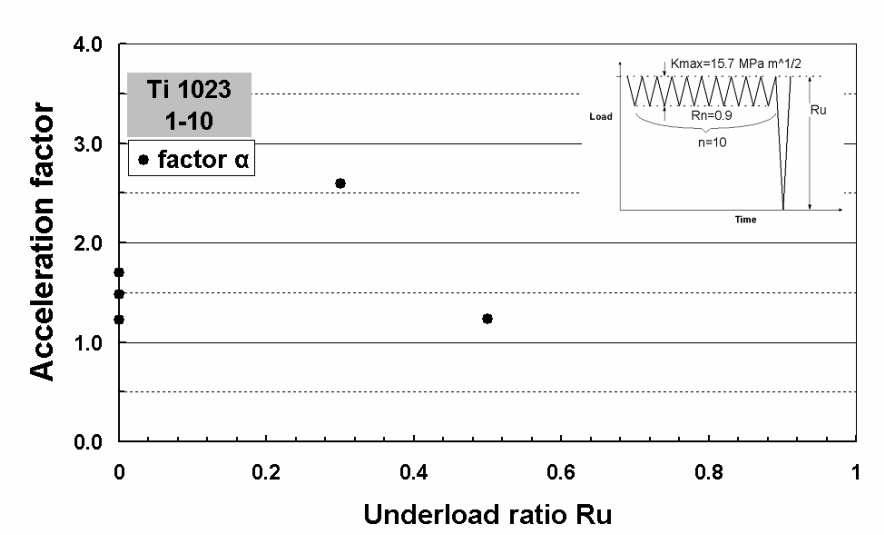

Figure 8.20_ The variation of the acceleration factor α in terms of the R_u on Ti1023.

The mean values of the crack opening level of the underload cycles for each test can be found in table A7 in MPa $m^{1/2}$ and in fraction of the maximum load in the loading cycle. Figure 8.22 gives the measured crack opening level in terms of R_u. Underload cycles at Ru = 0.3 exhibit closure levels of $0.35K_{max}$. Underloads at R_u = 0 have closure levels of $0.29K_{max}$. This shows that the effective part of the underload cycles is similar between cycles at R_u = 0 and 0.3. Underloads at R_u = 0.5 have closure levels at 0.59 K_{max}. Both underloads cycles at R_u = 0.3 and 0.5 have closure levels close to the minimum load of the cycle. It appears that

underload cycles approach the fully effective cycle from low R_u ratio (close to diagonal dotted line).

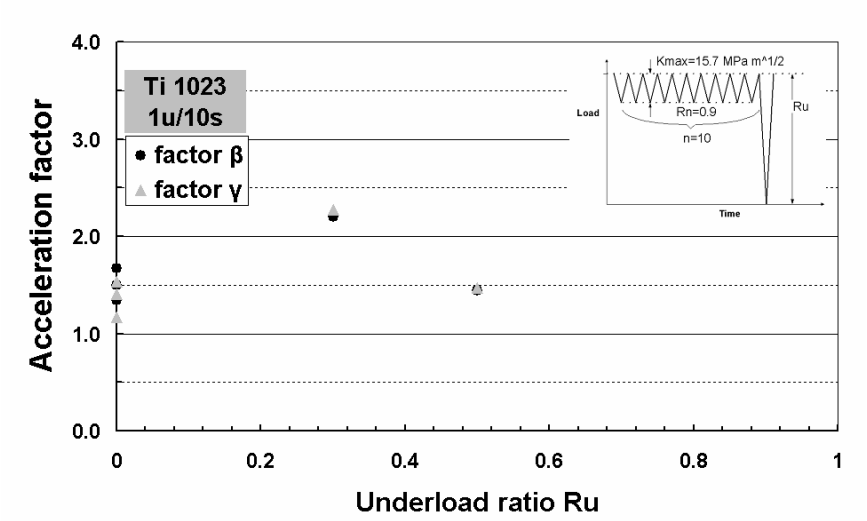

Figure 8.21_ The variation of the acceleration factor β and γ in terms of the R_u on Ti1023.

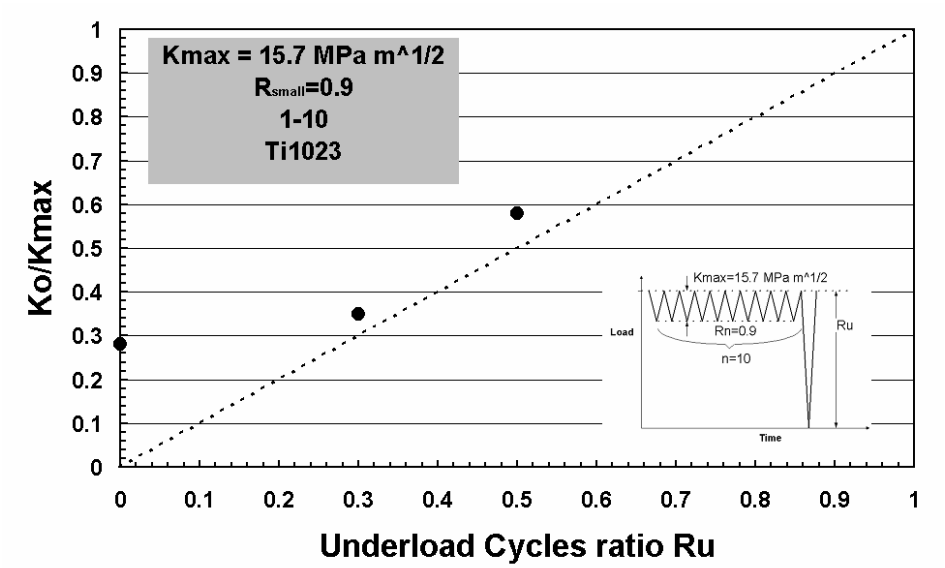

Figure 8.22_ The variation of the crack opening level in terms of R_u on Ti1023.

The values of Δd_{mn} and the fitted curves on the experimental data, during the tests are plotted for each small cycle in the figure 8.23. The tests containing underloads at R_u = 0 and 0.3 exhibits the same trend in the Δd_{mn}, which shows that small cycles have very similar effects on the crack tip deformation. On the other hand, when R_u of the underloads is 0.5, small cycles do not have great influence on

the crack tip deformation although the loading conditions are exactly the same as in the other cases.

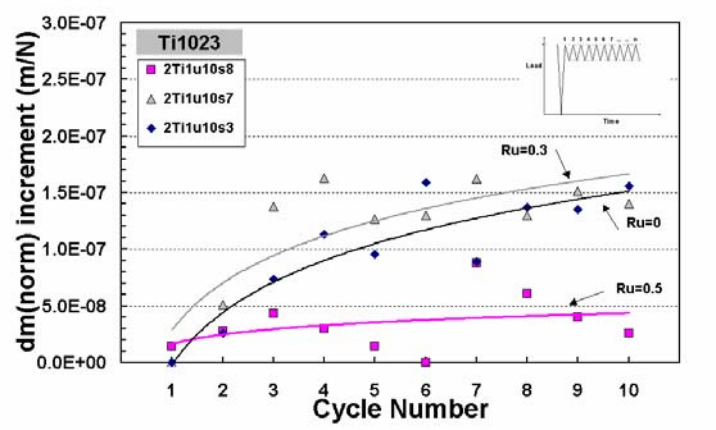

Figure 8.23_ The variation of the normalized dm with the small cycles (R_n=0.9) and the R_U value.

8.4.2.1.5 Effect of the R_n ratio of the small cycles

Two SVAL tests were conducted to investigate the effect of the R ratio of the small cycles. The small ratios R_n were 0.7 and 0.4. Test sequence was 10 small cycles followed by 1 underload. K_{max} was kept at the value of 15.7 MPa $m^{1/2}$. Loading test conditions and crack lengths can be seen in table 18.

The fatigue crack growth rates $(da/dN)_{sequ}$ were measured during each test and the $(da/dN)_s$ were determined and plotted in terms of R_n in figure 8.24. The fatigue crack growth rates $(da/dN)_s$ become faster as the amplitude of the small cycles increases and its R_n ratio becomes lower. The fatigue crack growth rates $(da/dN)_s$ calculated for the CAL linear sum fatigue damage are slower than the experimental measurements. The difference in the values depends on the R_n.

The values of the factors α were calculated and presented in table A7. Figure 8.25 gives the variation of the acceleration factors α as a function of R_n. Acceleration of crack growth rates of the SVAL sequences are between 1 and 2 and exhibit very small trend to increase as the R_n of the small cycles decreases.

The acceleration factors β and γ were also calculated and presented in table A7. Figure 8.26 gives the variation of the acceleration factors β and γ as a function of the R_n. The factors α, β and γ exhibit similar values.

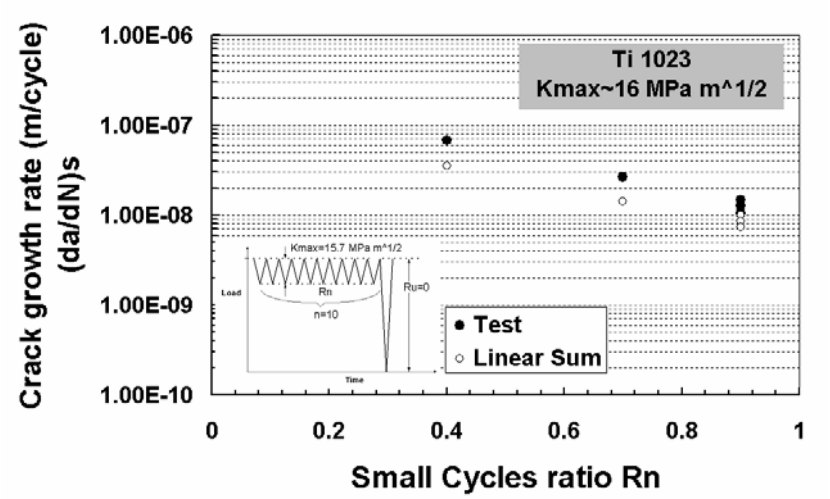

Figure 8.24_ The $(da/dN)_s$ values and the linear summation prediction in terms of the number of the R_n on Ti1023.

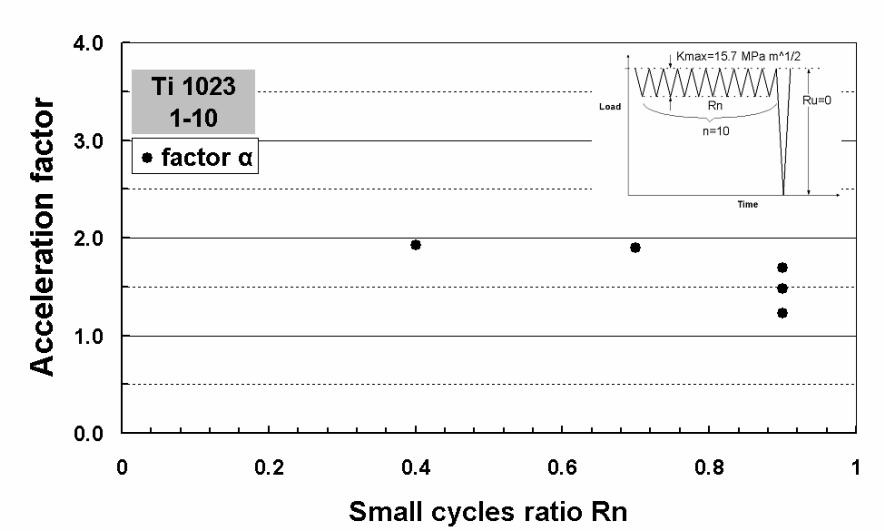

Figure 8.25_ The variation of the acceleration factor α in terms of the R_n on Ti1023.

The mean values of the crack opening level of the underload cycles for each test can be found in table A7 in MPa $m^{1/2}$ and in fraction of the maximum load in the loading cycle. Figure 8.27 gives the measured crack opening level in terms of R_n. Underload cycles at Ru = 0 exhibit very similar crack opening levels. The value is at 0.28-0.29 of K_{max}. This shows that the effective parts of the underload cycles

are very similar. Their crack opening values are lower than the CAL values and therefore contribute to the accelerated crack growth rates.

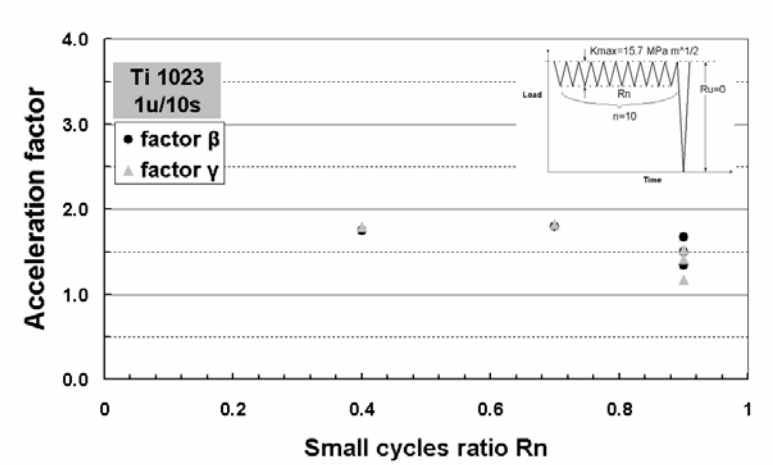

Fatigue 8.26_ The variation of the acceleration factor β and γ in terms of the R_n on Ti1023.

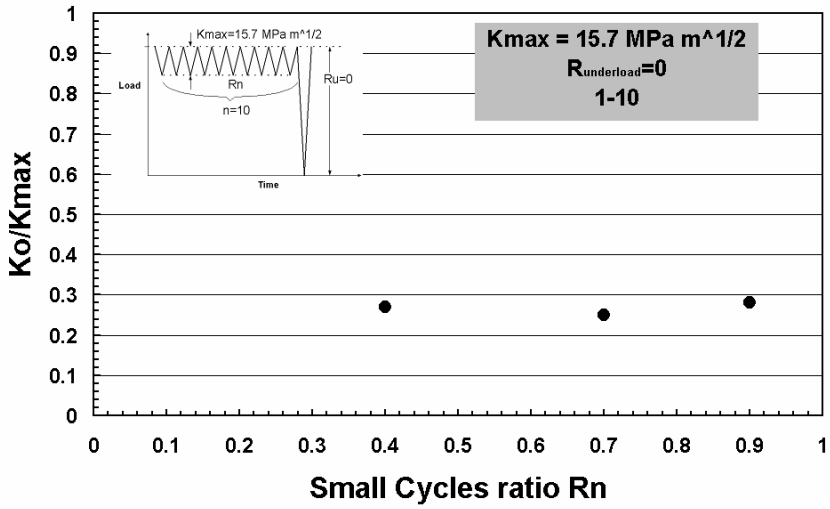

Figure 8.27_ The variation of the crack opening level of the underload in terms of R_n on Ti1023.

It is obvious that the small cycles under these sequences have become damaging. Hence, each small cycle contributes to the total crack propagation with a respective crack increment, which has an effect on d_{max}. Therefore, crack tip plastic deformation changes due to the growing crack and hence no relevant information can be drawn from the examination of d_{max} and Δd_{mn}.

8.4.2.2 Al8090 - Sequences containing an underload

8.4.2.2.1 Effect of the number of small cycles (R_n = 0.9)

In this set of tests, the maximum applied load P_{max} remains the same for the entire loading spectrum. Hence, the maximum stress intensity factor K_{max} of the small and underload cycles was the same. The starting value of K_{max} was 14.1 MPa $m^{1/2}$. The R_u ratio of the underloads is zero, which makes ΔK_u = 14.1 MPa $m^{1/2}$. Starting ΔK_n was 1.41 MPa $m^{1/2}$ and R_n ratio was 0.9. The number of n small cycles was varied form 1 to 1000.

The characteristic values of $(da/dN)_{sequ}$, which correspond to the crack growth increment of around 1.5 mm, are presented in the table A8 and they are plotted together with linear summation prediction in terms of the number of the small cycles n in the figure 8.28. The $(da/dN)_s$ reduces as the number of the small cycles increases and the underloads become more rare and they are higher than the linear summation prediction.

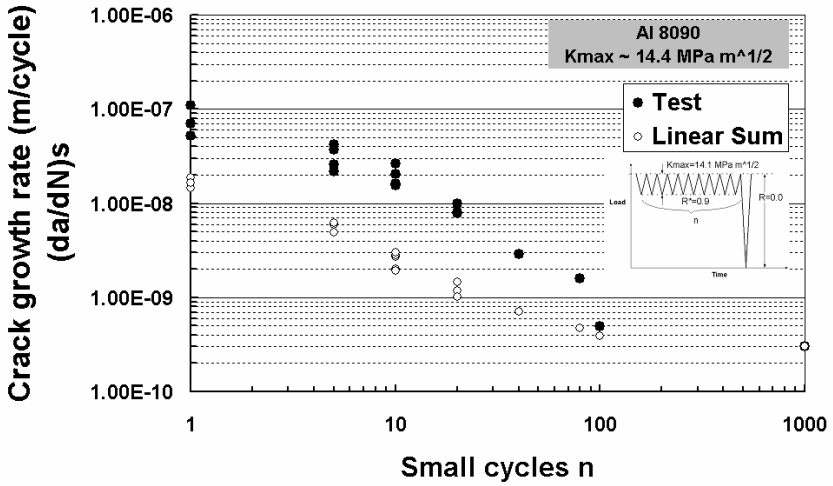

Figure 8.28_ The $(da/dN)_s$ values and the linear summation prediction in terms of the number of the small cycles n on Al8090.

The acceleration factors α were calculated and presented in table A8 for each test. Figure 8.29 gives the variation of the acceleration factors α as the number of the small cycles in a sequence changes from 1 to 1000. The acceleration factor α forms a bell shape curve as the number of small cycles n varies from 1 to 1000.

The peak value of the factor α is 9.4 and appears at n=10. When n=1 factor α is around 5 and increases as the number of the small cycles n increases to the value of the 10. After the peak value, factor α decreases until it reaches it minimum value of 1 at n=1000. The test scatter is large, but the effect of the small cycles on the crack growth rates is clear.

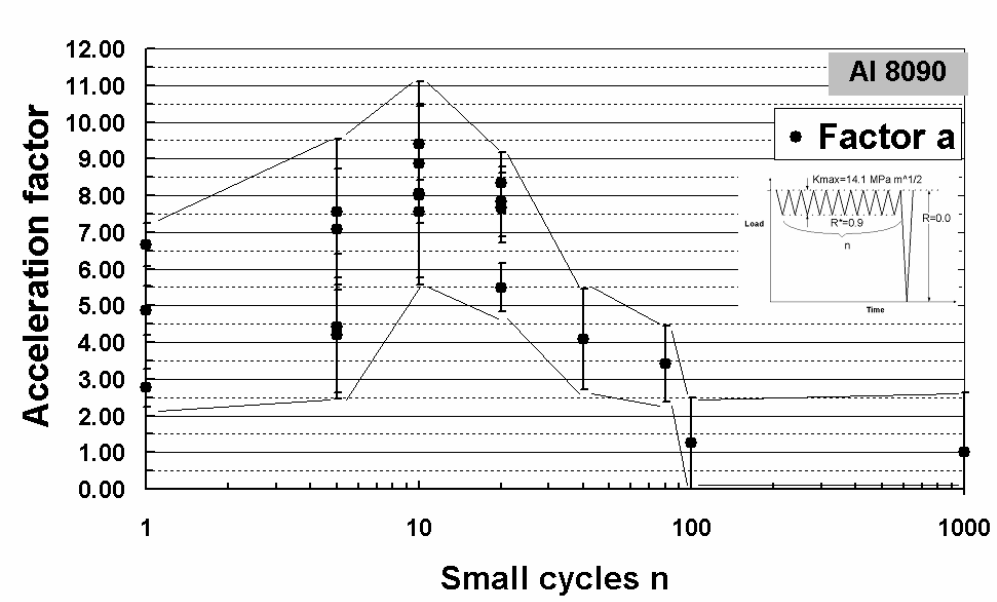

Figure 8.29_ The variation of the acceleration factor α in terms of the n small cycles in the sequence on Al8090. Error bands are indicated.

The acceleration factors β and γ were also calculated and presented in table A8. Figures 8.30 gives the variation of the acceleration factors β and γ as the number of the small cycles in a sequence changes from 1 to 1000. Factors β and γ exhibit the same bell shape curve with maximum value of 13 and 8.5 respectively, at n=10.

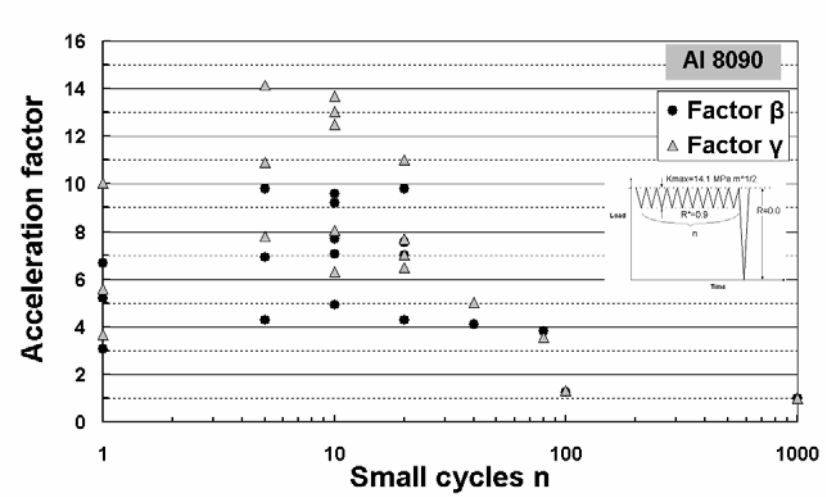

Figure 8.30_ The variation of the acceleration factor β and γ in terms of the n small cycles in the sequence on Al8090.

Figure 8.31 gives the measured crack opening level in terms of n. The mean values of the crack opening load of the underload cycles can be found in table A8 for each test in MPa $m^{1/2}$ and in fraction of the maximum load of the loading cycle. The closure level is $0.54K_{max}$ after 1 small cycle and decreases to 0.34 K_{max} as the number of small cycles increase to 10. At n=20, the crack closure level remains the same, but increases above 0.45 K_{max} as the n values becomes larger than 40.

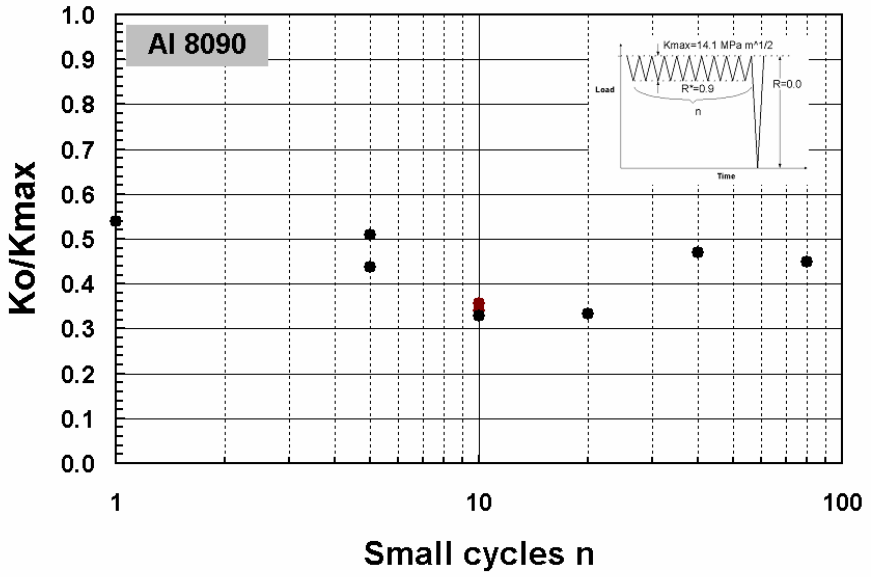

Figure 8.31_ The variation of the crack closure measurements in terms of the n small cycles in the sequence on Al8090.

Figure 8.32 shows the Δd_{mn} data points and the fitted curves for the tested loading sequences. The Δd_{mn} increases sharply in the initial few small cycles. After 10 small cycles the increase of Δd_{mn} is very small. This behaviour is very clear at sequences 1underload/40small and 1underload/80small, where a large number of data are available. The Δd_{mn} appears to increase sharper at sequences containing small numbers of small cycles.

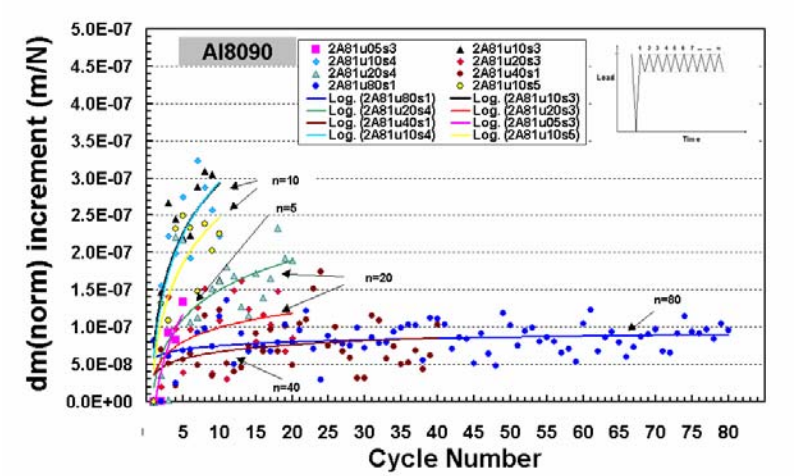

Figure 8.32_ The variation of the normalized d_m with the small cycles (R_n=0.9) and the number of small cycles n in a sequence.

8.4.2.2.2 Effect of the K_{max}

Four SVAL tests were conducted in order to investigate the effect of K_{max} on the acceleration factor α. 10 small cycles following by 1 underload was the selected cycle sequence. K_{max} was 7.05, 17.63, and 23.5 MPa $m^{1/2}$ for these three tests. Stress intensity range of small cycles was kept at the threshold of 1.41 MPa $m^{1/2}$.

The values of $(da/dN)_{sequ}$, are presented in the table A8 and they are plotted together with linear summation prediction K_{max} in the figure 8.33. The $(da/dN)_s$ reduces as the K_{max} becomes lower. It can be observed the trend of the $(da/dN)_s$ to approach the threshold value of 10^{-10} m/cycle at K_{max} = 5 MPa $m^{1/2}$, which is the intrinsic K_{max} threshold value, $K_{max,T}$. The $(da/dN)_s$ are high than the linear summation prediction depending on the level of K_{max}.

The acceleration factors α were calculated and presented in table A8 for each test. Figure 8.34 gives the variation of the acceleration factors α as K_{max}. Acceleration factor α is increasing from 3.5 to 14 as the K_{max} of the sequence is increasing. The factors β and γ (table A8) exhibit very similar behaviour.

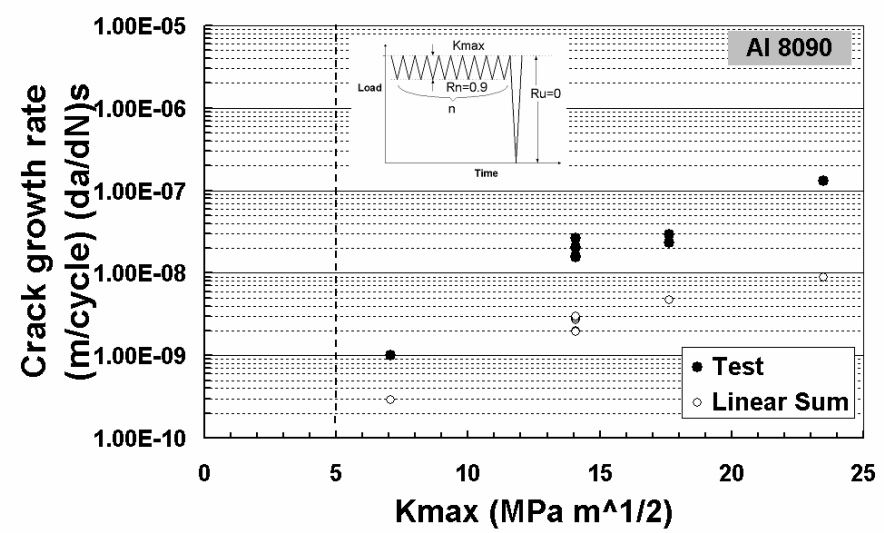

Figure 8.33_ The $(da/dN)_s$ values and the linear summation prediction in terms of the number of the K_{max} on Al8090.

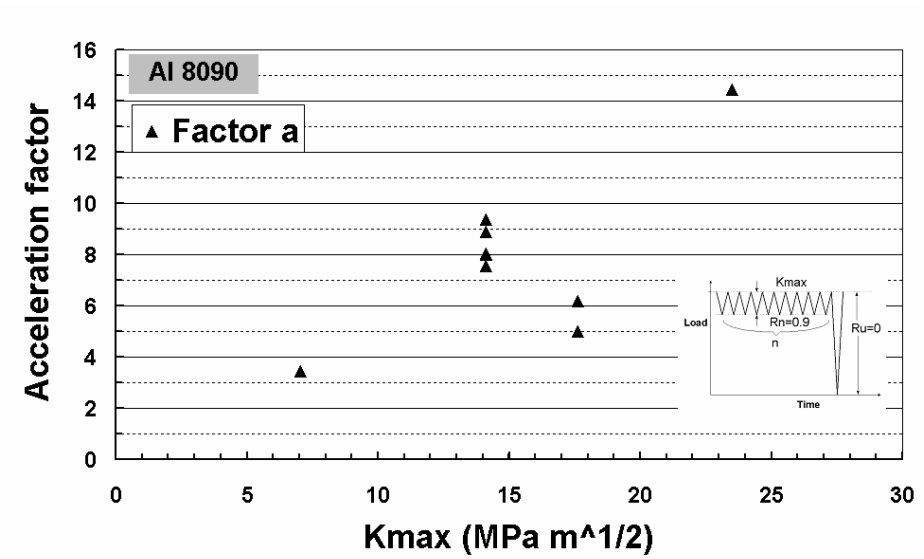

Figure 8.34_ The variation of the acceleration factor α in terms of the K_{max} on Al8090.

Figure 8.35 gives the measured crack opening level as a function of K_{max}. The values can be found in table A8. The crack closure levels are lower than 0.5 K_{max}, with a trend to decrease as K_{max} increases. The minimum value is 0.31 K_{max} at K_{max}=23.5 MPa $m^{1/2}$.

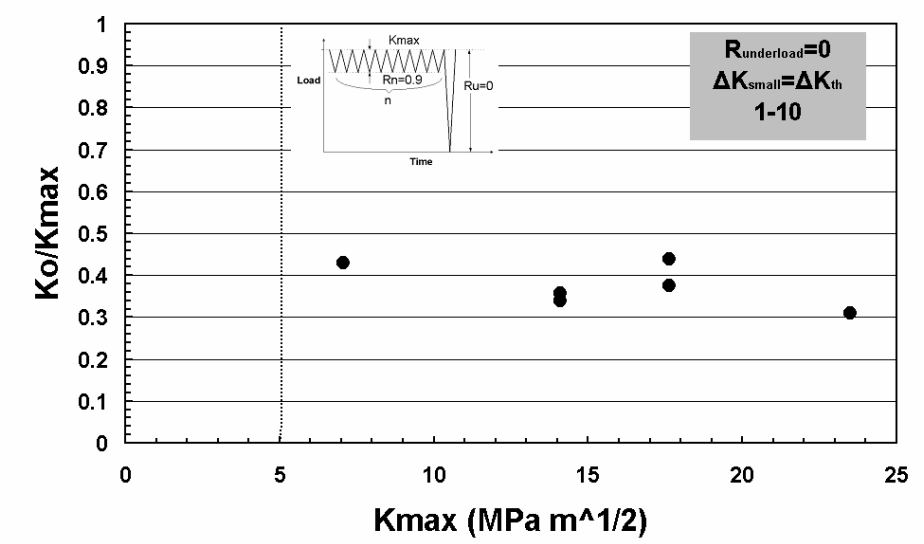

Figure 8.35_ The variation of the crack opening level in terms of K_{max} on Al8090.

Figure 8.36 shows the Δd_{mn} data points and the fitted curves for the tested loading sequences. It appears that when the applied K_{max} is high enough, in the present case larger than 14 MPa $m^{1/2}$, the Δd_{mn} and hence the d_{max} increases as more small cycles are applied. The same does not apply when the K_{max} is low and approaches the $K_{max,T}$.

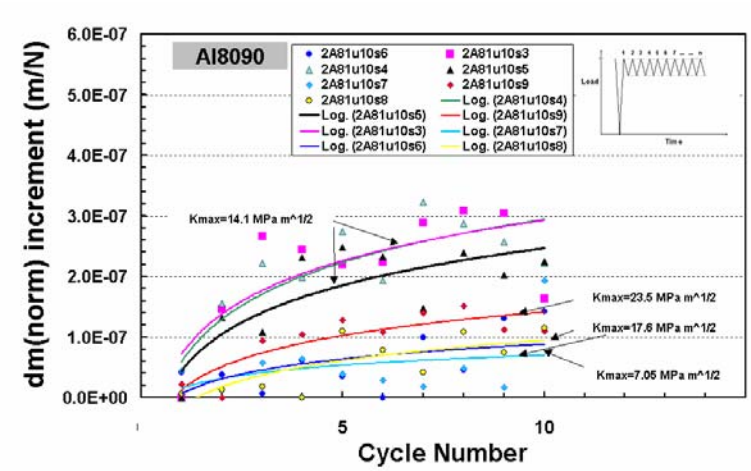

Figure 8.36_ The variation of the normalized d_m with the small cycles (R_n=0.9) and the K_{max} level.

8.4.2.2.3 Effect of the R_u ratio of the Underload Cycles

Two SVAL tests were conducted to investigate the effect of the R ratio of the underload cycles. The underload ratios R_u were 0.3 and 0.5. Tests sequence was 10 small cycles followed by 1 underload. K_{max} was at the value of 14.1 MPa $m^{1/2}$. Loading test conditions and crack lengths can be seen in table A8.

The values of $(da/dN)_s$, are presented in the table A8 and they are plotted together with linear summation prediction in terms of the number of the small cycles n in the figure 8.37. The $(da/dN)_s$ decline smoothly as the R_u becomes higher.In all cases, the $(da/dN)_s$ are high than the linear summation prediction depending on the level of R_u.

The acceleration factors α were calculated and presented in table A8 for each test. Figure 8.38 gives the variation of the acceleration factors α as R_u. Acceleration factor remains at the levels of 9 to 10 when the R ratio of underload cycles is reduced from 0 to 0.3. At high R ratio of underload the acceleration is reduced but remains at high levels. The factors β and γ (table A8) exhibit very similar behaviour.

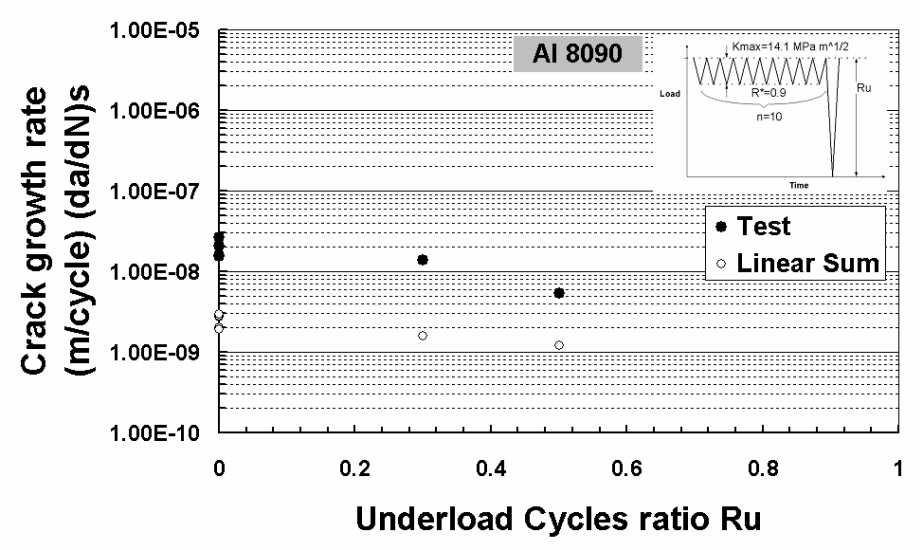

Figure 8.37_ The $(da/dN)_s$ values and the linear summation prediction in terms of the number of the R_u on Al8090.

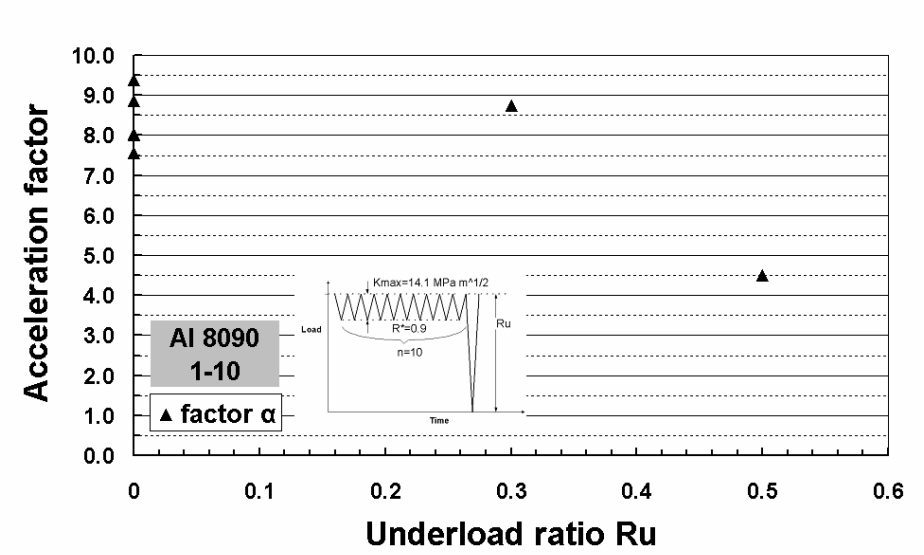

Figure 8.38_ The variation of the acceleration factor α in terms of the R_u on Al8090.

Figure 8.39 gives the measured crack opening level as a function of R_u. The values can be found in table A8. The diagonal line indicates the fully effective cycle. At R_u = 0.3 closure level remains at the same low levels as at R_u=0 and is very close to the minimum applied load. At R_u = 0.5 crack closure is 0.5 K_{max} which makes the cycle fully effective.

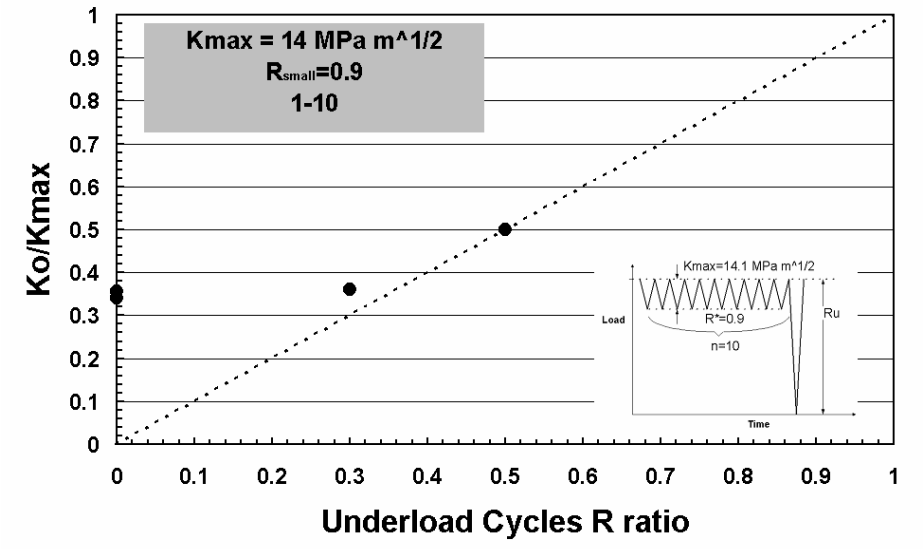

Figure 8.39_ The variation of the crack opening level in terms of R_u on Al8090.

Figure 8.40 shows the Δd_{mn} data points and the fitted curves for the tested loading sequences. The tests exhibits the same trend in the Δd_{mn}, which shows that

small cycles have very similar effects on the crack tip deformation. When R_u of the underloads is 0.5, small cycles appear to have the smallest influence on the crack tip deformation.

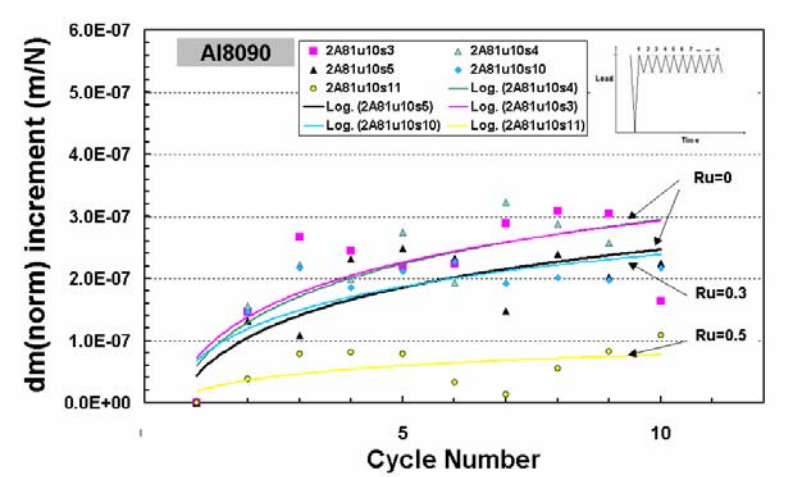

Figure 8.40_ The variation of the normalized dm with the small cycles (R_n=0.9) and the R_U value.

8.4.2.2.4 Effect of the R_n ratio of the small Cycles

Two SVAL tests were conducted to investigate the effect of the R ratio of the small cycles. The small ratios R_n were 0.7 and 0.4. Test sequence was 10 small cycles followed by 1 underload. K_{max} was at the value of 14.1 MPa $m^{1/2}$. Loading test conditions and crack lengths can be seen in table 18.

The values of $(da/dN)_s$, are presented in the table A8 and they are plotted together with linear summation prediction in terms of the number of the small cycles n in the figure 8.41. The $(da/dN)_s$ increase as the R_n becomes lower. In all cases, the $(da/dN)_s$ are high than the linear summation prediction depending on the level of R_n.

The acceleration factors α were calculated and presented in table A8 for each test. Figure 8.42 gives the variation of the acceleration factors α as R_n. Acceleration factor α decreases sharply as the small cycles ratio R_n approaches 0.7 and their stress intensity range becomes from the threshold value of 1.41 to 4.23 MPa $m^{1/2}$. When the ratio R_n of the small cycles in 0.4, a significant increase of the

acceleration factor is observed. The factors β and γ (table A8) exhibit very similar behaviour.

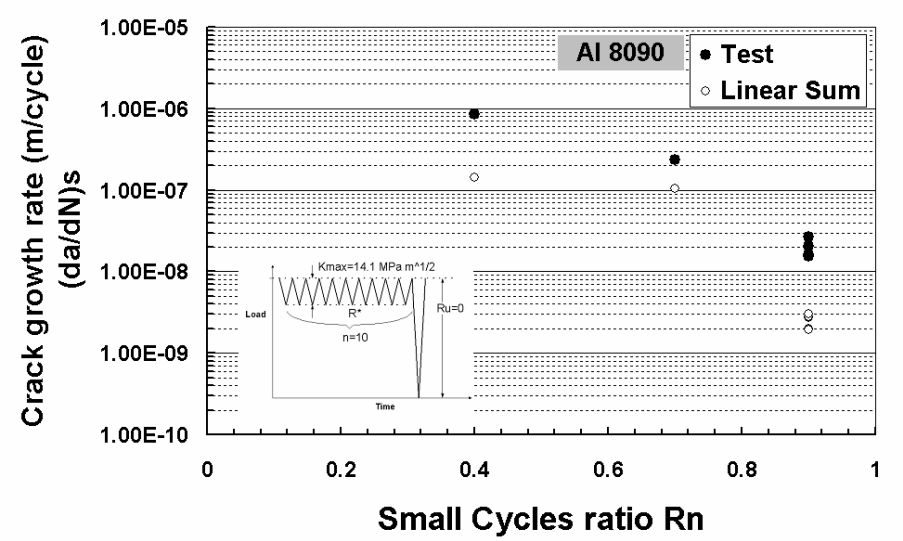

Figure 8.41_ The $(da/dN)_s$ values and the linear summation prediction in terms of the number of the R_n on Al8090.

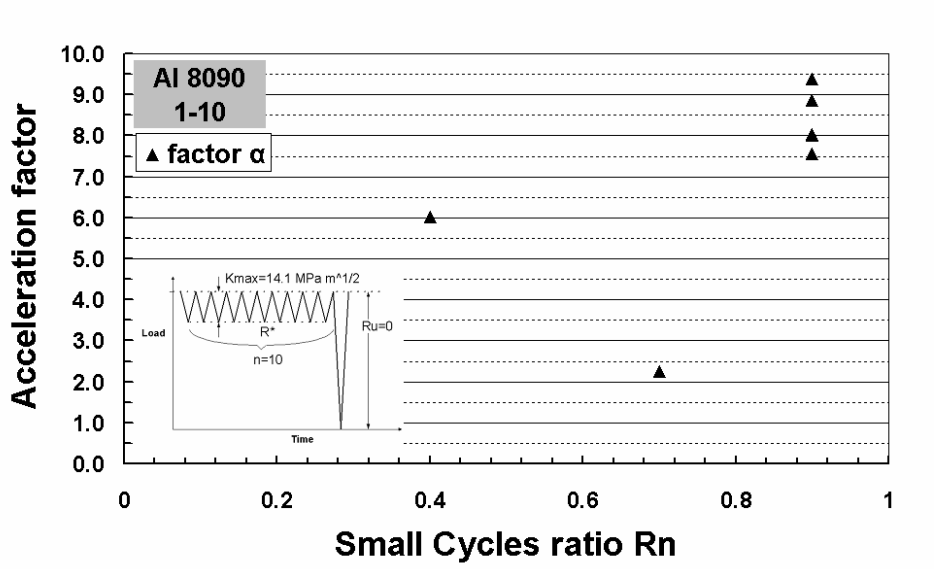

Figure 8.42_ The variation of the acceleration factor α in terms of the R_n on Al8090.

As the small cycles ratio R_n approaches 0.7 from 0.9, the stress intensity range changes from the threshold value of 1.41 to 4.23 MPa $m^{1/2}$. This means that the small cycles are no longer inactive and they contribute to the crack growth. In figure 8.43 one can see that when the small cycles are damaging, closure level of the underloads increases towards the CAL value. The values of the crack opening

load of the underload cycles for each test can be found in table A8 in MPa $m^{1/2}$ and in fraction of the maximum load in the loading cycle.

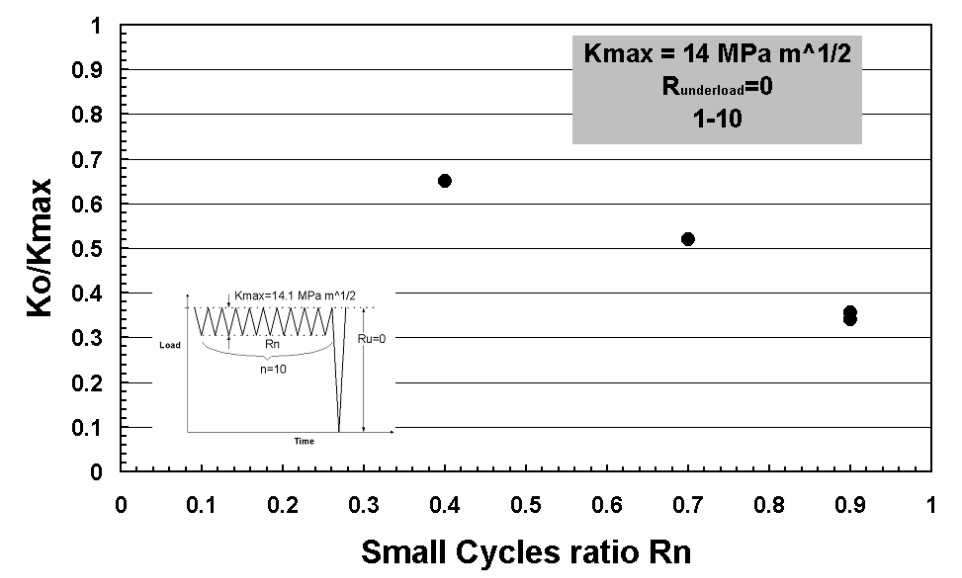

Figure 8.43_ The variation of the crack opening level of the underload in terms of R_n on Al8090.

It is obvious that the small cycles under these sequences have become damaging. Hence, each small cycle contributes to the total crack propagation with a respective crack increment, which has an effect on d_{max}. Therefore, crack tip plastic deformation changes due to the growing crack and hence no relevant information can be drawn from the examination of d_{max} and Δd_{mn}.

8.4.2.3 Al7010 - Sequences containing an underload

8.4.2.3.1 Effect of the number of small cycles (R_n = 0.9)

In this set of tests, the maximum applied load P_{max} remains the same for the entire loading spectrum. Hence, the maximum stress intensity factor K_{max} of the small and underload cycles was the same. The starting value of K_{max} was 12 MPa $m^{1/2}$. The R_u ratio of the underloads is zero, which makes ΔK_u = 12 MPa $m^{1/2}$. Starting ΔK_n was 1.2 MPa $m^{1/2}$ and R_n ratio was 0.9. The number of n small cycles was varied from 1 to 100.

The characteristic values of $(da/dN)_{sequ}$, which correspond to the crack growth increment of around 1.5 mm, are presented in the table A8 and they are plotted together with linear summation prediction in terms of the number of the small cycles n in the figure 8.44. The $(da/dN)_s$ reduces as the number of the small cycles increases and the underloads become more rare. The experimental and the predicted crack growth rates do not exhibit big differences, with the experimental measurements being slighly higher.

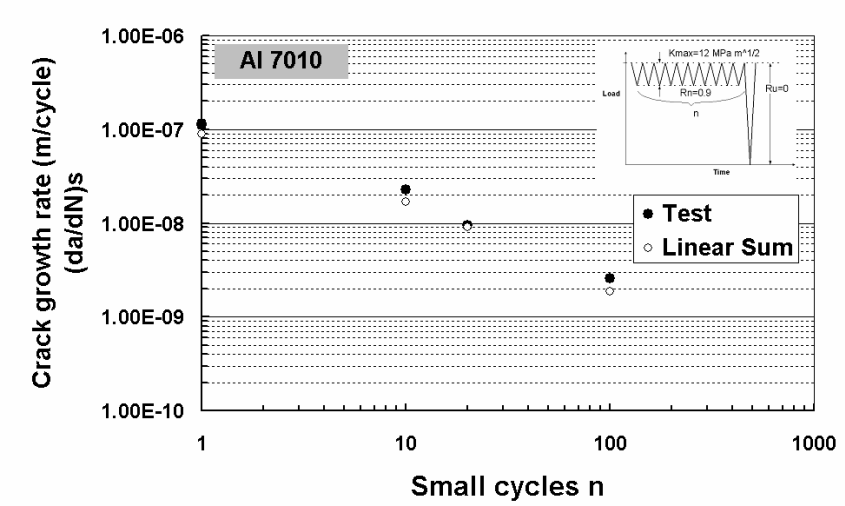

Figure 8.44_ The $(da/dN)_s$ values and the linear summation prediction in terms of the number of the small cycles n on Al7010.

The acceleration factors α were calculated and presented in table A8 for each test. Figure 8.45 gives the variation of the acceleration factors α as the number of the small cycles in a sequence changes from 1 to 100. Factor α is between 1 and 1.5 for every number of small cycles n. The factors β and γ (table A8) exhibit very similar behaviour.

Figure 8.46 gives the measured crack opening level in terms of n. The mean values of the crack opening load of the underload cycles can be found in table A8 for each test in MPa $m^{1/2}$ and in fraction of the maximum load of the loading cycle. The crack opening values do not change with the number of small cycles prior the underload. Hence, the effect of the small cycles on the underloads on this material is small and reaches its maximum after the first few cycles. The crack opening values do not differ significantly from the CAL values.

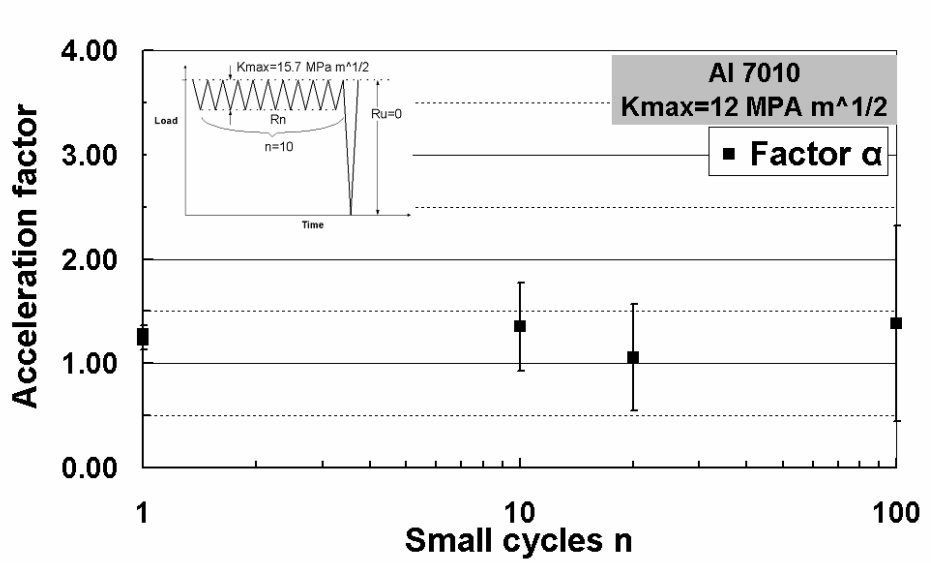

Figure 8.45_ The variation of the acceleration factor α in terms of the n small cycles in the sequence on Al7010. Error bands are indicated.

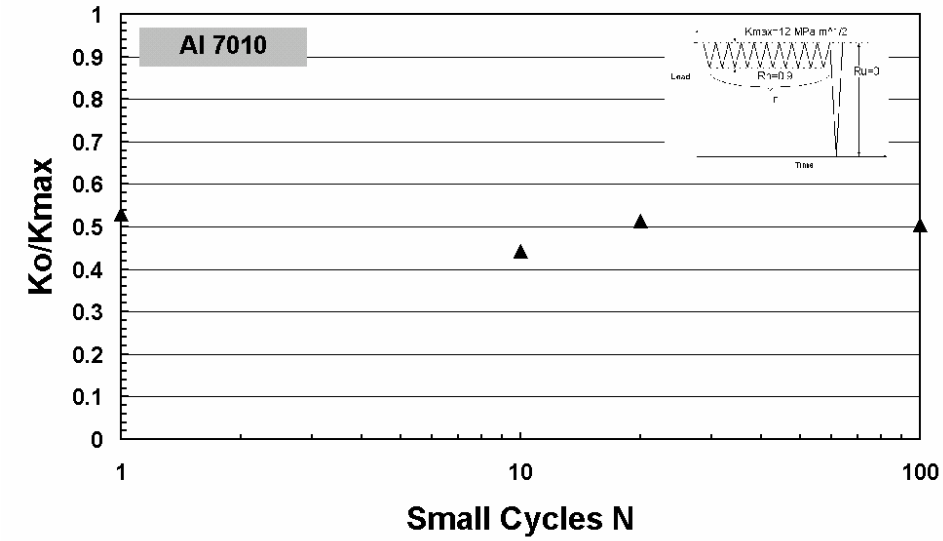

Figure 8.46_ The variation of the crack closure measurements in terms of the n small cycles in the sequence on Al7010.

Figure 8.47 shows the Δd_{mn} data points and the fitted curves for the tested loading sequences. Test sequences with 1underload/10small and 1underload/20small show that the Δd_{mn} changes fast and reaches its maximum value in the first few cycles. Test sequences 1underload/100small clearly indicates that there is no significant change in Δd_{mn} after the few first small cycles. Overall, the change of Δd_{mn} in the tested sequences is not very significant.

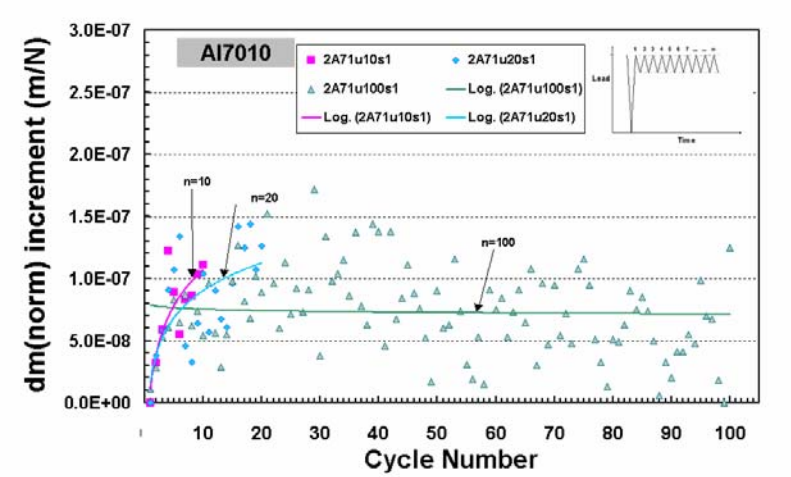

Figure 8.47_ The variation of the normalized d_m with the small cycles (R_n=0.9) and the number of small cycles n in a sequence.

8.4.2.3.3 Effect of the K_{max}

Three SVAL tests were conducted in order to investigate the effect of K_{max} on the acceleration factor α. 10 small cycles following by 1 underload was the selected cycle sequence. K_{max} was 12, 15, and 20 MPa $m^{1/2}$ for these three tests. The stress intensity range of small cycles was at the threshold of 1.2 MPa $m^{1/2}$.

The values of $(da/dN)_s$, are presented in the table A8 and they are plotted together with linear summation prediction in terms of K_{max} in the figure 8.48. The $(da/dN)_s$ reduces as the K_{max} becomes lower. The $(da/dN)_s$ are high than the linear summation prediction depending on the level of K_{max}. The experimental and the predicted crack growth rates do not exhibit big differences.

The acceleration factors α were calculated and presented in table A8 for each test. Figure 8.49 gives the variation of the acceleration factors α as K_{max}. Values of factor α are again between 1.5 and 1 and very close to the linear summation prediction. The factors β and γ (table A8) exhibit very similar behaviour.

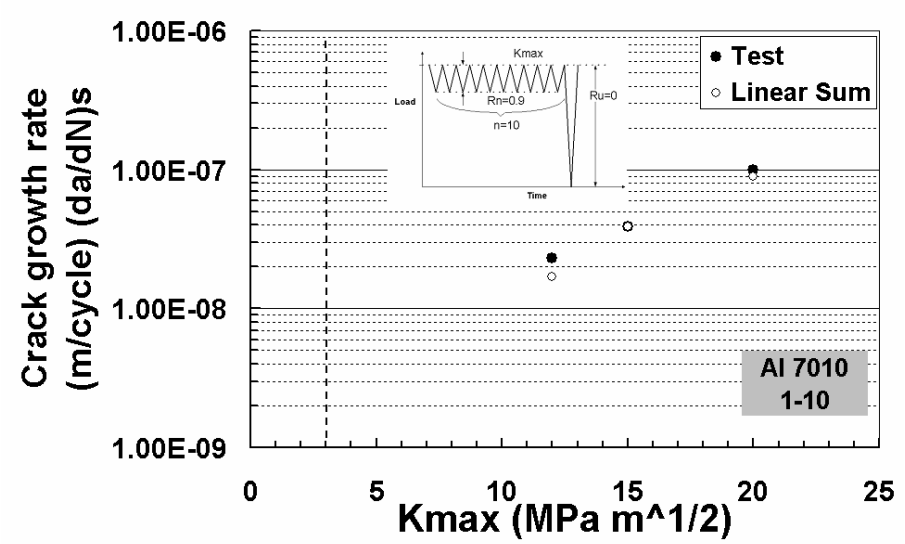

Figure 8.48_ The $(da/dN)_s$ values and the linear summation prediction in terms of the number of the K_{max} on Al7010.

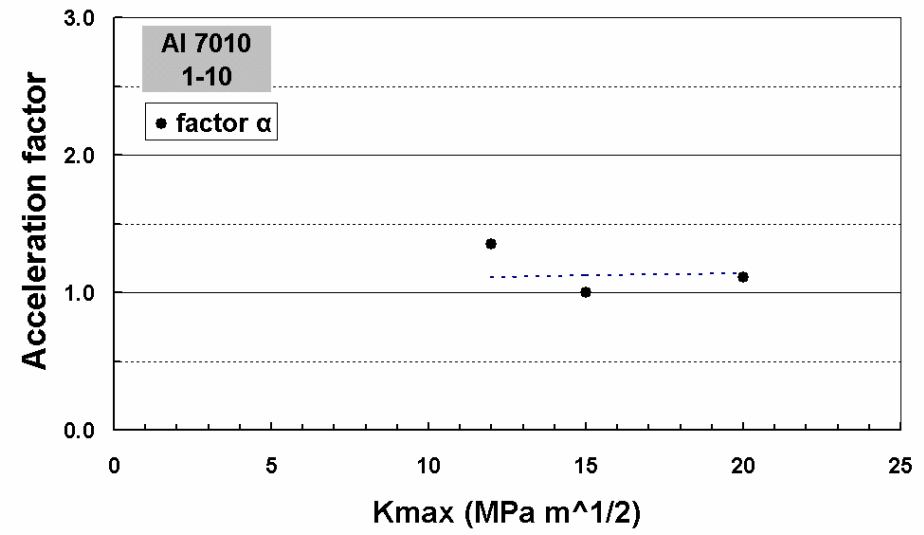

Figure 8.49_ The variation of the acceleration factor α in terms of the K_{max} on Al7010.

Figure 8.50 gives the measured crack opening level as a function of K_{max}. The values can be found in table A8. Crack closure levels are ranged from 0.44 to 0.51 K_{max} as K_{max} changes from 12 to 20 MPa $m^{1/2}$. It is obvious that the crack opening values are very close to the CAL levels.

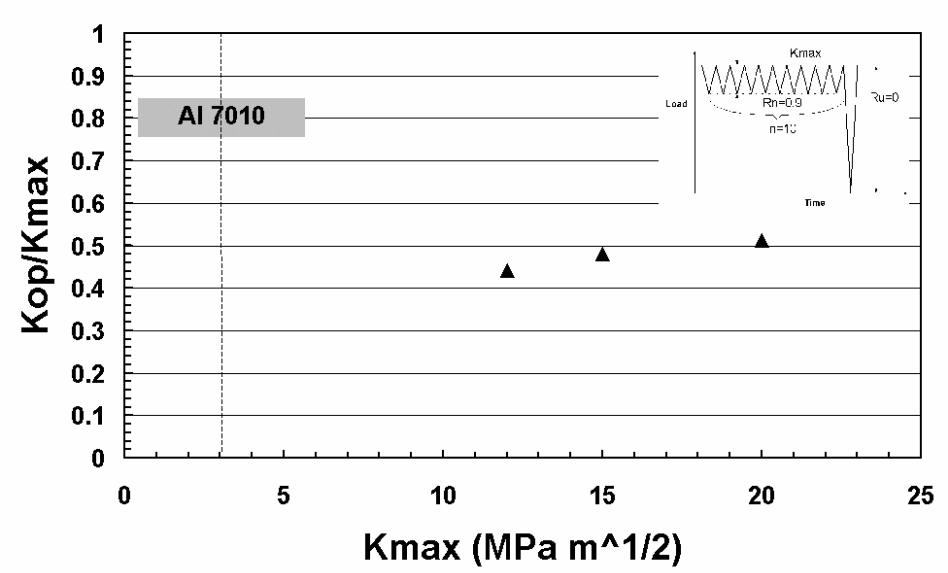

Figure 8.50_ The variation of the crack opening level in terms of K_{max} on Al7010.

Figure 8.51 shows the Δd_{mn} data points and the fitted curves for the tested loading sequences. In all three tests, Δd_{mn} exhibits the same behaviour in terms of the applied small cycles. The changes in d_{mn} are practically the same, as the K_{max} increases from 12 to 20 MPa $m^{1/2}$.

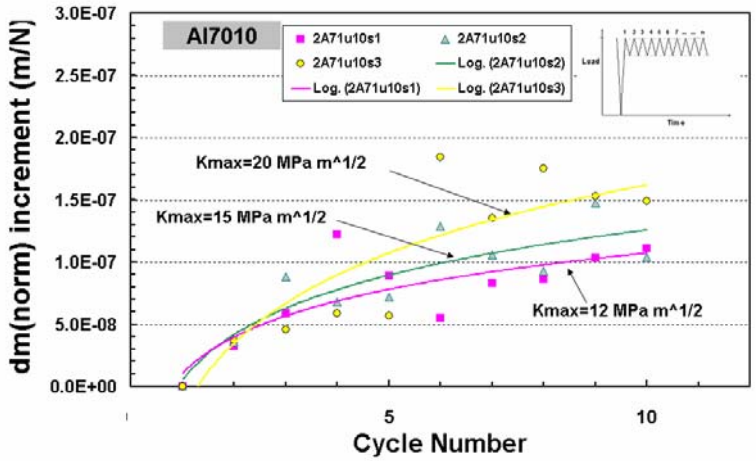

Figure 8.51_ The variation of the normalized d_m with the small cycles (R_n=0.9) and the K_{max} level.

8.4.4 Block Testing

Test **R11T** on Ti 1023**:** Figure 8.52 shows the variation of the crack closure values during each part of the test. Table A10 provides the characteristic values of the crack growth rates and closure levels of each part. During the first part of the test, under CAL at R=0, closure are building up till the value of 0.4 K_{max}. During the application of the SVAL sequence, closure reduced to 0.28 K_{max} after 0.4mm of crack increment and remains to this level for the rest of the crack growth. The application of CAL causes the increase of crack closure again. After 1mm of crack growth the closure value is around 0.31K_{max}. After 1.3mm of growth, closure has not reach the CAL levels. And this is reflected to the crack growth rates, which are faster that the CAL rates (figure 8.53).

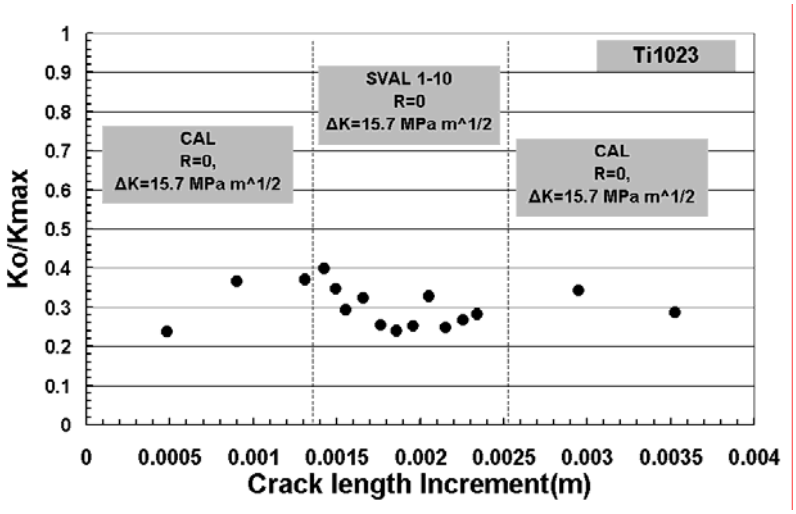

Figure 8.52_ Transient effect of the crack closure values between SVAL and CAL tests on Ti1023.

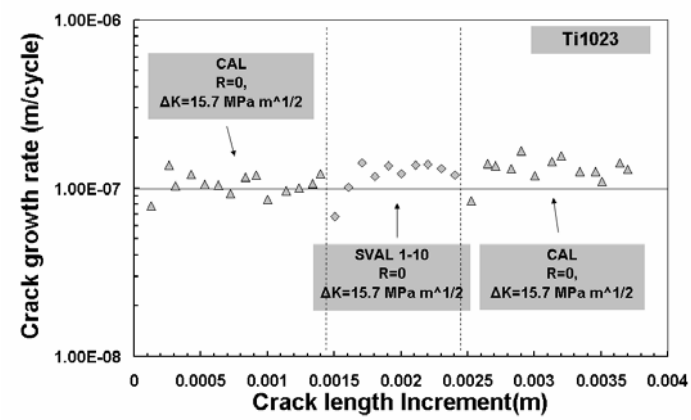

Figure 8.53_ Crack growth rates of the 1/10 sequence between CAL at R=0 and ΔK=15.7 MPa $m^{1/2}$.

Test **R11A8** on Al8090**:** Figure 8.54 shows the variation of the crack closure values during each part of the test. Table A11 provides the characteristic values of the crack growth rates and closure levels of each part. During the first part of the test closure levels remain constant with a mean value of 0.33 K_{max}. During the application of the CAL closure is building up to the CAL levels of 0.6-0.7K_{max}. The application of SVAL causes the reduction of closure. Crack closure reaches the minimum after crack growth of 0.6 to 0.8 mm (figure 8.55). After this initial increment, crack grows at stable rates under the effect of reduced crack closure.

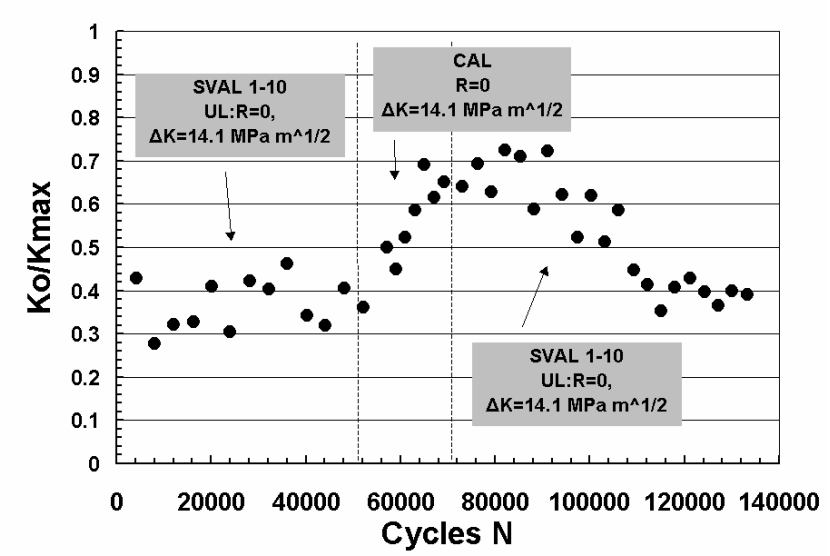

Figure 8.54_ Transient effect of the crack closure values between SVAL and CAL tests.

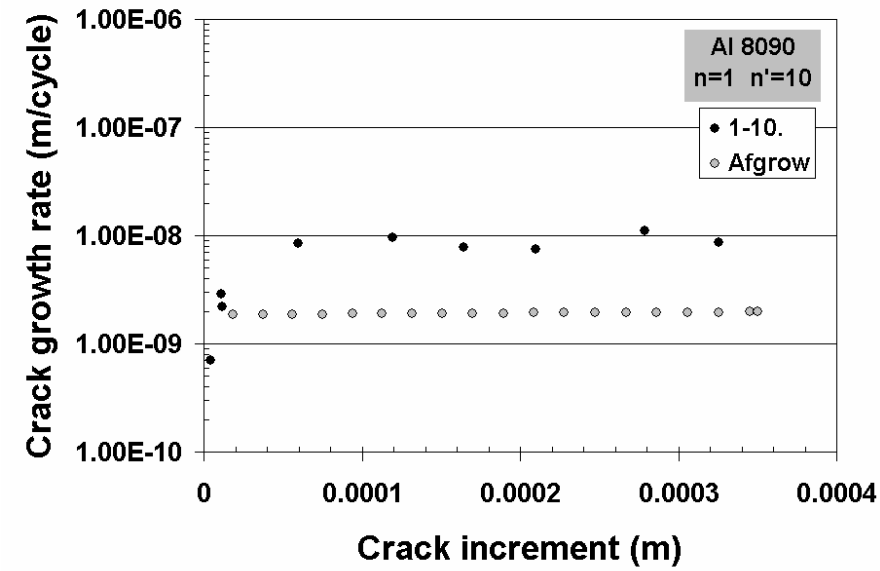

Figure 8.55_ Crack growth rates of the 1/10 sequence after CAL at R=0 and ΔK=14.1 MPa $m^{1/2}$ and comparison with Afgrow prediction.

8.5 CVAL Testing

Four different omission levels of the Rotarix spectrum (Rotarix 16, 20, 24, 32) were tested. Cycles were progressively gated out of the original Rotarix spectrum to produce the 4 different spectra. The Rotarix 16 spectrum is the largest spectrum containing 99.4% of the original spectrum, 90% of which are the high R ratio small cycles. The Rot 20 and 24 spectra are very similar. The matrix with the 4 spectra is given below (table 8.6).

Table 8.6_Rotarix Spectra Characteristics

Omission range level*	Rainflow cycle count in length	Reduction(%)
Original Rot	1989925	
16	1978108	0.6
20	113063	94.3
24	110907	94.4
32	51404	97.4

*Omission range level is the maximum cycle range retained.

The nature of the spectrum used is typical for rotary wing structures. There is a large number of small cycles at high R-values along with a relatively low number of unloading cycles. The Rotarix spectrum represents 140 flights and 190.5 hours of flight.

The experimental and the AFGROW linear summation prediction results together with the initial crack lengths and the loading conditions are listed in Table 8.7 for Ti1023, Al8090 and Al7010. The corresponding acceleration factors are also listed. Figure 8.56 and 8.57 show the crack propagation as the loading cycles were applied on Ti1023, Al8090 and Al7010. The same figures include the linear summation prediction curves. The AFGROW linear summations are plotted against the experimental results in the figure 8.58-59 for the three materials.

The Rot16 produced significant lower life comparing with linear summation, when applied on Ti1023 and Al8090. The decrease is 68% for the Ti1023 and 48% for the Al8090. The acceleration factors were varied from 1 to 3.2 depending on the material. For Al7010, life prediction and experimental life are very close resulting in an acceleration factor close to unity.

Figure 8.57 shows the effect of the spectrum on the fatigue life on Al7010. As the small cycles are progressively removed from the spectrum (Rot16 to Rot32), the fatigue life decreases. This is expected as the fraction of the large cycles within the spectrum increases. Rot20 and Rot24 produce identical fatigue lives, as expected, because both of these spectra are similar.

Table 8.7 CVAL Experimental Results and Life Predictions on Ti1023, Al8090 and Al7010

		Ti 1023	Al 8090	Al 7010			
Spectrum		Rot16	Rot16	Rot16	Rot20	Rot24	Rot32
Initial Crack Length	Mm	29.2	33.0	15.9	16.3	16.3	15.7
Final Crack Length	Mm	29.7	37.1	Failure	failure	failure	failure
Total Cycles (Experimental)	N	1963333	3957977	6314679	1295019	1296284	671129
Total Cycles (Linear Prediction)	N	6205008	7039150	6533657	1413196	1398946	885173
Acceleration Factor	B	3.16	1.78	1.04	1.09	1.08	1.31

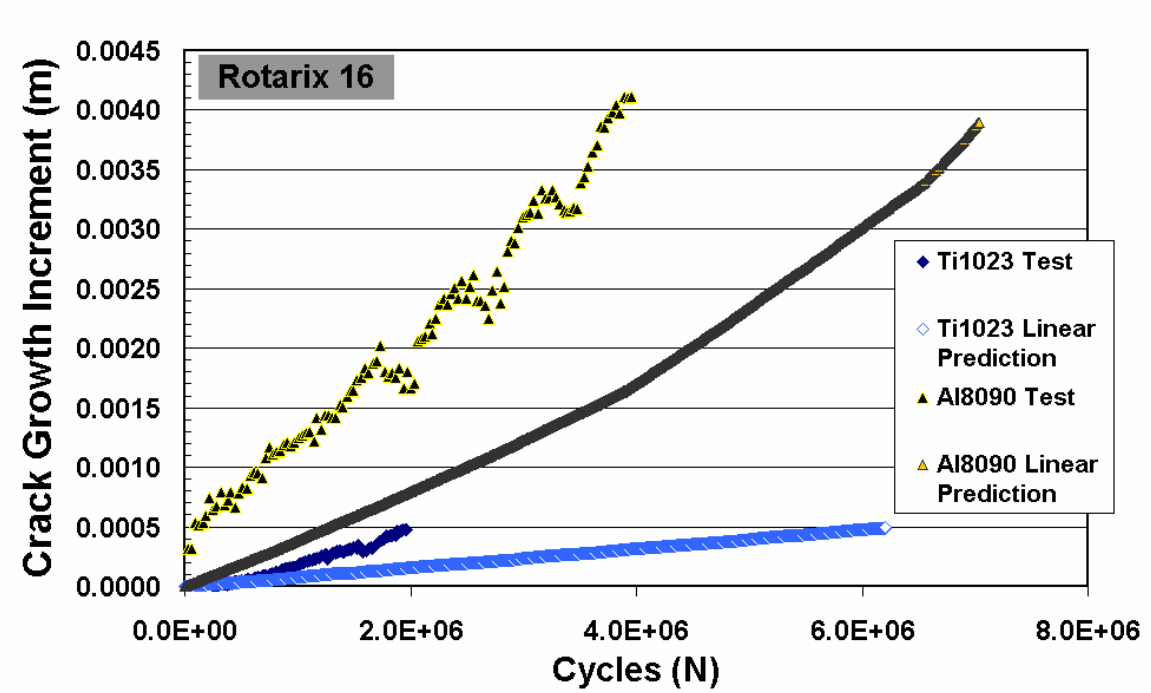

Figures 8.56_ Fatigue crack propagation on Ti1023, Al8090 and Al7010 under the action of Rot16 spectrum and the respective linear summations.

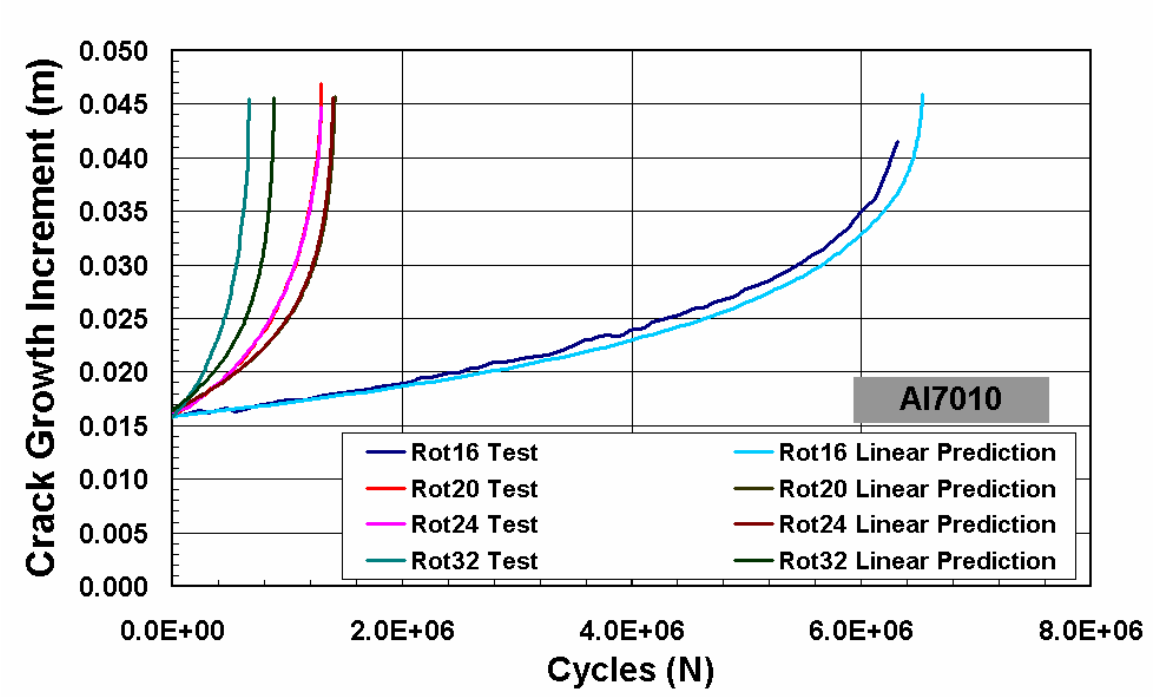

Figures 8.57_ Fatigue crack propagation on Al7010 under the action of Rot16, Rot20, Rot24 and Rot32 spectra and the respective linear summations.

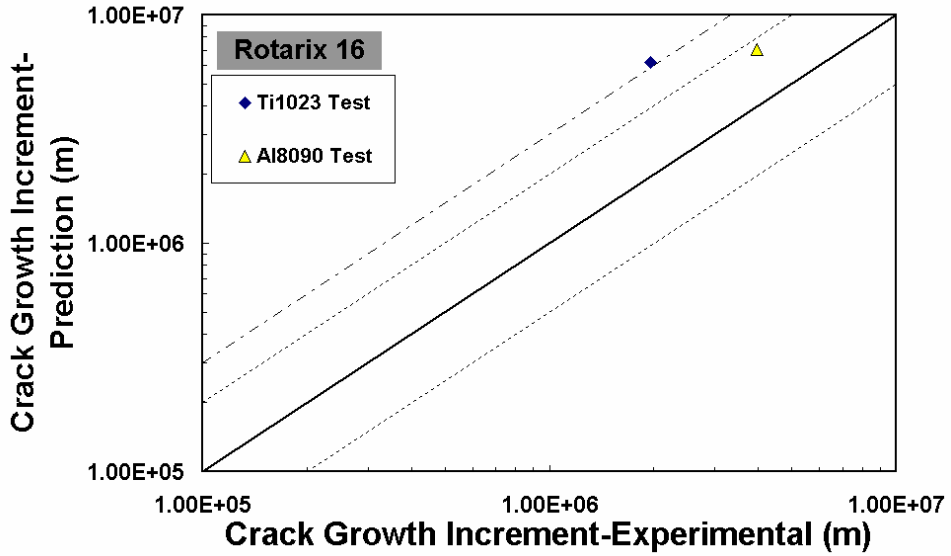

Figures 8.58_ Comparison between experimental results and linear sum predictions under Rot16 for Ti1023 and Al8090.

Figure 8.58 shows the linear prediction for the each spectrum on Al7010. In relation with the linear summation prediction, the acceleration effects are limited for the four different spectra.

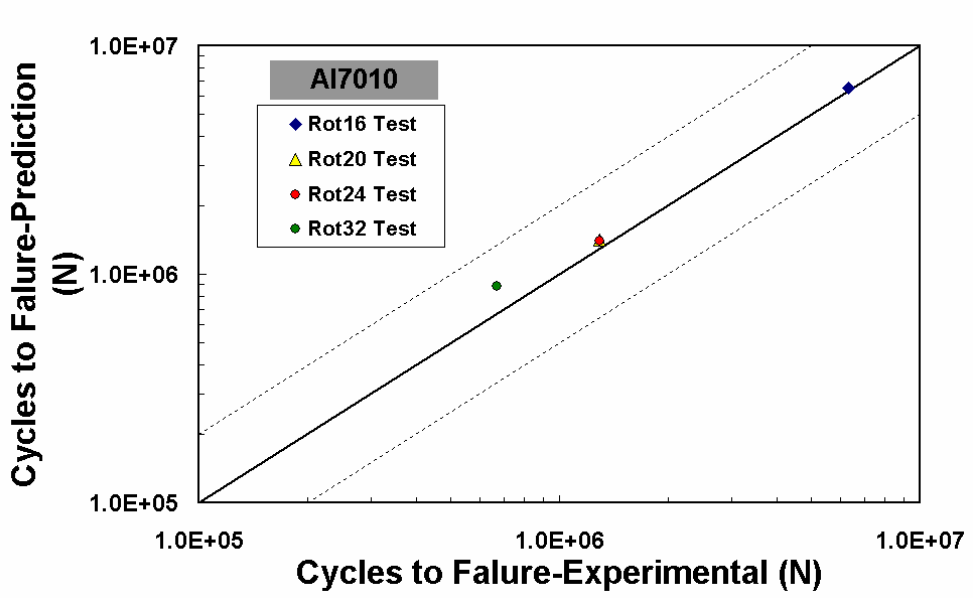

Figures 8.59_ Comparison between experimental results and linear sum predictions under Rot16 to Rot32 for Al7010.

Fatigue crack growth rates were generated from the tests and predictions data and they were plotted against crack length increment. Figures 8.60-61 show crack growth rate plotted against crack length increment for experimental data and the predictions for the three materials under Rot16 to Rot 32 spectra.

Figure 8.61 shows the experimental and the linear predicted crack growth rates for the four spectra on Al7010. The experimental crack growth rates compare well with the no-load interaction growth rates. Some differences can be found in small crack lengths and stress intensity factors, where experimental crack growth rates are slightly faster, especially in Rot32 case.

Figure 8.58 shows the experimental and the linear predicted crack growth rates for Rot16 on Ti1023 and Al8090. The experimental crack growth rates are distinguishably faster than the linear predictions on Al8090. The same observation can be made on the measurements of the crack growth rates under Rot16 on Ti1023, where the difference is more than 200% (acceleration factor of 3).

Rot16 spectrum has different effect when acting on different materials. This can be clearly seen by the observation of the crack growth rates on Ti1023, Al8090 and Al7010 (figures 8.60). It is expected that the crack growth rates will depend on

the material properties and the applied loads. When the test results are compared with the linear summation predictions, it is revealed that the load interactions have significant differences depending on the alloy. Ti1023 exhibits accelerated effects of a factor of 3.1, and Al8090 of a factor of around 2. On the other hand, Al7010 does not exhibit significant load interaction effects (factor β=1.04).

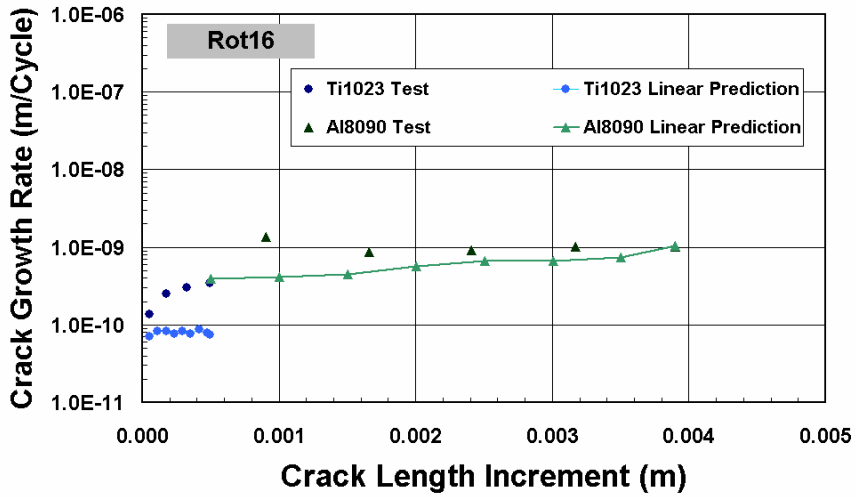

Figures 8.60_ Crack growth rates for Ti1023 and Al8090 under the action of Rot16 spectrum and the respective linear summations.

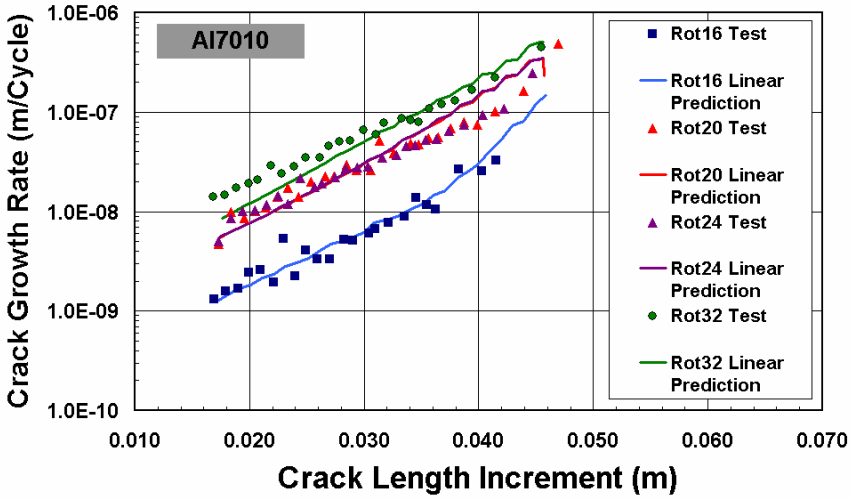

Figures 8.61_ Crack growth rates for Al7010 under the action of Rot16 to Rot32 spectra and the respective linear summations.

CHAPTER 9

DISCUSSION – UNDERLOADS AND CLOSURE MECHANISMS

9.1 Introduction

The results of the test program are reviewed, discussed and interpreted in relation with the existing published scientific work on this field in the following paragraphs. The discussion will be carried out, initially on the subjects of Constant Amplitude Loading, and near threshold fatigue crack growth behaviour. The discussion on the crack growth mechanisms and modeling on combined effect of the underload and the small cycles and the load interaction effects for each alloy follows. The CVAL tests are discussed in the light of the test findings at the end of the chapter.

The accuracy of the crack length measurement system has a direct impact to the error bands of the measured crack growth rates and the related acceleration factors. The error bands are one order of magnitude larger for the aluminium alloys. The cycle interval used for the determination of the crack growth rates has also a great influence in the error bands. The errors decrease drastically as the crack growth rates are derived using larger intervals. Generally, faster growing cracks will have larger errors since they require small cycle intervals for the determination of the crack growth rates. Although, because of their fast crack growth rates, the errors remain a small fraction of the measured values. The same applies to the calculation of the acceleration factors.

9.2 Crack Closure Measurements And The $\Delta K_{eff,exp}$ Curve

The crack closure is the premature contact between the surface of the crack and is attributed to the crack wake plasticity and the mismatch between the crack surface due to the asperities. Crack closure can be measured from 'physical' compliance curves. The initial deviation from the linearity in the given compliance plot is associated with the crack closure and the lower limit of the ΔK_{eff} range of the loading cycle. A big variety of approaches in respect with the measurement techniques and the closure point determination have been used in the international research. Schijve has reviewed the various measurement techniques and he has concluded that the compliance curve technique is a powerful tool [55]. Yigeng et al. have conducted a detailed experimental and analytical research on the issue of the

accurate measurement of the crack closure using the compliance techniques [59]. Their suggestions were adopted and adjusted in this study according to its needs.

The point of the initial crack surface contact was selected as the crack closure point. At the point of the first surface contact, the crack tip movement freezes. The further reduction of the load has as a result that a progressively larger area of crack surface comes into contact. This is reflected by the change of slope in the compliance curve. During this process the crack tip should not move and thus no further fatigue damage is introduced [63]. This mechanism is active in the case of plasticity induced closure. In the case of asperity induced closure such as fracture surface roughness, the crack tip movement may continue as the load decreases below the initial point of surface contact (figure 9.1). The lower point of the ΔK_{eff} range in the cycle will be a function of the asperity geometry. Kujawski [142] and Donald [61] have studied the above closure mechanism and reached a very similar conclusion. Their concept improved the crack growth data correlation in the near-threshold area. The two different mechanisms co-exist in the fatigue crack growth. The dominant mechanism depends on the material and the applied loading.

Lang has simulated the closure effect on the crack growth with a rigid wedge [29]. His theoretical approach concluded that the amplitude experienced by the crack tip is determined by the relationship $\Delta K_{tip} = K_{max} - K_w$ (figure 4.10). In reality, the compliance curve deviation from the linear is much smaller than what is assumed in the model. In the present study, most of the displacement curves exhibit the form shown in figure 6.21. In such cases, the closure levels of the loading cycles are around 97% of the applied K_{min} and the crack closure has a very small and insignificant effect on crack growth. The same observation was made by Sadananda et al. [43]. When only the closure effect is taken into account, the resulting values of ΔK_{eff} is impossible to correlate the crack growth data in terms of a unique $\Delta K_{eff,exp}$ curve. But according to the Lang's approach known as K_{PR} approach, a stress intensity factor level exists within the cycle, which distinguishes the actual effective and non-effective part of the loading cycle. The K_{PR} approach attributes this stress intensity factor to the change of the stresses in front of the crack tip from positive to negative.

The crack growth and closure data is used in order to determine the ΔK_{eff}. It is obvious that measured crack growth rates and closure levels during the tests are

significantly influenced by the load interaction effects caused from the large change of loads between the precracking and the actual test. Although, ΔK_{eff} is considered as the unique expression of the closure mechanism and therefore, in theory, able to explain the effects on crack growth under every loading situation (CAL, overloads, random loading, etc.). Hence, even though the load interaction effects have an undoubted influence on the closure levels and the crack growth rates, which alter them compared to the CAL conditions, the effective part of the cycle should fall into the unique ΔK_{eff} band. Alternatively, it can be stated that the effective part of the cycle should be individually and solely associated with a unique crack growth rate for a specific material, independent of the actual amplitude of the loading cycle. The assessment of the crack closure results is based on the above statement. The failure of the correlation of effective ranges of the cycles during every test would indicate that the crack closure mechanism is not able to explain fatigue crack closure under these conditions.

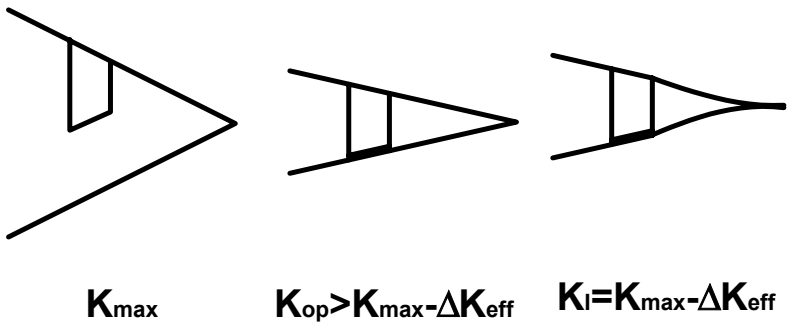

Figure 9.1_ Crack surface movement during the unloading part of the cycle due to asperity induced closure.

9.3 Constant Amplitude Loading and Crack Opening Level

The main objective of the application of CAL cycles on the specimens was to generate adequate crack opening data under CAL conditions. The cycles were applied on various crack lengths for relatively short crack increments. Due to the fatigue loading history on the crack wake, the measured crack growth data contains some degree of load interaction effects. As a result, it is possible for the crack to grow faster or slower than the established CAL crack growth rates. This result is obvious when the measured data are compared with the CAL curve for each material on figure 8.1-3. For the determination of the level of the crack opening

load during CAL growth, only the data that correlates very well with CAL curves was used. Hence, the crack opening values of R=0 cycles were established at 0.4-0.44K_{max} at K_{max}>15 MPa $m^{1/2}$ for Ti1023, 0.6-0.8K_{max} at K_{max}>14 MPa $m^{1/2}$for Al8090, and 0.54-0.56K_{max} at K_{max}>12 MPa $m^{1/2}$ for Al7010. Wu et. al. conducted crack growth and closure measurements on Al8090 T8711 and found that crack opening level is between 0.65 and 0.8 K_0/K_{max} in the range of 4-10 MPa $m^{1/2}$ [137]. Lee et al. have been derived the same conclusions [138]. The crack opening values can be assessed as typical values for the examined alloys [17].

The crack opening values suggest that different material characteristics and microstructures under the same environmental conditions develop different crack closure behaviours. This is a general conclusion well established in the international literature [17].

In relation to the material microstructure, it can be seen that even though the two aluminium alloys have similar mechanical characteristics, they present different crack opening values. The fractographic examination of the fracture surface of the two alloys (for example figures 8.5 and 8.6) revealed that Al8090 produces a lot of high surface roughness compared to the Al7010 under the same loading condition. Hence, the closure behaviour is effected from plasticity and roughness on Al8090. On Al7010, the surface roughness is much smaller and so is the CAL closure level. The effect of plasticity on crack closure appears to become the dominant factor on Al7010. Therefore, it can be suggested that the different roughness effects is the reason for the different CAL closure level, since there are only small differences in the material properties. Bergner et al. [136] have suggested that crack growth rates on Al8090 are significantly affected by the roughness induced closure. They measured the roughness on M(T) specimens between 37.2 and 50.8μm.

On Ti1023, the fractographic examination showed that the surface roughness is very small. On figure 8.5 it can be observed the limited surface roughness and the intense plastic deformation of the crack wake. Figure 9.2 shows the Hooke's area for the three materials. Taking into account the alongation of each material (table 6.2, 6.4 and 6.6), it can be concluded that aluminium alloys are more ductile than the titanium. This material property allows the aluminium alloys to sustain larger plastic deformations and create larger plastic zones under the same stress intensity factors and for the same geometry. Therefore, it is expected that because of the larger plastic deformation, crack surfaces will come into contact faster in

aluminium alloys than in titanium under constant amplitude loading. Additionally, the produced roughness on the surface during the crack growth is larger in aluminium alloys, contributing significantly to the rise of the crack closure level. The comparison of the closure level between the Ti1023 and the Al7010, at which crack closure is governed by the plasticity, confirms that the titanium has a lower closure value compared to the aluminium.

Even though only some of the CAL crack growth data was used for the CAL crack opening determination, all the measured data was included for the determination of the effective stress intensity factor range ΔK_{eff} curve. This was done under the hypothesis that closure governs the load interaction effects on the crack growth and this is reflected by the formation of a unique ΔK_{eff} curve. Hence, both CAL crack growth data with and without load interaction effects can be used to examine whether or not the ΔK_{eff} curve is formed.

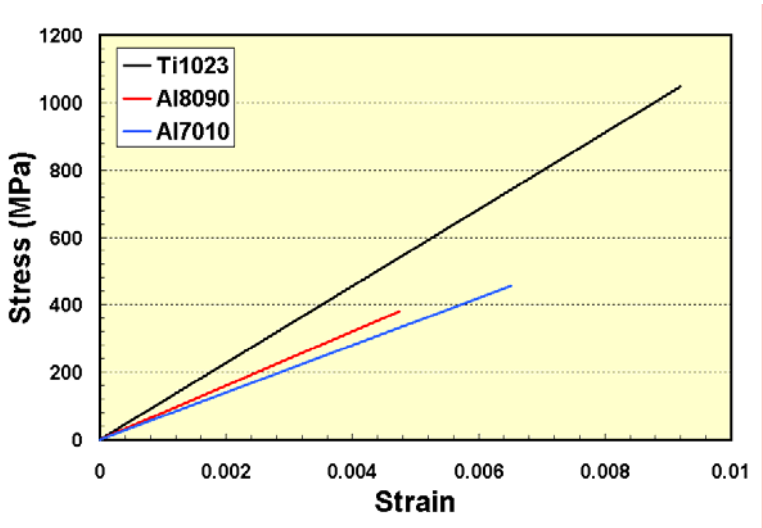

Figure 9.2_ The linear elastic region (Hooke's area) for Ti1023, Al8090 and Al7010. The lines are drawn up to the yielding stress σ_{YS}.

9.4 Threshold Stress Intensity Range Factors

The threshold stress intensity range factors ΔK_{th} measurement are plotted in figure 9.3 to 5 in terms of the final R ratio for each material. The plots have been supported with extra points from ref. [86, 146, 147]. The values measured in this

study are remarkably similar with those reported in ref. [86, 146, 147] for all three material alloys.

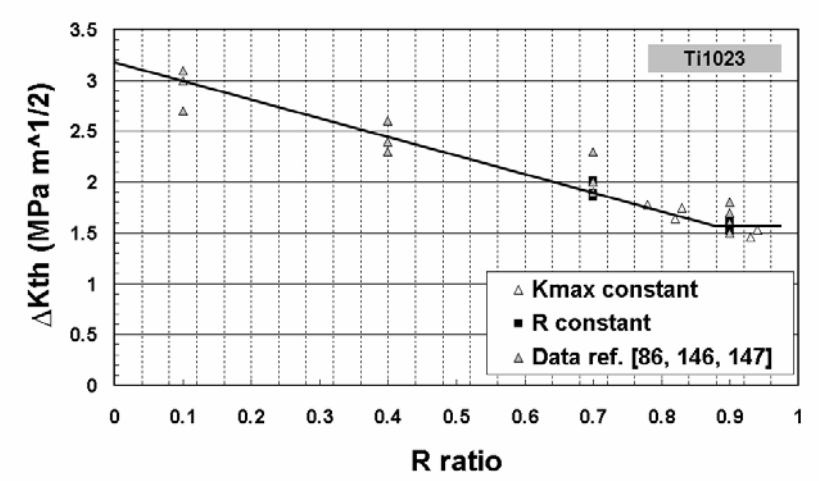

Figure 9.3_ Threshold values of ΔK using R and K_{max} constant techniques on Ti1023 plotted versus R. Literature data on the same material have been added.

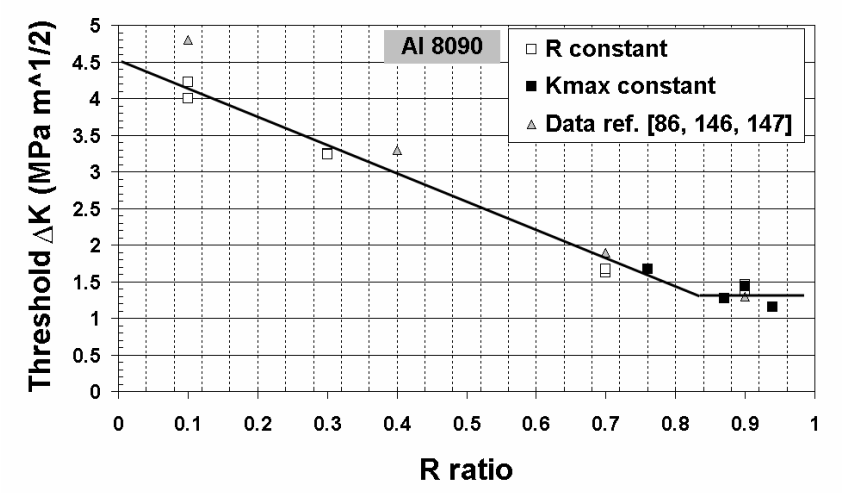

Figure 9.4_ Threshold values of ΔK using R and K_{max} constant techniques on Al8090 plotted versus R. Literature data on the same material have been added.

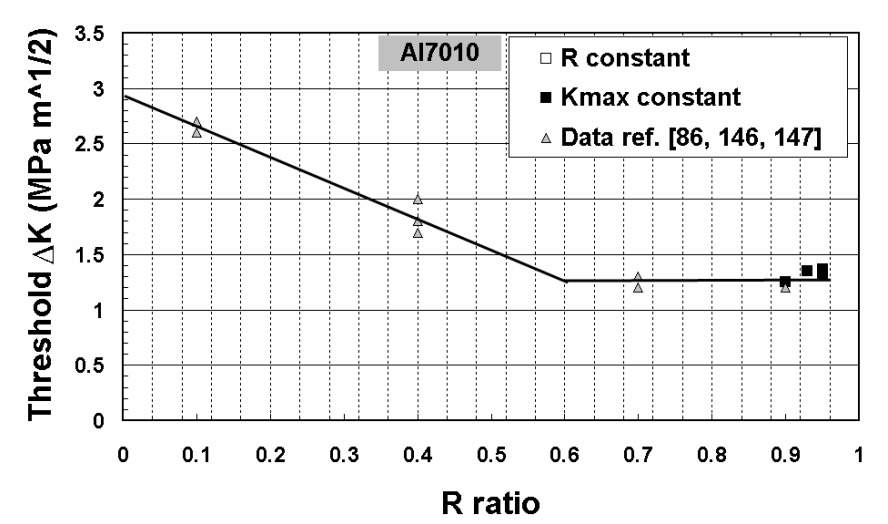

Figure 9.5_ Threshold values of ΔK using K_{max} constant techniques on Al7010 plotted versus R. Literature data on the same material have been added.

The series of tests confirm the general material trend that lower values of threshold occur at higher R [17]. The trend of ΔK_{th} in terms of R ratio seems to be a linear reduction up to around the R ratio value of 0.88 for the Ti1023. From that point and on, further increase of the R ratio do not reduce the value of ΔK_{th}. The sign of a plateau is observed in the threshold behaviour at the high R ratio region in the figure 9.3.

The same observations can be concluded for both Al8090 and Al7010. For Al8090, the linear reduction of ΔK_{th} is up to around the R ratio value of 0.83. From that point and on, further increases of the R ratio do not reduce the value of ΔK_{th}. The sign of a plateau is again obvious in the threshold behaviour of the material at the high R loading ratio region (figure 9.4). For Al7010, the linear reduction of ΔK_{th} is up to around the R ratio value of 0.6. From that point and on, further increase of the R ratio do not reduce the value of ΔK_{th}. The plateau exists in the threshold behaviour of the Al7010 at the high R loading ratio region as well (figure 9.5).

The R ratio and K_{max} constant techniques for the determination of threshold ΔK_{th} do not seem to end up in significantly different test results for all three materials. The threshold measurements form one individual curve, independent of the technique used for their determination. The R ratio constant technique can determine values of threshold ΔK_{th} at the overall range of R ratio. Although, testing at high R ratio demands the starting ΔK be very low. The problem is that starting

from low ΔK the crack is not allowed to propagate long enough until the establishment of threshold, crack growth rates is possible to contain load interaction effects from the previous fatigue loading history, and the crack growth rates da/dN may not smoothly and successfully approach the threshold ΔK_{th}. The K_{max} constant technique mainly results values of ΔK_{th} at a high R ratio, even when the applied K_{max} is relatively low.

Threshold values are also plotted in terms of the maximum stress intensity factor at the establishment of the threshold, $K_{max,th}$. The plots are shown in figure 9.6 to 8 for the three alloys. This representation of the data helps to establish the ΔK_T and $K_{max,T}$ values, and to the understanding of the interpretation between the K_{max} and the ΔK factor in the fatigue crack growth.

On Ti1023, the test results form a straight line parallel to the $K_{max,th}$ axis at ΔK_{th}=1.57 MPa $m^{1/2}$. The threshold value of ΔK appears to be constant in this region. This value is the ΔK_T. The test shows at the low R ratio form an almost straight line parallel to the ΔK_{th} axis. All these values correspond to the same $K_{max,th}$ value, which is the $K_{max,T}$. The values of ΔK_T and $K_{max,T}$ for Ti1023 can be abstracted from figure 9.6 and it is 1.57 and 3.3 MPa $m^{1/2}$, respectively. ΔK_T and $K_{max,T}$ can be considered as the two limits below which crack growth will not occur. In the midrange of the plot, there is a large concave curvature in the curve. The large curvature is indicative of the interaction between K_{max} and ΔK in this area of the fatigue crack growth.

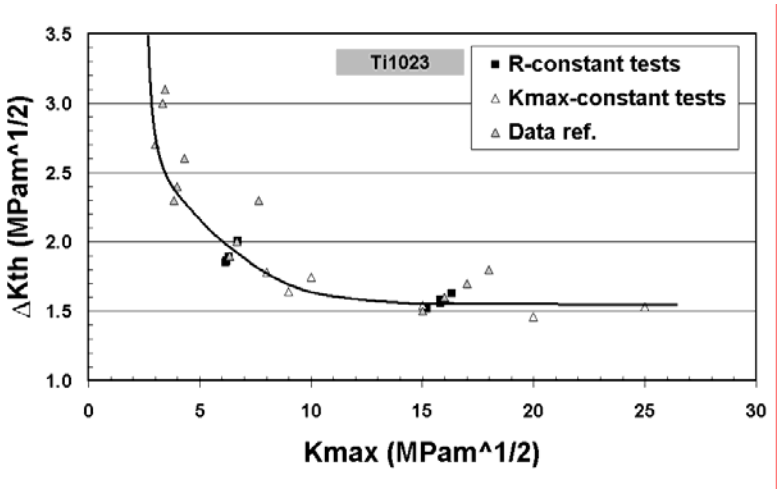

Figure 9.6_ Threshold values of ΔK using R and K_{max} constant techniques on Ti1023 plotted versus K_{max}. Literature data on the same material have been added.

A similar shape curve shown in figure 9.7 is formed for Al8090. The test results are in a straight line parallel to the $K_{max,th}$ axis at ΔK_{th}=1.4 MPa $m^{1/2}$ and parallel to the ΔK_{th} axis at $K_{max,th}$=5 MPa $m^{1/2}$. Hence, the values of ΔK_T and $K_{max,T}$ for Al8090 are established from figure 9.7 and they are 1.4 and 5 MPa $m^{1/2}$, respectively. In the midrange, there is a noticeable curvature in the curve, although the to crack propagation limits are well defined. The curvature suggests that on Al8090, the interaction between K_{max} and ΔK is limited to a smaller area of the fatigue crack growth.

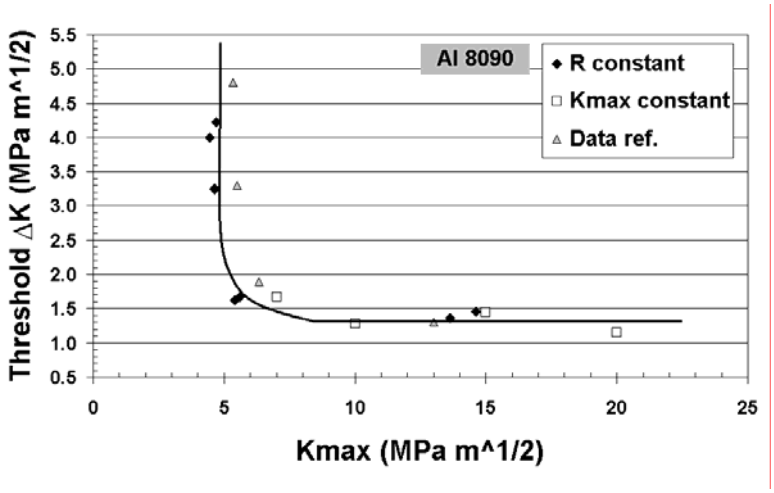

Figure 9.7_ Threshold values of ΔK using R and K_{max} constant techniques on Al8090 plotted versus K_{max}. Literature data on the same material have been added.

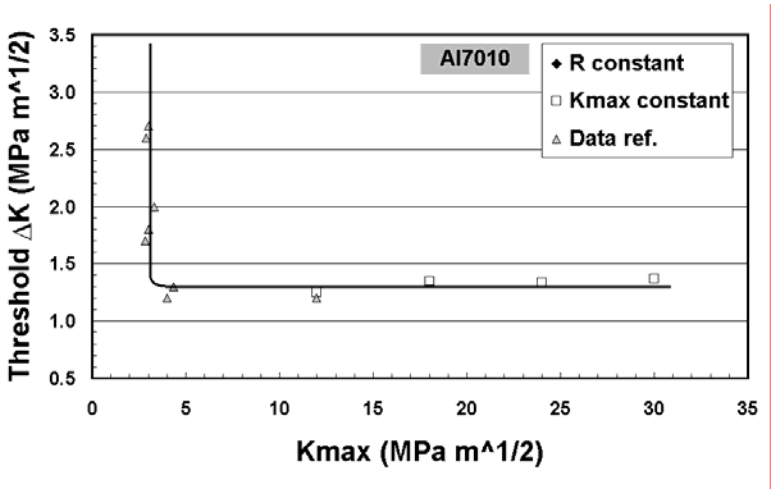

Figure 9.8_ Threshold values of ΔK using K_{max} constant techniques on Al7010 plotted versus K_{max}. Literature data on the same material have been added.

Threshold values are also plotted in terms of the $K_{max,th}$ for A7010. The plot is shown in figure 9.8. The values of ΔK_T and $K_{max,T}$ are established at 1.25 and 3 MPa

$m^{1/2}$, respectively. Al7010 presents an almost perfect L-shape curve, with very well defined crack propagation limits.

Table 9.1_ Details on the Intrinsic Threshold Loading Levels of the three alloys

	Ti1023	Al8090	Al7010
ΔK_T (MPa $m^{1/2}$)	1.57	1.4	1.25
$K_{max,T}$ (MPa $m^{1/2}$)	3.3	5	3
R_T	0.88	0.83	0.6
Band of K_{max} where the curvature in the ΔK_{th} and K_{max} exists (MPa $m^{1/2}$)	3.3 – 14	5 – 8.9	-

ΔK_{th} vs. K_{max} plot shows that K_{max} constant method determines the lower part of the curve. At the limit of K_{max}, $K_{max,T}$, the technique can not determine the larger values of ΔK_{th}. The ΔK_T value is considered the value of ΔK_{th} in which the effect of crack closure is eliminated, since its R ratio is very high. Remaining at the area of low K_{max}, larger values of ΔK_{th} occur when the final R ratio becomes lower. These values are parallel to the ΔK_{th} axis (y axis) and they are determined mainly by the R constant technique. This observation can be attributed to the gradual development of crack closure as the R ratio decreases. Closure causes the premature stop of the crack propagation at a ΔK_{th} larger than ΔK_T because of the reduction of R ratio. The effect of the residual stresses ahead of the crack tip should remain the same since no change in K_{max} occurs, and therefore limited in respect with the change of ΔK_{th} value. Hence, the higher values of ΔK_{th} at low R ratios are the result of the path that the load approaches the threshold. The loading path is defined by the testing technique for the determination of threshold.

The effect of crack closure on the determination of ΔK_{th} is supported from simple observation of low magnification fracture surfaces. The fracture surfaces are rough and intensively deformed when ΔK_{th} are large and R ratios low in contrast with the smoother surface produced by small ΔK_{th} at high R ratios. Figure 8.5 shows the produced surfaces on Al8090 from the test 1A801th1 (constant R=0.1). The difference in the surface roughness produced by the near-threshold fatigue is obvious. Figure 9.9 shows the test 1Ti10th, which was conducted at K_{max} constant 10 MPa $m^{1/2}$. The starting R was 0.1 and the ending 0.83. It is clear that as the R ratio increased during the test the plastic deformation of the crack wake indicated by the smooth peaks and valleys on the pictures reduces. Hence, the crack closure is gradually eliminated. The fracture surfaces are not sharp and hence roughness-induced closure should have a less important role in the crack propagation. Similar

fracture surface with intensive plastic deformations occurred from the rest of the K-decreasing tests on Ti1023. These facts point out that closure mechanism significantly affects determination of ΔK_{th} and further more the fatigue crack growth.

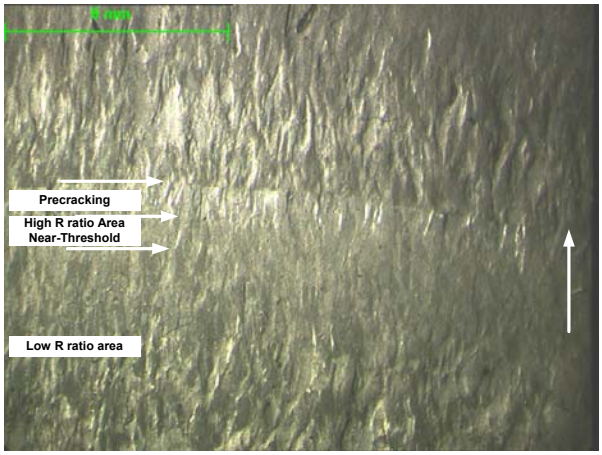

Figure 9.9_ Ti1023 fracture surface produced from test 1Ti10th (threshold test at $R_{initial}$=0.1, K_{max}=10 MPa $m^{1/2}$) and from a precracking procedure ΔK=7 MPa $m^{1/2}$ R=0.3. The growth direction is from the bottom to the top.

There is an extensive research on the investigation of the fatigue crack growth in terms of the two parameters ΔK_{th} and $K_{max,th}$. Vasudevan and Sadananda were the first ones that examined the fatigue phenomenon in terms of these two criteria [44, 22, 24]. They stated that both K_{max} and ΔK must exceed certain critical values $K_{max,T}$ and ΔK_T for a crack to propagate. The two criteria have to be met simultaneously. They suggest that the ΔK_{th} varies uniquely with K_{max}, independent of the test method. Their suggestion is proven correct by the test results of this study. The results indicate that the threshold parameters $K_{max,T}$ and ΔK_T are material properties that are intrinsically related to fatigue mechanism. Also, the data indicates that the two critical thresholds can be obtained from any set of experiments as long as the tests are both high and low R values.

The curvature in the ΔK_{th} and K_{max} suggests that the two critical K_{max} and ΔK_{th} that must be satisfied simultaneously must have synergistic interactions, although in each R regime, one or the other is controlling the crack growth rates [139]. This is supported by the observation of the measured crack growth rates during the K_{max} constant tests on the three materials. On Ti1023, the tests conducted at K_{max}>14 MPa $m^{1/2}$ produce the same crack growth rate curve. At K_{max}<14 MPa m1/2 the fatigue tests form a different curve as a result of the simultaneous effect of the K_{max}

and ΔK_{th}. The effects are mirrored in the ΔK_{th} vs. K_{max} plot with the curvature. On Al8090, only the test at K_{max}=7MPa $m^{1/2}$ has different crack growth rates. This K_{max} value is close to the $K_{max,T}$ and therefore the curvature is small. On Al7010, all the crack growth rates form one curve. Although the values of K_{max} are much higher that the K_{maxT}. The additional measurements show that the curvature is extremely small.

Newman recognizes the dependence of the near-threshold fatigue crack growth on both ΔK and K_{max} [72]. In his tests at different K_{max} levels on three different aluminium alloys, among them Al8090, he observed faster crack growth rates above a certain level of K_{max}. The level was different for each material. Based on fractographic observation, he concluded that increasing levels of K_{max} cause increasing levels of crack-tip process zone damage. The interaction between K_{max} and crack-tip zone damage, expressed by the ΔK, is revealed by the curvature in the ΔK_{th} and K_{max} plot. Above a certain limit of K_{max}, the crack-tip process zone damage reaches a maximum. That is the point where the curve becomes parallel to the K_{max} axis in the plot and the ΔK reaches the limit ΔK_T .

9.5 Effect of Underloads on the Thresholds

The objective of this set of tests was to examine the effect that a number of large underload cycles will cause to the established value of threshold stress intensity factor ΔK_{th}. It has been suggested that the presence of large underload cycles can alter the behaviour of the threshold loading cycles in a way that small cycles become more damaging [84].

The crack growth rates after the application of underloads found to be very close or below the threshold limit of 10^{-10} m/cycle. Increasing the number of underload cycles seems to have little systematic effect on threshold value of ΔK. The effects of up to 50 underload cycles are considered not to be significant, taking into account the range of measured threshold value crack growth rates in R constant threshold tests prior to the underloads.

The test showed that the underload cycles do not affect the action of the small cycles at high R ratio, in this case 0.7 and 0.9. These observations are in line with the work of Topper et al. about the effects of tension-compression cycles on

the crack closure of the following cycles at smaller amplitude and high R ratio [97]. Figure 9.10 and 9.11 show the measurements of crack opening closure during small cycles at R of 0.8 and 0.5 after the application of an underload. In the case of R=0.8 cycles, the crack opening point does not reach the minimum load during the cycle. In the case of R=0.5 cycles, the crack opening point is below the minimum load during the first few cycles (fully effective cycles) and then builds up to a high level between the maximum and minimum loads of the small cycle.

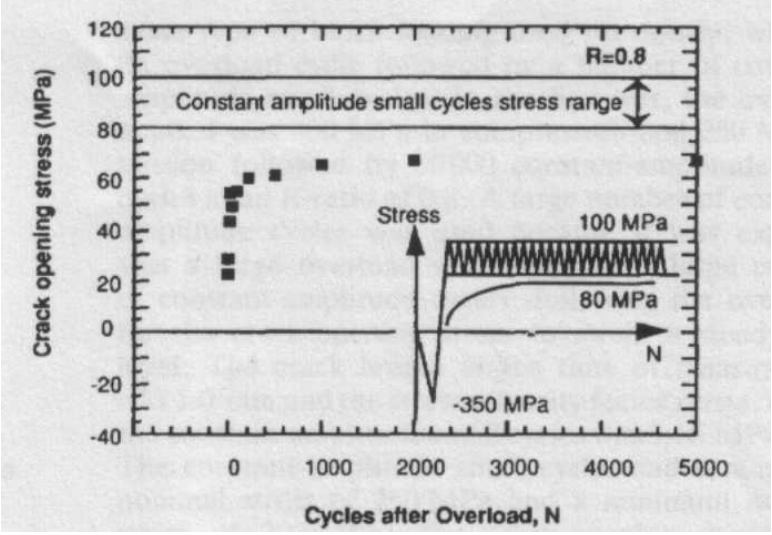

Figure 9.10_ Crack opening stress build up measurements for R=0.8 [97]

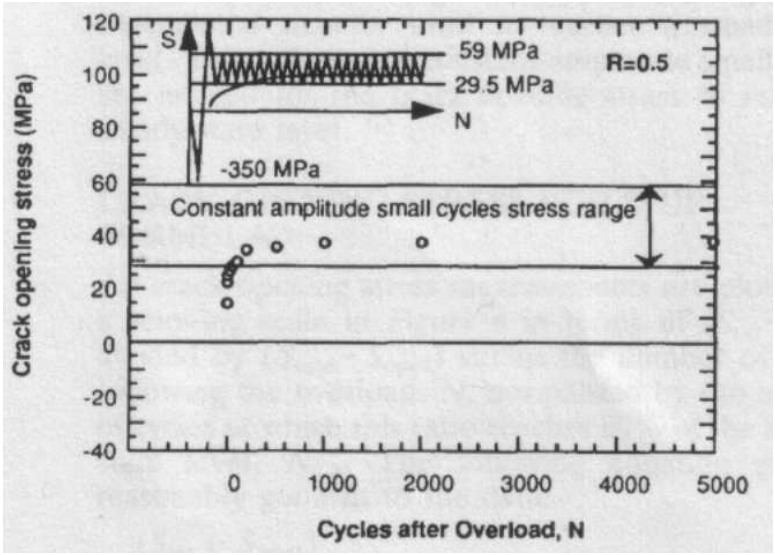

Figure 9.11_ Crack opening stress build up measurements for R=0.5 [97]

9.6 Underload Testing - SVAL

The results show that cracks under variable amplitude loading can grow faster than the linear summation life prediction, when they are subjected to small amplitude cycles at high R ratio and large amplitude cycles at low R ratio or underloads. The acceleration effects have different values depending on the number n of the small cycles, the K_{max}, and the R ratio of the small and the underload cycle. The effect of each of these loading factors has a different effect on different material as was shown by the experiment.

It is unlikely that these results are a consequence of errors in constant amplitude data. Figure 7.5 and 7.7 shows excellent agreement of curve fits with the growth rate data points for the Ti1023 and Al7010. When the Al8090 CAL data (figure 7.6) used to calculate the crack growth increment of an underload sequence using linear summation of the growth rates of individual cycles, it will play a major role in causing variability of the acceleration factor α. Considering the large number of tests and the consistency in the measured and calculated data in all three materials, the observation of changes in acceleration factors suggests that these effects are a consequence of load interaction between low and high R cycles.

These results confirm previous reported underload effects by a number of workers [85, 96, 148]. Acceleration effects reported by Fleck [85] under very different load conditions and different materials than those used in the present work reveal a similar curve to figure 8.29 with a maximum at 10 minor cycles per underload. The acceleration factor was 1.8, considerably less than that reported for Al8090, although similar to the factors reported on high strength titanium 10-2-3. However, reference [148] has reported acceleration factors expressed in terms of crack growth increment of up to 100. Expressed in terms of crack increment, the present results have a maximum acceleration factor of 14, rather than 10.

The discrepancies in the acceleration factors in the literature emphasise the significance of data representation in reporting acceleration effects. Results can be presented as (a) a ratio of growth rates, (b) a ratio of crack increments, or (c) a ratio of cycles to produce a defined increment. In the present study, acceleration factors β, and γ have very similar values to the factor α and they follow the same paths in terms of the loading variables for each material.

9.6.1 Ti1023

The tests on Ti1023 revealed that the acceleration factor, which indicates the differences in the crack growth rates between the SVAL sequence and the CAL linear sum, is constant around the value 1.6 in relation with the number n of the small cycles. In other words, the crack grows 1.6 times faster than the CAL prediction when 1 threshold cycle follows 1 underload to zero load. The same acceleration is achieved when the number of the threshold cycles increases up to 1000 cycles. This shows that the interaction of the small and large cycle on Ti1023 is immediate and reaches its maximum in the first few small cycles. The application of more small cycles does not alter the effect on the crack growth. The limited crack opening data for test results under 1u/10n at Kmax=15.7 MPa $m^{1/2}$ shows that the value of closure is 0.29 K_{max}. Since the rest of the underload tests have the same K_{max} and very similar acceleration effects, it can be assessed that the closure of their underload cycles is around 0.3 K_{max}.

Under the application of the small cycles no crack growth occurs practically. Considering also that the applied load remains the same, the crack tip is under the same ΔK_n and R_n ratio. Hence, one could expect that no change occurs in the crack opening displacement. Measurements of the crack opening displacement suggest that a change in the maximum value of the crack displacement occurs as more small cycles are applied.

During the loading at this level, the reverse plastic zone size is 0.3% of the plastic zone size according to the Irwin relationship (equ. 3-6). It means that the area of the plastic zone that is constantly under tension is very large. It has also been established that the plastic zone is not located solely ahead of the crack tip but also is developed in a small distance behind the crack tip [140, 141, 16] as shown in figure 9.12. Hence, because the reverse plastic zone is very small, the area of the crack fracture surface that is constantly under tension is very large. The COD measurements suggests that the plastic deformation behind the crack tip changes, in our case it stretches the material in the loading direction (figure 9.13), under the action of the ΔK_{th} cycles on the stationary crack. This behaviour is unlikely to be attributed to change in the plastic deformation ahead of the crack tip and the crack growth because of the load characteristics of the small cycles.

A finite element model has been developed by Russ et al. to simulate the behaviour of the underload and the small high R ratio cycles in terms of the crack tip displacement and the occurring crack opening and closing loading point on Ti17 [101]. They have shown that under plane strain, two small cycles at R_n=0.7 have different maximum displacement when a large tension-tension underload is interspersed in between them. Figure 9.14 shows the analysed loading sequence and their experimental and FEA results. The difference in the displacement between point (a) and (b) is around 0.1 μm. This takes into account the effect on the displacement of both the underload cycle, which has produced a crack growth of 1μm, and of the first small cycle, which acts on a stationary crack.

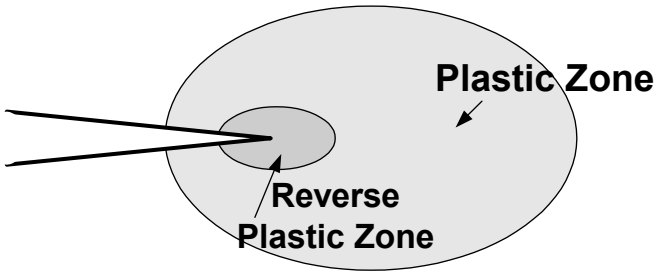

Figure 9.12_ The developed plastic and reverse plastic zone cyclic loading.

The above observation lead to the conclusion that the plasticized material behind the crack tip is stretched to the inner of the material due the tensile stresses within the plastic zone as shown in figure 9.14. This will result the crack surface to move apart. Hence, during the unloading to low R ratios, the crack surfaces will come into contact later than expected according to the CAL data. This procedure can take place in a small area behind the crack tip. Pippan et al. have shown that even a small area in contact, smaller than the size of the plastic zone, behind the crack tip is enough to significantly freeze the crack tip movement, to reduce the effectiveness of the externally applied loading cycle and therefore to shield the crack growth [35]. Their analysis was done using an elastic-plastic analysis under plane strain conditions. They have also shown that crack closure occurs under plane staine conditions and it is able to shield significantly the crack. As a consequence of the above, the action of the small high R ratio cycles will decrease the crack opening point of large low R cycles and the crack growth will be accelerated.

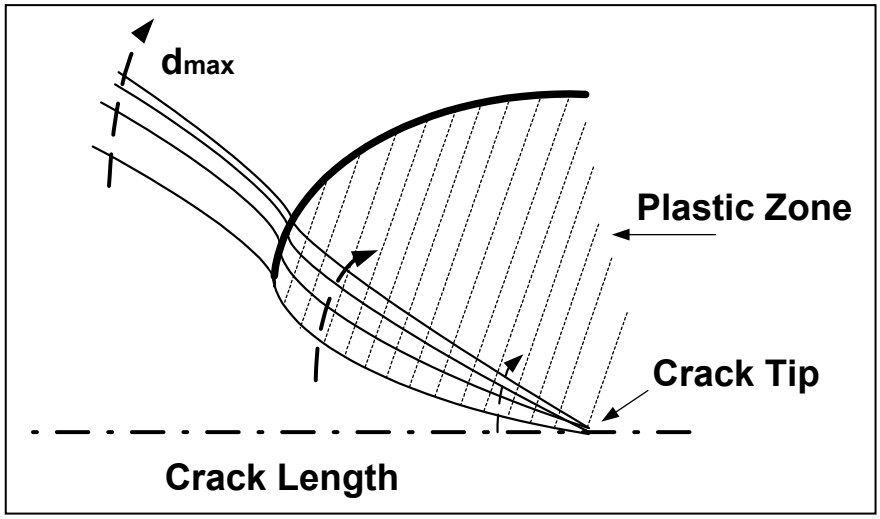

Figure 9.13_ Stretching of the plasticized material behind the crack tip under the action of high R ratio small cycles.

When K_{max} is the variable, acceleration values on Ti1023 are between 1 and 2 with a trend to increase as the K_{max} increases. The crack growth rates of the SVAL spectrum (figure 8.14) are very close to CAL data for low values of K_{max} and deviate as K_{max} increases. The crack closure levels of the underload cycles in the SVAL sequence is between 0.2 and 0.3 K_{max} for the whole range of the tested K_{max} (figure 8.17), significant lower than the CAL level. The reason for the changes in the acceleration factor with the K_{max} should be a variation of CAL crack closure levels in relation with the K_{max} level. The examination of the CAL data show that CAL closure values are around 0.33 K_{max} in the K_{max} range of 5 to 10 MPa $m^{1/2}$ and increase as K_{max} rises. This conclusion is in line with the observation that the crack propagation in the region of K_{max} between 3.3 and 14 MPa $m^{1/2}$ is controlled by both K_{max} and ΔK. Therefore, it is assessed that the CAL closure levels are between 0.3 and 0.4 K_{max} in this region of K_{max}.

The normalised d_m confirms the observation that the maximum displacement increases as the small cycles are applied. Figure 8.18 show that the maximum displacement becomes bigger as the K_{max} increases, although at K_{max} level higher than 15 MPa $m^{1/2}$ the effect seems to stabilise.

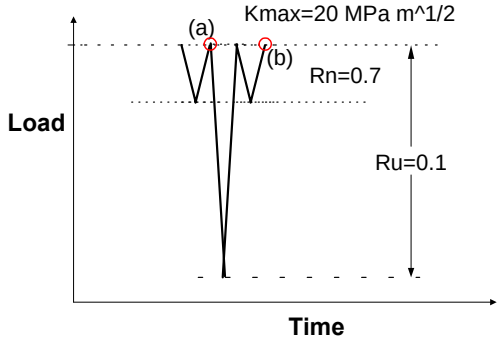

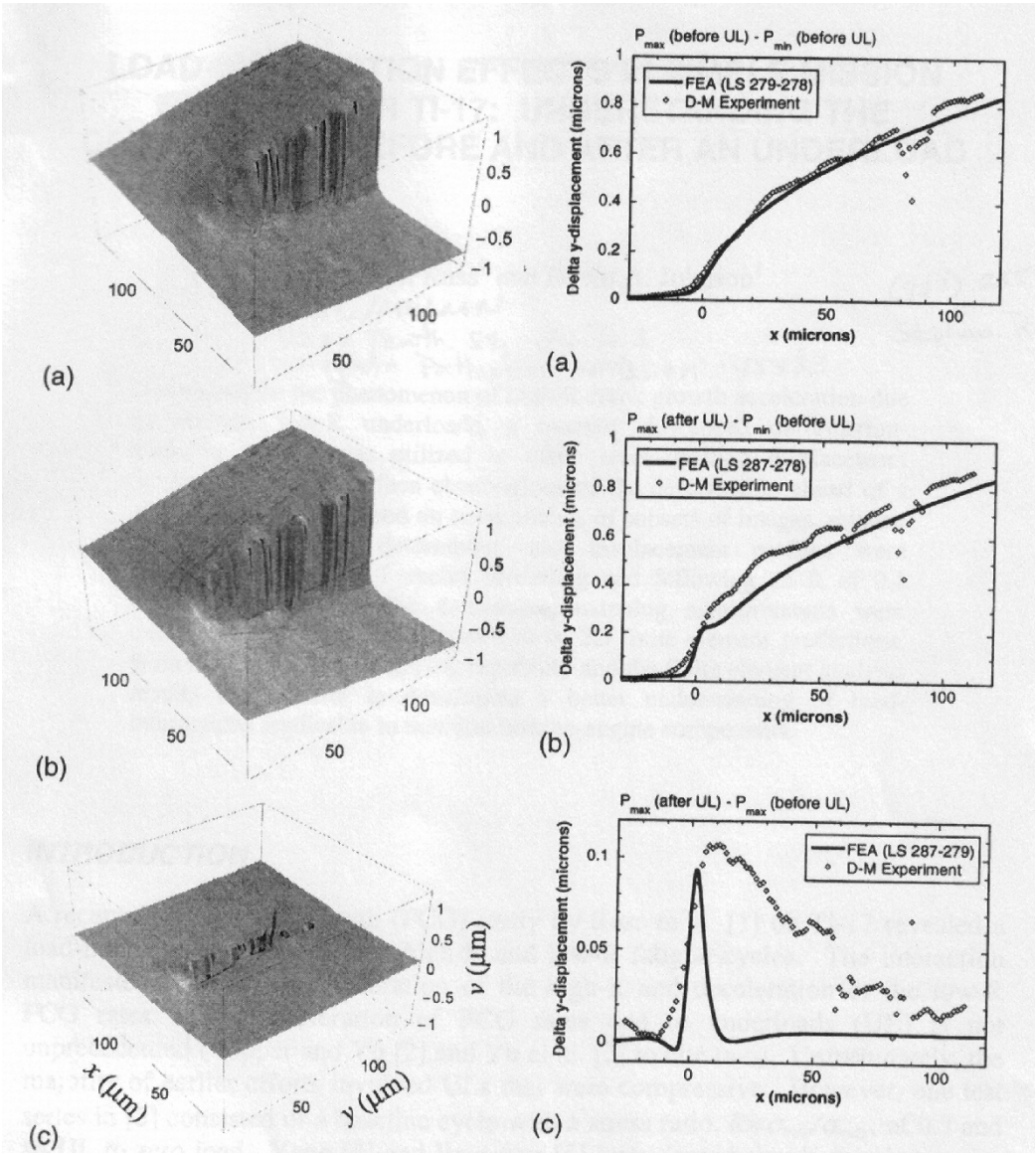

Figure 9.14_ The pictures in the left hand side column show the y-component of the displacement vector. The plots on the right hand side column give the comparison between FEA displacement results and deformation mapping measured in y-direction. (a) is for Pmax=20 MPa $m^{1/2}$ of the R=0.7 before the underload (point 1), (b) is for Pmax=20 MPa $m^{1/2}$ of the R=0.7 after the underload (point 2), and (c) the difference between the two [97]

The test conducted under the sequences with R_n=0.7 and K_{max}=6.86 MPa $m^{1/2}$ reveal no acceleration effects. Hence, it is expected that the underload cycles cause damage according to the CAL crack growth data. And as a result, the crack opening levels of these cycles are the same as the CAL level at R=0 and K_{max}~7 MPa $m^{1/2}$. Generally, it can be concluded that the rise of the K_{max} level change the crack growth mechanism in the Ti1023 and increases the acceleration effects on the crack growth.

The acceleration factor α is around 1.5 for the sequences containing underload cycles at the R_u ratio of 0 and close to 1 when underloads have R_u ratio of 0.5. Sequences containing underload cycles at R_u ratio of 0.3 exhibit a factor α of 2.6 (figure 8.20). This is a result of the larger deviation from the CAL crack growth rates, which decreases as the R_u ratio of the underload cycles increases (figure 8.19). The cause of this behaviour lies on the fact that changes of crack closure levels of the underload cycles in a SVAL sequence follow a different path than those of CAL cycles at the same R ratio (figure 9.15). The CAL closure data can be estimated, based on the experimental ΔK_{eff}. Hence, underloads in SVAL test become more rapidly close to full effectiveness. Underload cycles of R_u of 0.3 K_{max} exhibit closure levels of 0.35K_{max}.

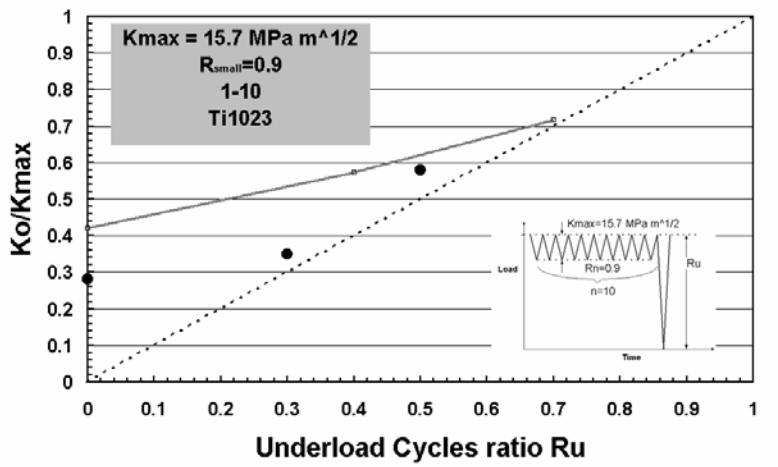

Figure 9.15_ The crack opening points for the underload SVAL spectra and CAL as a function of underload R_u ratio.

The measurements of normalised d_m on tests with R_u variable show that although the maximum displacement increases as the small cycles are applied the effect becomes smaller as the R_u rises. At low R_u ratios the effect are very similar. This is because the closure point is around 0.3 K_{max} in the sequence case where

R_u=0. Hence, any change in the K_{min} will have only a small effect on the crack growth rates, the surface deformation and the closure point, since the rest of the loading parameters remain the same.

The acceleration of crack growth rates of the SVAL sequences are between 1 and 2 and exhibit very small trend to increase as the R_n of the small cycles decreases (figure 8.25). It was found that the underload cycles have the same reduction in their crack closure independently of the R_n of the small cycles. So small cycles at 0.4 affect at the same degree the underload as the 0.9 cycles. Although, the decrease of closure in the underload is not adequate to explain the recorded acceleration in every case. It was shown that the small cycles at R=0.7 are fully effective and the cycles at R=0.4 are accelerated. Obviously, the underload cycles do change the closure level on the small cycles. The reduced crack closure of the underloads causes the following small cycles at R_n=0.4 and ΔK=9.42 MPa $m^{1/2}$ to become more effective and thus the SVAL sequence more damaging. This mechanism is shown in figures 9.10 and 11 and is extensively studied and reported in the literature [97].

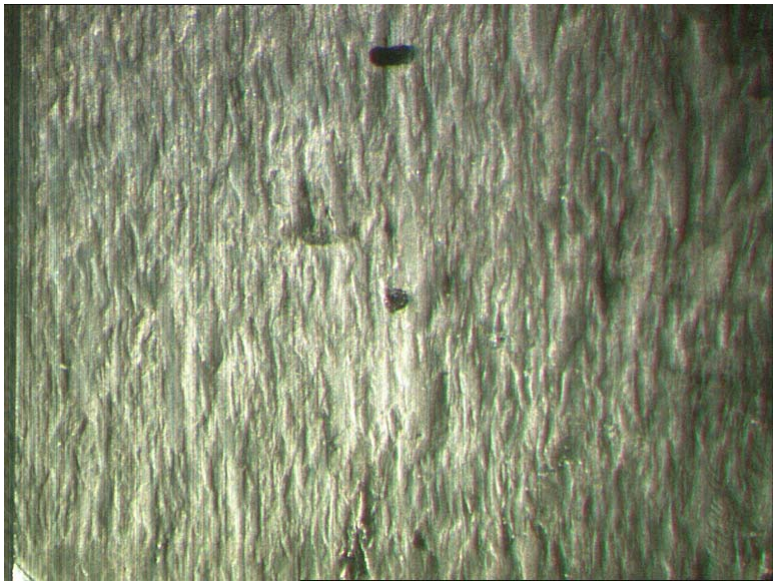

Figure 9.16_ Low magnification picture of the fracture surface of specimen 2cct25 showing crack length from 0.014 to ~0.031 m. The fracture surface is the result of five different test sequences and the CAL precracking. Crack growth is form the bottom to the top.

Low magnification fracture surface of a Ti1023 specimen is shown in pictures 9.16. The fracture surfaces are the result of various types of underload sequences. Figure 9.16 contains sequences with 1u/10n at various K_{max} R_u and R_n. Although the

surface are the result of difference underloading sequence their appearance is very similar. Intense plastic deformation is very obvious throughout the crack length, an indication of crack growth in the Paris regime.

9.6.1.1 Transient Effects Between SVAL and CAL on Ti1023

The transient effects between the CAL at R=0 and SVAL test with cycle sequence 1/10 at K_{max}=15.7 MPa $m^{1/2}$ were also recorded. The test results show that during the first part of the test, under CAL at R=0, closure builds up till the value of 0.4 K_{max}. During the application of the SVAL sequence, closure reduced to 0.28 K_{max} after 0.4mm of crack increment and remains to this level for the rest of the crack growth. The application of CAL causes the increase of crack closure again, but the full recovery to the CAL level is not achieved and the crack growth rates remain faster than the CAL rates. This suggests that the fatigue loading history plays an important role in the closure level and the effects of following cycles.

From the CAL and pre-cracking test results and based on the previous findings as well, it can be concluded that the small cycles change the effect of the closure behaviour of the first few underloads that follow but this effect is quickly vanished as more underload is applied.

9.6.2 Al7010

Low magnification fracture surfaces of Al7010 specimens are shown in pictures 9.17. The fracture surfaces are the result of various types of CAL and underload sequences. The loading type is indicated on the pictures. It can be easily observed that the fracture surfaces are smoother than those of Ti1023. Indication of plastic deformation can be seen. In contrast with Ti1023, a small degree of roughness has been developed on the surface. Although, the changes in the fracture roughness or plasticity with the applied sequence are not very clear. Careful observation shows that high roughness is produced by the sequences with the faster crack growth rates.

The acceleration factor on Al7010 α exhibits very low values at around 1.3 as the number of small cycles n varies from 1 to 100. The test scatter is relatively low.

The value of 1.3 is achieved from the first small cycle and this shows that the interaction of the small and large cycle on Al7010 is immediate and reaches its maximum very quickly. The application of more small cycles does not alter the effect on the crack growth. The crack opening data for test shows that the value of closure is 0.5 K_{max}. The very small difference in terms of the roughness and the plasticity between the CAL and the underloading SVAL surfaces (figure 9.17) confirm that the small acceleration effects are valid and that the cycles in the SVAL spectra behave as in CAL.

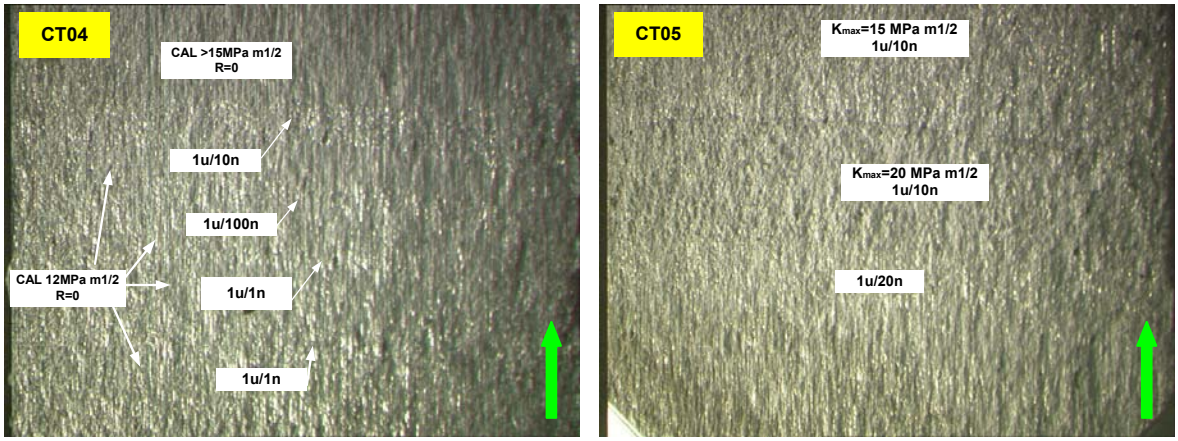

Figure 9.17_ Low magnification pictures of the fracture surface of Al7010 specimen. The fracture surfaces are the result of different types of SVAL sequences and the CAL. The crack growth is indicated by the green arrow.

The measurements of normalised d_m on the tests with the variable n show that although the maximum displacement increases as the small cycles are applied, its behaviour is not the same for every sequence. It can be observed that sequences with smaller n have a sharper and bigger change in the maximum crack mouth displacement. Although the amount of data and the scatter of the data introduce doubts about the validity of this observation. On Ti1023, it was shown that the d_m changes because of the changes in the crack tip plasticity. The introduction of a small degree of roughness is possible to affect the way that the small cycles affect the changes in the crack tip. So, even if the progressively more applied small cycles do not have an significant impact on the crack tip plastic deformation, they do have an effect on the crack growth, the fracture surface formation in terms of roughness, and finally the change of the maximum displacement and the closure level.

No significant acceleration effect was measured between small and underload cycles at higher level of K_{max}. Acceleration factors are vary close to 1 and the crack opening levels for these case very close to the CAL levels. The d_m behaviour is very similar when K_{max} ranges from 10 to 20 MPa $m^{1/2}$. Regardless the recorded changes in the crack tip plasticity, the closure levels do not change. Hence, it could be concluded that the crack closure is mainly affected by the surface roughness, since fractographic picture show that it remains almost unchanged with various applied CAL and SVAL sequences.

Test observations have lead to the conclusion that the driving mechanism of the crack closure and the fatigue crack growth has changed from the Ti1023 to Al7010. The aluminium alloy, which has different mechanical and microstructural properties, appears to be governed mainly by the roughness induced closure. The plasticity induced closure has a secondary role. The small changes in the fracture roughness between the CAL and SVAL sequences are the reason for the very low acceleration factors on this aluminium alloy.

9.6.3 Al8090

Low magnification fracture surfaces of Al8090 specimens are shown in figure 9.18. The fracture surfaces are the result of various types of CAL and underload sequences. The loading type is indicated on the pictures. It can be easily observed the change in the fracture roughness with the applied sequence and their relation with the corresponding crack growth rates. The roughness is indicated from the presence of dark and smooth areas on the surfaces, which are evidence of contact and rubbing between them. Less small cycles and higher K_{max} in a sequence produce faster crack growth rates and rougher surfaces. Intense plastic deformation in not obvious in the pictures, which reveals that plasticity-induced closure has a secondary role in the crack growth on Al8090. Studies on various aluminium alloys showed that Al8090 develops the highest surface roughness [136] and that is the case comparing the roughness on Al8090 with Al7010. It is worth noting some cases of asymmetric paths through the specimen thickness that the crack follows as propagates (figure 9.18). This observation has also been recorded from other independent studies on the Al8090 crack propagation [146]. The findings were attribute to the characteristic material's microstructure. In some

extent, the crack paths are responsible for the large scatter in the acceleration factors and the CAL crack growth rates.

The acceleration factor α on Al8090 forms a bell shape curve as the number of small cycles n varies from 1 to 1000. The peak value of the factor α is 9.4 and appears at n=10. When n=1, factor α is around 5 and in increases as the number of the small cycles n increases to the value of the 10. After the peak value, factor α decreases until it reaches it minimum value of 1 at n=1000. The test scatter is large, but the effect of the small cycles on the crack growth rates is clear. Factors β and γ exhibit the same bell shape curve with maximum value of 10 and 14 respectively, around n=10.

The acceleration behaviour of the crack growth on Al8090 is very different from that on Ti1023 and Al7010. In contrast with these materials, the effect of the small cycles is achieved around n=10 and then decreases again. The measurement of crack opening load has the same shape in terms of the n. This shows that the acceleration is related with the reduction of closure from the CAL level. The crack growth rates of the underload cycles as they have been determined in Chapter 9, show again the characteristic bell shape curve with the peak at n=10.

The measurements of normalised d_m on the tests with variable n show that although the maximum displacement increases as the small cycles are applied. But the amount of increase in not the same for every sequence. It can be observed that sequences with large acceleration factor have big change in the maximum crack mouth displacement. The sequences at 1u/40n and 1u/80n behave very similarly. On Ti1023 it was shown that the changes in d_m is manly the result of the changes in the crack tip plasticity and not of the surface roughness. This cannot be the case in Al8090 because the progressively more applied small cycles have an effect on the crack growth, the fracture surface formation in terms of roughness and plasticity, and finally the change of the maximum displacement.

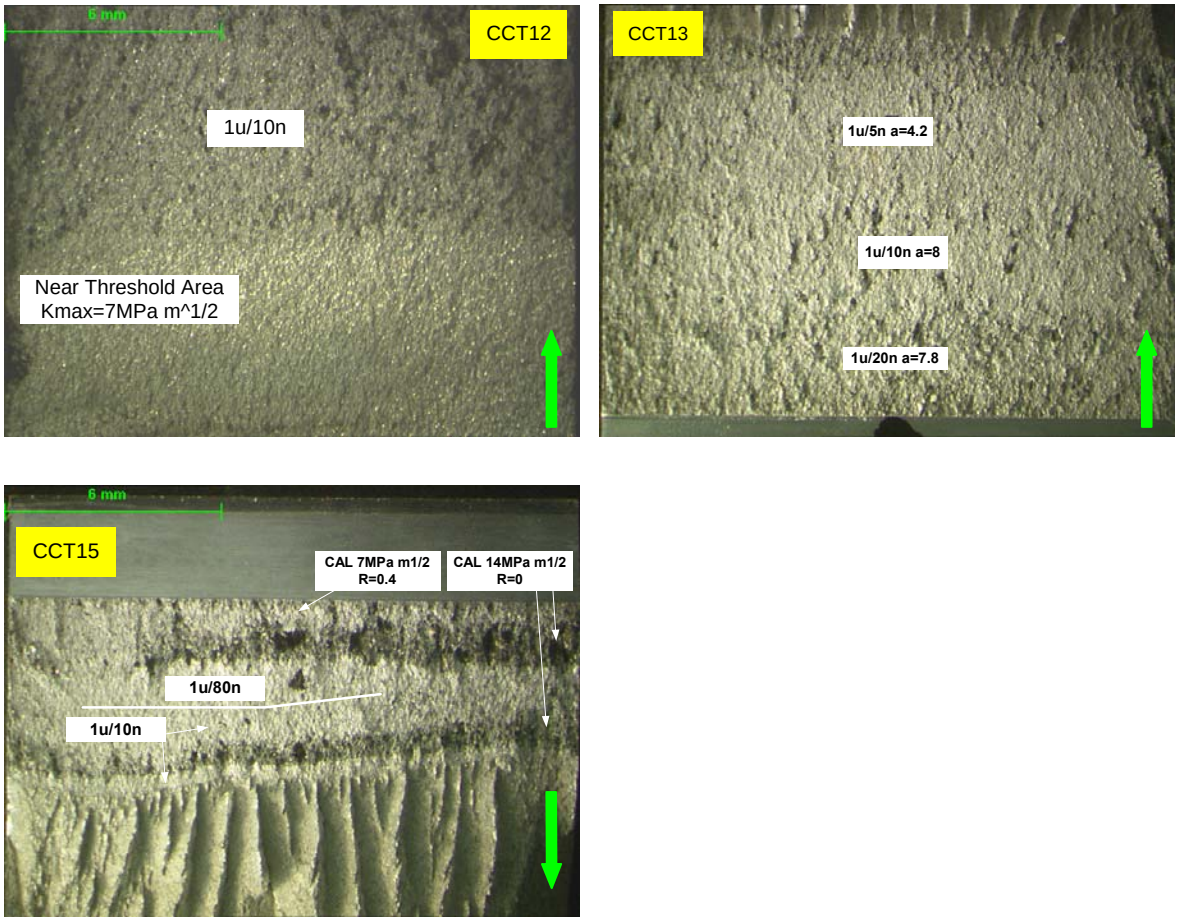

Figure 9.18_ Low magnification pictures of the fracture surface of Al8090 specimen. The fracture surfaces are the result of different types of SVAL sequences and the CAL. The crack growth is indicated by the green arrow.

The study of fracture surfaces produced by different SVAL sequences show that the crack surface is smoother as the underloads become more rare within the sequence (figures 9.18). Sequences containing 1 to 10 small cycles exhibit similar very rough surfaces. The form of the fracture surfaces is closely related to the crack growth rate of the crack as it has been shown in the section on thresholds (figure 8.5). Hence, the sequences with small number of n have very fast crack growth and high surface roughness. The signs of the plastic deformation are limited. A simple comparison with Ti1023 fracture surfaces, which are highly plasticized, indicates the difference. This evidence together with d_m behaviour lead to the conclusion that on Al8090, the crack closure and changes of it are related with changes mainly in fracture roughness and secondly in plasticity of the crack wake. The significance of fracture roughness in the crack closure has been recognized and its effects in it have been studied [148, 149, 99]. Their research point out that, because of its microstructure, the Al8090 behaves as a multi-layer structure with relative lower

strength in the grain boundaries compared to that of the matrix. This behaviour leads to the distinct surface characteristics.

Although, the surfaces produced by CAL at the same level of loading (K_{max}~14 MPa $m^{1/2}$, R=0) have high roughness comparing with the SVAL tests. This shows that the presents of the small cycles decreases the crack growth rates and so the surface roughness. As a result of that, the crack opening point will fall and the ΔK_{eff} of the cycle will rise. As the number of small cycles n increases towards 1000, their contribution to the damage that the sequence causes becomes dominant. According to the CAL data, in one sequence of 1u/1000n, the small cycles produce a crack growth of 1000x2.4 10^{-10} = 2.4 10^{-7} m, and the one underload 1x2.84 10^{-8} =2.84 10^{-8} m. In this case the small cycles produce damage around 10 times more that the underload and they are the main crack growth driver. Therefore the small cycles effect on the underload is limited.

Table 9.2 summarizes the effect of the number of small cycles on the closure level of the underload, the spectrum acceleration factor and the normalized d_m increment. The values can be used in order to correlate analytically the experimental observation.

Table 9.2_ Closure values, acceleration factors, and Δd_{mn} under the action of the small cycles.

No small cycles	1	5	10	20	100
K_0/K_{max}	0.54	0.48	0.34	0.34	~0.5
. α	4.75	5.5	8.5	7	1.5
Δd_{mn} (m/N)	-	2.5 10^{-7}	3.0 10^{-7}	1.5 10^{-7}	0.5 10^{-7}

As a conclusion, it could be stated that the progressively increase of the number of small cycles will dominate the crack propagation, and it will drive the acceleration factors back to unity and the crack growth to the CAL behaviour. The return of the crack growth to the CAL behaviour is a strong indication that the presence of the underload cycles within a sequence do not cause any kind of acceleration to high R ratio cycles. Although this conclusion has been made on Al8090, it can be applied to the cases of Ti1023 and Al7010. This conclusion is in line with the finding from the study of the crack growth behaviour on Ti1023.

When K_{max} is the variable, acceleration values on Al8090 increase from 3.5 to 14 as the K_{max} increases from 7 to 24 MPa $m^{1/2}$. The $(da/dN)_{sequ}$ reduces, as the K_{max} becomes lower. The trend of the $(da/dN)_{sequ}$ to approach the threshold value of

10^{-10} m/cycle at K_{max} = 5 MPa $m^{1/2}$, which is the intrinsic K_{max} threshold value, $K_{max,T}$ can be observed. The crack closure levels are lower than 0.5 K_{max}, with a trend to decrease as K_{max} increases. The results suggest that the action of underload takes place from low K_{max} values. Because of the fracture surface forms (figure 9.18) and the changes in the d_m behaviour in terms of the K_{max}, all the above observations with respect of the physical mechanism for the crack growth on Al8090 are valid.

The acceleration factor α is around 8.5 for the sequences containing underload cycles at the R_u ratio of 0 and 0.3, and close to 1 when underloads have R_u ratio of 0.5. This is a result of the large deviation of the experimental data from the CAL crack growth rates, which are decreasing as the R_u ratio of the underload cycles increases (figure 9.19). The CAL closure data can be estimated using the experimental findings. The underloads in SVAL test have significantly lower closure points, which become rapidly close to full effectiveness (R_u ~ 0.3). According to the CAL data and the experimental K_{eff}, the cycles should be fully effective at R ratio larger than 0.6.

The measurements of normalised d_m on tests with R_u variable show that although the maximum displacement increases as the small cycles are applied the effect becomes smaller as the R_u rises. At low R_u ratios the effect is very similar. This is because the closure point is higher than 0.3 K_{max} in the sequence case where R_u=0. Hence, any change in the K_{min} will have no effect on the crack growth rates, the surface roughness and the closure point, since the rest of the loading parameters remain the same.

The acceleration of crack growth rates under the SVAL sequences exhibit the same variation in terms of R_n as in Ti1023 (figure 8.42). Sequences with R_n 0.9 and 0.4 have higher acceleration than this with R_n at 0.7. The measurements of crack opening load showed that the crack closure of the underload cycles at R_n=0.4 sequence is at the CAL level (~0.65K_{max}) and decreases towards the value 0.35K_{max} as the R_n increases. At R_n=0.4 the underload is not accelerated. Hence, the sequence acceleration comes from the increase of the effectiveness of the small cycles due to the presence of the underload. The mechanism is well described by Topper et al. [97] and is shown in figures 11.10 and 11. The small cycles progressively affect the closure level of the underload as the R_n increases.

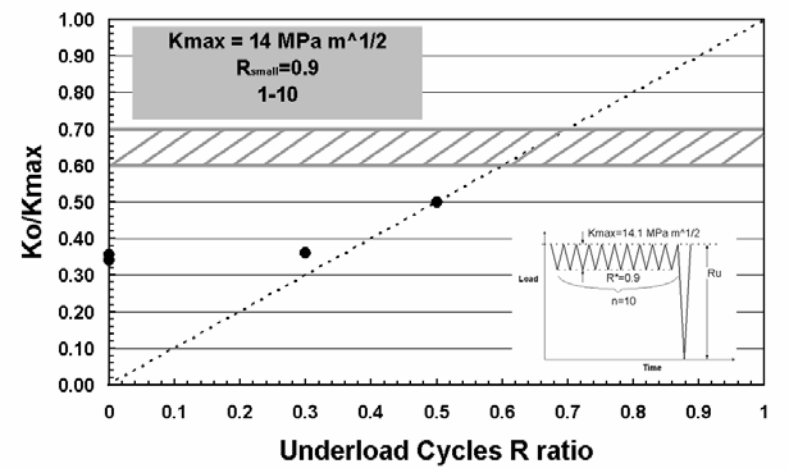

Figure 9.19_ The crack opening level for the underload SVAL spectra and CAL as a function of underload R_u ratio.

9.6.3.1 Transient Effects Between SVAL and CAL on Al8090

The transient effects between the CAL at R=0 and SVAL tests with cycle sequence 1/10 at K_{max}=14 MPa $m^{1/2}$ were also recorded. Figure 9.20 shows the variation of the crack closure values during each part of the test in terms of crack length. The test results show that during the first part of the test, under SVAL, the closure levels remain constantly low around 0.34 K_{max}. During the application of the CAL closure builds up to the CAL levels of 0.6-0.7K_{max}. This is achieved after 1 mm of crack growth, which is around 2 times the monotonic plastic zone under the applied K_{max}. The application of SVAL causes a very sharp reduction of closure. The crack closure reaches the minimum after crack growth of 0.025 mm, which is the size of half the plastic zone. This indicates that the effect of the small cycles on the underload cycles is immediate and related with both plasticity and roughness on the crack surface.

From the CAL and precracking test results and based on the previous findings as well, it can be concluded that the small cycles do change the closure behaviour of the first few underloads that follow but this effect is quickly vanished as more underload are applied.

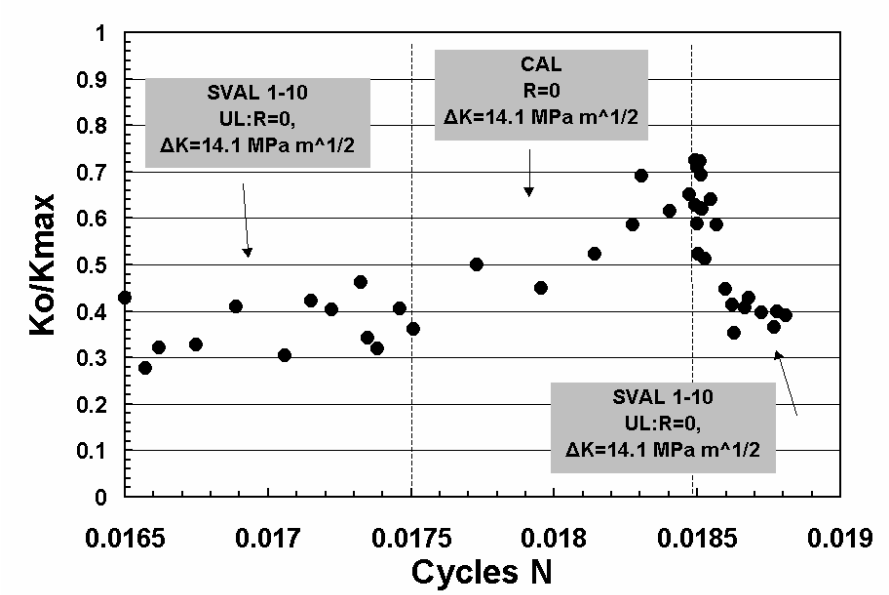

Figure 9.20_ The transient effect of the crack opening points between underloading SVAL and CAL test on Al8090.

9.7 CVAL Testing

The test results show that the cracks under the various versions of helicopter loading spectrum can grow faster than the linear summation life prediction. The acceleration effects have different values depending on the version of the Rotarix spectrum and the material. The effect of K_{max} of the Rotarix spectrum on the crack growth was not examined in this study. The underload sequence tests were simplified version of the helicopter spectra. Through the study of the fatigue crack growth under the SVAL together with the CVAL tests, a better understuding is gained on the CVAL spectra effects on the driving mechanism of crack growth.

The CVAL test results confirm previous reported effects by a number of workers [144]. The reported acceleration effects under the same load conditions and materials with those used in the present work reveal very similar results [84, 109]. The maximum acceleration on TI1023 was 2.6 under Rot16 and on Al7010 1.32 under Rot32. Ranganathan [145] has reported a 2.1 factor in the crack growth acceleration under an aircraft spectrum on Al8090. On Al2024 no acceleration was observed, showing that the acceleration effects depend on the material. Together

with the present results, they give confidence that the recorded effects are true and not an artifact.

The progressively elimination of the low amplitude cycles in the helicopter spectrum leads to shorter lives. That is expected since the fraction of the large amplitude in the applied spectrum increases. The Rot32 spectrum showed an acceleration of 1.31. The spectrum contains medium to low R ratio cycles. The study of crack growth rates (figure 8.61) shows that the acceleration comes from the initial stages of the test where the K_{max} level is close to 10 MPa $m^{1/2}$. Because small cycles do not exist in the Rot32 spectra, the acceleration comes from the transition of the crack opening point between low - high cycles. Newman has shown the closure transition and the increase of the effectiveness of some cycle under Rot32 spectrum for Al7010 using the FASTRAN model. The Rot16-24 spectra had no acceleration in the crack growth rates.

The observations under CVAL tests on Al7010 are consistence with the SVAL test results, where small accelerations were observed. Therefore, the underloading SVAL tests are a good representation of the helicopter spectra, as both the SVAL and CVAL have similar loading conditions, crack growth rates and acceleration factors. Hence, the fatigue driving mechanisms described for the Al7010 underload SVAL tests can be considered active under the Rotarix.

The effect of the different material on the crack growth under the most representative helicopter spectrum, Rot16, was examined. The ratio of medium to small cycles is around 1/10 and the ratio of large to small cycles is around 1/1000. It was found that the Ti1023 has the largest acceleration factor of 3.16 and the Al7010 the smallest at 1.04. On Al8090 the factor is 1.78.

Most of the SVAL underloading sequence have given factors lower than 2 on Ti1023. The combination of the SVAL tests 1u/10n with R_n=0.9 and R_u=0.3 with α=2.6, and 1u/1000n with R_n=0.9 and R_u=0 with α=1.6 is a good simplified version of the Rot16. Given the fact that the fact that K_{max} remain at a constant level during the tests because of the same crack growth, the fatigue crack growth mechanism of CVAL can estimated based on the analyzed driving mechanisms in the SVAL tests. Hence, it can be concluded that, the action of the small high R ratio cycles significantly affects the plasticity behind the crack tip and decreases the crack

opening point of the low and medium R ratio cycles. As a results the crack growth will accelerate under the Rot16 spectrum.

On Al8090, the underloading test gave a large range of acceleration factors, up to 12. Based on the SVAL tests 1u/10n with R_n=0.9 and R_u=0.3 with α=2.6, and 1u/1000n with R_n=0.9 and R_u=0 with α=1.6, and that the K_{max} remain at a constant level during the tests, the CVAL fatigue mechanism approached. The two SVAL tests exhibit different mechanisms. The reduction of roughness drives the acceleration factor to higher values and the crack growth at the threshold area produces no acceleration. Combination of these two opposite effects is possible to produce acceleration factors similar to the factor recorded in the Rot16 test.

On Al7010, the underloading tests are more limited but the results are clear and consistent showing factor lower than 2. The CVAL tests produced very similar factors with the SVAL tests. Hence, because of the similarities in the loading characteristics, the CVAL fatigue mechanism approached. It can be concluded that the Al7010 is governed mainly by the roughness induced closure and the plasticity induced closure has a secondary role. The changes in the fracture roughness could be the reason for the very low acceleration factors on the alloy under Rot16.

CHAPTER 10

INTEPRETATION OF FATIGUE CRACK GROWTH RATES WITH CRACK CLOSURE

10.1 Evaluation of the crack growth rates for the loading cycles in a sequence containing one underload cycle

The crack growth rate results of the test program on the three different alloys are interpreted in order to evaluate the ΔK_{eff} concept of crack growth. The crack growth rates of the underload are calculated and they are correlated with the respective crack closure measurements. The outcome of this analysis reveals whether or not a narrow ΔK_{eff} curve is formed from the SVAL and CAL test results. The analysis is carried out for each material.

During the underload testing on Ti1024, the value of ΔK_n has a maximum increase of 12% after 2 mm of crack when the test starting value of ΔK_n is 1.57 MPa $m^{1/2}$. According to the CAL data for the material, the corresponding growth will be in the range of the 10^{-10} to 4 10^{-10} m/cycle. The applied loading spectra contain a 10^4 to 10^6 small cycles. Therefore, it is expected that according to the CAL data, the fatigue damage caused by the small cycles will be smaller than 10^{-5} m for most of the cases. If the measured crack growth increment is taken into account (>1mm), the damage caused by the small cycles is only a very small fraction of the total growth. Even if the largest acceleration factor is considered (~3) to be applied on the small cycles (accelerated crack growth rates of the small cycles), their total damage remains a small percentage of the crack growth. Hence, it can be assumed that the fatigue damage is mainly caused by the action of the large underloads. The same hypothesis can be applied in the analysis of the crack growth rates for the Al8090 and Al7010 SVAL tests.

10.1.1 Ti1023

10.1.1.1 Effect of number of small cycles n

When the total crack growth is attributed to the underload action and the number of underload in the spectrum is taken into account, fatigue crack growth rate of the underload cycles can be calculated. The values of the crack growth rate of the underloads are presented in table A7 and they are plotted in terms of the number of small cycles in figure 10.1. In the same figure the region of CAL crack growth rates at the same loading level can also be seen. The fatigue crack growth

rates of the underloads are constantly above the respective CAL crack growth rates. Their values do not vary with respect to the number of small cycles in the sequence. The values of $(da/dN)_u$ is between 1.2 and 1.7 10^{-7} m/cycle and the respective CAL crack growth rates are around 9 10^{-8} m/cycle, depending on the exact ΔK value of the calculation. The effect on the $(da/dN)_u$ from the action of the small threshold cycles is immediate (n=1) and remains the same as the n increases to high values (n=1000).

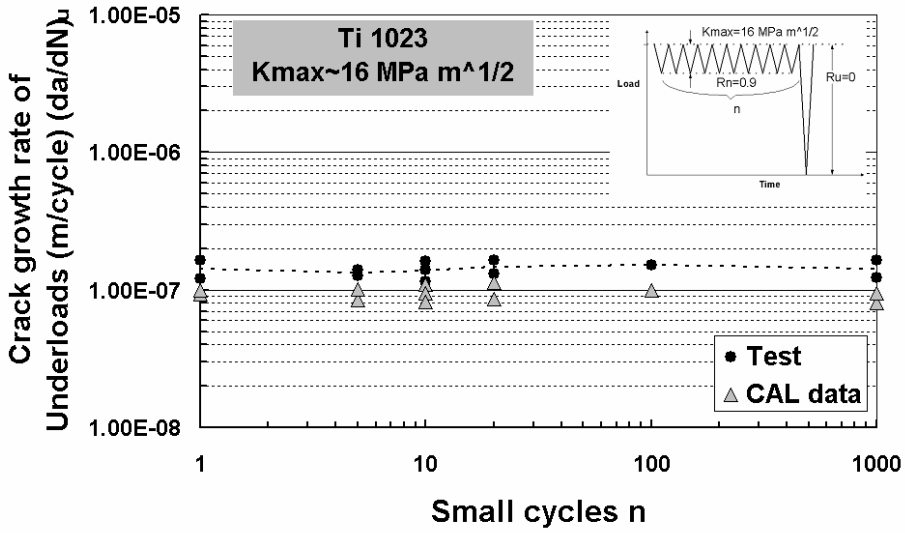

Figure 10.1_ The $(da/dN)_u$ and the CAL crack growth rates in terms of the number of the small cycles n on Ti1023.

10.1.1.2 Effect of K_{max}

Under the assumption that the fatigue damage is caused by the action of the large underloads and taking into account the number of underloads in the spectrum, the fatigue crack growth rate of the underload cycles was calculated. The values of the crack growth rate of the underloads are presented in table A7 and they are plotted in terms of K_{max} in figure 10.2. In the same figure the region of CAL crack growth rates at the same loading level can also be seen. The fatigue crack growth rates of the underloads are constantly above the respective CAL crack growth rates. SVAL crack growth rates are very close to CAL data for low values of K_{max} and deviate as K_{max} increases (figure 10.2).

It appears that when the applied K_{max} is high enough, in the present case larger than 15 MPa $m^{1/2}$, there is a clear difference between the SVAL and CAL

underload crack growth rates. The same does not apply when the K_{max} is low. The SVAL and CAL $(da/dN)_u$ tend to have the same value as K_{max} approaches the $K_{max,T}$ indicated by the dashed vertical line in figure 10.2. The same K_{max} area distinguishes accelerated and non-accelerated crack growth behaviour in the acceleration factor plot.

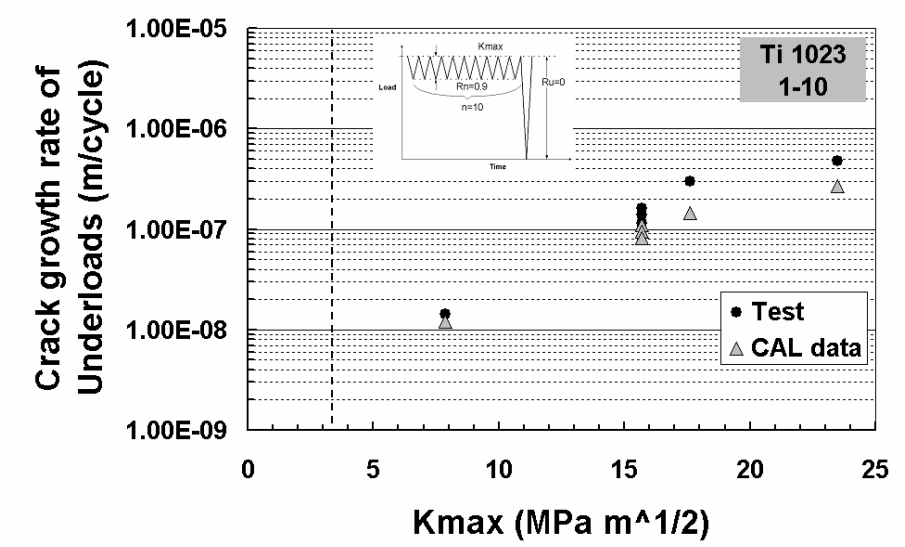

Figure 10.2_ The $(da/dN)_u$ and the CAL crack growth rates in terms of K_{max} level on Ti1023.

10.1.1.3 Effect of ratio of the underload cycles R_u

The values of the crack growth rate of the underloads are presented in table A7 and they are plotted in terms of R_u in figure 10.3. In the same figure the region of CAL crack growth rates of the same loading level can also be seen. The fatigue crack growth rates of the underloads are consistently above the respective CAL crack growth rates. It becomes clear that acceleration factor α is a result of the larger deviation of the $(da/dN)_u$ from the CAL crack growth rates, which are decreasing smoothly as the R_u ratio of the underload cycles increases. The decrease of SVAL $(da/dN)_u$ of the underload cycles declines more sharply that the CAL case after R_u = 0.3.

The CAL is influenced by the K_{max} and the R_u of the loading cycle, but in the case of the SVAL test, $(da/dN)_u$ is the result of the K_{max}, R_u and n. The additional effect of n alters the $(da/dN)_u$ from CAL behaviour.

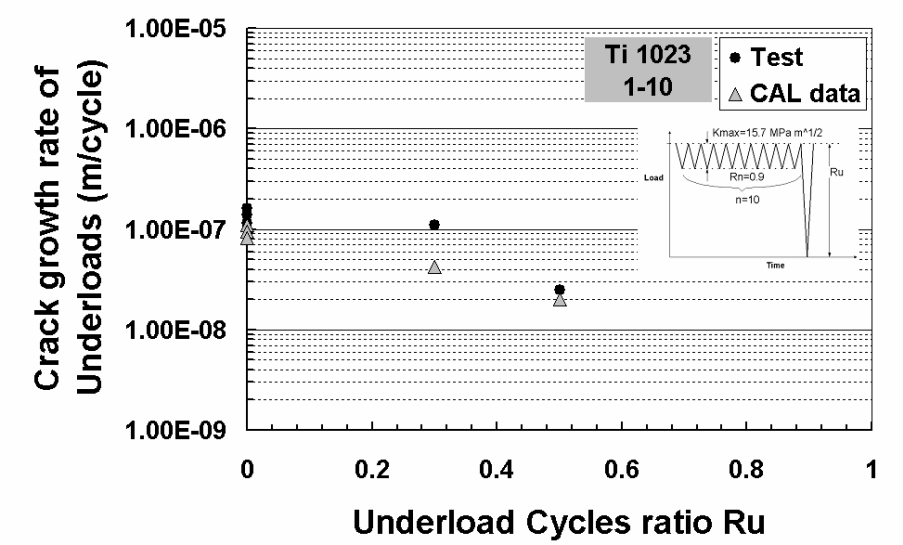

Figure 10.3_ The $(da/dN)_u$ and the CAL crack growth rates in terms of R_u ratio on Ti1023.

10.1.1.4 Effect of ratio of the underload cycles R_n

The assumption that the fatigue damage is caused by the action of the large underloads can be used only in the case of R_n = 0.9 where small cycles are at the threshold level. When R_n is lower than 0.9 and K_{max} is at 15.7 MPa $m^{1/2}$, small cycles cause fatigue damage that cannot be omitted.

In the two following tables 10.1, 10.2, it is examined whether or not the loading cycles in the SVAL sequences behave according to the CAL data. Table 10.1 presents the case that the underload cycles have CAL crack growth rates. The outcome is that the $(da/dN)_n$ is much faster than the CAL values. The measurements of the underload crack opening show that their values are lower than the CAL level. Hence, it is expected that the $(da/dN)_u$ will be accelerated in comparison with the CAL values. In the second case, the $(da/dN)_u$ are faster than the CAL values when the $(da/dN)_n$ was set according to the CAL data. The second case is closer to the reality. A more accurate estimation of the $(da/dN)_u$ can be achieved using the crack opening measurements in conjunction with previous findings.

Figure 8.33 shows that the closure level of the underload cycles are very similar and at 0.28-0.29 K_{max}. Therefore, they should have similar ΔK_{eff} and similar crack growth rates $(da/dN)_u$. Based on the crack opening measurements, $(da/dN)_u$ can be estimated. Figure 10.4 shows that the crack growth rates of the underload cycles plotted in terms of R_n have identical accelerated effect on the crack growth under every SVAL sequence. This is because of the same reduction of the crack closure of the underload cycles. In the same figure it can also seen the region of CAL crack growth rates of the same loading level. The values of the crack growth rate of the underloads are presented in table A7.

Table 10.1_ Crack growth rates of small and underload cycles when the underload cycles have CAL rates

R_n	n cycles/u cycles	Crack Increment (m)	$(da/dN)_n$ Result	CAL $(da/dN)_u$
0.7	4000/40000	0.0011	$1.93\ 10^{-8}$	$8.17\ 10^{-8}$
0.4	4000/40000	0.0028	$6.18\ 10^{-8}$	$8.17\ 10^{-8}$

Table 10.2_ Crack growth rates of small and underload cycles when the small cycles have CAL rates

R_n	n cycles/u cycles	Crack Increment (m)	CAL $(da/dN)_n$	$(da/dN)_u$ Result
0.7	4000/40000	0.0011	$6.98\ 10^{-9}$	$2.05\ 10^{-7}$
0.4	4000/40000	0.0028	$4.06\ 10^{-8}$	$2.94\ 10^{-7}$

Knowing the fatigue crack growth rates of the underloads, one can calculate the crack growth rates of the small cycles. For cycles at R_n = 0.7, da/dN = 7.0. 10^{-7} and for cycles at R_n = 0.4, da/dN = 5.48 10^{-8} m/cycle. These rates are higher than the CAL rates. The reduced crack closure of the underloads causes the following small cycles at R_n=0.4 and ΔK=9.42 MPa $m^{1/2}$ and at R_n=0.7 and ΔK=4.71 MPa $m^{1/2}$ to become more effective and thus the SVAL sequence more damaging. Hence, both underload and small cycles are accelerated compared with the CAL conditions.

It becomes clear that acceleration factor α is a result of the deviation from the CAL crack growth rates, of both underload and small cycles. It suggests that when the small cycles become damaging, their closure levels are affected by the presence of the underload cycles. The effect of the small cycles on the closure level of the underloads exists at the same time. Table A7 provides the crack closure levels and the crack growth rates of these tests.

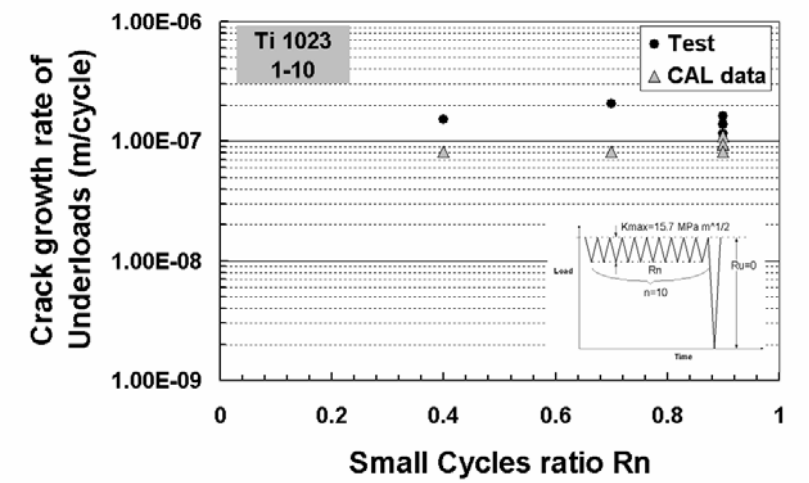

Figure 10.4_ The $(da/dN)_u$ and the CAL crack growth rates in terms of R_n ratio on Ti1023.

10.1.2 Al8090

10.1.2.1 Effect of number of small cycles n

The calculated values of the crack growth rate of the underloads are presented in table A8 and they are plotted in terms of the number of small cycles in figure 10.5. In the same figure the region of CAL crack growth rates of the same loading level can also be seen. Crack growth rate of underloads are increased even after 1 small cycle and reaches a peak value of 2.25 to 3 10^{-7} m/cycles. The rates approach the CAL rates as the number of small cycles n become bigger than 100. The CAL crack growth rates are independent of the number of the small cycles n and they fall into the same band around 2 10^{-8} m/cycle. These values are significantly lower than the calculated $(da/dN)_u$ with the exception of the value which corresponds to the n=1000.

10.1.2.2 Effect of K_{max}

The calculated values of the crack growth rate of the underloads are presented in table A8 and they are plotted in terms of the number of small cycles in figure 10.6. In the same figure the region of CAL crack growth rates of the same loading level can also be seen. Crack growth rates of the underload cycles plotted in

figure 10.6, are higher than the constant amplitude loading rates. The difference between SVAL and CAL $(da/dN)_u$ is getting smaller as the K_{max} is approaching the value $K_{max,T}$.

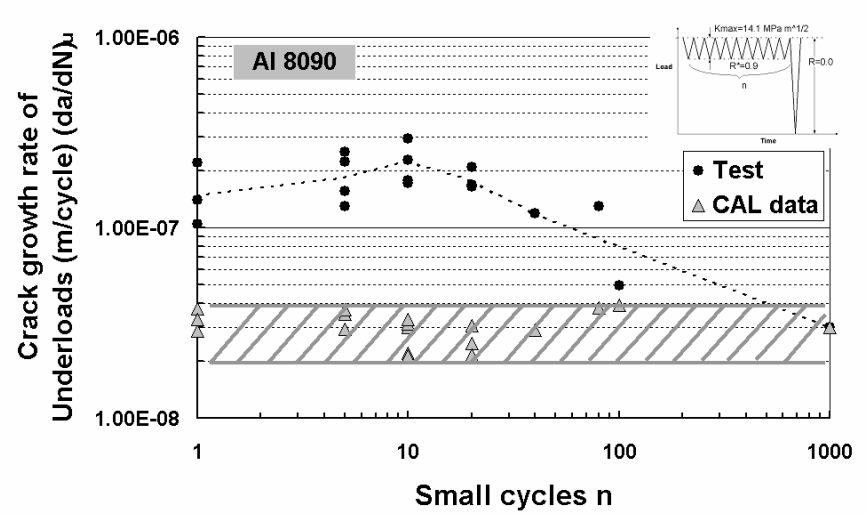

Figure 10.5_ The $(da/dN)_u$ and the CAL crack growth rates in terms of the number of the small cycles n on Al8090.

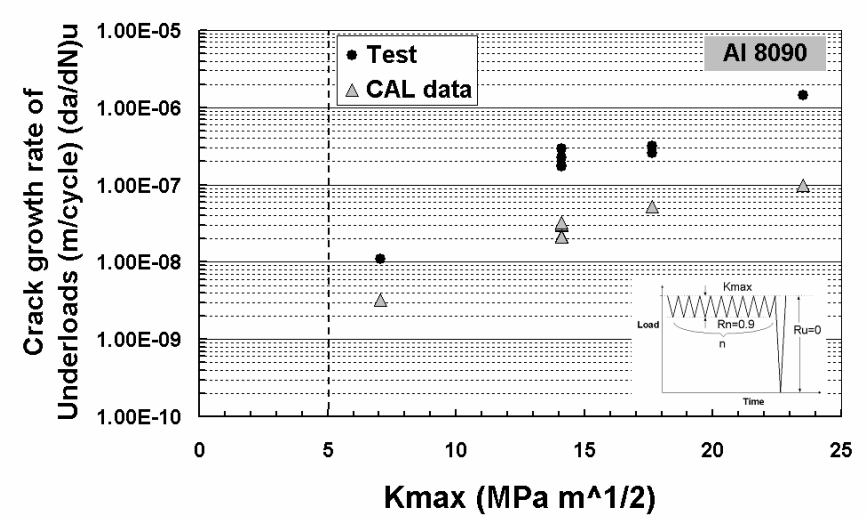

Figure 10.6_ The $(da/dN)_u$ and the CAL crack growth rates in terms of K_{max} level on Al8090.

10.1.2.3 Effect of ratio of the underload cycles R_u

The $(da/dN)_u$ are presented in table A8 and they are plotted in terms of R_u in figure 10.7. In the same figure the region of CAL crack growth rates of the same loading level can also be seen. At R_u= 0.5, $(da/dN)_u$ is still higher than the CAL

crack growth rate, but it is obvious that it approaches the CAL values faster as the R_u increases.

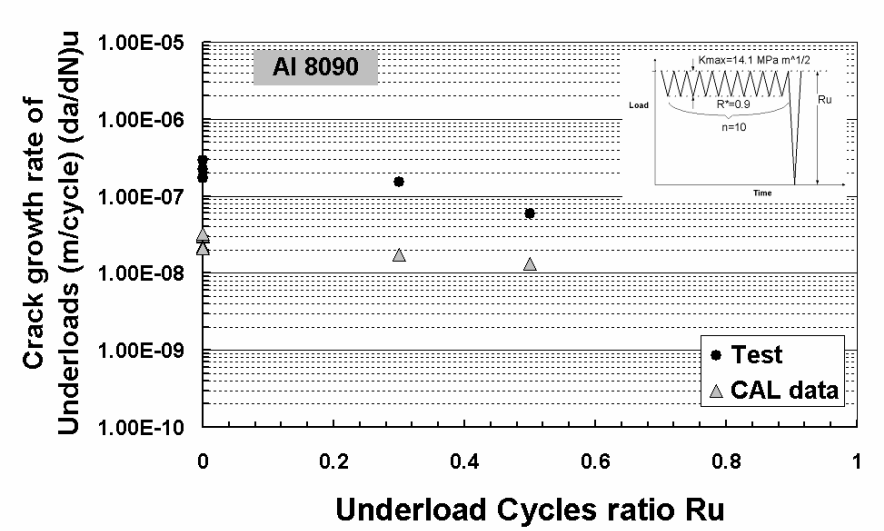

Figure 10.7_ The $(da/dN)_u$ and the CAL crack growth rates in terms of R_u ratio on Al8090.

10.1.2.4 Effect of ratio of the underload cycles R_n

The assumption that the fatigue damage is caused by the action of the large underloads can be used only in the case of R_n = 0.9 where small cycles are at the threshold level. When R_n is lower than 0.9 and K_{max} is at 14.1 MPa $m^{1/2}$, small cycles cause fatigue damage that can not be omitted.

In the two following tables 10.3 10.4, it is examined whether or not the loading cycles in the SVAL sequences behave according to the CAL data. Table 10.3 presents the case that the underload cycles have CAL crack growth rates. The outcome is that the $(da/dN)_n$ is much faster than the CAL values. The measurements of the underload crack opening show that their values are lower than the CAL level. Hence, it is expected the $(da/dN)_u$ to be accelerated in comparison with the CAL values. In the second case, the $(da/dN)_u$ are faster that the CAL values when the $(da/dN)_n$ was set according to the CAL data. The second case is closer to the reality. A more accurate estimation of the $(da/dN)_u$ can be achieved using the crack opening measurements in conjunction with previous findings.

When R_n is smaller than 0.9, the small cycles are no longer inactive and they contribute to the crack growth. In figure 8.49 one can see that when the small cycles are damaging, closure level of the underloads increases towards the CAL value. Based on the fact that similar ΔK_{eff} have similar crack growth rates (da/dN) and on the crack opening measurements, $(da/dN)_u$ can be estimated. The crack growth rates of the underload cycles are plotted in terms of R_n in figure 10.8. They are 7.2 10^{-8} and 4.0 10^{-8} m/cycle for R_n 0.7 and 0.4, respectively.

Table 10.3_ Crack growth rates of small and underload cycles when the underload cycles have CAL rates

R_n	n cycles/u cycles	Crack Increment (m)	$(da/dN)_n$ Result	CAL $(da/dN)_u$
0.7	9000/90000	0.002	1.92 10^{-8}	3.00 10^{-8}
0.4	5000/50000	0.006	1.17 10^{-7}	3.00 10^{-8}

Table 10.4_ Crack growth rates of small and underload cycles when the small cycles have CAL rates

R_n	n cycles/u cycles	Crack Increment (m)	CAL $(da/dN)_n$	$(da/dN)_u$ Result
0.7	9000/90000	0.002	8.68 10^{-9}	1.35 10^{-7}
0.4	5000/50000	0.006	1.13 10^{-8}	1.09 10^{-6}

Knowing the fatigue crack growth rates of the underloads, one can calculate the crack growth rates of the small cycles. For cycles at R_n = 0.7, da/dN = 1.5 10^{-8} and for cycles at R_n = 0.4, da/dN = 1.16 10^{-7} m/cycle. These rates are higher than the CAL rates. The reduced crack closure of the underloads causes the following small cycles at R_n=0.4 and ΔK=8.46 MPa $m^{1/2}$ and at R_n=0.7 and ΔK=4.23 MPa $m^{1/2}$ to become more effective and thus the SVAL sequence more damaging. Hence, both underload and small cycles are accelerated comparing with the CAL conditions.

As in the case of Ti1023, the acceleration factor α is a result of the deviation from the CAL crack growth rates, of both underload and small cycles. It suggests that when the small cycles become damaging, their closure level is affected by the presence of the underload cycles. The effect of the small on the closure level of the underloads exists at the same time. Table A8 provides the crack closure levels and the crack growth rates of these tests.

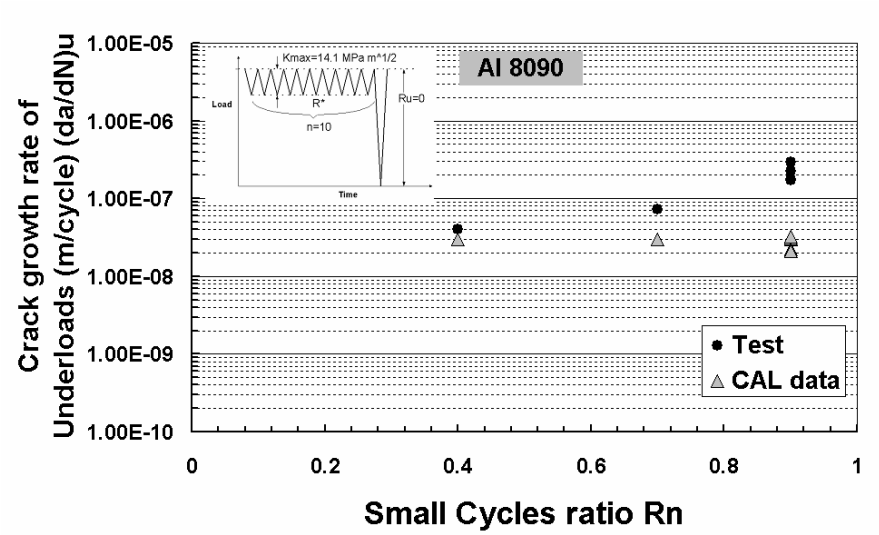

Figure 10.8_ The $(da/dN)_u$ and the CAL crack growth rates in terms of R_n ratio on Al8090.

10.1.3 Al7010

10.1.3.1 Effect of number of small cycles n

The calculated values of the crack growth rate of the underloads are presented in table A9 and they are plotted in terms of the number of small cycles in figure 10.9 together with the CAL crack growth rates of the same loading level. The faster crack growth rates of underloads are the reason of the small acceleration of crack growth under the SVAL sequences. The difference between SVAL and CAL $(da/dN)_u$ is approximately the same for the whole range of n, which suggest that the effect of the small cycles is immediate although small.

10.1.3.2 Effect of K_{max}

The $(da/dN)_u$ are presented in table A9 and they are plotted in terms of the number of small cycles in figure 10.10 together with the CAL crack growth rates of the same loading level. Crack growth rates of the underloads are very close to the CAL rates.

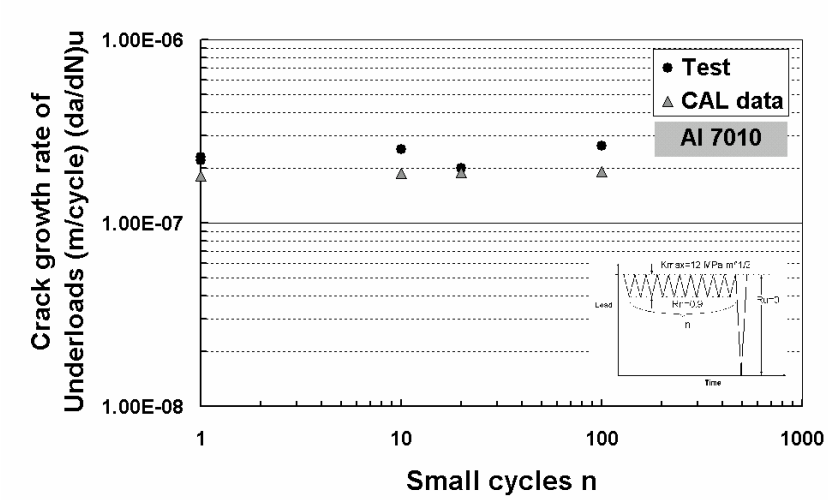

Figure 10.9_ The $(da/dN)_u$ and the CAL crack growth rates in terms of the number of the small cycles n on Al7010.

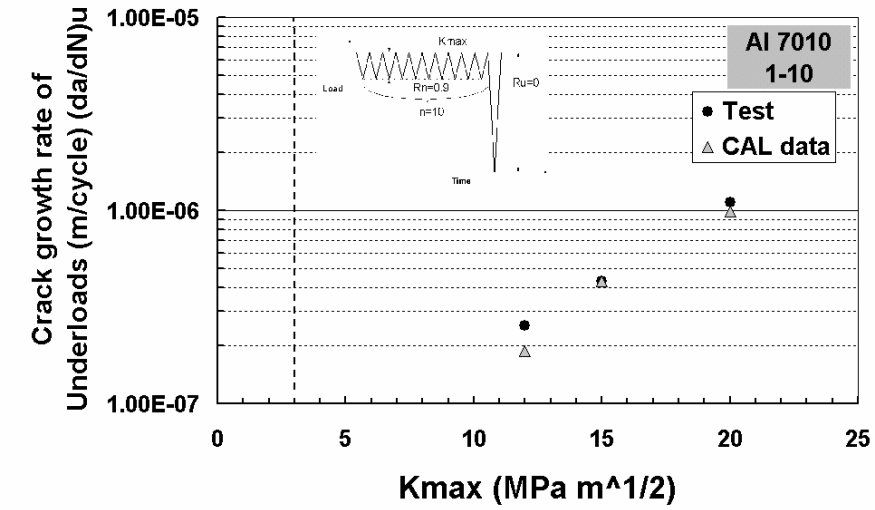

Figure 10.10_ The $(da/dN)_u$ and the CAL crack growth rates in terms of K_{max} level on Al7010.

10.2 ΔK_{eff} Determination Based on Closure Concept

The effective stress intensity factor range ΔK_{eff} was determined using the relationship:

$$\Delta K_{eff} = K_{max} - K_o \qquad (10\text{-}1)$$

where, K_o is the crack closure load in terms of stress intensity factor. K_o was determined experimentally for various CAL and SVAL conditions. Thus, the determination of the ΔK_{eff} for each loading condition is possible. The measured crack growth rates are plotted versus the ΔK_{eff} results and the formation of a unique ΔK_{eff} curves is assessed for the three alloys.

10.2.1 ΔK_{eff} curve for Ti1023

ΔK_{eff} stress intensity ranges and crack growth rates of SVAL tests are plotted in figure 10.11. The results form a unique curve, which is at the left-hand side of the Fastran predicted curve using α=1. This curve is the characteristic ΔK_{eff} curve of the material. The crack growth rates and crack closure measurements of the SVAL, the CAL and the precracking procedures cycles were used in order to create the curve.

The formation of a unique ΔK_{eff} curve supports the consistency of the crack closure measurement and confirms that crack closure reduction is the mechanism causing the acceleration of the crack growth under sequences, which contain stress intensity range cycles at the threshold region and high R ratio and large stress intensity range underload cycles at low R ratio.

The ΔK_{eff} curve is placed on the left of the CAL data at R = 0.7 in the Paris regime. Because of the lack of experimental data, the lower part of the curve was drawn based on CAL data at R = 0.9, which is assumed as closure free. The position of the curve implies that closure exists even at high R ratio (=0.7) cycles.

10.2.2 ΔK_{eff} curve for Al8090

ΔK_{eff} stress intensity ranges and crack growth rates of SVAL tests are plotted in figure 10.12. The results form a unique curve, which is at the left-hand side of the high R ratio (0.7) CAL data. This curve is the characteristic ΔK_{eff} curve of the material. The crack growth rates and crack closure measurements of the SVAL, the CAL and the precracking procedures cycles were used in order to create the curve. Often cracks grow at different rates due to the transient effects and the nature of the material, which exhibits a big scatter in the CAL crack growth rates.

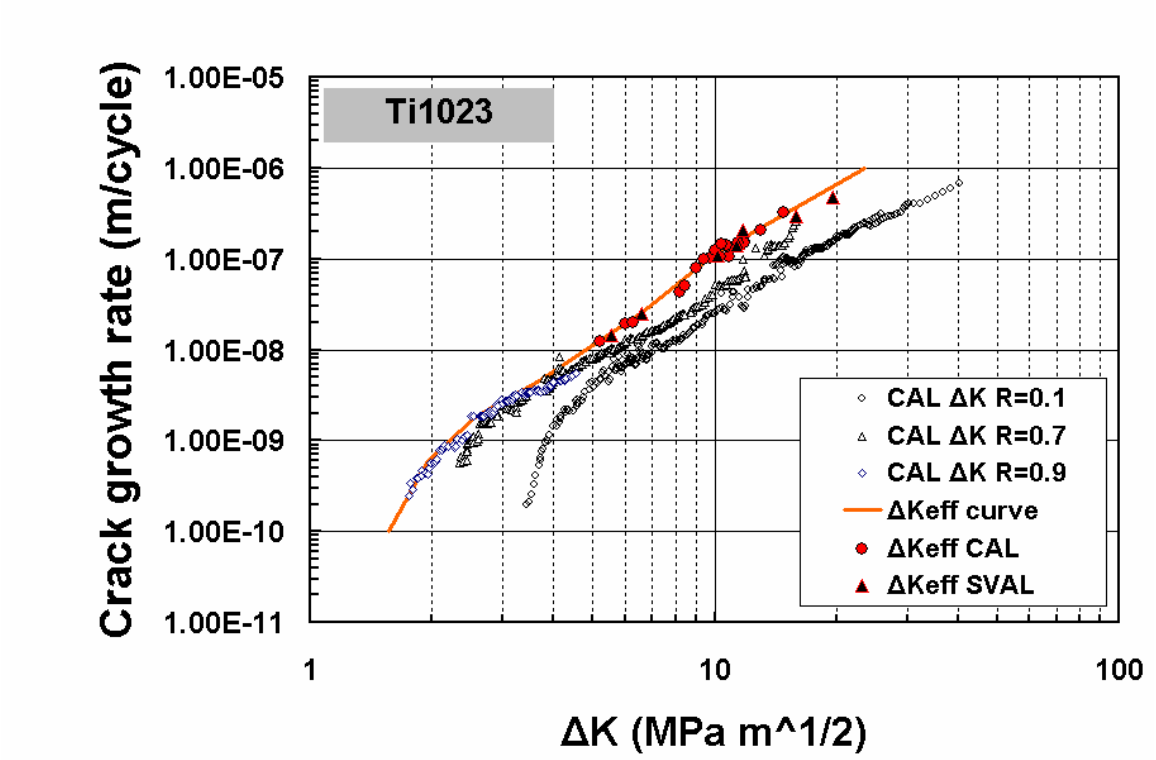

Figure 10.11_ Experimentally determined ΔK_{eff} curve of Ti1023 and comparison with CAL data

It is clear that a unique ΔK_{eff} curve is formed from the crack closure data. This fact points out the consistency of the crack closure measurement on Al8090. It is also confirms that crack closure reduction is the mechanism of the acceleration of the crack growth under the underloading sequences.

As for Ti1023, because of the lack of experimental data, the lower part of the curve was drawn based on CAL data at R = 0.9, which is assumed as closure free. The ΔK_{eff} curve is placed on the left of the CAL data at R = 0.7 in the Paris regime. The position of the curve implies that closure exist even at high R ratio (=0.7) cycles. The distance between the two curves is getting larger as the ΔK increases implying that the crack closure effect increases.

10.2.3 ΔK_{eff} curve for Al7010

ΔK_{eff} stress intensity ranges and crack growth rates of SVAL tests are plotted in figure 10.13. Results form a unique curve, which is on the top of the CAL data at

R = 0.9. This curve is the characteristic ΔK_{eff} curve of the material. The crack growth rates and crack closure measurements of the SVAL, the CAL and the precracking procedures cycles were used in order to create the curve.

It is clear again that a unique ΔK_{eff} curve is formed from the crack closure data indicating the consistency of the crack closure measurement on Al7010 and also confirming that crack closure reduction is the mechanism of the acceleration of the crack growth under the underloading sequences.

The ΔK_{eff} curve is placed on the left of the CAL data at R = 0.7 and on the top of R = 0.9 data until ΔK = 4 MPa $m^{1/2}$. Because of the lack of experimental data, the lower part of the curve was drawn based on CAL data at R = 0.9. The position of the curve implies that closure exist even at high R ratio (=0.7) cycles at the Paris regime.

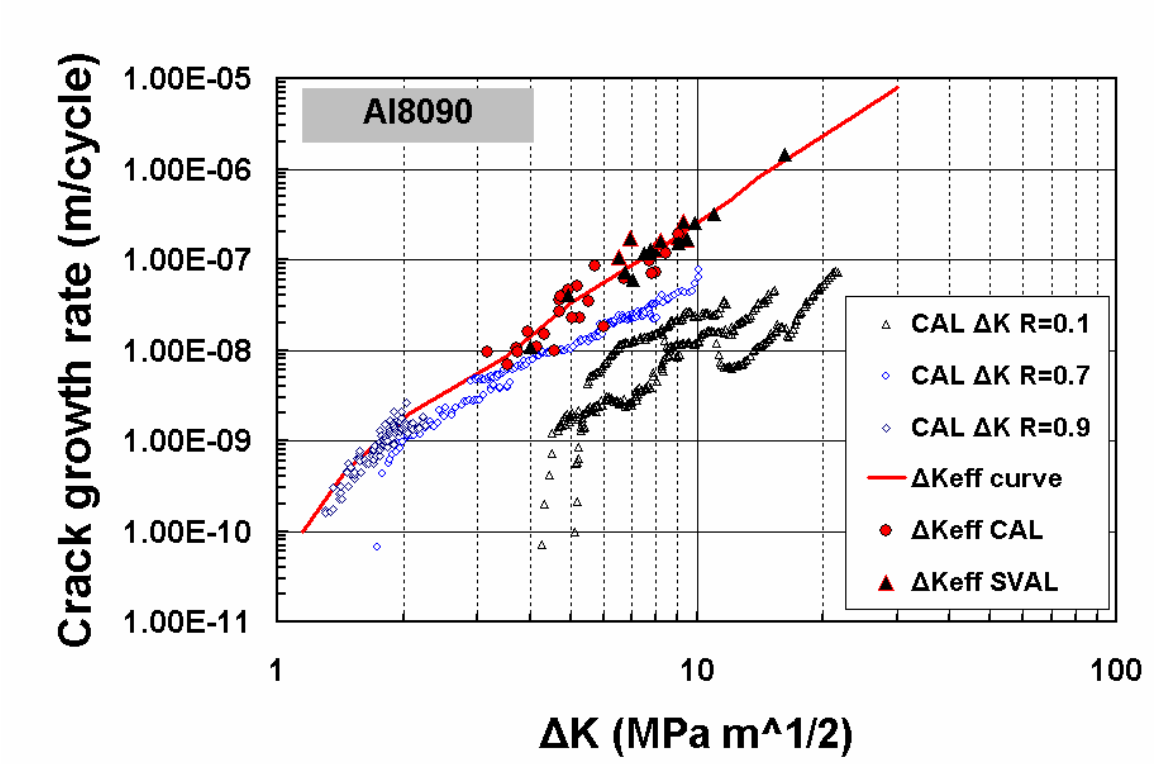

Figure 10.12_ Experimentally determined ΔK_{eff} curve of Al8090 and comparison with CAL data

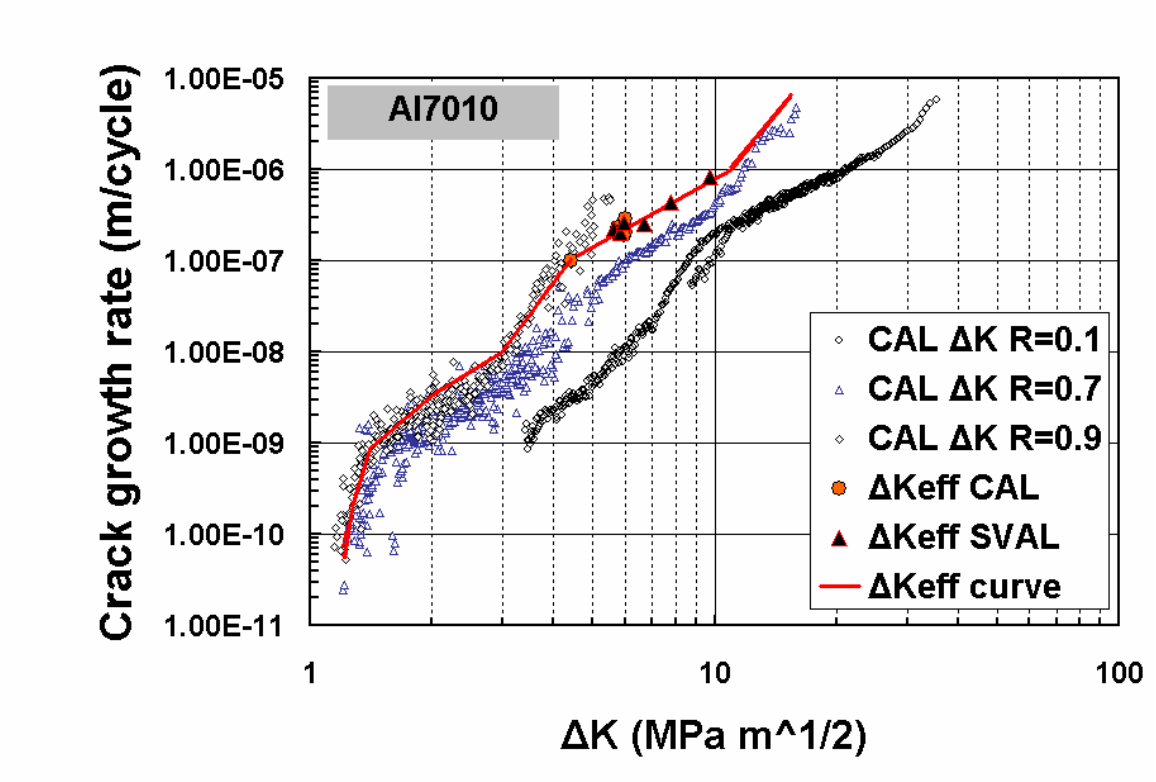

Figure 10.13_ Experimentally determined ΔK_{eff} curve of AL7010 and comparison with CAL data

10.2.4 The outcome considering the ΔK_{eff} curves

The interpretation of the crack growth data with the crack closure measurements has successfully correlated the crack growth rates in terms of the ΔK_{eff} into a very narrow band for Ti1023, Al8090 and Al7010. The experimental scatter band is considered low and the $\Delta K_{eff,exp}$ curves are clearly formed. This leads to the conclusion that crack closure measurements are able to describe adequately the crack growth mechanism in the conducted tests.

The comparison between the CAL data and the ΔK_{eff} curve provides a good estimation of the CAL crack closure levels at a wider range of ΔK amplitudes and R ratios. This kind of data could be used in order to be compared against crack closure predictions because it will provide significant information without involving significant amount of testing.

The position of the ΔK_{eff} curve for each material on the left hand side of the CAL 0.7 R ratio crack growth rates reveals the existence of crack closure even at high R ratio cycles. These effects on the Paris area of the crack growth are significant and cannot be ignored in the fatigue crack growth analysis.

CHAPTER 11

FATIGUE LIFE PREDICTIONS

11.1 Introduction

An extensive evaluation of the FASTRAN crack growth model was conducted. The life prediction model was used to predict the fatigue life under a selection of typical SVAL spectra, which contain n number of small cycles and 1 large underload. The values of n, K_{max}, R_u and R_n were different for each prediction based on the test conditions. The predictions were carried out for Ti1023, Al8090 and Al7010.

Three different cases of input were entered into the model. The first used the constraint factor α=1 and the ΔK_{eff} curve produced by the correlation of the CAL data of each material using this factor as shown in chapter 7. The second case used the experimentally determined ΔK_{eff} curve as a more representative curve for the material and the constraint factor α=1. Finally, the third case used again the experimentally determined ΔK_{eff} curve but with a constraint factor α=2.5, which simulates better the plane strain conditions of the Compact Tension test specimens (t=0.017m and w=0.07m). The rest of the input details considering the specimen geometry and the loading were exactly the same.

Life predictions were also preformed using the Rotarix spectra (Rotarix 16, 20, 24, 32). The comparison between the model against the linear summation and the experimental data is carried out. They were conducted using exactly the same material and the same Rotarix spectra. At the end of the chapter the life predictions are discussed under the light of the experimental findings and the international literature.

11.2 Fatigue Life Predictions For Sequences Containing One Underload

Table 11.1 summaries the FASTRAN life predictions and the crack opening level under the Rotarix spectra for the three different cases and for the three materials. Also, the experimental and the linear summation life are listed for each test. The predictions are compared with the measured fatigue cycles for each test. In the following figures, the perfect agreement is the solid line and the factor-of-two bands are shown by the dashed lines. The factor-of-10 is shown by the dash-dot line.

Table 11.1_ Fatigue life predictions and the crack opening level produced using FASTRAN (3 cases of input) and AFGROW linear summation for typical SVAL sequences on the three alloys.

Spectrum	Material	N_{exp}	AFGROW		FASTRAN					
			Linear Sum		α=1		ΔK_{eff}(exp) α=1		ΔK_{eff}(exp) α=2.5	
			N	β	N	K_0/K_{max}	N	K_0/K_{max}	N	K_0/K_{max}
1U-1n	Ti1023	44,000	69,960	1.59	85,872	0.5	104,440	0.5	40,094	0.31
Rn 0.9	Al8090	35,000	182,000	5.2	116,100	0.47	75,250	0.621	14,500	0.298
Ru 0.0	Al7010	10,000	10,000	1	4,300	0.5	4,000	0.5	2,000	0.31
1U-10n	Ti1023	330,000	442,200	1.34	539,847	0.5	649,770	0.5	257,675	0.31
Rn 0.9	Al8090	165,000	1,584,000	9.6	1,385,400	0.55	541,000	0.571	139,500	0.298
Ru 0.0	Al7010	88,000	140,800	1.6	88,275	0.5	85,129	0.5	40,500	0.311
1U-20n	Ti1023	202,000	317,140	1.57	382,918	0.5	462,945	0.5	179,277	0.31
Rn 0.9	Al8090	210,000	1,463,700	6.97	781,400	0.54	305,900	0.553	100,000	0.298
Ru 0.0	Al7010	168,000	168,000	1	104,685	0.5	101,500	0.5	50,200	0.31
1U-40n	Ti1023	-	-	-	-	-	-	-	-	-
Rn 0.9	Al8090	1,050,000	4,305,000	4.1	654,500	0.52	276,400	0.538	111,930	0.298
Ru 0.0	Al7010	-	-	-	-	-	-	-	-	
1U-100n	Ti1023	2,020,000	2,923,748	1.45	3,160,189	0.5	3,793,935	0.5	1,600,648	0.3
Rn 0.9	Al8090	2,020,000	2,484,600	1.23	1,307,000	0.505	693,200	0.533	317,847	0.298
Ru 0.0	Al7010	303,000	515,100	1.7	377,033	0.5	364,105	0.5	184,123	0.318
1U-10n	Ti1023	550,000	1,045,000	1.9	1,176,270	0.62	1,699,249	0.6	500,000	0.3
Rn 0.8	Al8090	550,000	1,820,500	3.31	695,300	0.57	635,500	0.567	186,700	0.283
Ru 0.0	Al7010	-	-	-	-	-	-	-	-	-
1U-10n	Ti1023	33,000	46,860	1.42	67,298	0.505	72,875	0.5	34,144	0.311
Rn 0.92	Al8090	55,000	365,750	6.65	172,700	0.5	37,330	0.453	13,000	0.293
Ru 0.0	Al7010	99,000	99,000	1	94,094	0.5	88,800	0.5	39,800	0.31
1U-10n	Ti1023	44,000	51,920	1.18	49,214	0.515	64,218	0.5	29,623	0.313
Rn 0.94	Al8090	44,000	651,200	14.8	166,900	0.42	63,500	0.441	33,000	0.296
Ru 0.0	Al7010	22,000	22,000	1	21,252	0.5	21,800	0.5	5,566	0.321
1U-10n	Ti1023	137,000	301,400	2.2	262,616	0.553	624,456	0.64	118,030	0.396
Rn 0.9	Al8090	137,000	1,048,050	7.65	800,400	0.6	353,400	0.612	105,150	0.388
Ru 0.3	Al7010	-	-	-	-	-	-	-	-	-
1U-10n	Ti1023	440,000	633,600	1.44	719,961	0.69	988,646	0.69	294,228	0.534
Rn 0.9	Al8090	330,000	1,425,600	4.32	1,009,000	0.66	546,200	0.673	205,315	0.53
Ru 0.5	Al7010	-	-	-	-	-	-	-	-	-
1U-10n	Ti1023	44,000	79,200	1.8	68,524	0.638	99,776	0.638	57,134	0.31
Rn 0.7	Al8090	55,000	138,600	2.52	173,200	0.585	80,800	0.618	49,896	0.3
Ru 0.0	Al7010	-	-	-	-	-	-	-	-	-
1U-10n	Ti1023	44,000	77,000	1.75	86,011	0.5	115,993	0.48	29,833	0.33
Rn 0.4	Al8090	99,000	703,890	7.11	281,400	0.608	90,700	0.616	28,727	0.3
Ru 0.0	Al7010	-	-	-	-	-	-	-	-	-

11.2.1 Ti1023

The experimental fatigue life for a specific crack extension was compared to the FASTRAN and linear predictions for various types of SVAL sequences as shown in Figure 11.1 to 11.4 for Ti1023. The calculations show that the FASTRAN model is able to predict crack growth acceleration effects comparing with the CAL data under the examined sequences and input cases. The degree of acceleration or retardation varies depending on the inputs and the loading sequence. The majority of the predictions are within a factor of 2 compared with the measured data. Figure 11.5 gives the crack opening point in terms of K_0/K_{max} for the different loading sequences and the different constraint factors and ΔK_{eff} curve.

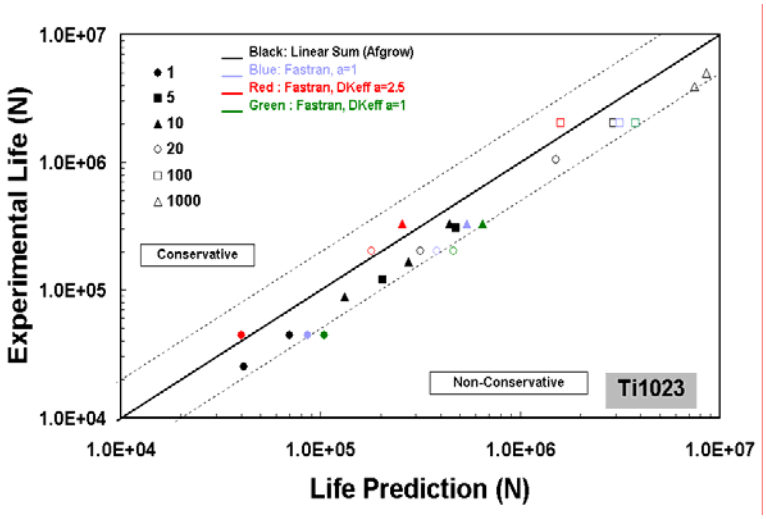

Figure 11.1_ Measured and FASTRAN predicted fatigue lives on Ti1023, for sequences with different n

It is observed that on Ti1023, in the cases that α=1 and the analytical effective curve $\Delta K_{eff,an}$, and $\Delta K_{eff,exp}$ with α=1, FASTRAN model produces lives longer than the recorded lives no matter the loading sequence. In the case that $\Delta K_{eff,exp}$ with α=2.5, most of the FASTRAN predictions are in the conservative side. The exception are the tests at very high maximum stress intensity factor, K_{max}=26.16 MPa $m^{1/2}$ and at R_n=0.7. Nevertheless, the FASTRAN prediction using $\Delta K_{eff,exp}$ with α=2.5 are extremely close to the experimental lives for Ti1023.

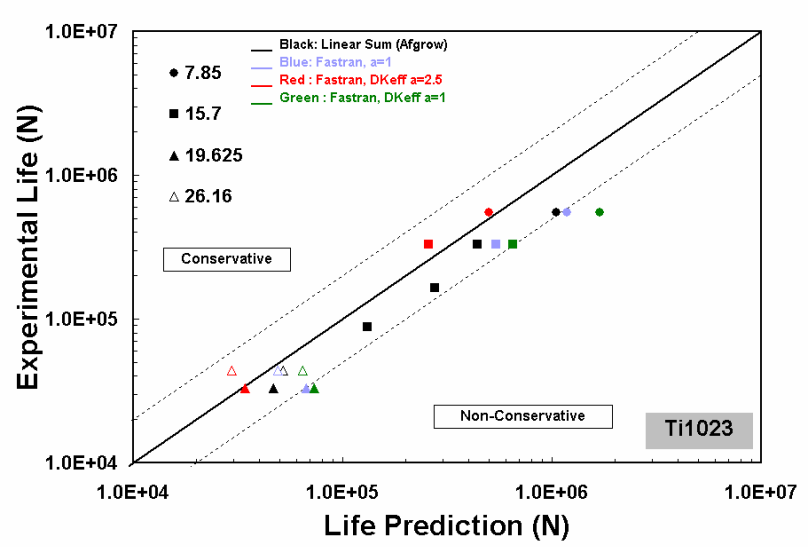

Figure 11.2_ Measured and FASTRAN predicted fatigue lives on Ti1023, for sequences with different K_{max}

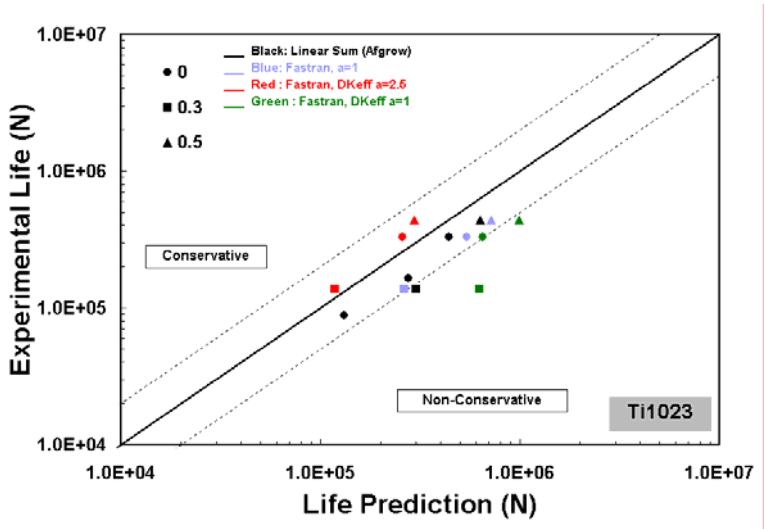

Figure 11.3_ Measured and FASTRAN predicted fatigue lives on Ti1023, for sequences with different R_u

The observation of the FASTRAN predictions using different constraint factor and effective stress intensity curves suggest that both of these inputs affect the final life. When the constraint factor remains constant, equal to 1, the experimentally determined ΔK_{eff} curve will produce slower crack growth rates since it is on the right-hand side of the ΔK_{eff} curve which was determined by FASTRAN using α=1 (figure 11.6). Hence, the predicted lives will be longer.

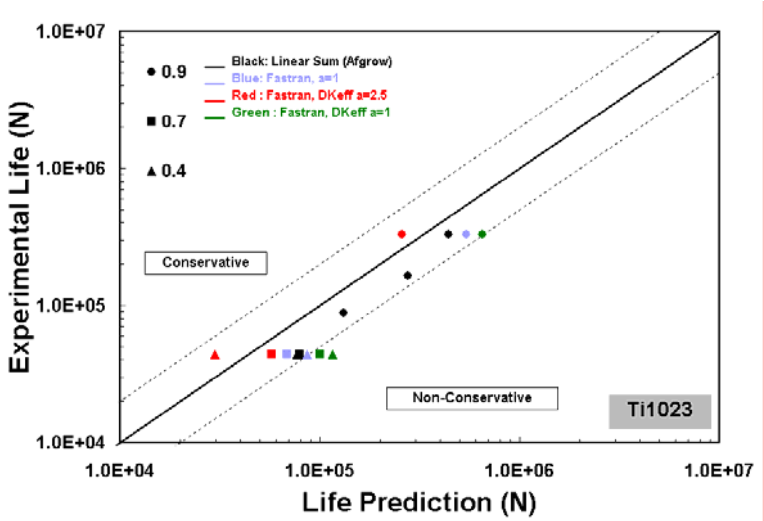

Figure 11.4_ Measured and FASTRAN predicted fatigue lives on Ti1023, for sequences with different R_n

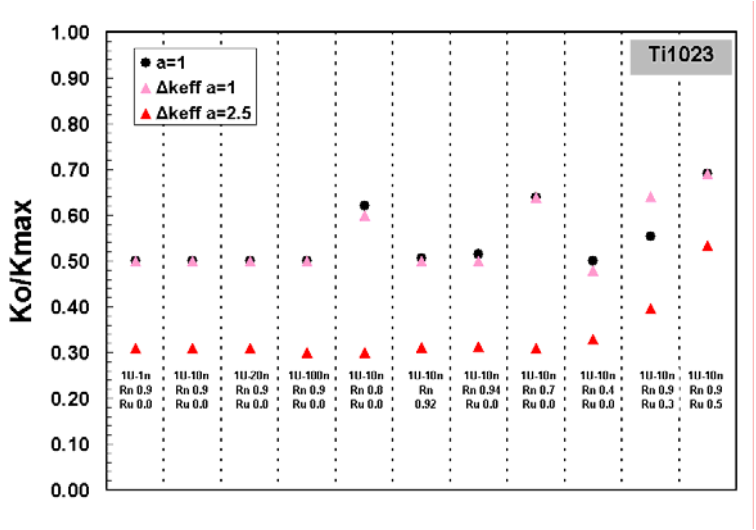

Figure 11.5_FASTRAN predicted crack opening values for the SVAL sequences on Ti1023

It is clear from the figure 11.6 that both of the curves are on the left-hand side of the high R ratio CAL data. These suggest that according to the model and the tests, crack closure exist even at the high level of R ratio.

Using the same ΔK_{eff} curve and changing the α, FASTRAN produces different lives. The lives are shorter when α=2.5 is used. It could be suggested that since α is closer to 3, which represents the plane stain conditions, the crack will grow faster and then the lives will be shorter. But, the constraint factor is used by the model to tune the CAL so that they collapse into the most narrow band. This band is then

described by the ΔK_{eff} curve. The produced ΔK_{eff} curve and the α at which the curve was produced are used in conjunction within the model to estimate the crack growth. Using the procedure of tuning the CAL, constraint α is considered to take into account the effect of the thickness. Its effect is to reduce the fatigue life as its value approaches to 3. This effect can be observed in all life predictions. The degree of the effect on the final life seems to depend on the applied spectrum, since the difference between the FASTRAN predictions using $\Delta K_{eff,exp}$ with α=1 and α=2.5 does not remain the same as the applied sequence changes.

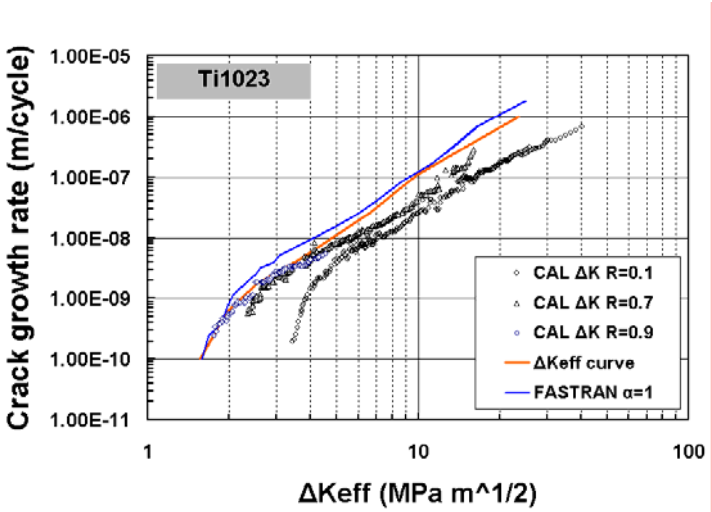

Figure 11.6_ ΔK_{eff} curve determined using FASTRAN model and experimental data and CAL data for Ti1023.

The crack closure levels, which are calculated during the life predictions, are affected by the effective curve and α, which were used as inputs. Figure 11.5 shows the level of crack closure of the underload for each sequence. When the model uses the value 1 for α, the closure levels are very similar. The values are 0.5 K_0/K_{max} or higher. When α=2.5, the underload closure level is at 0.3 K_0/K_{max} for the sequences containing R_u=0. The difference on the closure level between the case using the $\Delta K_{eff,exp}$ with α=1 and 2.5, suggest the change of α affects the crack closure level, even when the same ΔK_{eff} curve is used. The changes of the effective curve keeping the α constant have a limited effect since the two effective curves are very similar (figure 11.6).

11.2.2 Al8090

The experimental fatigue life for a specific crack extension was compared to the FASTRAN and linear predictions for various types of SVAL sequences as shown in figure 11.6 to 11.10 for Al8090. The calculations show that the FASTRAN model predicts crack growth acceleration effects comparing with the CAL data under the examined sequences and model input cases. The degree of acceleration varies depending on the inputs and the loading sequence. Figure 11.11 gives the crack opening point in terms of K_0/K_{max} for the different loading sequences and the different constraint factors and ΔK_{eff} curve.

In comparison with the test data, the use of experimental ΔK_{eff} with α=2.5 gave conservative life prediction (points with red colour). The degree of conservatism varies depending on the spectrum. The majority of the prediction was within the scatter band of 5. When analytical ΔK_{eff} curve and α=1 were input in the model, the life predictions were non-conservative in most of the case. The calculated lives were significantly longer than the case with the $\Delta K_{eff,exp}$ curve and α=2.5 and close to the linear summation prediction. Using the $\Delta K_{eff,exp}$ curve and α=1, FASTRAN simulations are faster and slower from the test results. The degree of scatter in the life predictions was from very good up to 5 times the test data.

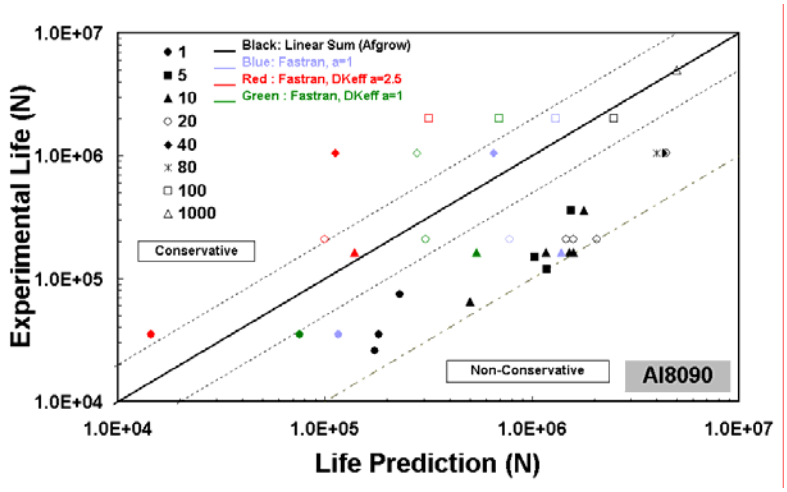

Figure 11.7_ Measured and FASTRAN predicted fatigue lives on Al8090, for sequences with different n

Althought the life prediction are very accurate for some loading sequences and model inputs, no obvious consistancy can be observed in relation with the spectrum, effective curve, and constraint factor.

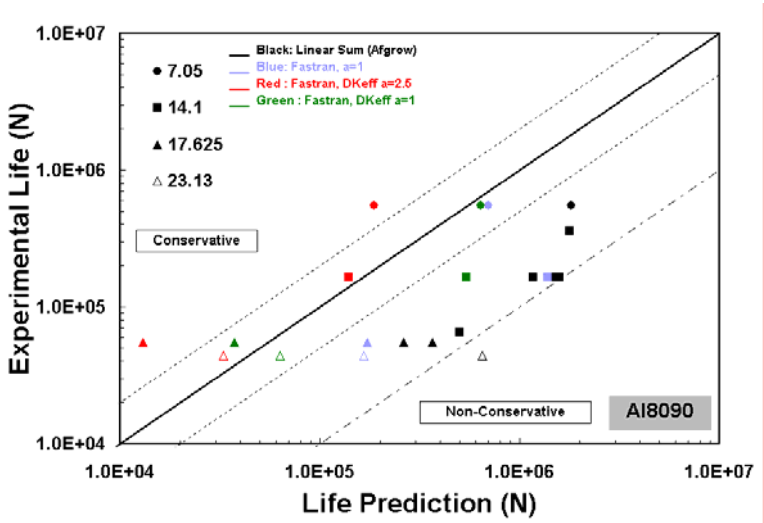

Figure 11.8_ Measured and FASTRAN predicted fatigue lives on Al8090, for sequences with different K_{max}

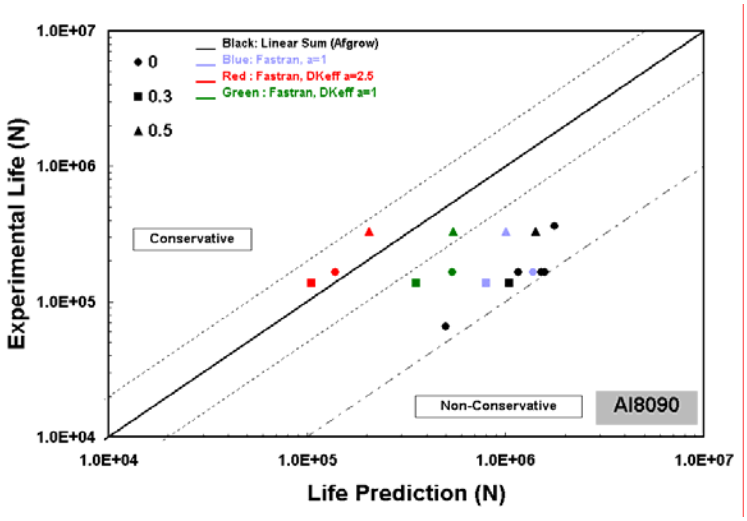

Figure 11.9_ Measured and FASTRAN predicted fatigue lives on Al8090, for sequences with different R_u

As in Ti1023 case, the FASTRAN predictions depend on the constraint factor and effective stress intensity curves, which are going to be used as inputs. But in contrast with Ti1023, when the constraint factor remains constant, equal to 1, the use of the experimentally determined ΔK_{eff} curve will produce faster crack growth rates since it is on the left-hand side of the ΔK_{eff} curve which was determined by FASTRAN using $\alpha=1$ (figure 11.12). Hence, the predicted lives will be shorter.

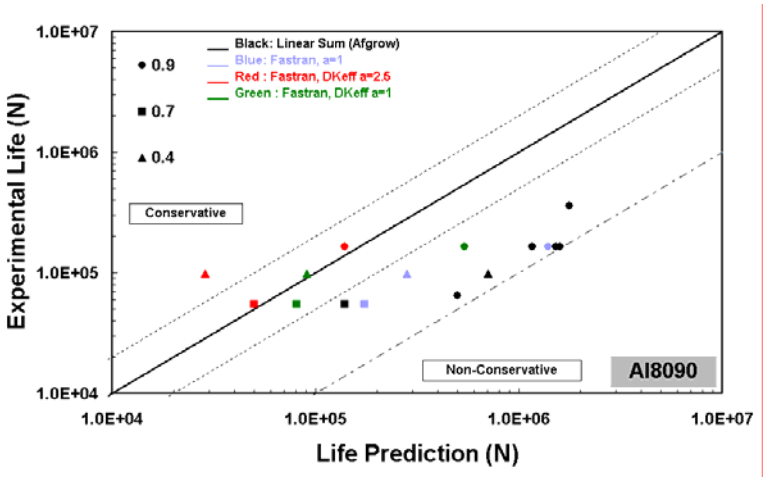

Figure 11.10_ Measured and FASTRAN predicted fatigue lives on Al8090, for sequences with different R_n

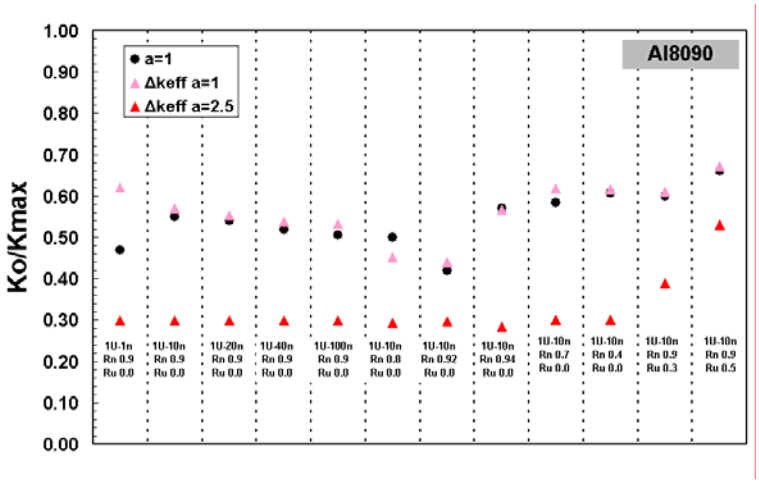

Figure 11.11_ FASTRAN predicted crack opening values for the SVAL sequences on Al8090

It is clear from the figure 11.12 that both of the curves are on the left-hand side of the high R ratio CAL data. These suggest that according to the model and the tests data, crack closure exist even at the high level of R ratio loading on Al8090.

Using the same ΔK_{eff} curve and changing the α, FASTRAN produces different lives. The lives are shorter when α=2.5 is used. The effect of α is the same as on Ti1023. It reduces the fatigue life as its value approaches to 3. This effect can be observed in all life predictions. The degree of the effect on the final life seems to depend on the applied spectrum, since the difference between the FASTRAN

predictions using $\Delta K_{eff,exp}$ with α=1 and α=2.5 does not remain the same as the applied sequence changes.

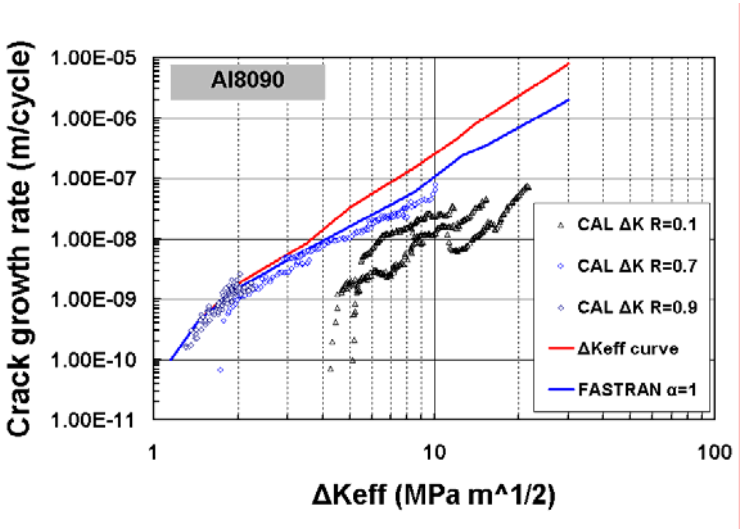

Figure 11.12_ ΔK_{eff} curve determined using FASTRAN model and experimental data and CAL data for Al8090.

The crack closure levels, which are calculated during the life predictions, are affected by the effective curve and α, which was used as inputs. Figure 11.11 shows the level of crack closure of the underload for each sequence. When the model uses the value 1 for α, the closure levels are overall very similar. The values are between 0.4 and 0.7 K_0/K_{max}. When α=2.5, the underload closure level is at 0.3 K_0/K_{max} for the sequences containing R_u=0. The difference on the closure level between the case using the $\Delta K_{eff,exp}$ curve with α=1 and 2.5, suggest the change of α affects the crack closure level on Al8090, even when the same ΔK_{eff} curve is used. The changes of the effective curve keeping the α constant have a small effect since the two effective curves are close to each other (figure 11.12).

11.2.3 Al7010

Figures 11.13 and 11.14 show the experimental fatigue life for a specific crack extension and the comparison to the FASTRAN and linear predictions for various types of SVAL sequences for Al7010. The calculations shown that the FASTRAN model predicts crack growth acceleration effects comparing with the CAL data up to 4 times under the examined sequences and model input cases. The degree of acceleration varies depending on the inputs and the loading sequence. Figure 11.15

gives the crack opening point in terms of K_0/K_{max} for the different loading sequences and the different constraint factors and ΔK_{eff} curve.

In comparison with the test data, the use of experimental ΔK_{eff} with α=2.5 gave the most conservative life prediction. The conservatism is higher than 2 times the measured lives and varies depending on the spectrum. In the cases where the analytical ΔK_{eff} curve with α=1 and the $\Delta K_{eff,exp}$ curve with α=2.5 were used as inputs, the model produced very similar life predictions for the most of the spectra. The calculated lives were very close to the test results for the most sequences.

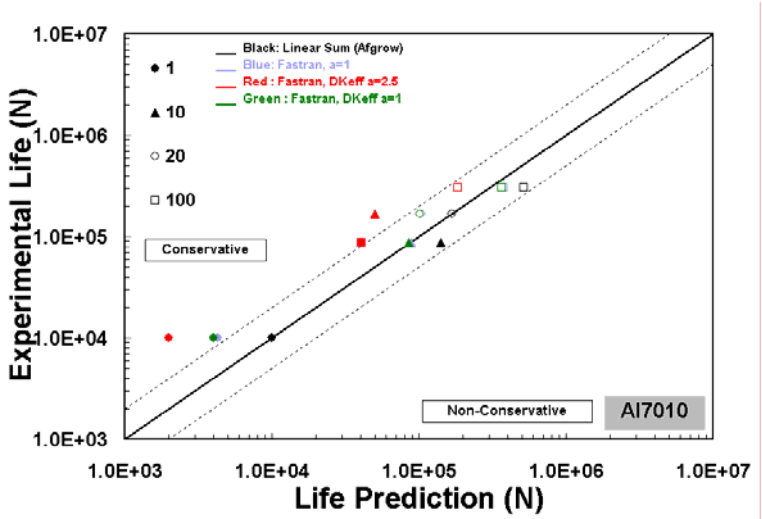

Figure 11.13_ Measured and FASTRAN predicted fatigue lives on Al7010, for sequences with different n

As in the other two materials, the FASTRAN predictions depend on the constraint factor and effective stress intensity curves, which are going to be used as inputs. When the constraint factor remains constant, equal to 1, the use of the experimentally determined ΔK_{eff} curve will produce very similar crack growth rates with the case that analytical ΔK_{eff} curve at α=1 was used in the model. The two ΔK_{eff} curves are almost one on the top of each other as it can be seen in figure 11.16. Hence, the predicted lives are almost the same as it was expected.

It is clear from the figure 11.16 that both of the effective curves follow the path of the R=0.7 CAL crack growth data. This suggests that according to the model and the tests data, crack closure exist up to R loading ratio of 0.7 on Al7010.

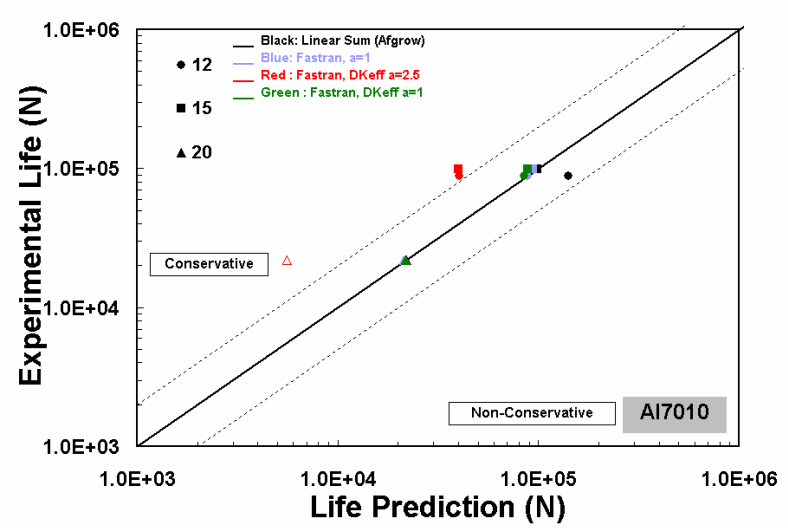

Figure 11.14_ Measured and FASTRAN predicted fatigue lives on Al7010, for sequences with different K_{max}

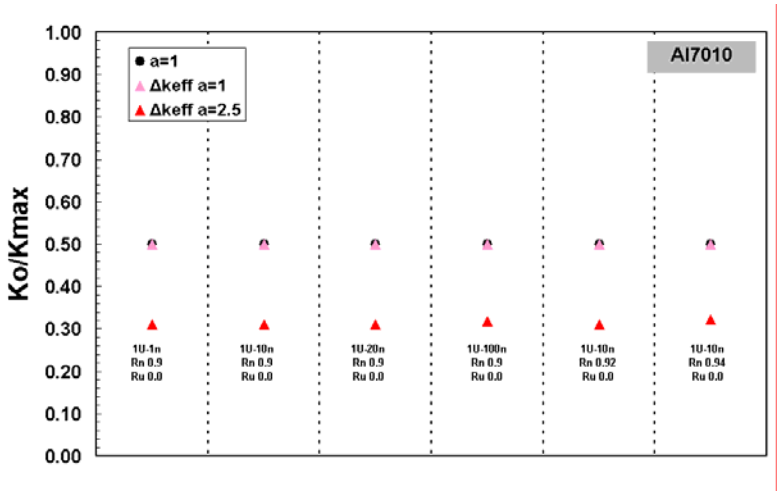

Figure 11.15_FASTRAN predicted crack opening values for the SVAL sequences on al7010

Using the same ΔK_{eff} curve and changing the α, FASTRAN produces different lives. The lives are shorter when α=2.5 is used. The changes in α alter the predicted fatigue life. This effect can be observed in all life predictions.

The crack closure levels, which are calculated during the life predictions, are affected by the effective curve and α, which was used as inputs. Figure 11.15 shows the level of crack closure of the underload for each sequence. When the model uses the value 1 for α, the closure levels are identical since ΔK_{eff} curves are almost the same. The values are 0.5 K_0/K_{max}. When α=2.5, the underload closure

level is at 0.3 K_0/K_{max} for the sequences containing R_u=0. The difference on the closure level between the case using the $\Delta K_{eff,exp}$ curve with α=1 and 2.5, suggest the change of α affects the crack closure level on Al7010, even when the same ΔK_{eff} curve is used and explains the faster crack growth in the case where input is α=2.5.

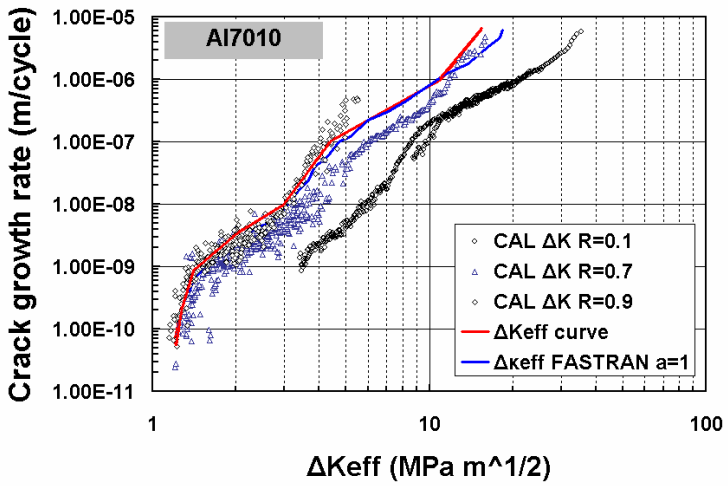

Figure 11.16_ ΔK_{eff} curve determined using FASTRAN model and experimental data and CAL data for Al809.

11.3 Fatigue Life Predictions For CVAL Sequences

Table 11.2 summaries the FASTRAN life predictions and the crack opening levels under the Rotarix spectra for the three different model input cases and for the three materials. Also, the experimental and the linear summation lives are listed for each test. The predictions are compared with the measured fatigue cycles for each test. In the following figures, the perfect agreement is the solid line and the factor-of-two bands are shown by the dashed lines. The factor-of-3 is shown by the dash-dot line.

The experimental fatigue life for a specific crack extension was compared to the FASTRAN and linear predictions for Rotarix 16 spectrum as shown in figure 11.17 for Ti1023, Al8090 and Al7010. The calculations shown that the FASTRAN model predict crack growth acceleration effects comparing with the CAL data under the examined material, sequences and model input cases. The degree of acceleration changes for each different case. The use of experimental ΔK_{eff} curve

with α=2.5 gave the shortest life prediction (points with red colour) in comparison with the rest of the models. On the other hand the use of analytical ΔK_{eff} curve and α=1 produced predictions closer to the CAL data.

Table 11.2_ Life predictions under the Rotarix spectra for Ti1023, Al8090 and Al7010

Spectrum	Material	N_{exp}	AFGROW		FASTRAN		
			Linear Sum		α=1	ΔK_{eff}(exp) α=1	ΔK_{eff}(exp) α=2.5
			N	β	N	N	N
Rot16	Ti1023	1,963,333	6,205,008	3.16	3,178,035	4,202,853	2,624,422
	Al8090	3,957,977	7,039,150	1.78	4,921,218	4,397,052	3,869,786
	Al7010	6,314,679	6,533,657	1.03	6,420,887	4,955,564	4,143,418
Rot20	Ti1023	-	-	-	-	-	-
	Al8090	-	-	-	-	-	-
	Al7010	1,295,019	1,413,196	1.09	901,360	746,488	713,480
Rot24	Ti1023	-	-	-	-	-	-
	Al8090	-	-	-	-	-	-
	Al7010	1,296,284	1,398,946	1.08	931,210	781,222	699,607
Rot32	Ti1023	-	-	-	-	-	-
	Al8090	-	-	-	-	-	-
	Al7010	671,129	885,173	1.32	502,684	417,172	348,627

When the experimental ΔK_{eff} curve with α=1 and α=2.5 were entered as inputs to the model, the life calculation correlated well with the test data for all three materials. For Ti1023, the predictions were non-conservative and for the Al7010 were conservative. On Al8090, the predictions were extremely accurate. Overall, the FASTRAN life predictions were within a factor of 2 from the test data.

It is obvious that the FASTRAN predictions depend on the constraint factor and effective stress intensity curves, which are going to be used as inputs. When the constraint factor remains constant, equal to 1, the calculated lives reflect the position of the analytical and experimental ΔK_{eff} curve in relation to each other. Hence, the final prediction is longer on Ti1023 when experimental ΔK_{eff} curve is used. The opposite occurs on Al8090.

The test results under the four simplified version of the helicopter spectrum are very close to the CAL crack growth behaviour with a small tendency to acceleration as the omission level increases as shown in figure 11.18. For the three input cases, the FASTRAN model predictions are presented for the four Rotarix

spectra in this graph. FASTRAN, having as input the analytical ΔK_{eff} curve at α=1, calculates conservative fatigue lives very close to the experimental data. When $\Delta K_{eff,exp}$ curve and α=2.5 are use into the FASTRAN model, the results are the most conservative predictions, but without being higher than a factor of 2. Overall, the model come up with very good outcome for the life predictions under Rotarix spectra on Al7010.

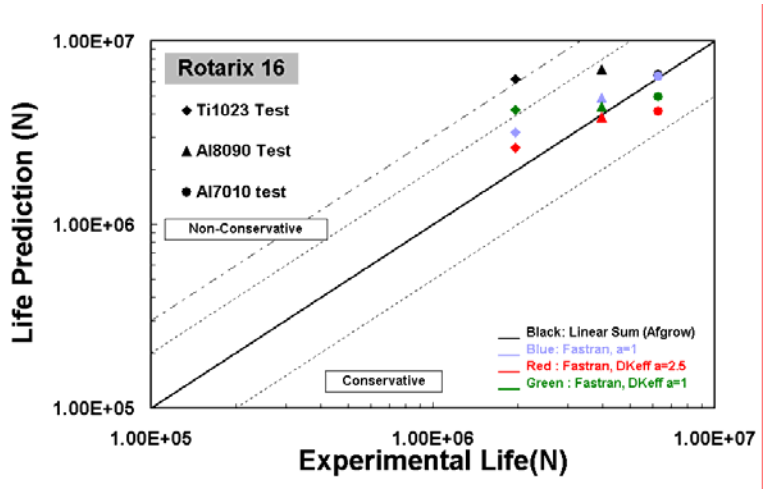

Figure 11.17_ Measured and FASTRAN predicted fatigue lives on Ti1023, Al8090 and Al7010, for Rot16 spectrum.

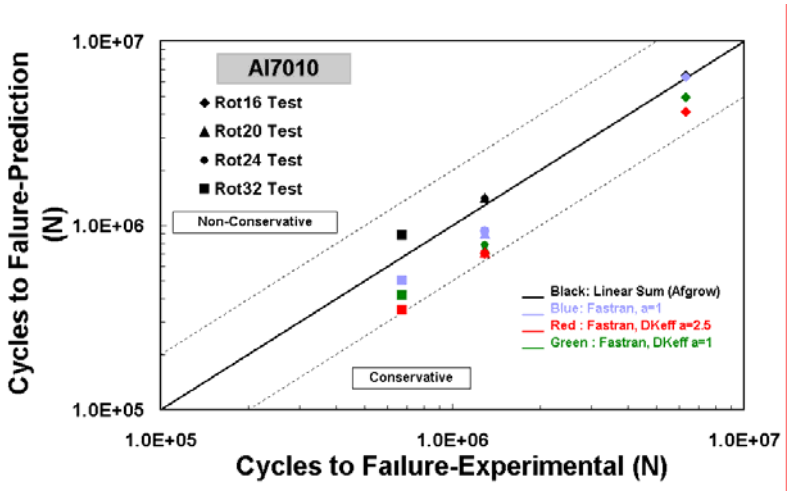

Figure 11.18_ Measured and FASTRAN predicted fatigue lives on Al7010, for Rot16 to32 spectra.

11.4 Discussion on Fatigue Crack Growth Predictions

This section is concerned with the application of a plasticity-induced crack-closure model, FASTRAN [143], to study fatigue-crack growth under various SVAL and rotorcraft load histories in the aluminium and titanium alloys. The model is based on a strip-yield model concept, but modified to leave plastically deformed material in the wake of the advancing crack. The model includes the influence of constraint factor (plane-stress or plane-strain behaviour) on the development of plasticity and crack closure.

Following the FASTRAN suggestions on the determination of the correct constraint factor for 17.5 mm specimen thickness (near plane strain condition), the model was used to correlate fatigue crack growth rate data under constant-amplitude loading for each material over a wide range in stress ratios and in crack growth rates. The values of 1, 1.5, 2, 2.5 were selected for the CAL data correlation. In contrast with the actual stress conditions on the crack tip which approach the plane strain condition due to large thickness, the results show that the CAL data for all three materials are best correlated from the constraint value 1.

The increase of alpha from 1 to 2.5 causes the produced ΔK_{eff} curve to move to the right and towards lower crack growth rates for a given ΔK_{eff} range. This observation is contradictory with the actual effect of the stress condition in the crack tip. It is well established that cracks grow faster in plane strain rather than in plane stress condition. This behaviour could characterize the constraint factor as a fitting parameter to the CAL data since it does not describe adequately the physical mechanism. Nevertheless, the value of a=1 with the analytically derived $\Delta K_{eff,an}$ curve was used as one case study of inputs in the FASTRAN model. It has been suggested to use a variable constraint factor for the crack growth predictions [143, 150]. The introduction of the variable had a great improvement on the prediction. This implies that the constraint factor depends also on the loading spectrum and the crack growth rates. All these information are not available prior to the predictions but they could be estimated based on the past experience [151]. It has been recognized that it is extremely difficult to quantify the parameters used in the model [116].

Based on the fact that the $\Delta K_{eff,an}$ curve is derived using the plasticity induced closure concept, useful observations can be made about the plasticity and roughness induced closure mechanism on the alloys by the study of the relative position of the experimental and analytical ΔK_{eff} curve. The $\Delta K_{eff,an}$ curve were compared with the $\Delta K_{eff,exp}$ curve for all three materials.

The comparison shows that on Ti1023, experimental effective curve is on the right of the analytical one with a=1. The correlation of the two curves is quite good, but better correlation could be achieved with a small increase in the constraint factor. This means that the under the actual conditions, crack closure mechanism is described adequately by the plasticity induced model with the closure levels derived from the plane stress condition values (a=1~1.5).

On Al7010, the experimental effective curve is on the top of the analytical one with a=1. The plasticity induced closure model under plane stress conditions accurately determines the closure levels and describes the fatigue crack growth.

On Al8090, experimental effective curve is on the left of the analytical one with a=1. No further decrease on the crack closure levels can be achieved using the plasticity induced model since the no further decrease in the constraint factor, which would result the movement of the curve to the left, is possible. The difference in the two curve can be attributed to the additional effect of the roughness induced closure. This conclusion is in line with the experimental observation of the crack growth under the underloading spectra.

Three different cases of FASTRAN inputs were used to predict the fatigue life under both SVAL and CVAL spectra on the titanium and aluminium alloys. The first case uses the $\Delta K_{eff,an}$ curve with a=1. The second case used the $\Delta K_{eff,exp}$ curve with a=1 and the third $\Delta K_{eff,exp}$ curve with a=2.5. The combination of different effective curves and α's allows the observation of their effects on the fatigue life predictions.

By using the same constraint factor, the effects of the different ΔK_{eff} curve can be seen. On Ti1023, the use of $\Delta K_{eff,exp}$ curve produces slower crack growth rates and thus longer live comparing with the prediction using the $\Delta K_{eff,an}$ curve. The effects of the changes of the position of the ΔK_{eff} curve are the respective in the Al8090 and Al7010.

By using the same ΔK_{eff} curve and changing the α, FASTRAN produces different lives. On Ti1023, when a=1, the model gives the longer lives. It could be suggested that this is an effect of the plane strain conditions in the crack tip. Although, it is not clear whether there is a result of the transaction of the crack growth between plane stress and plane strain conditions. The constraint factor could also be considered as a tuning parameter to the final fatigue life. The influence of the factor α in the life predictions have to be examined against experimental results from specimens under plane stress and plane strain conditions.

The input case using the $\Delta K_{eff,exp}$ curve with a=2.5 appears to give conservative results under all the spectra and for all the material. The life prediction for this input case is very good for Ti1023 and Al8090, but with a high degree of conservatism for Al7010. That is because the crack growth on Al7010 can be best described by the case with α=1.

Very similar conclusions can be drawn about the FASTRAN life predictions under the helicopter spectra in relation with the three different input cases. The best predictions are achieved from the input case which best describe the actual ΔK_{eff} curve and the crack tip conditions. The cases with a=1 and different ΔK_{eff} curve exhibits small differences in the final lives. This indicates that there is a small difference in the two curves at the higher levels of the ΔK_{eff}.

Based on the above, it can be concluded that the FASTRAN model describes adequately the plasticity induced closure mechanism under the examined loading spectra. The model gives very good life predictions as long as the effective curve and constraint factor inputs correspond to the actual physical fatigue crack growth mechanism. It is should be underlined that FASTRAN model does predict adequately the accelerated crack growth when the right inputs are entered.

CHAPTER 12

CONCLUSIONS AND FUTURE WORK

12.1 Conclusions

The principal conclusions drawn from this work are summarized as follows:

1. The interpretation of the crack growth data with crack closure measurements has successfully correlated the crack growth rates in terms of the ΔK_{eff} into a very narrow band for Ti1023, Al8090 and Al7010 and the $\Delta K_{eff,exp}$ curve is clearly formed. The crack closure measurements are able to describe adequately the crack growth mechanism in the conducted tests.

2. Different material characteristics and microstructures under the same environmental conditions develop different crack closure behaviours. The crack opening values are typical values for the Ti1023, Al8090 and Al7010. The crack opening values of R=0 cycles were established at 0.4-0.44K_{max} at K_{max}>15 MPa $m^{1/2}$ for Ti1023, 0.6-0.8K_{max} at K_{max}>14 MPa $m^{1/2}$for Al8090, and 0.54-0.56K_{max} at K_{max}>12 MPa $m^{1/2}$ for Al7010.

3. The R ratio and K_{max} constant techniques for the determination of threshold ΔK_{th} do not seem to end up in significantly different test results on all three materials. The threshold measurements form one individual curve, independently of the technique used for their determination. The ΔK_{th} can be determined using either of the two test techniques.

4. The trend of ΔK_{th} in terms of R ratio seems to be a linear reduction up to around a critical R ratio value for the three alloys. The critical R ratio value is different for each alloy. At R ratios higher than R_T a plateau is formed.

5. Threshold values plotted in terms of the maximum stress intensity factor at the establishment of the threshold, $K_{max,th}$, reveal the existence of the ΔK_T and $K_{max,T}$ values for each alloy. The threshold parameters $K_{max,T}$ and ΔK_T are material properties that are intrinsically related to the fatigue mechanism. The curvature in the ΔK_{th} and K_{max} curve suggests that the two critical K_{max} and ΔK_{th} that must be satisfied simultaneously must have synergistic interactions, although in each R regime, one or the other is controlling the crack growth rates. Ti1023 has the large curvature and on Al7010 is non-existing. This conclusion is based on the

use of an automated load reduction system. Other techniques with more irregular load reduction may not produce the same data.

6. The high values of ΔK_{th} at low R ratios are the result of the path that the load approaches the threshold. The ΔK_{th} values increase from the gradual development of crack closure as the R ratio decreases.

7. The cracks under variable amplitude loading can grow faster than the linear summation life prediction, when they are subjected to small amplitude cycles at high R ratio and large amplitude cycles at low R ratio or underloads. The acceleration effects have different values depending on the number n of the small cycles, the K_{max}, and the R ratio of the small and the underload cycle. The effect of each of these loading factors has different effects on the three materials.

8. The acceleration factor α is around 1.6 for Ti1023 and 1.3 for Al7010 in relation with the number of small cycles in a loading sequence. On Al8090, factor α forms a bell shape curve as the number of small cycles n varies. The peak value of the factor is 9.4 and appears at n=10.

9. Closure measurements have shown that the crack growth acceleration is attributed to the action of the small high R ratio cycles, which decrease the crack opening point of large low R cycles. The observation is common for the three alloys. Also it was observed that the underload cycles do not affect the action of the small cycles at 0.7 and 0.9 R ratio.

10. The observations are consistent with an approach that different fatigue mechanisms are responsible for the reduction of the closure load on each material. On Ti1023, the plastic deformation behind the crack tip changes in a way that the crack surfaces move apart under the maximum load and a stationary crack. The mechanism is active but with limited influence on the aluminium alloys. The small effect of the plastic deformation of the material and the small changes in surface roughness produce small changes on crack closure on Al7010. On Al8090, roughness induced closure changes with the applied sequence governs the acceleration effects.

11. The rise of the K_{max} level changes the crack growth mechanism in the Ti1023 and increases the acceleration effects on the crack growth. On Al7010, the K_{max} effect is limited on the acceleration factors due to the small changes in the crack closure. On Al8090, the acceleration effects increase as the K_{max} value increases, with effect for the low K_{max} areas.

12. The change of the underload R_u ratio and the change in the consequent K_{min} have only a small effect on the crack growth rates and the underload closure point. The acceleration effects are due to the different way that the closure load changes comparing with the CAL values as the Ru increases. The observation applies on both Ti1023 and Al8090.

13. The change of the small cycles R_n ratio causes different acceleration effects on the crack growth rates. The effects are due to the combined change of the closure load of both the small and the underload cycles. The observation applies on both Ti1023 and Al8090.

14. Measurements of crack closure reveal the way that the crack closure builds up and decrease between CAL cycles and 1u/10n sequence on both Ti1023 and Al8090. The tests showed that the fatigue history plays an important role in the way that the crack closure changes and the crack growth.

15. The test results show that cracks under the various versions of helicopter loading spectrum can grow faster than the linear summation life prediction. The acceleration effects have different values depending on the version of the Rotarix spectrum and the material.

16. The effect of the different material on the crack growth under the most representative helicopter spectrum, Rot16, was examined. It was found that the Ti1023 has the largest acceleration factor of 3.16 and the Al7010 the smallest at 1.04. On Al8090 the factor is 1.78.

17. The best FASTRAN life predictions are achieved from the input cases that best describe the actual ΔK_{eff} curve and crack tip conditions. The conclusion is valid for both SVAL and CVAL prediction on the three material alloys.

18. The FASTRAN model describes adequately the plasticity induced closure mechanism under the examined loading spectra. The model does predict adequately the accelerated crack growth when the right inputs are entered. These differences in CVAL can be attributed to the effects a combination of different underloading SVAL spectra.

12.2 Future Work

1. Investigation of the role of the residual stresses effect on the crack growth under the combined action of small high R ratio cycles and underload. The research should consider evaluation of existing fatigue prediction models using the residual stress concepts such that K_{PR} model.

2. Analysis of the plastic deformation around the crack tip and the crack surface deformation under the action of the underloading sequences tested in this study using Finite Element Model simulations. Correlation of the finding with experimental measurements.

3. Extend the fatigue crack growth database on different types of material alloys such as high strength steels.

4. Detailed study of the microstructure, the alloys and the fracture surfaces produced by the underloading tests and examination against the suggested fatigue mechanisms.

5. Investigation on the mechanism responsible for the change of the Al8090 fracture roughness in relation with the fraction of underload cycles within a SVAL loading sequence.

6. The blind determination of the correct constraint value α for the FASTRAN model without the involvement of the experimental information was proven very difficult. Additionally, some observations of the effect of α are contradictory with the actual effect of the stress condition in the crack tip. Further investigation of the role and the importance of the constraint factor α in the model and on the life prediction must be examined.

References:

[1] Hall, A.D., 'Helicopter Fatigue Evaluation', Helicopter Fatigue-A review of current requirements and substantiation procedures, AGARD Report No 674, p. 13-20, September, 1978

[2] McGuigan, M.J., 'Helicopter Component Fatigue Life Determination', Helicopter Fatigue Life Assessment, AGARD Conference Proceedings No 297, p. 9-1 – 9-10, September, 1980

[3] FAA Airworthiness Regulations, Part 29, Transport Category Helicopters, Section 29.571, Fatigue Evaluation of Structure, Federal Aviation Administration, US Department of Transport

[4] FAA Advisory Circular, AC 29.571-1, Fatigue Evaluation of Transport Category Rotorcraft Structure, Federal Aviation Administration, US Department of Transport

[5] Paris, P. C., Bucci, R. J., Wessel, E. T., Clark, W. G., Mager, T. R., 'Extensive study of low fatigue crack rates in A533 and A508 steels', In Stress Analysis and Growth of Cracks, Special Technical Publications 513, ASTM, pp. 141-176, 1972

[6] Everett, Jr, R.A., 'A Comparison of Fatigue Life Prediction Methodologies for Rotorcraft', NASA Technical Memorandum TM 102759, December 1990

[7] Miner, M. A., 'Cumulative Damage in Fatigue', Journal of Applied Mechanics, 12, pp. 159-164, 1954

[8] Marquet, T., Struzik, A., 'Damage tolerance applied to metallic components', 24th European Rotorcraft Forum, Marseilles, France September 1998

[9] Crawford, C.C., Carlson, R.L., Bates, P.R., 'Damage Tolerance Analysis for Rotorcraft: What the issues are,' 17th European Rotorcraft Forum, Berlin, Germany, September 24-26, 1991

[10] Tapavicza M.V., Och, F., 'Application of Damage Tolerance Concepts for MBB Helicopters', AGARD Conference Proceedings No 297, September, pp. 4-1 – 4-8, , 1980

[11] Parker, A. P., 'The Mechanics of Fracture and Fatigue', E.& F. N. Spon Ltd, ISBN 0 419 11460 2, 1981

[12] Irwin, G. R., 'Analysis of stress and strain near the end of a crack traversing a plate', Journal of Applied Mechanics 24, 361-4,1957

[13] Westergaard, H. M., 'Bearing pressures and cracks', Journal of Applied Mechanics 61, A49-53, 1939

[14] Tada, G., Paris, P., Irwin, G., 'The stress Analysis Of Cracks Handbook', Del Research Corporation, Hellertown, PA, 1973

[15] Rooke, D.P., Cartwright, D.J., 'Compendium Of Stress Intensity Factors', Her Majesty's Stationary Office, England, 1976

[16] Suresh, S., 'Fatigue of Materials', Cambridge University Press, Second Edition, ISBN 0 521 57847 7, 1998

[17] Irwin, G. R., 'Plastic zone near a crack and fracture toughness', In Proceeding of the Seventh Sagamore Ordnance Materials Conference, vol. IV, pp. 63-78, New York: Syracuse University, 1960

[18] Dugdale, D.S., 'Yielding Of Steel Sheets Containing Slits', Journal of the Mechanics and Physics of Solids, vol 8, pp. 100-108, 1960

[19] Rice, J. R., 'Mechanics of crack tip deformation and extension by fatigue', Fatigue and Crack Propagation, ASTM STP 415, American Society of Testing and Materials, pp 247-311, 1967

[20] Paris, P. C., Gomez, M. P., & Anderson, W. P., 'A rational analytic theory of fatigue', The Trend in Engineering 13, 9-14, 1961

[21] Paris, P. C. & Erdogan, F., 'A critical analysis of crack propagation laws', Journal of Basic Engineering 85, 528-34, 1963

[22] Edwards, P. R., Dart, J., 'Standardised fatigue loading sequences for helicopter rotors (Helix and Felix), Part 2 Final definition of Helix and Felix'. Technical Report 84084, Royal Aircraft Establishment, August 1984

[23] Vasudevan, A.K., Sadananda, K., Lout, N., 'A review of crack closure, fatigue crack threshold and related phenomena', Material Science and Engineering, A188, pp. 1-22, 1994

[24] Taberning, B., Powell, P., & Pippen, R., 'Resistance curves for the threshold of fatigue crack propagation in particle reinforced Aluminium Alloys', Fatigue Crack Growth Thresholds, Endurance Limits, and Design, ASTM STP 1372, J. C. Newman, Jr. and R. S. Piasciak, Eds., American Society for Testing and Materials, West Conshohocken, PA, 2000

[25] Miller, K. J., 'The three thresholds for fatigue crack propagation', Fatigue nad Fracture Mechanics: 27th Volume, ASTM STP 1296, R. S. Piascik, J. C. Newman, and N. E. Dowling, Eds, American Society of Testing Materials, pp 267-286, 1997

[26] Forman, R.G., Kearney, V.E., and Engle, R.M., 'Numerical Analysis Of Crack Propagation In A Cyclic Loaded Structure', Journal of Basic Engineering, vol 89D, No. 3, pp. 459-464, 1967

[27] Christensen, R. H., 'Metal Fatigue', New York: McGraw Hill, 1959

[28] Elber, W., 'The significance of fatigue closure', Damage Tolerance In Aircraft Structures, ASTM STP 486, American Society of Testing and Materials, 1971, pp. 230-242

[29] Willeborg, J., Engle, R.M., Wood, H.A., 'A crack growth retardation model using an effective stress concept', AFFDL-TR-71-1, Air Force Flight Dynamics Laboratory, Wright-Patterson Air Force Base, OH, Jan 1971

[30] Schijve, J., 'Fatigue crack propagation in light alloy sheet material and structures', Advances in Aeronautical Sciences, Vol. 3, Prgamon Press, pp. 387-408, 1962

[31] Lang, M., Marci, G., 'Reflecting on the mechanical driving force of the fatigue crack propagation', Fatigue and Fracture Mechanics: Twenty-Ninth Volume, ASTM STP 1332, Eds: T.L. Panontin and S.D. Sheppard, American Society for Testing and Materials, West Conshohocken, PA, 1999

[32] Stewart, A. T., 'The influence of enviroment and stress ratio on fatigue crack growth at near threshold stress intensities in the low alloy steels', Engineering Fracture Mechanics 13, pp. 463-478, 1974

[33] Tsukuda, H., Ogiyama, H., Shiraishi, T., 'Fatigue Crack Growth And Closure At High Stress Ratios', Fatigue Fract. Engng. Mater. Struct. Vol 18 No 4, PP. 503-514, 1995

[34] Yigeng, X., Gegson , P, J., Sinclair, I., 'Systematic Assessment And Validation Of Compliance-Based Crack Closure Measurements In Fatigue', Material Science and Engineering, A284, pp. 114-125, 2000

[35] Pippan, R., Riemelmoser, F. O., ' Visualization of the Plasticity-Induced Crack Closure Under Plane Strain Conditions', Engineering Fracture Mechanics Vol 60, No 3, PP. 315-322, 1998

[36] Riemelmoser, F. O., Pippan, R., Stuwe, H.P., 'An argument for cycle-by-cycle propagation of fatigue cracks at small stress intensity ranges', Acta Matallurgica., 46, 5, pp. 1793-1799, 1998

[37] Wallhead, I. R., Edwards, L., 'A Study Of Crack Closure Using The Optical Method Of Caustics And Consequences For The Use Of Δk_{eff} As A Fatigue Crack Driving Force', Engineering Fracture Mechanics, Vol. 60, No 3, pp. 291-302, 1998

[38] Sadananda, K., Vasudevan, A.K., Glinka, G., 'Critical Parameters For Fatigue Damage', International Journal of Fatigue 23, pp. S39-S53, 2001

[39] Budiansky, B., Hutchinson, J. W., 'Analysis of closure in fatigue crack growth', Journal of Applied Mechanics, 45, pp. 267-276, 1978

[40] Riemelmoser, F. O. Pippan, R., 'Crack Closure: A Concept of Fatigue Crack Growth Under Examination', Fatigue Fract. Engng. Mater. Struct. Vol 20, No 11, PP. 1529-1540, 1997

[41] Riemelmoser, F. O. Pippan, R., 'Mechanical Reasons For Plasticity-Induced Crack Closure Under Plane Strain Conditions', Fatigue Fract. Engng. Mater. Struct. 21, PP. 1425-1433, 1998

[42] Kim, J. H., Lee, S. B., 'Behavior of Plasticity-Induced Crack Closure and Roughness-Induced Crack Closure in Aluminum Alloy', International Journal of Fatigue 23, pp. S247-S251, 2001

[43] Jung, H. Y., Antolovich, S. Y., 'Fatigue Crack Closure As A Function of Crack Length In Al-Li Alloys', Engineering Fracture Mechanics Vol 54, No 3, PP. 307-324, 1996

[44] Parry, M. R., Syngellakis, S., Sinclair, I., 'Numerical Modeling of Combined Roughness And Plasticity-Induced Crack Closure Effects In Fatigue', Numerical Science and Engineering A291, pp. 224-234, 2000

[45] Lang, M., Marci, G., 'The Influence Of Single And Multiple Overloads On Fatigue Crack Propagation', Fatigue Fract. Engng. Mater. Struct. 22, PP. 257-271, 1999

[46] Lang, M., Huang, X., 'The Influence Of Compressive Loads On Fatigue Crack Propagation In Metals', Fatigue Fract. Engng. Mater. Struct. 21, PP. 65-83, 1998

[47] Lang, M., 'Description Of Load Interaction Effects By The ΔK_{eff}-Concept', In Advances in Fatigue Crack Closure Measurements and Analysis, ASTM STP 1343, ASTM, PA, pp. 207-223, 1998

[48] Sadananda, K., Vasudevan, A.K, 'Short Crack Growth Behavior', Fatigue and Fracture Mechanics: 27^{th} Volume, ASTM 1396, ASTM, pp. 301-316, 1997

[49] Sadananda, K., Vasudevan, A.K., Holtz, R. L., Lee, E. U., 'Analysis Of Overload Effects And Related Phenomena', International Journal of Fatigue 21, pp. S233-S246, 1999

[50] Lout, N., Sadananda, K., Duesbery, M., Vasudevan, A.K 'A theoretical evaluation of crack closure', Metallurgical Transactions A, 24A,pp. 2225-2232, 1993

[51] Donald, J. K., Bray, G. H., Bush, R. W., 'Introducing the K_{max} sensitivity Concept For Correlating Fatigue Crack Propagation', High Cycle Fatigue Of Structural Materials: Symposium Proceeding in Honor of Prof. Paul C. Paris, PA:TMS, pp. 123-141, 1998

[52] Wilkinson, A. J., Robert, S. G., 'A Dislocation Model For The Two Critical Stress Intensities Required For Threshold Fatigue Crack Propagation', Scripta Materialia, Vol. 35 No 11, pp. 1365-1371, 1996

[53] Liu, H. W., 'A Dislocation Barrier Model For Fatigue Crack Growth Threshold', International Journal of Fracture 93, pp. 261-280, 1998

[54] Hammouda, M. M. I., El-Sehily, B. M., De Los Rios, E. R., 'The Significance Of Crack Tip Deformation For Short And Long Fatigue Cracks', Fatigue Fract. Engng. Mater. Struct. Vol 19 No 4, PP. 475-484, 1996

[55] Toyosada, M., Niwa, T., 'The Significance Of RPG Load For Fatigue Crack Propagation And The Development Of A Compliance Measuring System', International Journal of Fracture 67, pp. 217-230, 1994

[56] Toyosada, M., Niwa, T., Sakai, J., 'Physical Meaning Of ΔK_{RP} And Fatigue Crack Propagation In The Residual Stress Distribution Field', International Journal of Fatigue Vol 19, No 1, pp. S161-S166, 1997

[57] Tong, F. C., Gray, T. G. F., 'Fatigue Crack Closure Study Based On Whole-Field Displacements', International Journal of Fatigue Vol. 18, No 8, pp. 593-601, 1996

[58] Schijve, J., 'Fatigue Crack Closure, Observations And Technical Significance', Report LR-485, Department of Aerospace Engineering, Delft University of Technology, April 1986

[59] Fleck, N. A., 'An Investigation Of Fatigue Crack Closure', Report CUED/C-MATS/TR. 104, Engineering Department, Cambridge University, May 1984

[60] Yieshieng, W., Schijve, J., 'Fatigue Crack Closure Measurements On 2024-T3 Sheet Specimens', Fatigue Fract. Engng. Mater. Struct. Vol 18 No 9, PP. 917-921, 1995

[61] Lee, C. S., Park, C. G., Chang, Y. W., 'Precise Determination Of Fatigue Crack Closure In Al Alloys', Material Science and Engineering, A216, pp. 131-138, 1996

[62] Brahma, K. K., Dash, P. K., Dattaguru, B., 'Observation Of Crack Closure Using A Crack Mouth Opening Displacement Gauge', International Journal of Fatigue Vol. 11, No 1, pp. 37-41, 1989

[63] Donald, J. K., 'Introducing The Compliance Ratio Concept For Determining Effective Stress Intensity', International Journal of Fatigue Vol. 19, No 1, pp. S191-S195, 1997

[64] Donald, J. K., Paris, P. C., 'An evaluation of ΔK_{eff} estimation procedures on 6061-T6 and 2024-T3 aluminium alloys', International Journal of Fatigue 21, pp. S47-S57, 1999

[65] Newman, J, C., Jr., 'An Evaluation Of Plasticity-Induced Crack Closure Concept And Measurements Method', In Advances in Fatigue Crack Closure Measurements and Analysis, ASTM STP 1343, ASTM, PA, pp. 128-144, 1999

[66] Zhang, S, J., Doker, H., Nowack, H., Schulte, K., Trautmann, K. H., 'Exact Determination Of Δk_{eff} And Crack Propagation Prediction For Selected Loading Sequences', In: Advances in Fatigue Lifetime Predictive Techniques, ASTM STP 1211, ASTM, PA, pp. 54-71, 1993

[67] Lawson, L., Chen, E.Y., Meshii, M., 'Near-Threshold fatigue: a review', International Journal of Fatigue, 21, S15-S34, 1999

[68] ASTM standards E647, Standard Test Method for Measurement of Fatigue Crack Growth Rates. American Society for Testing and Materials

[69] Surech, S., 'Micromechanisms of Fatigue crack growth retardation following overloads', Engineering Fracture Mechanics, Vol. 18, No 3, pp. 577-593, 1983

[70] Liaw, P. K., 'Overview of crack closure at near –threshold fatigue crack growth levels', In Mechanics of Fatigue Crack Closure, ASTM STP 982, ASTM, PA, pp. 62-92, 1998

[71] Pippan, R., Hageneder, P., Knabl, W., Clemens, H., Hebesberger, T., Tabering, B., 'Fatigue threshold and crack propagation in TiAl sheets', Intermatallics, 9, pp. 89-96, 2001

[72] Kardomateas, G.A., Carlson, R.L., 'Predicting the effects of load ratio on the fatigue crack rate and fatigue threshold', Fatigue & Fracture of Engineering Materials & Structures, 21, 411-423, 1998

[73] Newman, J. A., Riddell, W. T., Piascik, R. S., 'Effects of K_{max} on Fatigue crack growth threshold in aluminium alloys', In Fatigue Crack growth thresholds, endurance limits and design, ASTM STP 1372, ASTM, West Conshohochen, PA, pp. 63-77, 200

[74] Xu-Dong Li, Edwards, L., 'Theoretical modelling of fatigue threshold for aluminium alloys', Engineering Fracture Mechanics, 54, pp. 35-48,1996

[75] Wilkinson, A. J., Roberts, S. G., 'A dislocation model for the two critical stress intensities required for the threshold fatigue crack propagation', Scripta Metarialia, Vol. 35, No 11, pp. 1365-1371, 1996

[76] Lenets, Y. N., Nicholas, T., 'Load history dependence of fatigue crack growth thresholds for a Ti-alloy', Engineering Fracture Mechanics, Vol 60, No 2, pp187-203, 1998

[77] Vasudeven, A. K., Sadanada, K., Lout, N., 'A review of crack closure, fatigue crack threshold and related phenomena', Material Science and Engineering, A188, pp. 1-22, 1994

[78] Vasudeven, A. K., Sadanada, K., Lout, N., 'Dislocation behavior under fatigue' TMS annual meeting, Feb 10-13, ASM-MSD, pp. 395-402

[79] Vasudeven, A. K., Sadanada, K., Lout, N., 'Two critical stress intensities for threshold fatigue crack propagation', Scripta Metallurgica, 28, pp. 65-70, 1993

[80] Vasudeven, A. K., Sadanada, K., 'Classification of fatigue crack growth behavior', Metallurgical and Materials Transactions A, 26A, pp. 1221-1234, 1995

[81] Boyce, B. L., Ritchie, R. O., 'Effects of load ratio and maximum stress intensity on the fatigue threshold in Ti-6Al-4V', Engineering Fracture Mechanics, 68, pp. 129-147, 2001

[82] Deshpande, V. S., Needleman, A., Van Der Giessen, E., 'A discrete dislocation analysis of near-threshold fatigue crack growth', Acta Metarialia, 49, pp. 3189-3203, 2001

[83] FAA Advisory Circular, AC 29.571-1, Fatigue Evaluation of Transport Category Rotorcraft Structure, Federal Aviation Administration, US Department of Transport

[84] Buller, R. G., 'Investigation of helicopter loading spectra variations on fatigue growth in Titanium and Aluminium Alloys', Ph.D thesis, Cranfield University, April 1999

[85] Fleck, N. A., 'Fatigue crack growth due to periodic underloads and overloads' Acta Metall. Vol 33, No 7, pp. 1339-1354, 1985

[86] Buller, R. G., Jenkins, S., 'WP320-Material Data and component tests on WHMS 640 (Ti-10V-2Fe–3Al)', Final report, GKN Westland Helicopters, LR97, 182 DTI-LINK RA/6/30/06, 1998

[87] Skorupa, M., Schijve, J., Skorupa, A., Machniewicz, T., 'Fatigue crack growth in a structural steel under single and multiple periodic overload cycles', Fatigue Fract. Engng. Mater. Struct., 22, pp. 879-887, 1999

[88] Russell, S. G., 'A new model for fatigue crack growth retardation following an overload', Engineering Fracture Mechanics, Vol. 33, No 6, pp. 839-854, 1989

[89] Kuo, A. S., Guillaume, M., Michel, S., 'Residual stress model for spectrum crack growth analysis', International Journal Of Fracture, 85, pp. L17-L23, 1997

[90] Sadananda, K., Vasudevan, A. K., 'Short crack growth and internal stresses', International Journal of Fatigue, Vol 19, No 1, pp. S99-s108, 1997

[91] Tsukuda, H., Ogiyama, H., Shiraishi, T., 'Fatigue Crack Growth And Closure At High Stress Ratios', Fatigue Fract. Engng. Mater. Struct. Vol 18 No 4, PP. 503-514, 1995

[92] Ellyin, F., Wu, J., 'A numerical investigation on the effect of an overload on fatigue crack opening and closure behaviour', Fatigue Fract. Engng. Mater. Struct. Vol, 22, PP. 835-847, 1999

[93] Schijve, J., 'Fatigue of Structures and Materials', Kluwer Academic Publishers, ISBN 0 7923 7013 9, 2001

[94] Macha, D. E., Grandt, A. F., Jr., and Wicks, B. J., 'Effects of Gas Turbine Engines Load Spectrum Variables on Crack Propagation', Effect of load Spectrum Variable on fatigue Crack Initiation and Propagation, ASTM STP 714, ASTM, 108-127, 1980

[95] Carlson, R. L., Kardomateas, G.A., 'Effects of compressive load excursion on fatigue crack growth', International Journal of Fatigue, 16, 141-146, 1994

[96] Dabayeh, A. A., Xu, R. X., Du, B. P., Topper, T. H., 'Fatigue of cast aluminium alloys under constant and variable- amplitude loading', International Journal of Fatigue 18, 2, 95-104, 1996

[97] Dabayeh, A. A., Topper, T. H., 'Changes in crack opening stress after underloads and overloads in 2024-T351 aluminium alloy', International Journal of Fatigue Vol 17, No 4, pp. 261-269, 1995

[98] Khalil, M., Topper, T. H., Soudki K., 'Modeling of Crack-Opening Stress Levels under Different Service Loading Spectra and Stress Levels for a 1045 Annealed Steel', Proceedings ICF 10, Hawaii, USA, December 2001

[99] Ranganathan, N., Adiwijayanto, F., Petit, J., Bailon, J. P., 'Fatigue crack propagation mechanism in an aluminium lithium alloy', Acta Metall. Mater., Vol 43, No 3, pp. 1029-1035, 1995

[100] Topper, T. H., Yu, M. T., 'The effect of overloads on threshold and crack closure', , International Journal of Fatigue Vol 16, pp. 141-146, 1994

[101] Russ, S. M., Johnson, D. A., 'Load-Interaction effects in simple mission spectra for Ti-17: Understanding the deformation before and after an underload', Proceedings of 8th International Fatigue Congress, Stockholm, Sweden, June 2002

[102] Hawkyard, M., Powell, B.E., Stephenson, J.M., McElhone, M., 'Fatigue crack growth from simulated fligth cycles involving superimposed vibrations', International Journal of Fatigue 21, S59-S68,1999

[103] Hawkyard, M., Powell, B. E., Hussey, I., Crabowski, L., 'Fatigue crack growth under the conjoint action of major and minor stress cycles', Fatigue Fract. Engng. Mater. Struct. Vol, 19, No 2/3, PP. 217-227, 1996

[104] Yang, R., 'Prediction of fatigue crack growth under complex loading cycles', Fatigue, Vol 16 pp. 397-402, 1994

[105] Abelkis, P. R., 'Effects of Transport Aircraft Wing Loads Spectrum Variation on Fatigue Crack Growth Rates', Effect of load Spectrum Variable on fatigue Crack Initiation and Propagation, ASTM STP 714, D. F. Brayn and J. M. Potter, Eds, American Society for Testing and Material, 1980, pp. 143-169

[106] de Jonge, J. B and Nederveen, A., 'Effects of Gust Load Alleviation on Fatigue Crack Growth in ALCLAD 2024-T3', Effect of load Spectrum Variable on fatigue Crack Initiation and Propagation, ASTM STP 714, D. F. Brayn and J. M. Potter, Eds, American Society for Testing and Material,170-184, 1980

[107] Dill, H. D., Saff, C. R., and Potter, J. M., 'Effects of Fligther Attach Spectrum on Crack Growth', Effect of load Spectrum Variable on fatigue Crack Initiation and Propagation, ASTM STP 714, D. F. Brayn and J. M. Potter, Eds, American Society for Testing and Material, 205-217, 1980

[108] Larson, C. E., White, D. J., and Gray, T. D., 'Evaluating Spectrum Effects in U.S. Air Force Attack/Figther/Trainer Individual Aircraft Tracking', Effect of load Spectrum Variable on fatigue Crack Initiation and Propagation, ASTM STP 714, D. F. Brayn and J. M. Potter, Eds, American Society for Testing and Material, 218-227, 1980

[109] Buller, R. G., and Irving, P., E., 'Prediction of fatigue life under helicopter loading spectra for safe life and damage tolerance design', *Fatigue and Fracture Mechanics 29th vol* ASTM STP 1332, ASTM, pp 727-742, USA, 1999

[110] Ranganathan, N., 'Certain aspects of variable amplitude fatigue', Proceedings of 8th International Fatigue Congress, Stockholm, Sweden, June 2002

[111] Wanhill, R. J. H., Schijve, J., 'Current status of flight simulation fatigue crack growth concepts', National Aerospace Lab., NLR MP 88001 U, The Netherlands, 1977

[112] Wanhill, R. J. H., 'Flight simulation fatigue crack propagation evaluation of candidate lower wind skin materials with particular consideration of spectrum truncation', , National Aerospace Lab., NLR TR 7092 U, The Netherlands, 1979

[113] Kim, C. Y., Song, J. H., 'Fatigue crack closure and growth behaviour under random loading', Engineering Fracture Mechanics, Vol 49, No 1, pp. 105-120, 1994

[114] Sunder, R., ' Near- Threshold Fatigue Crack Growth Prediction Under Spectrum Loading', Advances in Fatigue Lifetime Predictive Techniques, ASTM STP 1122, ASTM, Philadelphia, pp. 161-175, 1992

[115] Newman, J.C., Jr., ' Prediction of fatigue crack growth under variable amplitude and spectrum loading using a crack closure model', Design of fatigue and Fracture Resistant Structures, ASTM STP 761, ASTM, pp. 255-277, 1982

[116] Harter, James A., "AFGROW Users manual, Version 4.0001.11.8, Technical Memorandum," AFRL-VA-WP-TR-2000-XXXX, AFWAL Flight Dynamics Laboratory, Wright-Patterson AFB, OH, 2000

[117] Willeborg, J., Engle, R.M., Wood, H.A., 'A crack growth retardation madel using an effective stress concept', AFFDL-TR-71-1, Air Force Fligth Dynamics Laboratory, Wrigth-Patterson Air Force Base, OH, Jan 1971

[118] de Koning, A. U., 'A simple crack closure model for prediction of fatigue crack growth rates under variable amplitude loading', Fracture Mechanics, ASTM STP 743, ASTM, pp. 63-85, 1981

[119] Newman, J.C., Jr., 'A crack closure model for predicting fatigue crack growth under aircraft spectrum loading', Methods and models model for predicting fatigue crack growth under random loading, ASTM STP 748, ASTM, pp. 53-84, 1981

[120] Salvetti, A., Lazzeri, L., Pieracci, A., 'An assessment of fatigue crack growth prediction models for aerospace structures', AGARD Meeting on 'An Assessment Of Fatigue Damage and Crack Growth Prediction Techniques', pp. 6-1 – 6-19, September 1993

[121] Lazzeri, L., Pieracci, A., Salvetti, A., 'An evaluation of fatigue crack growth prediction methods used in aircraft design', Proceeding of ICAF 95, Melbourne, Australia, June 1995

[122] Wonzumi, J.T., Spamer, T., and lambert, G. E., 'An Engineering Model for Assessing Load Sequencing Effects', Effect of load Spectrum Variable on fatigue Crack Initiation and Propagation, ASTM STP 714, ASTM, pp. 128-142, 1980

[123] Johnson, W. S., 'Multi-Parameter Yield Zone Model for Predicting Spectrum Crack Growth', Methods and Models for Predicting Fatigue Crack Growth Under Random Loading, ASTM STP 748, ASTM, pp. 85-102, 1981

[124] Chang, J.B., Szamossi, M., and Liu, K.W., 'Random Spectrum Fatigue Crack Life Predictions With or Without Considering Load Interactions', Methods and Models for Predicting Fatigue Crack Growth Under Random Loading, ASTM STP 748, ASTM, pp. 115-132, 1981

[125] Kraken, Users Manual, nCode International Ltd., Sheffield, U.K., 1995

[126] Schijve, J., 'Prediction Method For Fatigue Crack Growth In Aircraft Material', In Fracture Mechanics: Twelfth Conference, Special Technical Publication 700, Philadelphia: ASTM, pp. 3-34, 1980

[127] Sunder, R., 'Contribution of Individual Load Cycles to Crack Growth Under Air craft Spectrum Loading ', Advances in Fatigue Lifetime Predictive Techniques, ASTM STP 1122, ASTM, Phladelphia, pp. 176-190, 1992

[128] van de Linder, H.H., de Koning, A.U., Lof, C.J., 'New Analytical Model for Prediction of Fatigue Crack Growth Under Realistic Loading', International Journal of Vehicle Design, Vol 7, No 3/4, pp. 288-305, 1986

[129] Hewitt, R.L., Collins, P.G., 'Crack Growth Predictions Using a Crack Closure Model', AGARD Meeting on 'An Assessment Of Fatigue Damage and Crack Growth Prediction Techniques', pp. 3-1 – 3-23, September 1993

[130] Ibso, J.B., Agerskov, H., 'An Analytical Model for Fatigue Life Prediction Based on Fracture Mechanics and Crack Closure', Journal of Construct. Steel Res. 37, 3, pp. 229-261, 1996

[131] Newman, Jr. J. C., Armen, H., 'Elastic plastic analysis of a propagating crack under cyclic loading', AIAA Journal, Vol 13, pp. 1017-1023, 1975

[132] Ohji, K., Orura, K., Ohkubo, Y., 'Cyclic analysis of a propagating crack and its correlation with fatigue crack growth', Engineering Fracture Mechanics, Vol 17, pp. 457-463, 1975

[133] Ibso, J. B., Agerskov, H., 'An analytical model for fatigue life predictions based on fracture mechanics and crack closure', J. Construct. Steel Res., Vol 37, No 3 pp. 229-261, 1996

[134] Daniewicz, S. R., Collins J. A., Houser D. R., 'An elastic-plastic analytical model for predicting fatigue crack growth in arbitrary edge-cracked two-dimensional geometries with residual stress', Fatigue, Vol 16, pp. 123-133, 1994

[135] Newman, J.C., Jr., 'A crack opening stress equation for fatigue crack growth'. International Journal of Fracture, 24, pp. R131-R135, 1984

[136] Bergner, F., Zouhar, G., Tempus, G., 'The material-dependent variability of fatigue crack growth rates of aluminium alloys in Paris regime', International Journal of Fatigue, 23, 383-394, 2001

[137] Wu, X.J., Wallace, W., Koul, A.K., Raizenne, M.D., 'Near-Threshold fatigue crack growth in Al8090 Al-Li Alloy', Metallurgical and Materials Transactions A, 26A, 2973-2982, 1995

[138] Kumai, S., Higo, Y., 'Effects of Delamination on fatigue crack growth retardation after single tensile overload in Al-Li alloys', Material Science an Engineering, A221, 154-162, 1996

[139] Vasudevan, A.K., Sadananda, K., 'Classification of fatigue crack growth behavior', Metallurgical and Materials Transactions A, 26A, 1221-1234, 1995

[140] Fleck, N.A., Newman, J.C., 'Analysis Of Crack Closure Under Plane Strain Conditions', Report CUED/C-MATS/TR127, Engineering Department, Cambridge University, May 1986

[141] Fleck, N.A., 'Finite Element Analysis Of Plasticity-Induced Crack Closure Under Plane Strain Conditions', Report CUED/C-MATS/TR128, Engineering Department, Cambridge University, May 1986

[142] Kujawski, D., 'Enhanced Model of The Partial Crack Closure For Correlation Of R-Ratio Effects In Aluminium Alloys', International Journal of Fatigue Vol. 23, pp. 95-102, 2000

[143] Newman, J. C., Jr., 'FASTRAN II – A Fatigue Crack Growth Structural Analysis Program', NASA Technical Memorandum 104159, 1992.

[144] Lazzeri, L., Ratti, G., 'Fatigue Crack Propagation In Thin 2024 Sheets Under Typical Helicopter Spectra', Proceeding of 8th ICF 02, Stockholm, Sweden, June 2002

[145] Ranganathan, N., 'Certain Aspects of Variable Amplitude Fatigue', Proceeding of 8th ICF 02, Stockholm, Sweden, June 2002

[146] Buller, R. G., Jenkins, S., 'WP310-Material Data and component tests on EM120 (8090 T852)', Final report, GKN Westland Helicopters, LR97,224, 1998

[147] Jenkins, S., 'WP810-Material Characterization and Enhanced Safe Life Data Collection', Issue 1, GKN Westland Helicopters, LR02,024, 2002

[148] Koterazawa, R., Mudjijana, Qinsheng, Y., Tian-Jian, W., and Nosho, T., 'Acceleration Of Fatigue Crack Growth Under Intermittent Overstressing With Different Mean Stress Levels', Fatigue Fract. Engng. Mater. Struct., Vol 17, No 9, pp. 1033-1041, 1994

[149] Cui, J., Fu, Y., Li, N., Sun, J., He, J., Dai, Y., 'Study Of Fatigue Crack Propagation And Extrinsic Toughening Of An Al-Li Alloy', Material Science an Engineering, A281, pp. 126-131, 2000

[150] Newman, J. C., Jr., Bigelow, C. A., Shivakumar, K. N., 'Three Dimensional Elastic-Plastic Finite Element Analysis of Constrain Variations In Cracked Bodies', Engineering Fracture Mechanics, vol46, pp 1-13, 1993.

[151] McMaster, F. J., Smith, D. J., 'Prediction of Fatigue Crack Growth In Aluminium Alloys 2024-T351 Using Constraint Factors', International Journal of Fatigue, 23, S93-S101, 2001

[152] Marci, G., 'The ΔK_{eff} concept: A unique and complete description of Fatigue Crack Propagation ', Engineering Fracture Mechanics, vol55, pp 95-114, 1996.

[153] Rosenberger, A. H., Larsen, J. M., Lang, M., 'Predicting Fatigue Growth Using The K_{PR} Concept', Proceeding of 8th ICF 02, Stockholm, Sweden, June 2002

[154] Boyer, R., R., Rosenburg, H., W., 'Ti-10V-2Fe-3Al Properties', in R.R Boyer and H.W Rosenburg (Eds.) Beta Titanium Alloys in the 1980's, Proceedingd of a symposium sponsored by the Titanium Committee of AIME, The Metallurgical Society, Atlants, Georgia, p441-456, March 1983

[155] Reynolds, M., A., Fitzsimmons, P., E., Harris, J., G., 'Presentation of the Properties of a new High Strength Aluminium Alloy Designated 7010', Aluminium Alloys in the Aircraft Industry, Proceedings of Symposium, Turin, October, 1976

[156] Stress Intensity Factors Handbook, Vol1, Committee on Fracture Mechanics, The Society of Material Science, Japan, Y. Murakami Ed. Permagon Press, 1987

[157] Wei, R. P., an Brazil, R. L., 'An assessment of A-C and D-C potential systems for monitoring fatigue crack growth', fatigue Crack Growth Measurement and Data Analysis. ASTM STP 738, S.J. Hudak, Jr. and R. J. Bussi, Eds, American Society of Testing and Material, pp. 103-119, 1981

[158] Beauchamp, K., G., 'Signal Processing Using Analog and Digital Techniques', George Allen & Unwin Ltd, ISBN 0 04 621019 9, 1973

[159] Harter, J., A., 'Comparison of Contemporary FCG Life Prediction Tools', International Journal of Fatigue, 21, S181-S158, 1999

[160] Newman, J. C., Jr., Nagaralu, R., Slater, N., R., 'Prediction of Crack Growth in an Aluminium and Titanium Alloy under Rotorcraft Spectrum Loading', Proceeding of 8th ICF 02, Stockholm, Sweden, June 2002

APPENDIX A

Table A1._ Crack lengths and loading conditions for SVAL testing on Ti 1023

Test ID	Sample ID	K_{max} (MPa $m^{1/2}$)	Small Cycles			Underload Cycles			Crack length (m)		Total Number of Cycles	Closure Data
			ΔK_n (MPa $m^{1/2}$)	R_n	n	ΔK_u (MPa $m^{1/2}$)	R_u	n_u	Starting	Final		
2Ti1u01s1	2ccT20	15.7	1.57	0.9	1	15.7	0	1	0.0223	0.0255	$4.4\ 10^4$	N/A
2Ti1u01s2	2ccT24	15.7	1.57	0.9	1	15.7	0	1	0.0204	0.0218	$2.5\ 10^4$	N/A
2Ti1u05s1	2ccT23	15.7	1.57	0.9	5	15.7	0	1	0.029	0.0390	$30.7\ 10^4$	N/A
2Ti1u05s2	2ccT24	15.7	1.57	0.9	5	15.7	0	1	0.0171	0.0194	$12\ 10^4$	N/A
2Ti1u10s1	2ccT20	15.7	1.57	0.9	10	15.7	0	1	0.014	0.01806	$33\ 10^4$	N/A
2Ti1u10s2	2ccT24	15.7	1.57	0.9	10	15.7	0	1	0.0145	0.0161	$16.5\ 10^4$	N/A
2Ti1u10s3	2ccT25	15.7	1.57	0.9	10	15.7	0	1	0.0287	0.0297	$8.8\ 10^4$	v
2Ti1u10s4	2ccT28	7.85	1.57	0.8	10	7.85	0	1	0.0149	0.0156	$55\ 10^4$	V
2Ti1u10s5	2ccT25	17.63	1.57	0.92	10	19.63	0	1	0.031	0.0318	$3.3\ 10^4$	V
2Ti1u10s6	2ccT25	23.5	1.57	0.94	10	26.17	0	1	0.0331	0.0346	$4.4\ 10^4$	v
2Ti1u10s7	2ccT25	15.7	1.57	0.9	10	10.99	0.3	1	0.0158	0.0169	$13.7\ 10^4$	V
2Ti1u10s8	2ccT25	15.7	1.57	0.9	10	7.85	0.5	1	0.0189	0.020	$44\ 10^4$	V
2Ti1u10s9	2ccT25	15.7	4.71	0.7	10	15.7	0	1	0.0262	0.0273	$4.4\ 10^4$	V
2Ti1u10s10	2ccT25	15.7	9.42	0.4	10	15.7	0	1	0.0223	0.0251	$4.4\ 10^4$	V
2Ti1u20s1	2ccT17	15.7	1.57	0.9	20	15.7	0	1	0.026	0.03448	$1.05\ 10^6$	N/A
2Ti1u20s2	2ccT26	15.7	1.57	0.9	20	15.7	0	1	0.0357	0.0370	$20.2\ 10^4$	N/A
2Ti1u100s1	2ccT20	15.7	1.57	0.9	100	15.7	0	1	0.0185	0.02129	$202\ 10^4$	N/A
2Ti1u1000s1	2ccT27	15.7	1.57	0.9	100	15.7	0	1	0.037	0.03769	$500.5\ 10^4$	N/A
2Ti1u1000s2	2ccT40	15.7	1.57	0.9	1000	15.7	0	1	0.0389	0.0397	$393\ 10^4$	N/A

Table A1._ Crack lengths and loading conditions for SVAL testing on Ti 1023. Continue…

Test ID	Sample ID	K_{max} (MPa $m^{1/2}$)	Small Cycles			Underload Cycles			Crack length (m)		Total Number of Cycles	Closure Data
			ΔK_n (MPa $m^{1/2}$)	R_n	n	ΔK_u (MPa $m^{1/2}$)	R_u	n_u	Starting	Final		
71	2ccT17	6.34	1.9	0.7	20	6.34	0	1	0.0246	0.02492	10^6	N/A
72	2ccT32	6.34	1.9	0.7	1000	6.34	0	1	0.014	0.0141	10^6	N/A
73	2ccT32	6.34	1.9	0.7	2000	6.34	0	1	0.016	0.0162	10^6	N/A
74	2ccT32	6.34	1.9	0.7	4000	6.34	0	1	0.0165	0.0165	10^6	N/A
75	2ccT32	6.34	1.9	0.7	5000	6.34	0	1	0.015	0.015	10^6	N/A
76	2ccT32	6.34	1.9	0.7	10000	6.34	0	1	0.0147	0.01471	10^6	N/A
77	2ccT32	6.34	1.9	0.7	20000	6.34	0	1	0.0175	0.01751	10^6	N/A
78	2ccT32	6.34	1.9	0.7	50000	6.34	0	8	0.0185	0.0185	10^6	N/A
79	2ccT32	6.34	1.9	0.7	1000	6.34	0	5	0.0225	0.02252	10^6	N/A
710	2ccT32	6.34	1.9	0.7	2000	6.34	0	5	0.0235	0.023	10^6	N/A
711	2ccT32	6.34	1.9	0.7	4000	6.34	0	5	0.02557	0.0259	10^6	N/A
712	2ccT32	6.34	1.9	0.7	5000	6.34	0	5	0.0275	0.0274	10^6	N/A
713	2ccT32	6.34	1.9	0.7	10000	6.34	0	5	0.0295	0.0294	10^6	N/A
714	2ccT32	6.34	1.9	0.7	20000	6.34	0	5	0.0305	0.0305	10^6	N/A
715	2ccT32	6.34	1.9	0.7	50000	6.34	0	5	0.0315	0.03151	10^6	N/A
716	2ccT31	6.34	1.9	0.7	1000	6.34	0	20	0.014	0.01404	10^6	N/A
717	2ccT31	6.34	1.9	0.7	2000	6.34	0	20	0.015	0.01503	10^6	N/A
718	2ccT31	6.34	1.9	0.7	4000	6.34	0	20	0.017	0.01701	10^6	N/A
719	2ccT31	6.34	1.9	0.7	5000	6.34	0	20	0.0235	0.03251	10^6	N/A
720	2ccT31	6.34	1.9	0.7	10000	6.34	0	20	0.0255	0.02559	10^6	N/A
721	2ccT31	6.34	1.9	0.7	20000	6.34	0	20	0.0275	0.02752	10^6	N/A
722	2ccT32	6.34	1.9	0.7	50000	6.34	0	20	0.0325	0.0325	10^6	N/A

Table A1._ Crack lengths and loading conditions for SVAL testing on Ti 1023. Continue…

Test ID	Sample ID	K_{max} (MPa $m^{1/2}$)	Small Cycles			Underload Cycles			Crack length (m)		Total Number of Cycles	Closure Data
			ΔK_n (MPa $m^{1/2}$)	R_n	n	ΔK_u (MPa $m^{1/2}$)	R_u	n_u	Starting	Final		
723	2ccT31	6.34	1.9	0.7	1000	6.34	0	50	0.02251	0.02262	10^6	N/A
724	2ccT31	6.34	1.9	0.7	2000	6.34	0	50	0.0207	0.02081	10^6	N/A
725	2ccT31	6.34	1.9	0.7	4000	6.34	0	50	0.0215	0.02152	10^6	N/A
726	2ccT31	6.34	1.9	0.7	5000	6.34	0	50	0.0245	0.02455	10^6	N/A
727	2ccT31	6.34	1.9	0.7	10000	6.34	0	50	0.0265	0.02563	10^6	N/A
728	2ccT31	6.34	1.9	0.7	20000	6.34	0	50	0.0285	0.02857	10^6	N/A
729	2ccT31	6.34	1.9	0.7	50000	6.34	0	50	0.0295	0.02953	10^6	N/A
730	2ccT26	6.34	1.9	0.7	1000	6.34	0	50	0.016	0.01609	10^6	N/A

Table A2._ Crack lengths and loading conditions for SVAL testing on Al 8090

Test ID	Sample ID	K_{max} (MPa $m^{1/2}$)	Small Cycles			Underload Cycles			Crack length (m)		Total Number of Cycles	Closure Data
			ΔK_n (MPa $m^{1/2}$)	R_n	n	ΔK_u (MPa $m^{1/2}$)	R_u	n_u	Starting	Final		
2A81u01s1	CCT06	14.1	1.41	0.9	1	14.1	0	1	0.0315	0.03553	$7.5\ 10^4$	N/A
2A81u01s2	DCT08	14.1	1.41	0.9	1	14.1	0	1	0.0144	0.01656	$3.5\ 10^4$	N/A
2A81u01s3	CCT11	14.1	1.41	0.9	1	14.1	0	1	0.0197	0.02254	$2.6\ 10^4$	V
2A81u05s1	CCT09	14.1	1.41	0.9	5	14.1	0	1	0.03	0.03992	$36\ 10^4$	N/A
2A81u05s2	DCT08	14.1	1.41	0.9	5	14.1	0	1	0.017	0.0225	$15\ 10^4$	N/A
2A81u05s3	CCT11	14.1	1.41	0.9	5	14.1	0	1	0.0238	0.0294	$12\ 10^4$	V
2A81u05s4	CCT13	14.1	1.41	0.9	5	14.1	0	1	0.02	0.0229	$12\ 10^4$	V
2A81u10s1	CCT12	14.1	1.41	0.9	10	14.1	0	1	0.033	0.04363	$63\ 10^4$	N/A
2A81u10s2	DCT08	14.1	1.41	0.9	10	14.1	0	1	0.0285	0.0325	$16.5\ 10^4$	N/A
2A81u10s3	CCT11	14.1	1.41	0.9	10	14.1	0	1	0.0304	0.03457	$16.5\ 10^4$	V
2A81u10s4	CCT13	14.1	1.41	0.9	10	14.1	0	1	0.0168	0.0191	$16.5\ 10^4$	V
2A81u10s5	CCT15	14.1	1.41	0.9	10	14.1	0	1	0.0165	0.01753	$6.5\ 10^4$	V
2A81u10s6	DCT 09	7.05	1.41	0.8	10	7.05	0	1	0.0167	0.01727	$55\ 10^4$	V
2A81u10s7	CCT 16	17.63	1.41	0.92	10	17.63	0	1	0.0155	0.01662	$5.5\ 10^4$	V
2A81u10s8	CCT 16	17.63	1.41	0.92	10	17.63	0	1	0.0166	0.0178	$5.5\ 10^4$	V
2A81u10s9	CCT 16	23.5	1.41	0.94	10	23.5	0	1	0.0321	0.0381	$4.4\ 10^4$	V
2A81u10s10	DCT 09	14.1	1.41	0.9	10	9.87	0.3	1	0.0234	0.0251	$13.7\ 10^4$	V
2A81u10s11	CCT 16	14.1	1.41	0.9	10	7.05	0.5	1	0.0321	0.0337	$33\ 10^4$	v
2A81u10s12	DCT 09	14.1	4.23	0.7	10	14.1	0	1	0.0197	0.0217	$5.5\ 10^4$	v
2A81u10s13	CCT 16	14.1	8.46	0.4	10	14.1	0	1	0.0259	0.0319	$9.9\ 10^4$	V

Table A2._ Crack lengths and loading conditions for SVAL testing on Al 8090. Continue…

Test ID	Sample ID	K_{max} (MPa $m^{1/2}$)	Small Cycles			Underload Cycles			Crack length (m)		Total Number of Cycles	Closure Data
			ΔK_n (MPa $m^{1/2}$)	R_n	n	ΔK_u (MPa $m^{1/2}$)	R_u	n_u	Starting	Final		
2A81u20s1	CCT03	14.1	1.41	0.9	20	14.1	0	1	0.0156	0.02407	105 10^4	N/A
2A81u20s2	DCT08	14.1	1.41	0.9	20	14.1	0	1	0.037	0.03915	21 10^4	N/A
2A81u20s3	CCT11	14.1	1.41	0.9	20	14.1	0	1	0.0355	0.03687	21 10^4	V
2A81u20s4	CCT13	14.1	1.41	0.9	20	14.1	0	1	0.015	0.016	21 10^4	v
2A81u40s1	CCT 16	14.1	1.41	0.9	40	14.1	0	1	0.0232	0.024	105 10^4	V
2A81u80s1	CCT 15	14.1	1.41	0.9	80	14.1	0	1	0.0157	0.0167	105 10^4	V
2A81u100s1	CCT04	14.1	1.41	0.9	100	14.1	0	1	0.0279	0.02889	202 10^4	N/A
2A81u1000s1	CCT04	14.1	1.41	0.9	1000	14.1	0	1	0.0302	0.03154	500.5 10^4	N/A

Table A3._ Crack lengths and loading conditions for SVAL testing on Al 7010

Test ID	Sample ID	K_{max} (MPa $m^{1/2}$)	Small Cycles			Underload Cycles			Crack length (m)		Total Number of Cycles	Closure Data
			ΔK_n (MPa $m^{1/2}$)	R_n	n	ΔK_u (Mpa $m^{1/2}$)	R_u	n_u	Starting	Final		
2A71u01s1	CT 04	12	1.2	0.9	1	12	0	1	0.0308	0.0317	10^4	V
2A71u01s2	CT 04	12	1.2	0.9	1	12	0	1	0.033	0.0335	10^4	N/A
2A71u10s1	CT 04	12	1.2	0.9	10	12	0	1	0.038	0.0401	$8.8\ 10^4$	V
2A71u10s2	CT 05	15	1.2	0.92	10	12	0	1	0.0223	0.0263	$9.9\ 10^4$	V
2A71u10s3	CT 05	20	1.2	0.94	10	12	0	1	0.0191	0.0213	$2.2\ 10^4$	V
2A71u20s1	CT 05	12	1.2	0.9	20	12	0	1	0.0161	0.0174	$16.8\ 10^4$	V
2A71u100s1	CT 04	12	1.2	0.9	100	12	0	1	0.034	0.0345	$30.3\ 10^4$	V

Table A4._ Crack lengths and loading conditions for CAL -Precracking procedures conducted on CT specimens on Ti1023

	Sample ID	Test ID	Following Test	K_{max} (MPa $m^{1/2}$)	R	ΔK_{eff} (Mpa $m^{1/2}$)	Initial crack length (m)	Crack length increment (m)	Total Number of Cycles	Closure Data
CAL - Precracking procedures	c222-16	2Tpr1	2Ti1u10s4	8.16	0.02	8	0.014	0.0009	176.5 10^3	V
	c222-15	2Tpr2	2Ti1u10s6	16.32	0.02	16	0.0318	0.0013	10^3	V
	c222-15	2Tpr3	2Ti1u10s9	15.71	0.02	15.4	0.0251	0.0011	11.5 10^3	V
	c222-15	2Tpr4	2Ti1u10s10	15.71	0.02	15.4	0.0206	0.0017	11 10^3	V
	c222-15	2Tpr5	2Ti1u10s7	15.57	0.05	14.8	0.014	0.0018	19.6 10^3	V
	c222-15	2Tpr6	2Ti1u10s8	14.28	0.3	10	0.0169	0.002	26.5 10^3	V
	c222-15	2Tpr7	-	15.77	0.03	15.3	0.0346	0.002	14 10^3	V
	C222-14	2Tpr8	-	16.1	0	16.1	0.036	0.05	425 10^3	V
				16.6	0	16.6				
				18.5	0	18.5				
				21	0	21				
				25.5	0	25.5				
				28.96	0	28.96				
	C222-14	2Tpr9		15	0	15	0.022	0.003	23 10^3	V
				15.5	0	15.5				
				17	0	17				
	C222-14	2Tpr10	-	11.67	0.4	7	0.016	0.001	54 10^3	V
	C222-14	2Tpr11	-	12	0.4	7.2	0.0194	0.001	51.5 10^3	V

Table A5._ Crack lengths and loading conditions for CAL - Precracking procedures conducted on CT specimens on Al8090

	Sample ID	Test ID	Following Test	K_{max} (MPa $m^{1/2}$)	R	ΔK_{eff} (MPa $m^{1/2}$)	Initial crack length (m)	Crack length increment (m)	Total Number of Cycles	Closure Data
CAL - Precracking procedures	CCT15	2A8pr1	2A81u80s1	14.1	0.4	8.46	0.024	0.0019	16.4 10^3	V
	CCT16	2A8pr2	-	14	0	14	0.0178	0.001522	416 10^3	V
	CCT16	2A8pr3	-	14	0	14	0.0193	0.000989	72 10^3	V
	CCT16	2A8pr4	2A81u40s1	13.33	0.4	8	0.0223	0.00205	755 10^3	V
	CCT15	2A8pr5	2A81u80s1	14	0	14	0.0143	0.001358	19.5 10^3	V
	DCT09	2A8pr6	2A81u10s6	7	0	7	0.014	0.0027	472 10^3	V
	CCT16	2A8pr7	2A81u10s7	17.56	0.1	15.8	0.014	0.001632	11.4 10^3	V
	CCT16	2A8pr8	2A81u10s9	12.5	0.4	7.5	0.034	0.001385	34.5 10^3	V
	DCT09	2A8pr9	2A81u10s12	13.68	0.05	13	0.0176	0.001687	18 10^3	V
	CCT16	2A8pr10	2A81u10s13	11.67	0.4	7	0.024	0.0019	150 10^3	V
	DCT09	2A8pr11	2A81u10s10	10	0.2	8	0.0217	0.0017	68.5 10^3	V
	CCT16	2A8pr12	2A81u10s11	13.3	0.4	8	0.0302	0.0019	23.7 10^3	V
	CCT11	2A8pr13	2A81u01s3	11.1	0.1	10	0.014	0.0057	47.6 10^3	V
	CCT11	2A8pr14	2A81u05s3	11.1	0.1	10	0.0229	0.0009	44.1 10^3	V
	CCT11	2A8pr15	2A81u10s3	11.1	0.1	10	0.0294	0.001	45.4 10^3	V
	CCT11	2A8pr16	-	11.1	0.1	10	0.03457	0.00097	88 10^3	V
	CCT13	2A8pr17	2A81u20s4	11.1	0.1	10	0.014	0.001	28.5 10^3	V
	CCT13	2A8pr18	2A81u10s4	11.1	0.1	10	0.016	0.0008	25.3 10^3	V
	CCT13	2A8pr19	2A81u05s4	11.1	0.1	10	0.0191	0.0009	35 10^3	V
	CCT13	2A8pr20	-	11.1	0.1	10	0.0229	0.0015	50.5 10^3	V
	CCT03	2A8pr21	-	13	0	13	0.0287	0.004	297 10^3	V
				15.2	0	15.2				V
				16	0	16				V

Table A6._ Crack lengths and loading conditions for CAL - Precracking procedures conducted on CT specimens on Al 7010

	Sample ID	Test ID	Following Test	K_{max} (MPa $m^{1/2}$)	R	ΔK_{eff} (MPa $m^{1/2}$)	Initial crack length (m)	Crack length increment (m)	Total Number of Cycles	Closure Data
CAL – Precracking procedures	CT04	2A7pr1	2A71u01s1	12	0	12	0.029	0.0018	$7.83\ 10^3$	V
	CT04	2A7pr2	2A71u10s1	12	0	12	0.0374	0.0006	$3.8\ 10^3$	V
	CT04	2A7pr3	-	12	0	12	0.0355	0.0009	$6.4\ 10^3$	V
	CT05	2A7pr4	2A71u20s1	10	0.3	7	0.0145	0.0016	$18.5\ 10^3$	V
	CT04	2A7pr5	2A71u100s1	12	0	12	0.0328	0.0012	$8\ 10^3$	V
	CT05	2A7pr6	2A71u10s2	14.6	0.04	14	0.0213	0.001	$6.7\ 10^3$	V

Table A7._ Test Results for SVAL testing on Ti 1023

Test ID	K_{max} (MPa $m^{1/2}$)	R_u	R_n	Crack length (m)		$(da/dN)_n$		$(da/dN)_u$		Acceleration Factors			K_0 (MPa $m^{1/2}$)	K_0/K_{max}
				Starting	Final	test	Lin. Sum	test	Lin. Sum	α	β	γ		
2Ti1u01s1	15.7	0	0.9	0.0223	0.0255	$8.25\ 10^{-8}$	$4.66\ 10^{-8}$	$1.65\ 10^{-7}$	$9.32\ 10^{-8}$	1.77	1.59	1.44	N/A	N/A
2Ti1u01s2	15.7	0	0.9	0.0204	0.0218	$6.05\ 10^{-8}$	$4.96\ 10^{-8}$	$1.21\ 10^{-7}$	$9.91\ 10^{-8}$	1.22	1.65	1.23	N/A	N/A
2Ti1u05s1	15.7	0	0.9	0.029	0.0390	$2.34\ 10^{-8}$	$1.41\ 10^{-8}$	$1.40\ 10^{-7}$	$8.44\ 10^{-8}$	1.66	1.55	1.92	N/A	N/A
2Ti1u05s2	15.7	0	0.9	0.0171	0.0194	$2.12\ 10^{-8}$	$1.68\ 10^{-8}$	$1.27\ 10^{-7}$	$1.01\ 10^{-7}$	1.26	1.71	1.3	N/A	N/A
2Ti1u10s1	15.7	0	0.9	0.014	0.01806	$1.48\ 10^{-8}$	$1.00\ 10^{-8}$	$1.63\ 10^{-7}$	$1.10\ 10^{-7}$	1.48	1.34	1.41	N/A	N/A
2Ti1u10s2	15.7	0	0.9	0.0145	0.0161	$1.05\ 10^{-8}$	$8.57\ 10^{-9}$	$1.16\ 10^{-7}$	$9.43\ 10^{-8}$	1.23	1.67	1.17	N/A	N/A
2Ti1u10s3	15.7	0	0.9	0.0287	0.0297	$1.26\ 10^{-8}$	$7.43\ 10^{-9}$	$1.39\ 10^{-7}$	$8.17\ 10^{-8}$	1.70	1.55	1.53	4.40	0.28
2Ti1u10s4	7.85	0	0.8	0.0149	0.0156	$1.30\ 10^{-9}$	$1.10\ 10^{-9}$	$1.43\ 10^{-8}$	$1.21\ 10^{-8}$	1.18	1.18	1.17	2.28	0.29
2Ti1u10s5	19.63	0	0.92	0.031	0.0318	$2.70\ 10^{-8}$	$1.32\ 10^{-8}$	$2.97\ 10^{-7}$	$1.45\ 10^{-7}$	2.04	1.9	1.95	3.73	0.19
2Ti1u10s6	26.17	0	0.94	0.0331	0.0346	$4.33\ 10^{-8}$	$2.44\ 10^{-8}$	$4.76\ 10^{-7}$	$2.68\ 10^{-7}$	1.77	1.42	1.42	6.54	0.25
2Ti1u10s7	15.7	0.3	0.9	0.0158	0.0169	$1.00\ 10^{-8}$	$3.86\ 10^{-9}$	$1.10\ 10^{-7}$	$4.25\ 10^{-8}$	2.59	2.2	2.27	5.50	0.35
2Ti1u10s8	15.7	0.5	0.9	0.0189	0.020	$2.25\ 10^{-9}$	$1.82\ 10^{-9}$	$2.48\ 10^{-8}$	$2.00\ 10^{-8}$	1.23	1.44	1.47	9.11	0.58
2Ti1u10s9	15.7	0	0.7	0.0262	0.0273	$2.68\ 10^{-8}$	$1.41\ 10^{-8}$	$1.64\ 10^{-7}$	$8.17\ 10^{-8}$	1.90	1.8	1.82	3.93	0.25
2Ti1u10s10	15.7	0	0.4	0.0223	0.0251	$6.73\ 10^{-8}$	$3.50\ 10^{-8}$	$1.52\ 10^{-7}$	$8.17\ 10^{-8}$	1.92	1.75	1.8	4.24	0.27
2Ti1u20s1	15.7	0	0.9	0.026	0.03448	$7.80\ 10^{-9}$	$5.37\ 10^{-9}$	$1.64\ 10^{-7}$	$1.13\ 10^{-7}$	1.45	1.43	1.66	N/A	N/A
2Ti1u20s2	15.7	0	0.9	0.0357	0.0370	$6.21\ 10^{-9}$	$4.07\ 10^{-9}$	$1.30\ 10^{-7}$	$8.54\ 10^{-8}$	1.53	1.57	1.63	N/A	N/A
2Ti1u100s1	15.7	0	0.9	0.0185	0.02129	$1.50\ 10^{-9}$	$9.88\ 10^{-10}$	$1.52\ 10^{-7}$	$9.98\ 10^{-8}$	1.52	1.45	1.60	N/A	N/A
2Ti1u1000s1	15.7	0	0.9	0.037	0.03769	$1.22\ 10^{-10}$	$8.0\ 10^{-11}$	$1.22\ 10^{-7}$	$8.01\ 10^{-8}$	1.52	1.713	1.50	N/A	N/A
2Ti1u1000s2	15.7	0	0.9	0.0389	0.0397	$1.63\ 10^{-10}$	$9.4\ 10^{-11}$	$1.63\ 10^{-7}$	$9.41\ 10^{-8}$	1.73	1.9	1.88	N/A	N/A

Table A7._ Test Results for SVAL testing on Ti 1023. Continue…

Test ID	K_{max} (MPa $m^{1/2}$)	R_u	R_n	Crack length (m)		$(da/dN)_s$		$(da/dN)_u$		Acceleration Factors			K_0 (MPa $m^{1/2}$)	K_0/K_{max}
				Starting	Final	Test	Lin. Sum	Test	Lin. Sum	α	β	γ		
71	6.34	0	0.7	0.0246	0.02492	$3.0\ 10^{-10}$	$3.0\ 10^{-10}$	N/A	N/A	(1)	(1)	(1)	N/A	N/A
72	6.34	0	0.7	0.014	0.0141	$<10^{-10}$	$<10^{-10}$	N/A	N/A	(1)	(1)	(1)	N/A	N/A
73	6.34	0	0.7	0.016	0.0162	$<10^{-10}$	$<10^{-10}$	N/A	N/A	(1)	(1)	(1)	N/A	N/A
74	6.34	0	0.7	0.0165	0.0165	$<10^{-10}$	$<10^{-10}$	N/A	N/A	(1)	(1)	(1)	N/A	N/A
75	6.34	0	0.7	0.015	0.015	$<10^{-10}$	$<10^{-10}$	N/A	N/A	(1)	(1)	(1)	N/A	N/A
76	6.34	0	0.7	0.0147	0.01471	$<10^{-10}$	$<10^{-10}$	N/A	N/A	(1)	(1)	(1)	N/A	N/A
77	6.34	0	0.7	0.0175	0.01751	$<10^{-10}$	$<10^{-10}$	N/A	N/A	(1)	(1)	(1)	N/A	N/A
78	6.34	0	0.7	0.0185	0.0185	$<10^{-10}$	$<10^{-10}$	N/A	N/A	(1)	(1)	(1)	N/A	N/A
79	6.34	0	0.7	0.0225	0.02252	$<10^{-10}$	$<10^{-10}$	N/A	N/A	(1)	(1)	(1)	N/A	N/A
710	6.34	0	0.7	0.0235	0.023	$<10^{-10}$	$<10^{-10}$	N/A	N/A	(1)	(1)	(1)	N/A	N/A
711	6.34	0.3	0.7	0.02557	0.0259	$<10^{-10}$	$<10^{-10}$	N/A	N/A	(1)	(1)	(1)	N/A	N/A
712	6.34	0.5	0.7	0.0275	0.0274	$<10^{-10}$	$<10^{-10}$	N/A	N/A	(1)	(1)	(1)	N/A	N/A
713	6.34	0	0.7	0.0295	0.0294	$<10^{-10}$	$<10^{-10}$	N/A	N/A	(1)	(1)	(1)	N/A	N/A
714	6.34	0	0.7	0.0305	0.0305	$<10^{-10}$	$<10^{-10}$	N/A	N/A	(1)	(1)	(1)	N/A	N/A
715	6.34	0	0.7	0.0315	0.03151	$<10^{-10}$	$<10^{-10}$	N/A	N/A	(1)	(1)	(1)	N/A	N/A
716	6.34	0	0.7	0.014	0.01404	$<10^{-10}$	$<10^{-10}$	N/A	N/A	(1)	(1)	(1)	N/A	N/A
717	6.34	0	0.7	0.015	0.01503	$<10^{-10}$	$<10^{-10}$	N/A	N/A	(1)	(1)	(1)	N/A	N/A
718	6.34	0	0.7	0.017	0.01701	$<10^{-10}$	$<10^{-10}$	N/A	N/A	(1)	(1)	(1)	N/A	N/A
719	6.34	0	0.7	0.0235	0.03251	$<10^{-10}$	$<10^{-10}$	N/A	N/A	(1)	(1)	(1)	N/A	N/A
720	6.34	0	0.7	0.0255	0.02559	$<10^{-10}$	$<10^{-10}$	N/A	N/A	(1)	(1)	(1)	N/A	N/A
721	6.34	0	0.7	0.0275	0.02752	$<10^{-10}$	$<10^{-10}$	N/A	N/A	(1)	(1)	(1)	N/A	N/A
722	6.34	0	0.7	0.0325	0.0325	$<10^{-10}$	$<10^{-10}$	N/A	N/A	(1)	(1)	(1)	N/A	N/A

Table A7._ Test Results for SVAL testing on Ti 1023. Continue…

Test ID	K_{max} (MPa $m^{1/2}$)	R_u	R_n	Crack length (m)		$(da/dN)_s$		$(da/dN)_u$		Acceleration Factors			K_0 (MPa $m^{1/2}$)	K_0/K_{max}
				Starting	Final	Test	Lin. Sum	test	Lin. Sum	α	β	γ		
723	6.34	0	0.7	0.02251	0.02262	$<10^{-10}$	$<10^{-10}$	N/A	N/A	(1)	(1)	(1)	N/A	N/A
724	6.34	0	0.7	0.0207	0.02081	$<10^{-10}$	$<10^{-10}$	N/A	N/A	(1)	(1)	(1)	N/A	N/A
725	6.34	0	0.7	0.0215	0.02152	$<10^{-10}$	$<10^{-10}$	N/A	N/A	(1)	(1)	(1)	N/A	N/A
726	6.34	0	0.7	0.0245	0.02455	$<10^{-10}$	$<10^{-10}$	N/A	N/A	(1)	(1)	(1)	N/A	N/A
727	6.34	0	0.7	0.0265	0.02563	$<10^{-10}$	$<10^{-10}$	N/A	N/A	(1)	(1)	(1)	N/A	N/A
728	6.34	0	0.7	0.0285	0.02857	$<10^{-10}$	$<10^{-10}$	N/A	N/A	(1)	(1)	(1)	N/A	N/A
729	6.34	0	0.7	0.0295	0.02953	$<10^{-10}$	$<10^{-10}$	N/A	N/A	(1)	(1)	(1)	N/A	N/A
730	6.34	0	0.7	0.016	0.01609	$<10^{-10}$	$<10^{-10}$	N/A	N/A	(1)	(1)	(1)	N/A	N/A

Table A8._ Test Results for SVAL testing on Al 8090

Test ID	K_{max} (MPa $m^{1/2}$)	R_u	R_n	Crack length (m)		$(da/dN)_s$		$(da/dN)_u$		Acceleration Factors			K_0 (MPa $m^{1/2}$)	K_0/K_{max}
				Starting	Final	Test	Lin. Sum	Test	Lin. Sum	α	β	γ		
2A81u01s1	14.1	0	0.9	0.0315	0.03553	$5.20\ 10^{-8}$	$1.88\ 10^{-8}$	$1.04\ 10^{-7}$	$3.76\ 10^{-8}$	2.77	3.06	3.68	N/A	N/A
2A81u01s2	14.1	0	0.9	0.0144	0.01656	$7.00\ 10^{-8}$	$1.44\ 10^{-8}$	$1.40\ 10^{-7}$	$2.88\ 10^{-8}$	4.86	5.2	5.6	N/A	N/A
2A81u01s3	14.1	0	0.9	0.0197	0.02254	$1.10\ 10^{-7}$	$1.65\ 10^{-8}$	$2.20\ 10^{-7}$	$3.30\ 10^{-8}$	6.67	6.67	10.04	7.60	0.54
2A81u05s1	14.1	0	0.9	0.03	0.03992	$2.17\ 10^{-8}$	$4.89\ 10^{-9}$	$1.30\ 10^{-7}$	$2.93\ 10^{-8}$	4.43	4.29	7.81	N/A	N/A
2A81u05s2	14.1	0	0.9	0.017	0.0225	$3.69\ 10^{-8}$	$4.88\ 10^{-9}$	$2.21\ 10^{-7}$	$2.93\ 10^{-8}$	7.56	6.9	10.9	N/A	N/A
2A81u05s3	14.1	0	0.9	0.0238	0.0294	$4.16\ 10^{-8}$	$5.89\ 10^{-9}$	$2.50\ 10^{-7}$	$3.53\ 10^{-8}$	7.07	9.8	14.14	7.18	0.51
2A81u05s4	14.1	0	0.9	0.02	0.0229	$2.60\ 10^{-8}$	$6.20\ 10^{-9}$	$1.56\ 10^{-7}$	$3.72\ 10^{-8}$	4.19	9.8	14.14	6.16	0.44
2A81u10s1	14.1	0	0.9	0.033	0.04363	$2.05\ 10^{-8}$	$2.72\ 10^{-9}$	$2.26\ 10^{-7}$	$2.99\ 10^{-8}$	7.55	4.93	13.67	N/A	N/A
2A81u10s2	14.1	0	0.9	0.0285	0.0325	$2.66\ 10^{-8}$	$2.83\ 10^{-9}$	$2.92\ 10^{-7}$	$3.11\ 10^{-8}$	9.39	9.2	12.5	N/A	N/A
2A81u10s3	14.1	0	0.9	0.0304	0.03457	$2.65\ 10^{-8}$	$2.99\ 10^{-9}$	$2.92\ 10^{-7}$	$3.29\ 10^{-8}$	8.87	9.6	13.06	4.79	0.34
2A81u10s4	14.1	0	0.9	0.0168	0.0191	$1.60\ 10^{-8}$	$2.00\ 10^{-9}$	$1.76\ 10^{-7}$	$2.20\ 10^{-8}$	8.00	7.06	6.3	5.04	0.36
2A81u10s5	14.1	0	0.9	0.0165	0.01753	$1.55\ 10^{-8}$	$1.93\ 10^{-9}$	$1.71\ 10^{-7}$	$2.13\ 10^{-8}$	8.04	7.7	8.04	4.64	0.33
2A81u10s6	7.05	0	0.8	0.0167	0.01727	$1.00\ 10^{-9}$	$2.90\ 10^{-9}$	$1.10\ 10^{-8}$	$3.19\ 10^{-9}$	3.45	3.31	3.38	3.03	0.43
2A81u10s7	17.63	0	0.92	0.0155	0.01662	$2.90\ 10^{-8}$	$4.70\ 10^{-9}$	$3.19\ 10^{-7}$	$5.17\ 10^{-8}$	6.17	6.65	6.81	6.63	0.38
2A81u10s8	17.63	0	0.92	0.0166	0.0178	$2.35\ 10^{-8}$	$4.70\ 10^{-9}$	$2.59\ 10^{-7}$	$5.17\ 10^{-8}$	5.00	4.8	5.2	7.76	0.44
2A81u10s9	23.5	0	0.94	0.0321	0.0381	$1.30\ 10^{-7}$	$9.00\ 10^{-9}$	$1.43\ 10^{-6}$	$9.90\ 10^{-8}$	14.44	14.8	13.5	7.29	0.31
2A81u10s10	14.1	0.3	0.9	0.0234	0.0251	$1.40\ 10^{-8}$	$1.60\ 10^{-9}$	$1.54\ 10^{-7}$	$1.76\ 10^{-8}$	8.75	7.65	8.44	5.08	0.52
2A81u10s11	14.1	0.5	0.9	0.0321	0.0337	$5.40\ 10^{-9}$	$1.20\ 10^{-9}$	$5.94\ 10^{-8}$	$1.32\ 10^{-8}$	4.50	4.32	4.89	7.05	0.65
2A81u10s12	14.1	0	0.7	0.0197	0.0217	$2.37\ 10^{-7}$	$1.05\ 10^{-7}$	$7.20\ 10^{-8}$	$3.00\ 10^{-8}$	2.26	2.52	2.5	7.33	0.36
2A81u10s13	14.1	0	0.4	0.0259	0.0319	$8.50\ 10^{-7}$	$1.41\ 10^{-7}$	$4.00\ 10^{-8}$	$2.97\ 10^{-8}$	6.03	7.11	6.46	9.17	0.50

Table A8._ Test Results for SVAL testing on Al 8090. Continue…

Test ID	K_{max} (MPa $m^{1/2}$)	R_u	R_n	Crack length (m)		$(da/dN)_s$		$(da/dN)_u$		Acceleration Factors			K_0 (MPa $m^{1/2}$)	K_0/K_{max}
				Starting	Final	Test	Lin. Sum	Test	Lin. Sum	α	β	γ		
2A81u20s1	14.1	0	0.9	0.0156	0.02407	$8.02\ 10^{-9}$	$1.46\ 10^{-9}$	$1.68\ 10^{-7}$	$3.07\ 10^{-8}$	5.49	4.26	6.5	N/A	N/A
2A81u20s2	14.1	0	0.9	0.037	0.03915	$9.85\ 10^{-9}$	$1.18\ 10^{-9}$	$2.07\ 10^{-7}$	$2.48\ 10^{-8}$	8.35	9.8	11.02	N/A	N/A
2A81u20s3	14.1	0	0.9	0.0355	0.03687	$7.82\ 10^{-9}$	$1.02\ 10^{-9}$	$1.64\ 10^{-7}$	$2.14\ 10^{-8}$	7.67	6.97	7.02	5.93	0.42
2A81u20s4	14.1	0	0.9	0.015	0.016	$8.00\ 10^{-9}$	$1.02\ 10^{-9}$	$1.68\ 10^{-7}$	$2.14\ 10^{-8}$	7.84	7.54	7.68	4.70	0.33
2A81u40s1	14.1	0	0.9	0.0232	0.024	$2.90\ 10^{-9}$	$7.10\ 10^{-10}$	$1.19\ 10^{-7}$	$2.91\ 10^{-8}$	4.08	4.10	5.02	6.63	0.47
2A81u80s1	14.1	0	0.9	0.0157	0.0167	$1.60\ 10^{-9}$	$4.70\ 10^{-10}$	$1.30\ 10^{-7}$	$3.81\ 10^{-8}$	3.40	3.8	3.56	6.35	0.45
2A81u100s1	14.1	0	0.9	0.0279	0.02889	$4.90\ 10^{-10}$	$3.90\ 10^{-10}$	$4.95\ 10^{-8}$	$3.94\ 10^{-8}$	1.26	1.23	1.31	N/A	N/A
2A81u1000s1	14.1	0	0.9	0.0302	0.03154	$3.00\ 10^{-11}$	$3.00\ 10^{-11}$	$3.00\ 10^{-8}$	$3.00\ 10^{-8}$	1.00	1.00	1.00	N/A	N/A

Table A9._ Test Results for SVAL testing on Al 7010

Test ID	K_{max} (MPa $m^{1/2}$)	R_u	R_n	Crack length (m)		$(da/dN)_s$		$(da/dN)_u$		Acceleration Factors			K_0 (MPa $m^{1/2}$)	K_0/K_{max}
				Starting	Final	test	Lin. Sum	test	Lin. Sum	α	β	γ		
2A71u01s1	12	0	0.9	0.0308	0.0317	$1.10\ 10^{-7}$	$9.00\ 10^{-8}$	$2.20\ 10^{-7}$	$1.80\ 10^{-7}$	1.22	1.00	1.00	6.36	0.53
2A71u01s2	12	0	0.9	0.033	0.0335	$1.15\ 10^{-7}$	$9.00\ 10^{-8}$	$2.30\ 10^{-7}$	$1.80\ 10^{-7}$	1.28	1.00	1.00	N/A	N/A
2A71u10s1	12	0	0.9	0.038	0.0401	$2.30\ 10^{-8}$	$1.70\ 10^{-8}$	$2.53\ 10^{-7}$	$1.87\ 10^{-7}$	1.35	1.60	1.46	5.30	0.44
2A71u10s2	15	0	0.92	0.0223	0.0263	$3.90\ 10^{-8}$	$3.90\ 10^{-8}$	$4.29\ 10^{-7}$	$4.29\ 10^{-7}$	1.00	1.00	1.00	7.20	0.48
2A71u10s3	20	0	0.94	0.0191	0.0213	$1.00\ 10^{-7}$	$9.00\ 10^{-8}$	$1.10\ 10^{-7}$	$9.90\ 10^{-7}$	1.11	1.00	1.00	10.24	0.51
2A71u20s1	12	0	0.9	0.0161	0.0174	$9.52\ 10^{-9}$	$9.00\ 10^{-9}$	$2.00\ 10^{-7}$	$1.89\ 10^{-7}$	1.06	1.00	1.00	6.17	0.51
2A71u100s1	12	0	0.9	0.034	0.0345	$2.60\ 10^{-9}$	$1.88\ 10^{-9}$	$2.63\ 10^{-7}$	$1.90\ 10^{-7}$	1.38	1.70	1.97	6.05	0.5

Table A10._ Test Results for CAL -Precracking procedures conducted on CT specimens on Ti 1023

	Test ID	K_{max} (MPa $m^{1/2}$)	R	ΔK_{eff} (Mpa $m^{1/2}$)	Initial crack length (m)	Crack length increment (m)	(da/dN) test	K_0/K_{max}
CAL - Precracking procedures	2Tpr1	8.16	0.02	8	0.014	0.0009	$1.24\ 10^{-8}$	0.36
	2Tpr2	16.32	0.02	16	0.0318	0.0013	$1.55\ 10^{-7}$	0.28
	2Tpr3	15.71	0.02	15.4	0.0251	0.0011	$1.07\ 10^{-7}$	0.31
	2Tpr4	15.71	0.02	15.4	0.0206	0.0017	$1.56\ 10^{-7}$	0.24
	2Tpr5	15.57	0.05	14.8	0.014	0.0018	$1.02\ 10^{-7}$	0.37
	2Tpr6	14.28	0.3	10	0.0169	0.002	$8.00\ 10^{-8}$	0.37
	2Tpr7	15.77	0.03	15.3	0.0346	0.002	$1.50\ 10^{-7}$	0.25
	2Tpr8	16.1	0	16.1	0.036	0.05	$4.32\ 10^{-8}$	0.49
		16.6	0	16.6			$5.00\ 10^{-8}$	0.49
		18.5	0	18.5			$1.00\ 10^{-7}$	0.49
		21	0	21			$1.41\ 10^{-7}$	0.49
		25.5	0	25.5			$2.10\ 10^{-7}$	0.49
		28.96	0	28.96			$3.20\ 10^{-7}$	0.49
	2Tpr9	15	0	15	0.022	0.003	$1.23\ 10^{-7}$	0.33
		15.5	0	15.5			$1.46\ 10^{-7}$	0.33
		17	0	17			$1.52\ 10^{-7}$	0.33
	2Tpr10	11.67	0.4	7	0.016	0.001	$1.90\ 10^{-8}$	0.49
	2Tpr11	12	0.4	7.2	0.0194	0.001	$2.00\ 10^{-8}$	0.48

Table A11._ Test Results for CAL - Precracking procedures conducted on CT specimens on Al8090

	Test ID	K_{max} (MPa $m^{1/2}$)	R	ΔK_{eff} (MPa $m^{1/2}$)	Initial crack length (m)	Crack length increment (m)	(da/dN) test	K_0/K_{max}
CAL - Precracking procedures	2A8pr1	14.1	0.4	8.46	0.024	0.0019	$1.16\ 10^{-7}$	0.40
	2A8pr2	14	0	14	0.0178	0.001522	$9.50\ 10^{-9}$	0.77
	2A8pr3	14	0	14	0.0193	0.000989	$1.05\ 10^{-8}$	0.73
	2A8pr4	13.33	0.4	8	0.0223	0.00205	$9.60\ 10^{-9}$	0.72
	2A8pr5	14	0	14	0.0143	0.001358	$7.00\ 10^{-8}$	0.44
	2A8pr6	7	0	7	0.014	0.0027	$6.80\ 10^{-9}$	0.49
	2A8pr7	17.56	0.1	15.8	0.014	0.001632	$1.90\ 10^{-7}$	0.49
	2A8pr8	12.5	0.4	7.5	0.034	0.001385	$3.95\ 10^{-8}$	0.62
	2A8pr9	13.68	0.05	13	0.0176	0.001687	$9.57\ 10^{-8}$	0.44
	2A8pr10	11.67	0.4	7	0.024	0.0019	$1.60\ 10^{-8}$	0.66
	2A8pr11	10	0.2	8	0.0217	0.0017	$2.71\ 10^{-8}$	0.53
	2A8pr12	13.3	0.4	8	0.0302	0.0019	$8.50\ 10^{-8}$	0.57
	2A8pr13	11.1	0.1	10	0.014	0.0057	$3.60\ 10^{-8}$	0.58
	2A8pr14	11.1	0.1	10	0.0229	0.0009	$1.00\ 10^{-8}$	0.54
	2A8pr15	11.1	0.1	10	0.0294	0.001	$1.50\ 10^{-8}$	0.59
	2A8pr16	11.1	0.1	10	0.03457	0.00097	$1.10\ 10^{-8}$	0.51
	2A8pr17	11.1	0.1	10	0.014	0.001	$1.80\ 10^{-8}$	0.46
	2A8pr18	11.1	0.1	10	0.016	0.0008	$3.40\ 10^{-8}$	0.33
	2A8pr19	11.1	0.1	10	0.0191	0.0009	$2.30\ 10^{-8}$	0.50
	2A8pr20	11.1	0.1	10	0.0229	0.0015	$2.30\ 10^{-8}$	0.36
	2A8pr21	13	0	13	0.0287	0.004	$5.04\ 10^{-8}$	0.60
		15.2	0	15.2			$6.26\ 10^{-8}$	0.56
		16	0	16			$7.20\ 10^{-8}$	0.50

Table A12._ Crack lengths and loading conditions for CAL - Precracking procedures conducted on CT specimens on Al 7010

	Test ID	K_{max} (MPa $m^{1/2}$)	R	ΔK_{eff} (MPa $m^{1/2}$)	Initial crack length (m)	Crack length increment (m)	(da/dN) test	K_0/K_{max}
CAL – Precracking procedures	2A7pr1	12	0	12	0.029	0.0018	$2.30\ 10^{-7}$	0.52
	2A7pr2	12	0	12	0.0374	0.0006	$2.90\ 10^{-7}$	0.50
	2A7pr3	12	0	12	0.0355	0.0009	$2.00\ 10^{-7}$	0.50
	2A7pr4	10	0.3	7	0.0145	0.0016	$1.00\ 10^{-7}$	0.56
	2A7pr5	12	0	12	0.0328	0.0012	$2.00\ 10^{-7}$	0.52
	2A7pr6	14.6	0.04	14	0.0213	0.001	$1.90\ 10^{-7}$	0.59

APPENDIX B

Software Flowchart I

Constant Amplitude Load Case

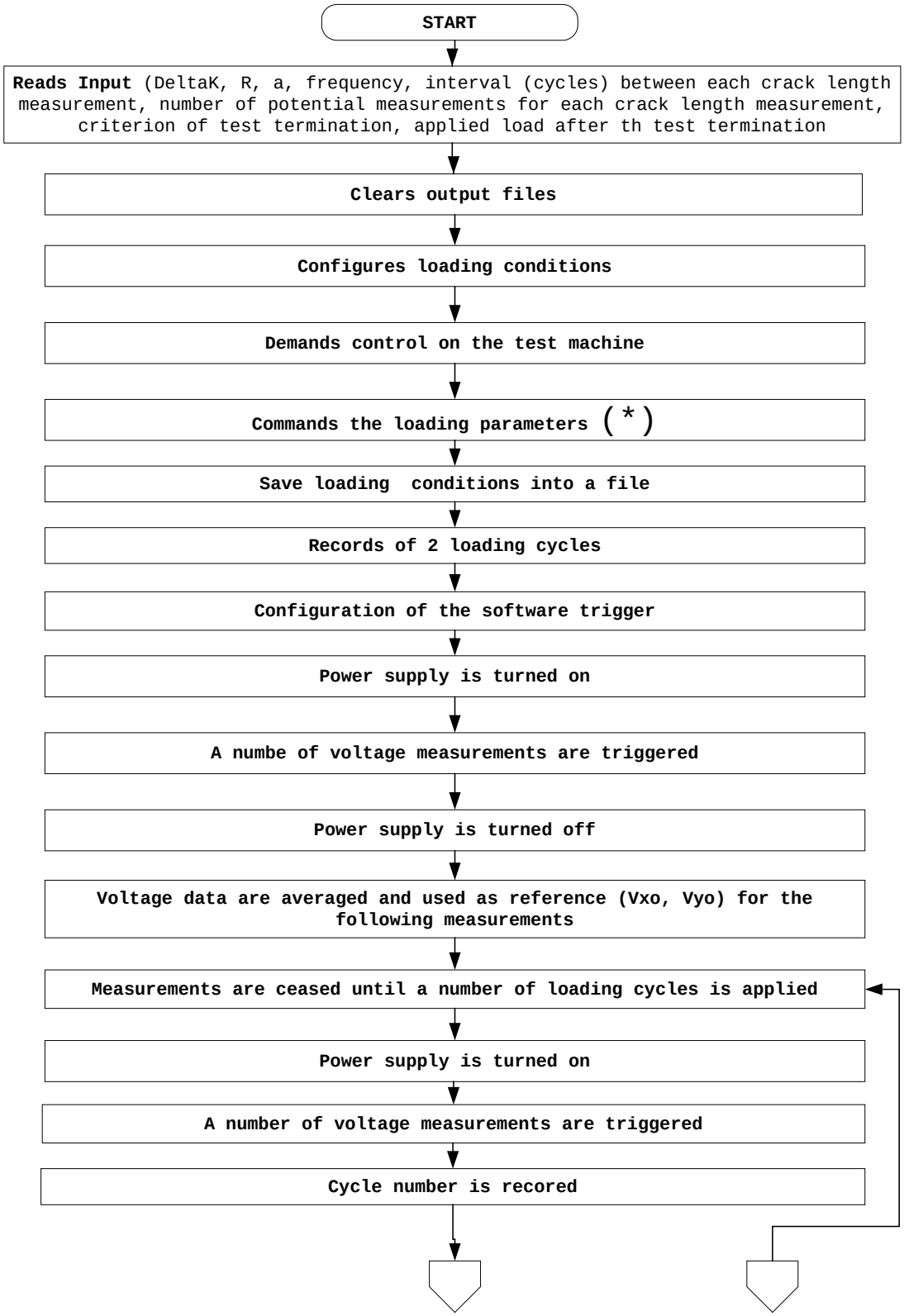

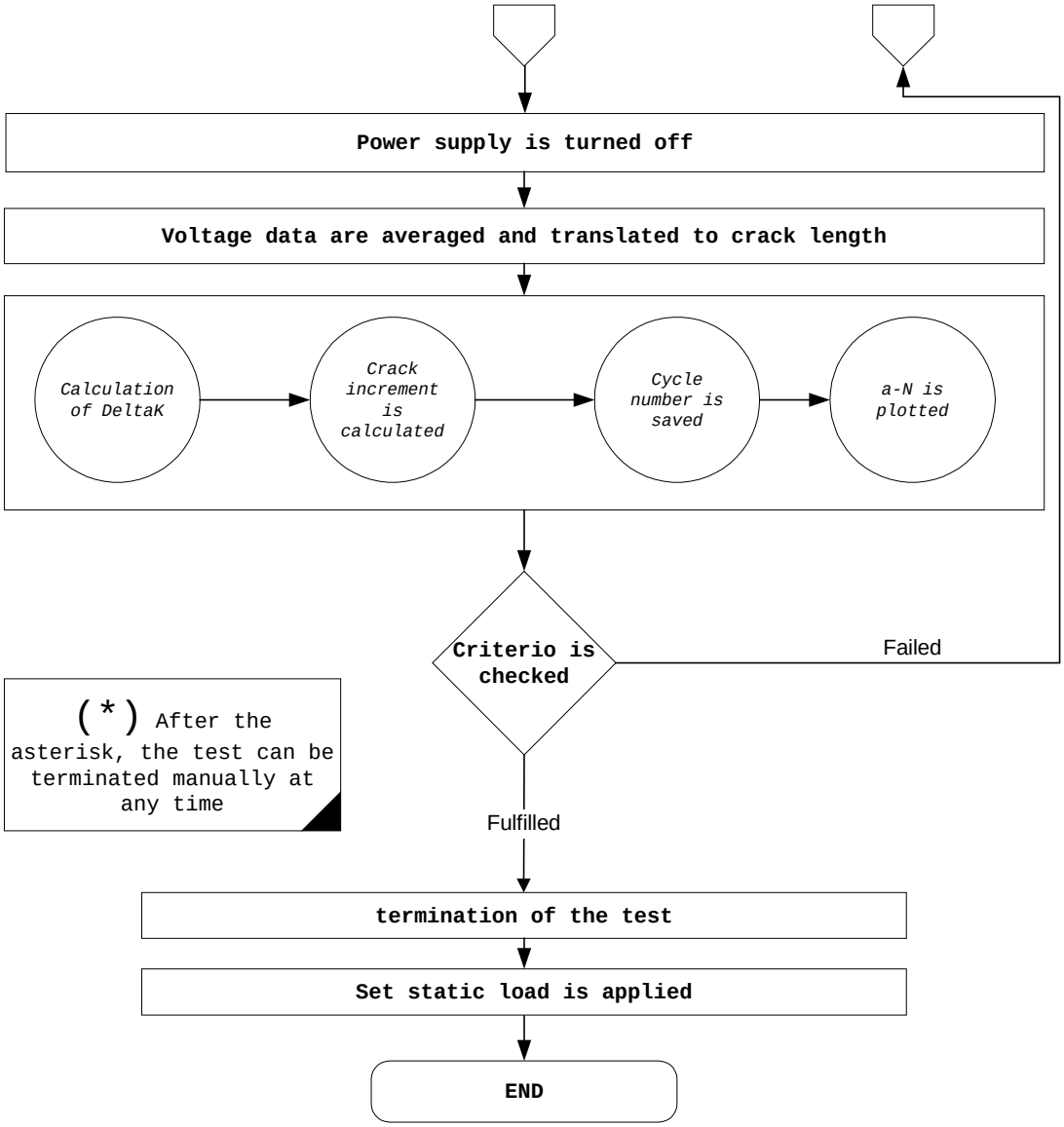
Power supply is turned off
Voltage data are averaged and translated to crack length
Calculation of DeltaK
Crack increment is calculated
Cycle number is saved
a-N is plotted
Criterio is checked
Failed
(*) After the asterisk, the test can be terminated manually at any time
Fulfilled
termination of the test
Set static load is applied
END

Software Flowchart II

Threshold Measurement Case

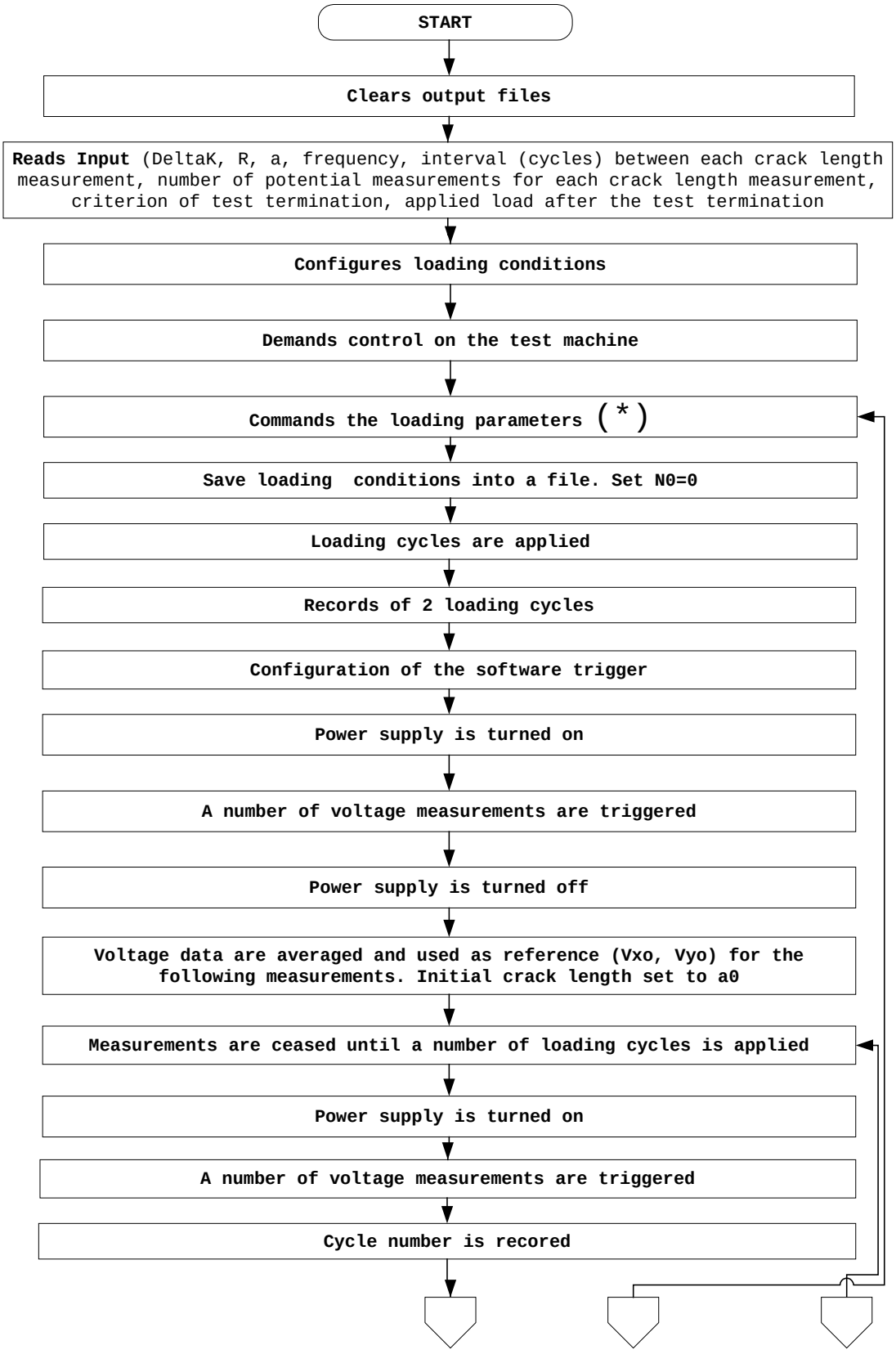

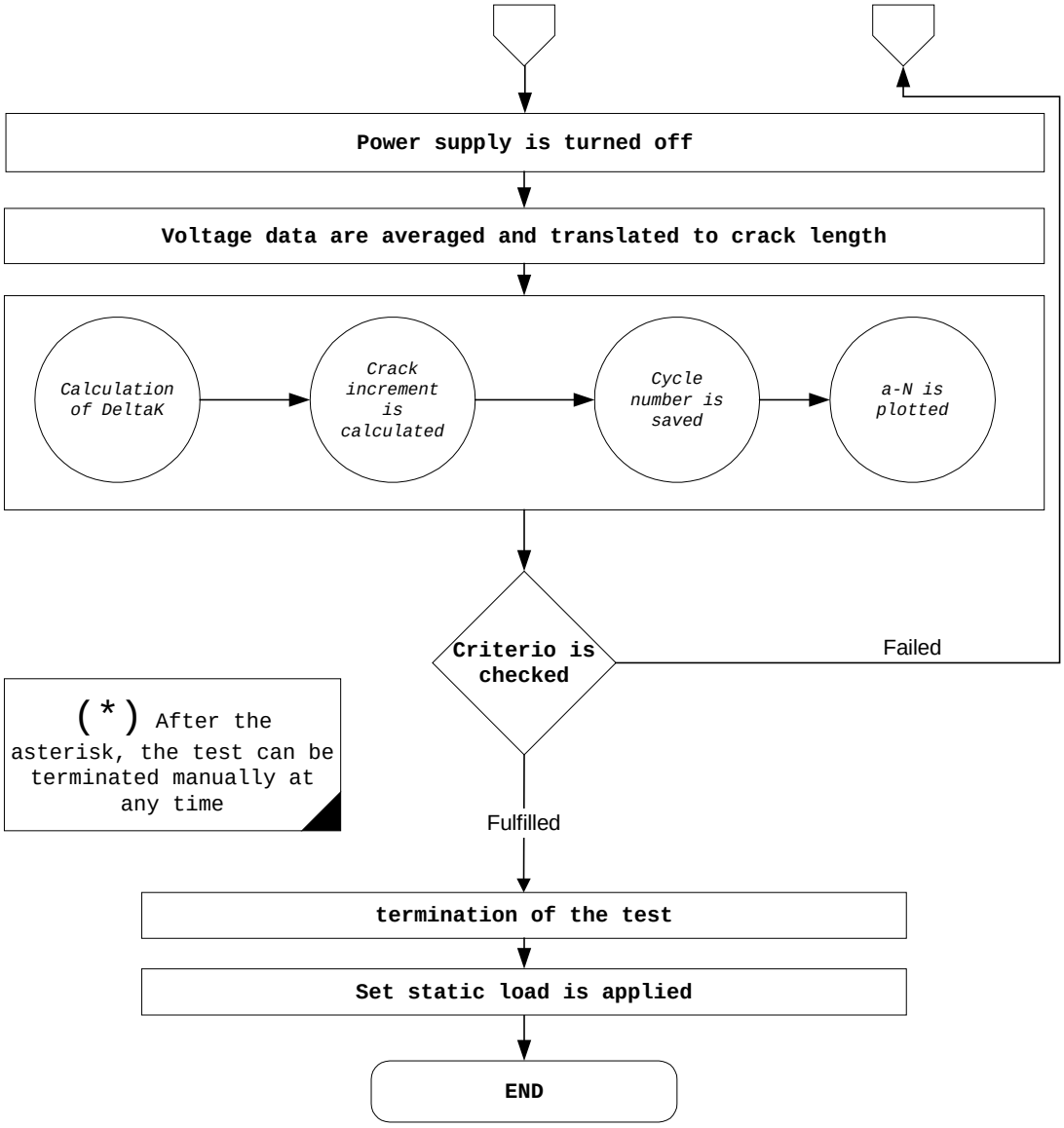
Power supply is turned off
Voltage data are averaged and translated to crack length
Calculation of DeltaK
Crack increment is calculated
Cycle number is saved
a-N is plotted
Criterio is checked
Failed
(*) After the asterisk, the test can be terminated manually at any time
Fulfilled
termination of the test
Set static load is applied
END

Software Flowchart III

Data acquisition Case

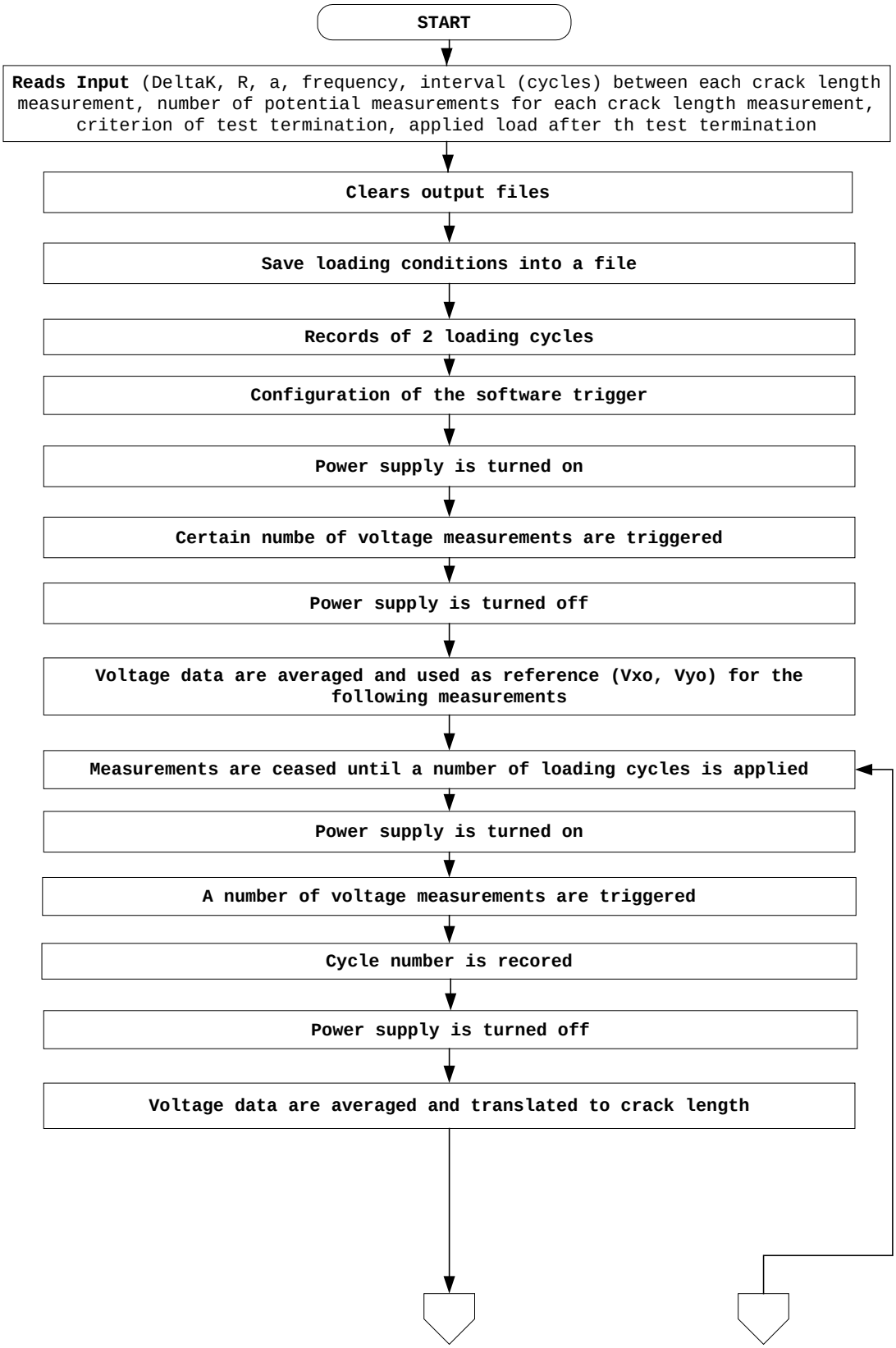

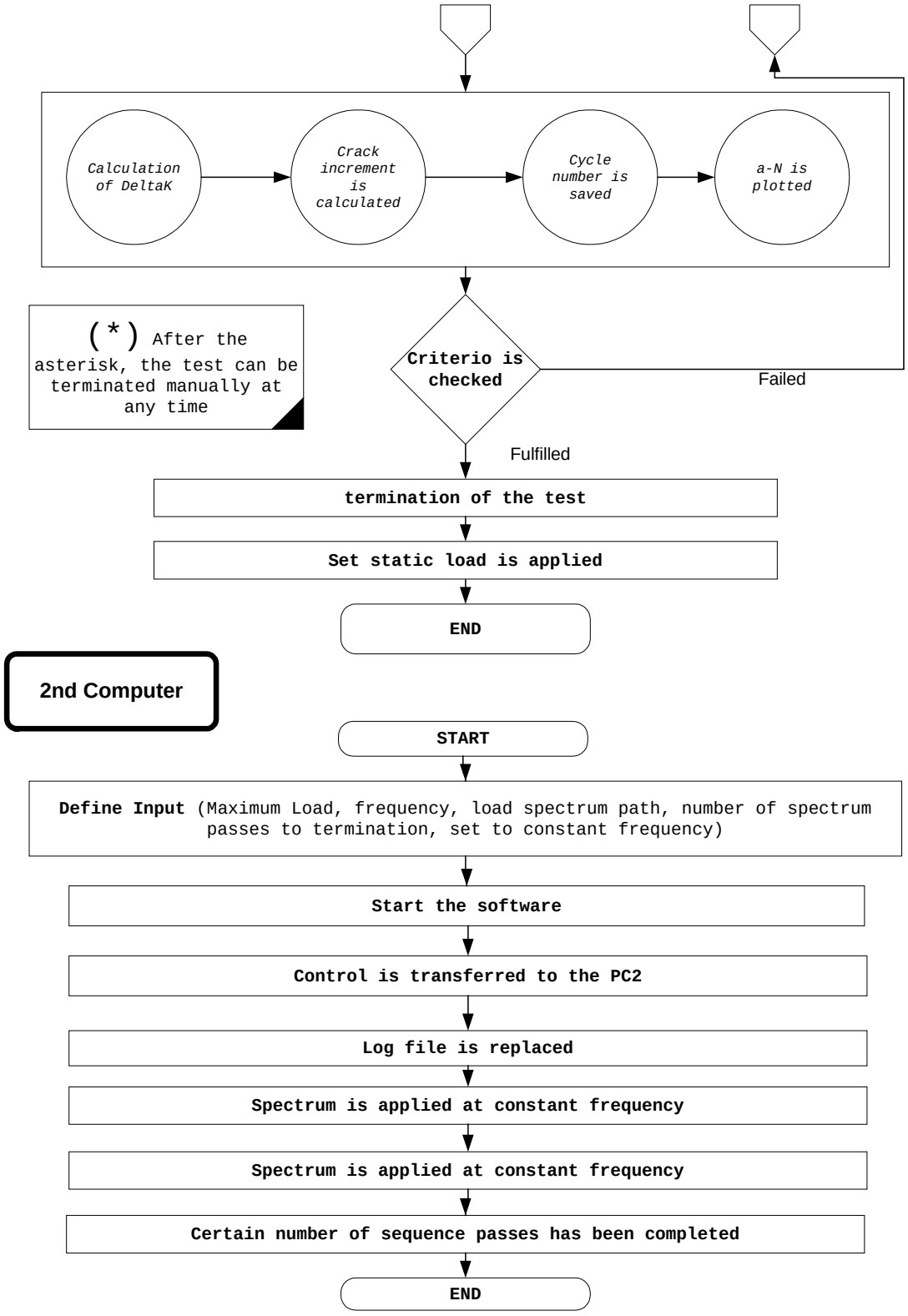
Calculation of DeltaK
Crack increment is calculated
Cycle number is saved
a-N is plotted
(*) After the asterisk, the test can be terminated manually at any time
Criterio is checked
Failed
Fulfilled
termination of the test
Set static load is applied
END
2nd Computer
START
Define Input (Maximum Load, frequency, load spectrum path, number of spectrum passes to termination, set to constant frequency)
Start the software
Control is transferred to the PC2
Log file is replaced
Spectrum is applied at constant frequency
Spectrum is applied at constant frequency
Certain number of sequence passes has been completed
END